



**NATIONAL TECHNICAL UNIVERSITY OF ATHENS
SCHOOL OF CIVIL ENGINEERING
INSTITUTE OF STEEL STRUCTURES**

**INVESTIGATION OF THE APPLICATION OF HIGH-STRENGTH STEEL IN
DISSIPATIVE ELEMENTS**

DOCTORAL THESIS OF
STELLA AVGERINOY

SUPERVISED BY
IOANNIS VAYAS, PROF. NTUA

ATHENS 2020



ΕΘΝΙΚΟ ΜΕΤΣΟΒΙΟ ΠΟΛΥΤΕΧΝΕΙΟ
ΣΧΟΛΗ ΠΟΛΙΤΙΚΩΝ ΜΗΧΑΝΙΚΩΝ
ΕΡΓΑΣΤΗΡΙΟ ΜΕΤΑΛΛΙΚΩΝ ΚΑΤΑΣΚΕΥΩΝ

ΔΙΔΑΚΤΟΡΙΚΗ ΔΙΑΤΡΙΒΗ

ΔΙΕΡΕΥΝΗΣΗ ΤΗΣ ΧΡΗΣΗΣ ΧΑΛΥΒΩΝ ΥΨΗΛΗΣ ΑΝΤΟΧΗΣ ΣΕ
ΣΤΟΙΧΕΙΑ ΑΠΟΡΡΟΦΗΣΗΣ ΕΝΕΡΓΕΙΑΣ

ΣΤΕΛΛΑ ΑΥΓΕΡΙΝΟΥ

ΕΠΙΒΛΕΠΩΝ

ΙΩΑΝΝΗΣ ΒΑΓΙΑΣ, ΚΑΘΗΓΗΤΗΣ ΕΜΠ

ΑΘΗΝΑ 2020



**NATIONAL TECHNICAL UNIVERSITY OF ATHENS
SCHOOL OF CIVIL ENGINEERING
INSTITUTE OF STEEL STRUCTURES**

INVESTIGATION OF THE APPLICATION OF HIGH-STRENGTH STEEL IN DISSIPATIVE ELEMENTS

DOCTORAL THESIS OF

STELLA AVGERINOY

Diploma in Civil Engineering, NTUA 2010

MSc in Analysis and Design of Earthquake Resistant Structures, NTUA 2012

The thesis is submitted to the School of Civil Engineering of the National Technical University of Athens in fulfillment of the requirements for the Degree of Doctor of Philosophy

ADVISORY COMMITTEE

I. VAYAS, Professor NTUA (supervisor)
C. GANTES, Professor NTUA
V. KOUMOYISIS, Emeritus Professor NTUA

EXAMINATION COMMITTEE

I. VAYAS, Professor NTUA (supervisor)
C. GANTES, Professor NTUA
V. KOUMOYISIS, Emeritus Professor NTUA
C.A. CASTIGLIONI, Professor POLIMI
B. HOFFMEISTER, Professor RWTH Aachen
D. VAMVATSIKOS, Assoc, Professor NTUA
P. THANOPOULOS, Lecturer NTUA

ATHENS 2020

© Copyright 2020 by Stella Avgerinou
All Rights Reserved

Neither the whole nor any part of this doctoral thesis may be copied, stored in a retrieval system, distributed, reproduced, translated, or transmitted for commercial purposes, in any form or by any means now or hereafter known, electronic or mechanical, without the written permission from the author. Reproducing, storing and distributing this doctoral thesis for non-profitable, educational or research purposes is allowed, without prejudice to reference to its source and to inclusion of the present text. Any queries in relation to the use of the present doctoral thesis for commercial purposes must be addressed to its author.

Approval of this doctoral thesis by the School of Civil Engineering of the National Technical University of Athens (NTUA) does not constitute in any way an acceptance of the views of the author contained herein by the said academic organisation (L. 5343/1932, art. 202).



**ΕΘΝΙΚΟ ΜΕΤΣΟΒΙΟ ΠΟΛΥΤΕΧΝΕΙΟ
ΣΧΟΛΗ ΠΟΛΙΤΙΚΩΝ ΜΗΧΑΝΙΚΩΝ
ΕΡΓΑΣΤΗΡΙΟ ΜΕΤΑΛΛΙΚΩΝ ΚΑΤΑΣΚΕΥΩΝ**

ΔΙΔΑΚΤΟΡΙΚΗ ΔΙΑΤΡΙΒΗ

**ΔΙΕΡΕΥΝΗΣΗ ΤΗΣ ΧΡΗΣΗΣ ΧΑΛΥΒΩΝ ΥΨΗΛΗΣ ΑΝΤΟΧΗΣ ΣΕ
ΣΤΟΙΧΕΙΑ ΑΠΟΡΡΟΦΗΣΗΣ ΕΝΕΡΓΕΙΑΣ**

ΣΤΕΛΛΑ ΑΥΓΕΡΙΝΟΥ

Δίπλωμα Πολιτικού Μηχανικού, ΕΜΠ 2010

Μεταπτυχιακό Δίπλωμα Ειδίκευσης «Δομοστατικός Σχεδιασμός και Ανάλυση Κατασκευών», ΕΜΠ
2012

Η διατριβή υποβλήθηκε στη Σχολή Πολιτικών Μηχανικών του Εθνικού Μετσόβιου Πολυτεχνείου
προς εκπλήρωση των προϋποθέσεων του τίτλου της Διδάκτορος Μηχανικού

ΤΡΙΜΕΛΗΣ ΣΥΜΒΟΥΛΕΥΤΙΚΗ ΕΠΙΤΡΟΠΗ

Ι. ΒΑΓΙΑΣ, Καθηγητής ΕΜΠ (επιβλέπων)
Χ. ΓΑΝΤΕΣ, Καθηγητής ΕΜΠ
Β. ΚΟΥΜΟΥΣΗΣ, Ομότιμος Καθηγητής ΕΜΠ

ΕΠΤΑΜΕΛΗΣ ΕΞΕΤΑΣΤΙΚΗ ΕΠΙΤΡΟΠΗ

Ι. ΒΑΓΙΑΣ, Καθηγητής ΕΜΠ (επιβλέπων)
Χ. ΓΑΝΤΕΣ, Καθηγητής ΕΜΠ
Β. ΚΟΥΜΟΥΣΗΣ, Ομότιμος Καθηγητής ΕΜΠ
C.A. CASTIGLIONI, Professor POLIMI
B. HOFFMEISTER, Professor RWTH Aachen
Δ. ΒΑΜΒΑΤΣΙΚΟΣ, Επικ. Καθηγητής ΕΜΠ
Π. ΘΑΝΟΠΟΥΛΟΣ, Λέκτορας ΕΜΠ

ΑΘΗΝΑ 2020

© Copyright 2020 Στέλλα Αυγερινού
Με επιφύλαξη παντός δικαιώματος

Απαγορεύεται η αντιγραφή, αποθήκευση σε αρχείο πληροφοριών, διανομή, αναπαραγωγή, μετάφραση ή μετάδοση της παρούσας εργασίας, εξ ολοκλήρου ή τμήματος αυτής, για εμπορικό σκοπό, υπό οποιαδήποτε μορφή και με οποιοδήποτε μέσο επικοινωνίας, ηλεκτρονικό ή μηχανικό, χωρίς την προηγούμενη έγγραφη άδεια του συγγραφέα. Επιτρέπεται η αναπαραγωγή, αποθήκευση και διανομή για σκοπό μη κερδοσκοπικό, εκπαιδευτικής ή ερευνητικής φύσης, υπό την προϋπόθεση να αναφέρεται η πηγή προέλευσης και να διατηρείται το παρόν μήνυμα. Ερωτήματα που αφορούν στη χρήση της εργασίας για κερδοσκοπικό σκοπό πρέπει να απευθύνονται προς το συγγραφέα.

Η έγκριση της διδακτορικής διατριβής από την Ανώτατη Σχολή Πολιτικών Μηχανικών του Εθνικού Μετσόβιου Πολυτεχνείου δεν υποδηλώνει αποδοχή των απόψεων του συγγραφέως (Ν. 5343/1932, Άρθρο 202).

To my daughter, Electra

To my mother, Maria

Στην κόρη μου και τη μάνα μου

Acknowledgements

First, I would like to express my gratitude to my supervisor Prof. Ioannis Vayas for his support, trust and collaboration during all these years. His inclination to combine experimental with analytical approaches in research and engineering practice, has been inspiring. Furthermore, he is a professor whose door is always open for his students, literally and figuratively. His scientific guidance and motivation have been invaluable. I would like to thank him for all the above and for his respectful treatment.

I would also like to deeply thank professors Charis Gantes and Vlassis Koumousis, members of my advisory committee, for their kind support and advice through the years. I would also like to express my appreciation to the rest members of my examination committee, professors Carlo Andrea Castiglioni, Benno Hoffmeister, Dimitrios Vamvatsikos and Pavlos Thanopoulos for taking the time to read my research and providing constructive comments. Prof. C.A. Castiglioni was supervising my MSc thesis on steel racks in Milano and provided me with valuable guidance while introduced me to the “world” of research projects; for all that I am deeply grateful. Prof. B. Hoffmeister was supervising the research project (“MATCH”) via which I obtained most of the experimental data used in this dissertation. Prof. D. Vamvatsikos has been a valuable source of advice and information since the first time I ran a dynamic analysis in OpenSees. P. Thanopoulos has been a valuable advisor as I would often address to him to discuss concerns about design or test-related issues.

Part of this research was carried out in the frame of the European research project “MATCH”. The financial contribution of the Research Fund for Coal and Steel (RFCS) of the European Community is acknowledged. I would like to thank all participants in the project for the productive and pleasant cooperation. Special thanks to the PhD students of University of Aachen and University of Thessaly with whom we had a closer collaboration.

During my time in the Institute of Steel Structures as a PhD student, I had the luck and opportunity to engage in numerous experimental campaigns. None of these would have been the same without the assistance of Dr. Xenofon Lignos and his passion for setting-up tests and creating new equipment in the Laboratory. In addition, the technical support by Stelios Katsatsidis and Spiros Papaveros was essential for the successful execution of the tests.

At the same time, I had the chance to work along talented students, researchers and engineers who helped me learn new things and largely contributed in creating a good working environment in NTUA. First of all, I would like to express my deepest gratitude to Dr. K. Adamakos with whom we had been working together since the first day I joined the Institute of Steel Structures. He has been

an excellent colleague to share an office with. Through the years, he has provided me with invaluable scientific and psychological support. Special thanks to M.E. Dasiou with whom we have often collaborated and who has always been willing to share her great engineering and research experience. Her expertise in Abaqus and mostly, her sense of humor have been valuable to me through our common time in the Laboratory. Many thanks to Dr. G. Dougka and Dr. D. Dimakogianni, for introducing me to the FUSEIS systems and providing guidance during my first steps as a researcher in NTUA. I would also like to express my gratitude to A. Spiliopoulos to whom I often addressed questions when designing the set-up for the MRF tests and who has always been eager to help me. Special thanks to Dr. K. Bakalis for sharing his expertise in performance-based earthquake engineering and answering my questions even after he had left NTUA and moved to Lausanne. Many thanks to PhD student D. Tsarpalis, for helping me combine my IDA results with the D.V. matlab routines. His help saved me computational time in a period when I was very stressed for time. I would also like to thank my former colleagues (many of them have made the transition from PhD students to Doctors) V. Melissianos, I. Thanasoulas, V. Karlos, P. Tsarpalis, S. Vernardos, Z. Fasoulakis for the collaboration and the time we shared in the Laboratory as well as some of the newest members, PhD students A. Chatzidaki, K. Vlachakis and S. Antonodimitraki.

I have been lucky enough to share my life with good friends. Amongst them I would like to express my deepest gratitude to Dafni, Eleana and Yiannos who have been by my side during all my endeavors and have never stopped having faith in me, even when I felt completely deprived of it.

Finally I would like to express my deepest gratitude to my family for supporting me in so many ways through the years. My father, being a civil engineer, has always been my advisor since I started my studies in NTUA. My mother is probably my biggest fan. If it were not for her help, especially during the last year where she took care of my baby, I would not have been able to complete my dissertation. My sister has been encouraging me in all phases of my life. My beloved Michail has been the “calm force” in my life and our daughter Electra has made me happier than I ever thought I could be.

Thank you.

Abstract

The term High-strength Steel (HSS) is currently used for steel grades with yield strength exceeding or equal to 460MPa. Production of HSS is the result of significant improvements in steel making technologies regarding metallurgy, rolling and heat treatment processes, achieved in the last decades. The structural application of HSS may reduce member sizes and workload of transportation and construction, thus providing significant economic, environmental and architectural advantages. However its application is still limited while its relevance to seismic design is currently under discussion.

The present thesis investigates experimentally and numerically the possible application of HSS in the dissipative elements of the innovative FUSEIS system. FUSEIS consists of a pair of closely-spaced strong columns rigidly connected via multiple dissipative links which may be beams or pins. The system resists lateral loads by developing axial forces in the columns and bending in the links while in case of pin links catenary action also develops. An important advantage of FUSEIS is reparability: in case of a strong earthquake damage is concentrated in the replaceable links, protecting the rest structural members.

The experimental investigations include large-scale cyclic tests on FUSEIS systems consisting of different types of links and steel grades (S355, S500, S700), conducted in the National Technical University of Athens. Relevant component tests, conducted in another Laboratory, are overviewed. Reference is also made to a previous experimental campaign involving FUSEIS with S235 links.

The tested systems are simulated via different models with increasing complexity and suggestions are given in order to approximate their response. Eventually, two case studies are designed according to the Eurocodes: a two-story and a five-story building including FUSEIS systems with S700 beam links. The structures are designed to comply with Eurocode's requirements although the application of HSS in dissipative members is not currently allowed. The case studies are subjected to performance-based evaluation, by using non-linear static and dynamic analyses while considering the response of their most critical components. Simulation of material non-linearity in the dissipative elements is based on the aforementioned test calibration. Given that the seismic design of buildings is governed by stiffness demands, the specific application of HSS does not fully benefit from the material's advantages. The models are assessed at two limit states following two different methodologies, both of which result in the acceptance of their design q-factor (equal to 3.5).

Overall, the objective of this study is to explore whether the hysteretic behavior of HSS can be sufficient for dissipative zones, rather than comparing it to conventional steels. Experimental and

numerical investigations provided affirmative results although further investigations would be required.

ΕΚΤΕΝΗΣ ΠΕΡΙΛΗΨΗ ΣΤΑ ΕΛΛΗΝΙΚΑ

1.1	Εισαγωγή – Δομή της εργασίας.....	E1
1.2	Χάλυβες υψηλής αντοχής: Εξέλιξη, δομικές εφαρμογές και κανονιστικό πλαίσιο	E2
1.3	Πειραματικές διερευνήσεις.....	E5
1.4	Αναλυτική και αριθμητική προσέγγιση	E13
1.5	Εφαρμογή σε κτίρια.....	E19
1.6	Σύνοψη και προτάσεις για περαιτέρω έρευνα	E29
1.7	Συμπεράσματα και πρωτότυπη συμβολή	E30

Εκτενής περίληψη στα ελληνικά

1.1 Εισαγωγή – Δομή της εργασίας

Οι εξελίξεις στον τομέα της παραγωγής του δομικού χάλυβα, τις τελευταίες δεκαετίες, έχουν οδηγήσει σε υλικά με υψηλότερες αντοχές και άλλα βελτιωμένα χαρακτηριστικά. Ο όρος χάλυβες υψηλής αντοχής (High Strength Steel, HSS) αναφέρεται σε χάλυβες που έχουν τάση διαρροής (f_y) μεγαλύτερη ή ίση των 460 MPa. Η χρήση των χαλύβων υψηλής αντοχής στις κατασκευές θα μπορούσε να αποφέρει σημαντικά οικονομικά και περιβαλλοντικά οφέλη, ωστόσο είναι ακόμα περιορισμένη. Επιπλέον η εφαρμογή τους σε μέλη απορρόφησης ενέργειας δεν προβλέπεται από τους ισχύοντες Αντισεισμικούς Κανονισμούς. Στην παρούσα διατριβή διερευνάται η χρήση χαλύβων υψηλής αντοχής στα στοιχεία απορρόφησης ενέργειας ενός καινοτόμου αντισεισμικού συστήματος. Το σύστημα αυτό ονομάζεται FUSEIS και αποτελείται από ένα ζεύγος ισχυρών υποστυλωμάτων σε μικρή απόσταση, τα οποία είναι άκαμπτα συνδεδεμένα μεταξύ τους με επάλληλα οριζόντια στοιχεία (δοκοί ή πείροι). Τα υποστυλώματα των FUSEIS σχεδιάζονται ικανοτικά έτσι ώστε η πλαστικοποίηση και κατ' επέκταση η κατανάλωση της σεισμικής ενέργειας να περιορίζεται στους αντικαταστάσιμους οριζόντιους συνδέσμους. Συνεπώς ένα βασικό πλεονέκτημα του συστήματος είναι η επισκευασιμότητα.

Μέχρι στιγμής, τα πειράματα σε φορείς από χάλυβες υψηλής αντοχής υπό ανακυκλιζόμενη φόρτιση είναι περιορισμένα. Η παρούσα εργασία αποσκοπεί να συνεισφέρει στην τρέχουσα συζήτηση της επιστημονικής κοινότητας πάνω στις πιθανές εφαρμογές των δομικών χαλύβων υψηλής αντοχής. Σε αυτά τα πλαίσια, διερευνάται πειραματικά και αριθμητικά η χρήση χαλύβων υψηλής αντοχής σε στοιχεία απορρόφησης ενέργειας FUSEIS. Στόχος της μελέτης δεν είναι να δείξει πως η συγκεκριμένη εφαρμογή πλεονεκτεί έναντι των συμβατικών χαλύβων αλλά να αποτιμήσει τη σεισμική απόκριση του συστήματος. Επιπλέον στόχος της διατριβής είναι να διευρύνει την έως τώρα διαθέσιμη βάση δεδομένων για τα συστήματα FUSEIS, τα οποία αναπτύχθηκαν σχετικά πρόσφατα. Τα FUSEIS με δοκούς ή πείρους από χάλυβα S235 έχουν μελετηθεί στο παρελθόν (Vayas et al. 2013, Δούγκα 2016, Δημακογιάννη 2017). Στην παρούσα έρευνα, τα πειράματα περιλαμβάνουν δοκίμια FUSEIS διαφορετικής διατομής (κοιλοδοκούς, δοκούς HEA και κυλινδρικούς πείρους) και υλικού (χάλυβες S355J2, S500MC, S700MC). Μέρος της έρευνας που παρουσιάζεται εκπονήθηκε στα πλαίσια του Ευρωπαϊκού ερευνητικού προγράμματος “MATCH” (RFSR-CT-2013-00024) και χρηματοδοτήθηκε από την Ευρωπαϊκή Ένωση (Research Fund for Coal and Steel – RFCS) (Feldmann et al. 2017). Στο πρόγραμμα “MATCH” συμμετείχαν, εκτός από το Εργαστήριο Μεταλλικών Κατασκευών του ΕΜΠ, το Πανεπιστήμιο του

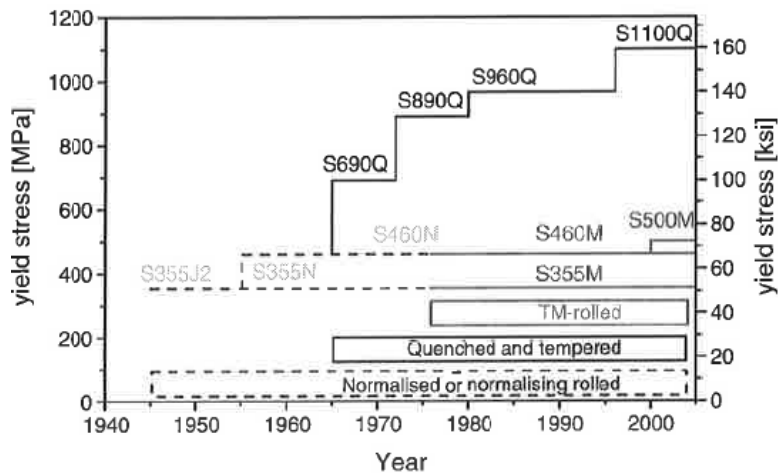
Άαχεν (συντονιστές), το Πανεπιστήμιο Θεσσαλίας, το Πανεπιστήμιο της Πίζα και οι εταιρείες ILVA Sra και RUUKKI-SSAB που παρείχαν τα πειραματικά δοκίμια.

Η διατριβή ξεκινά με μια βιβλιογραφική ανασκόπηση που αναπτύσσεται σε τρεις θεματικούς άξονες: (i) κανονιστικές απαιτήσεις σε σχέση με τις ιδιότητες του δομικού χάλυβα (ii) εξελίξεις και έρευνα σχετικά με τους χάλυβες υψηλής αντοχής (iii) συμβατικά και καινοτόμα αντισεισμικά συστήματα πλευρικής ευστάθειας. Ακολουθεί το κεφάλαιο με τις πειραματικές διερευνήσεις που περιλαμβάνει πειράματα σε συστήματα FUSEIS με χρήση διαφορετικών οριζόντιων στοιχείων απορρόφησης ενέργειας και πειράματα σε μεμονωμένα στοιχεία FUSEIS. Κατόπιν τα πειράματα προσεγγίζονται αναλυτικά και αριθμητικά. Το σύστημα FUSEIS συμπεριφέρεται ως μια κατακόρυφη δοκός τύπου Vierendeel. Βάση αυτού, προτείνεται μια εξίσωση που περιγράφει την φέρουσα ικανότητα του συστήματος με συνδέσμους δοκούς. Στο σύστημα με πείρους, αναπτύσσεται λειτουργία καλωδίου για μεγάλες επιβαλλόμενες μετατοπίσεις και κατ'επέκταση προτείνονται επιπλέον σχέσεις για τη φέρουσα ικανότητα του. Στη συνέχεια τα πειράματα προσομοιώνονται με τρία διαφορετικά λογισμικά αυξανόμενης πολυπλοκότητας, χρησιμοποιώντας δισδιάστατα ή τρισδιάστατα πεπερασμένα στοιχεία. Τέλος εξετάζονται δύο θεωρητικές κτιριακές εφαρμογές που σχεδιάζονται με βάση τους ισχύοντες κανονισμούς και οι οποίες υποβάλλονται σε μη γραμμικές στατικές και δυναμικές αναλύσεις. Πρόκειται για ένα δώροφο και ένα πενταώροφο κτίριο με συστήματα FUSEIS με συνδέσμους κοιλοδοκούς από χάλυβα S700, κατ'αντιστοιχία με τα πειραματικά δοκίμια. Στη φάση του σχεδιασμού αναδεικνύονται οι κρίσιμότεροι έλεγχοι που απορρέουν τόσο από την σχετική ευκαμψία των FUSEIS όσο και από την εφαρμογή χαλύβων υψηλής αντοχής. Στόχος της διερεύνησης δεν είναι να προτείνει βέλτιστη σχεδιαστική λύση από άποψη οικονομίας αλλά να εξετάσει κατά πόσο η σεισμική απόκριση του συστήματος με χάλυβα υψηλής αντοχής μπορεί να είναι αποδεκτή με βάση τα διαθέσιμα πειραματικά και αριθμητικά δεδομένα. Η αποτίμηση της συμπεριφοράς των εξεταζόμενων φορέων μέσω μη-γραμμικών προσαυξητικών δυναμικών αναλύσεων, επιβεβαιώνει την θεώρηση συντελεστή συμπεριφοράς ίσου με $q=3.50$.

1.2 Χάλυβες υψηλής αντοχής: Εξέλιξη, δομικές εφαρμογές και κανονιστικό πλαίσιο

Οι δύο συνηθέστερες μέθοδοι για αύξηση της αντοχής του χάλυβα είναι η κραμάτωση και η θερμική κατεργασία. Η αύξηση της αντοχής μέσω της αύξησης της περιεκτικότητας σε άνθρακα οδηγεί σε μείωση της ολκιμότητας και της συγκολλησιμότητας. Αντίθετα, ο συνδυασμός θερμικής κατεργασίας και κραμάτωσης επηρεάζει τη μικροδομή του χάλυβα και οδηγεί σε υλικά με μικρή

διάμετρο κόκκου και αυξημένη αντοχή και δυσθραυστότητα. Στο Σχήμα 1 συνοψίζονται χρονολογικά οι εξελίξεις στις τεχνολογίες παραγωγής χαλύβων και η αντίστοιχη αύξηση στις αντοχές των παραγόμενων υλικών. Όπως διακρίνεται, μετά τη δεκαετία του 1960 η ανάπτυξη μεθόδων θερμικής κατεργασίας (quenching and tempering - QT, thermo-mechanical rolling - TM) συντέλεσε στη δημιουργία χαλύβων υψηλής αντοχής.

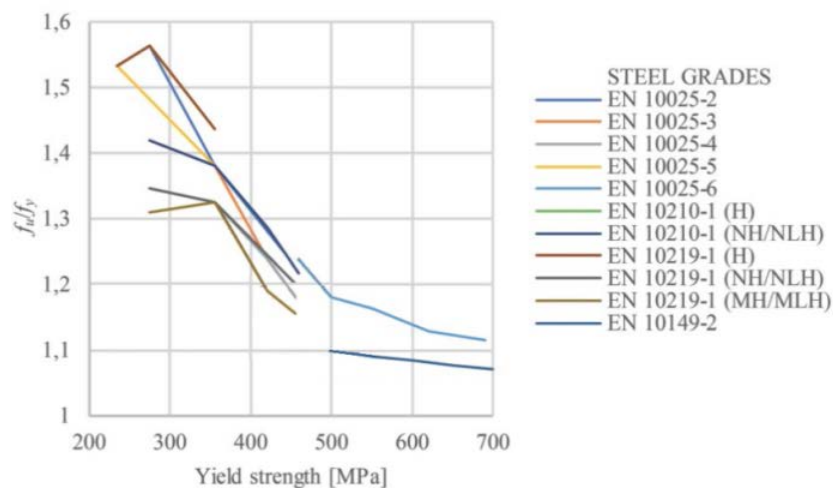


Σχήμα 1: Χρονολόγιο μεθόδων παραγωγής δομικών χαλύβων και αύξησης της αντοχής τους (Gunther et al. (Eds, 2005))

Παρά τα σημαντικά περιβαλλοντικά και οικονομικά οφέλη που μπορούν να προκύψουν από την χρήση χαλύβων υψηλής αντοχής στις κατασκευές, τα παραδείγματα εφαρμογής τους είναι ακόμα περιορισμένα. Τα πλεονεκτήματα των χαλύβων υψηλής αντοχής είναι περισσότερο εμφανή στη γεφυροποιία καθώς ο σχεδιασμός των κτιριακών έργων καθορίζεται συνήθως από απαιτήσεις σε δυσκαμψία και κατ'επέκταση από το μέτρο ελαστικότητας E , το οποίο είναι ίδιο σε όλους τους δομικούς χάλυβες. Παρακάτω αναφέρονται ορισμένες κατασκευές που περιλαμβάνουν χάλυβες υψηλής αντοχής:

- Γερμανία: γέφυρα Nesenbachtal (S690), γέφυρα Ρήνου στον άξονα Dusseldorf-Ilverich (S460), δικτύωμα οροφής στο Sony Centre (S460, S690), σύμμικτη γέφυρα Ingolstadt (S690QL)
- Γαλλία: κοιλαδογέφυρα Millau (S460ML)
- Σουηδία: γέφυρα Mittadalen (S690), στρατιωτική γέφυρα Fast Bridge 48 (S960, S1100)
- Κίνα: Εθνικό στάδιο, Phoenix International Media Center, αθλητικό κέντρο Shenzhen Bay, κεντρικά γραφεία CCTV ($Q460$, $f_y = 460$ MPa)
- Ιαπωνία: Landmark tower ($f_y = 600$ MPa)
- Αυστραλία: Star City, κτίριο Latitude (steels with f_y 650 and 690 MPa)
- Νότια Κορέα: βιβλιοθήκη SNU Kwanjeong, Lotte World Tower ($f_y = 650$ MPa)

Οι χάλυβες υψηλής αντοχής δεν έχουν ακόμα ενσωματωθεί πλήρως στους Κανονισμούς. Ενδεικτικά, ο Ευρωκώδικας περιλαμβάνει του χάλυβες έως S700 (EN1993-1-12), ο Αμερικάνικος κανονισμός (ANSI/AISC 360-16) περιλαμβάνει δομικούς χάλυβες με τάση διαρροής (f_y) έως 690MPa (A514) και ο Κινέζικος κανονισμός (GB50017-2017) καλύπτει χάλυβες με f_y έως 460MPa. Επιπλέον, η χρήση χαλύβων υψηλής αντοχής σε στοιχεία απορρόφησης ενέργειας δεν προβλέπεται ακόμα από τους Κανονισμούς. Αυτό οφείλεται, εν μέρει, στο οι χάλυβες αυτοί έχουν διαφορετικά μηχανικά χαρακτηριστικά από τους συμβατικούς χάλυβες. Οι βασικότερες διαφορές τους σχετίζεται με την περιοχή κράτυνσης στο διάγραμμα τάσεων-παραμορφώσεων καθώς οι χάλυβες υψηλής αντοχής συνήθως δεν διαθέτουν διακριτή περιοχή διαρροής και έχουν μικρότερους λόγους f_u/f_y (Σχήμα 2), με αποτέλεσμα μικρότερη ολκιμότητα.



Σχήμα 2: Λόγος f_u/f_y για διαφορετικούς δομικούς χάλυβες (van Es et al. 2018)

Ο Ευρωκώδικας 3 αναφέρεται στον σχεδιασμό χαλύβδινων κατασκευών προϋποθέτοντας ότι τα χρησιμοποιούμενα υλικά έχουν επαρκή πλαστιμότητα, όπως αυτή εκφράζεται μέσω του λόγου f_u/f_y , της οριακής παραμόρφωσης (ϵ_u) και της επιμήκυνσης στη θραύση (Πίνακας 1). Οι εμπειρικοί αυτοί κανόνες συχνά αμφισβητούνται.

Πίνακας 1: Απαιτήσεις πλαστιμότητας για δομικούς χάλυβες με βάση τον Ευρωκώδικα 3

Κριτήριο	EN1993-1-1 (S235-S460)	EN1993-1-12 (S500-S700)
f_u/f_y	≥ 1.10	≥ 1.05
Οριακή παραμόρφωση	$\geq 15\%$	$\geq 10\%$
Παραμόρφωση ϵ_u	$\geq 15 * f_y/E$	$\geq 15 * f_y/E$

1.3 Πειραματικές διερευνήσεις

Η πειραματική διερεύνηση περιελάβανε οκτώ πειράματα σε συστήματα FUSEIS με χρήση διαφορετικών οριζόντιων στοιχείων απορρόφησης ενέργειας (Πίνακας 2): (i) δύο συστήματα με κοιλοδοκούς από χάλυβα S700MC, (ii) τέσσερα συστήματα με δοκούς HEA από χάλυβα S355J2 και (iii) δύο συστήματα με κυλινδρικούς πείρους από χάλυβα S500MC. Οι περισσότερες δοκιμές διεξήχθησαν υπό ανακυκλιζόμενη φόρτιση είτε αυξανόμενου (I.A. – increasing amplitude) είτε σταθερού εύρους (C.A. – constant amplitude). Ο Πίνακας 3 δίνει τις βασικές ιδιότητες των υλικών.

Πίνακας 2: Πειραματικές διερευνήσεις σε συστήματα FUSEIS (για διαστάσεις βλ. Σχήμα 5)

Δοκιμή	Σύνδεσμος FUSEIS	Χάλυβας	B (mm)	L (mm)	Φόρτιση
T1	Κοιλοδοκοί	S700MC	1500	722	Ανακυκλ. (I.A.)
T2					Ανακυκλ. (C.A.)
T3	Δοκοί HEA	S355J2	1500	702	Ανακυκλ. (I.A.)
T4					Ανακυκλ. (C.A.)
T5					Ανακυκλ. (C.A.)
T6					Μονοτονική
T7	Πείροι	S500MC	1400	296	Ανακυκλ. (I.A.)
T8					Ανακυκλ. (C.A.)

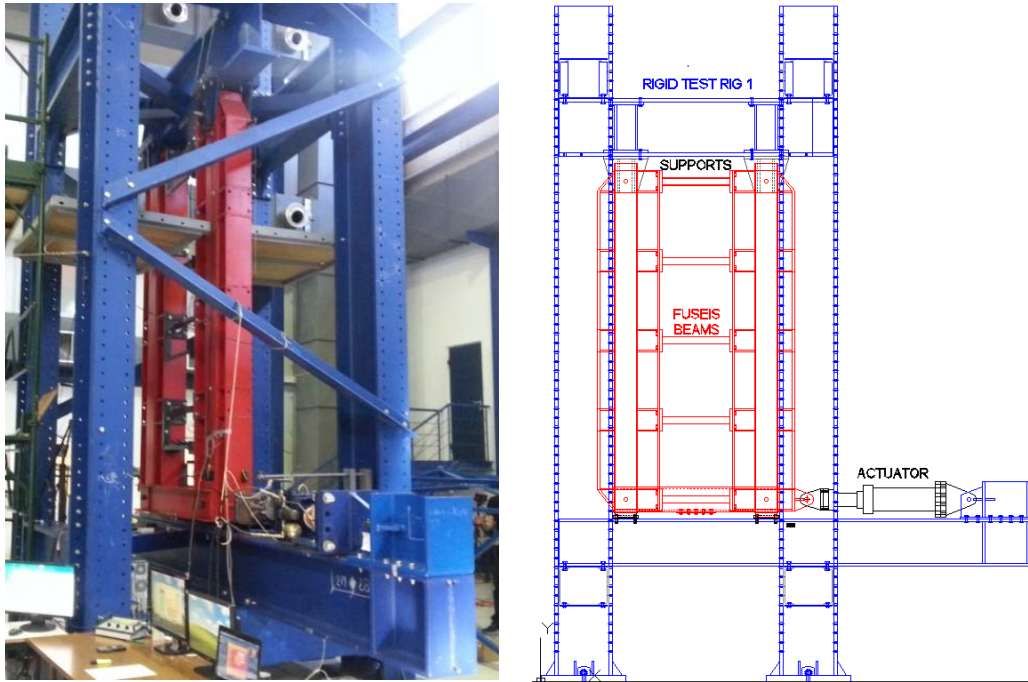
Σημείωση: Ανακυκλιζόμενη φόρτιση με κύκλους αυξανόμενου (I.A.) ή σταθερού εύρους

Πίνακας 3: Τάση διαρροής (f_y) και εφελκυστική αντοχή (f_u) των εξεταζόμενων υλικών

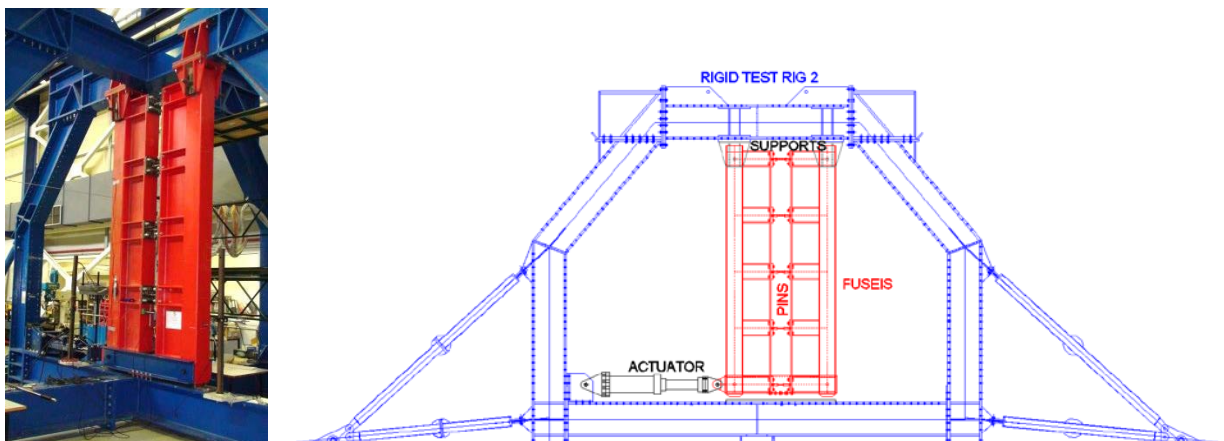
Χάλυβας	f_y (MPa)	f_u (MPa)
S355J2	440	605
S500MC	510	660
S700MC	740	845

Για τεχνικούς λόγους (διαθέσιμες διατομές και δυνατότητες συνεργαζόμενων Εργαστηρίων) τα εξεταζόμενα συστήματα δεν είχαν την ίδια φέρουσα ικανότητα. Οι πειραματικές διατάξεις για τα συστήματα με δοκούς και πείρους δίνονται στο Σχήμα 3 και στο Σχήμα 4, αντίστοιχα. Τα πειραματικά πλαίσια τοποθετήθηκαν ανάποδα: οι αρθρωτές στηρίξεις βρίσκονταν στην κεφαλή των υποστυλωμάτων FUSEIS ενώ οι οριζόντιες μετατοπίσεις ασκούσαν μέσω υδραυλικού εμβόλου στον πόδα τους. Στο Σχήμα 5 δείχνεται πως κάθε εξεταζόμενο σύστημα περιλάμβανε πέντε δοκίμια, αριθμημένα S1 έως S5. Οι δοκοί FUSEIS ήταν συγκολλημένες σε μετωπικές πλάκες

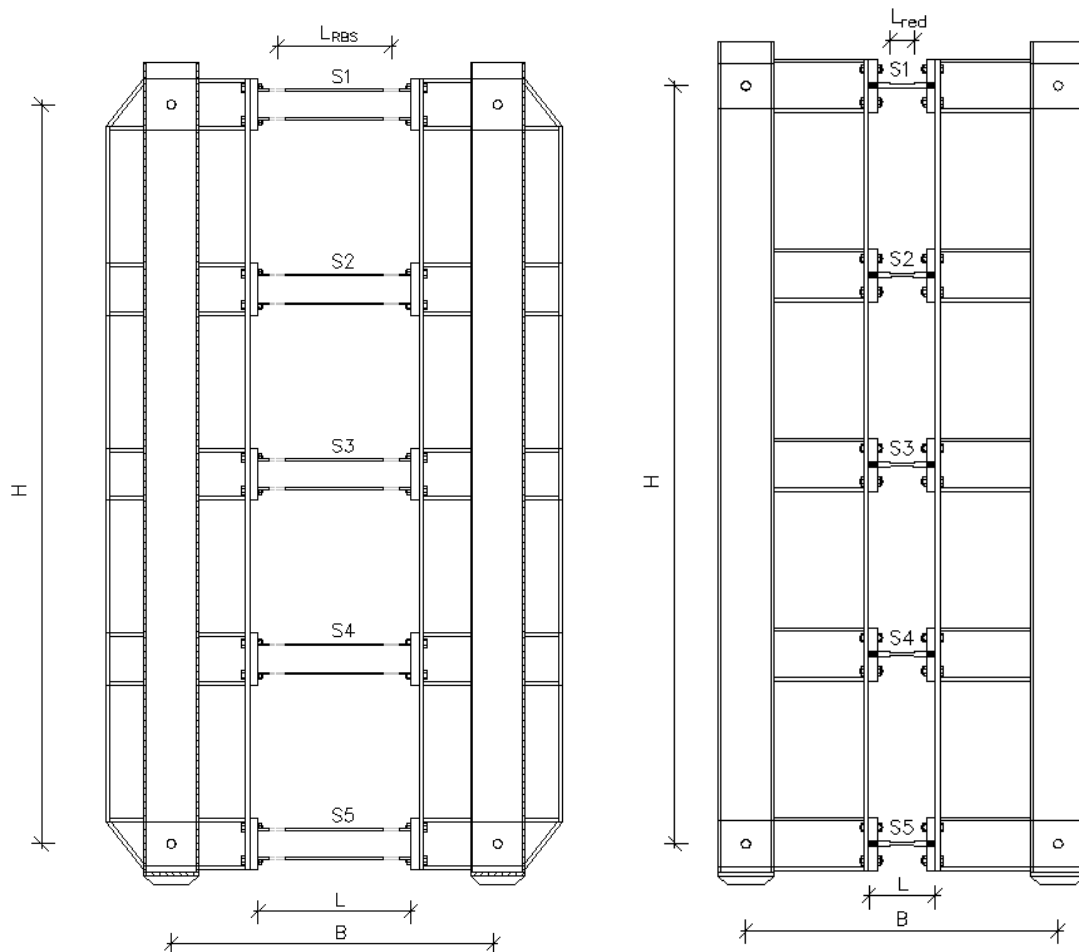
οι οποίες στη συνέχεια συνδέονταν κοχλιωτά με τα υποστυλώματα FUSEIS. Οι πείροι FUSEIS είχαν στα άκρα τους αντίρροπα σπειρώματα προς διευκόλυνση της συναρμολόγησής τους με τις μετωπικές πλάκες και τα υποστυλώματα. Στο Εργαστήριο του Αάχεν εκπονήθηκαν δοκιμές σε μεμονωμένα στοιχεία FUSEIS, με διατομές αντίστοιχες αυτών που χρησιμοποιήθηκαν στα συστήματα, τα αποτελέσματα των οποίων παρατίθενται και σχολιάζονται στη διατριβή.



Σχήμα 3: Πειραματική διάταξη συστήματος με δοκούς (Εργαστήριο Μεταλλικών Κατασκευών ΕΜΠ)



Σχήμα 4: Πειραματική διάταξη συστήματος με πείρους (Εργαστήριο Μεταλλικών Κατασκευών ΕΜΠ)



Σχήμα 5: Ορισμός βασικών διαστάσεων και αρίθμηση δοκιμών

Κατά τη διάρκεια των πειραμάτων πραγματοποιούνταν οι κάτωθι μετρήσεις:

- Επιβαλλόμενο φορτίο και μετατόπιση (έμβολο)
- Οριζόντιες μετατοπίσεις υποστυλωμάτων (βελόμετρα – LVDT)
- Διαφορικές μετατοπίσεις των άκρων των συνδέσμων FUSEIS (βελόμετρα – LVDT)
- Κλίση υποστυλωμάτων (κλισιόμετρα)
- Ολίσθηση μετωπικών πλακών (βελόμετρα – LVDT)
- Ανηγμένες παραμορφώσεις στο μέσον των συνδέσμων πείρων (μηκυνσιόμετρα - strain gages)

1.3.1 Πειράματα σε FUSEIS με δοκούς

Ο Πίνακας 4 και ο Πίνακας 5 συνοψίζουν τα βασικά χαρακτηριστικά των πειραματικών δοκιμών FUSEIS από χάλυβα S700 και S355, αντίστοιχα. Στην περίπτωση σχεδιασμού με απομειωμένες διατομές (RBS) παρατίθενται και οι ροπές αντίστασης (W) της πλήρους και της απομειωμένης διατομής, καθώς και ο λόγος των μηκών L_{RBS}/L (Σχήμα 5).

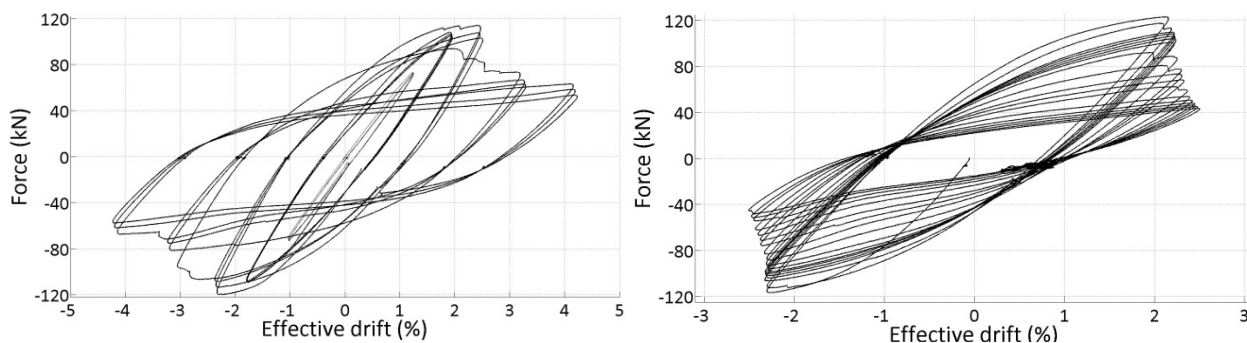
Πίνακας 4: Κοιλοδοκοί FUSEIS από χάλυβα S700 (πειράματα T1, T2)

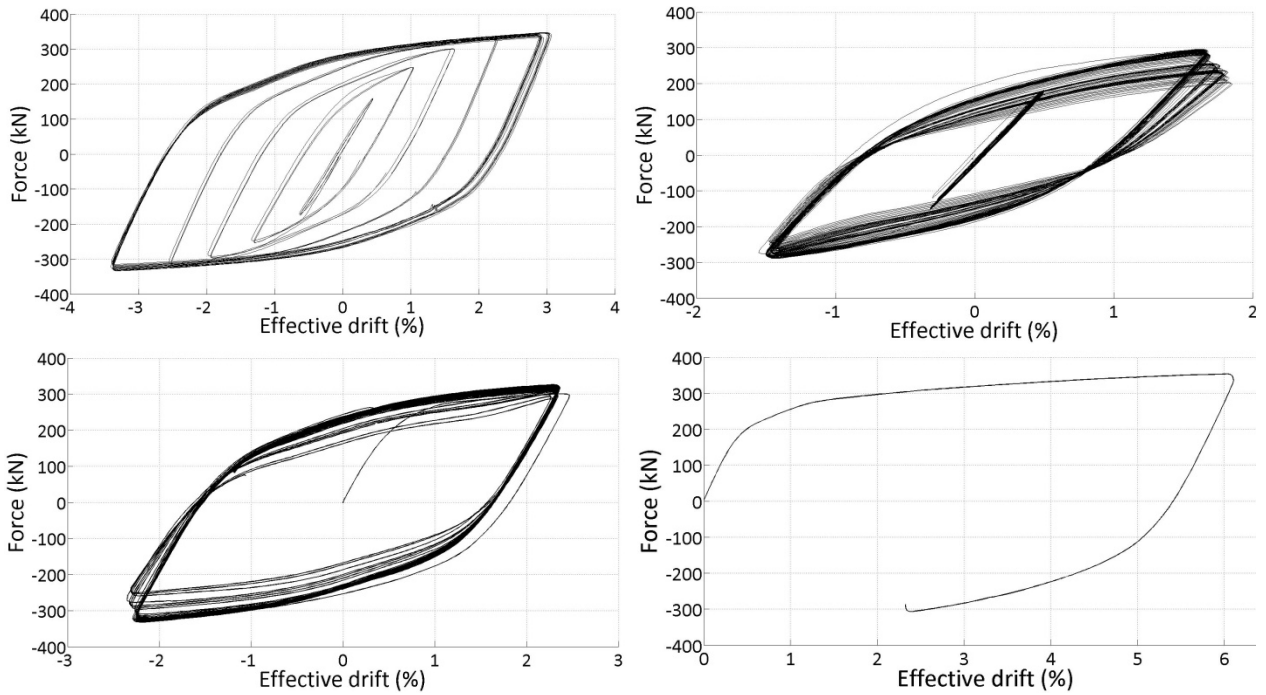
Δοκίμιο	Διατομή	L_{RBS}/L	Πλήρης διατομή		Απομειωμένη (RBS)	
			$W_{el} (m^3)$	$W_{pl} (m^3)$	$W_{el} (m^3)$	$W_{pl} (m^3)$
S1	SHS80*4	0.78	2.776E-05	3.307E-05	1.882E-05	2.334E-05
S2	CHS76*3	0.79	1.280E-05	1.700E-05	8.620E-06	1.220E-05
S3	CHS60*4	0.79	9.340E-06	1.270E-05	6.178E-06	8.992E-06
S4	SHS60*3	-	1.171E-05	1.395E-05	-	-
S5	SHS100*4	0.78	4.527E-05	5.330E-05	2.936E-05	3.640E-05

Πίνακας 5: FUSEIS δοκίμια HEA από χάλυβα S355 (πειράματα T3 έως T6)

Δοκίμιο	Διατομή	L_{RBS}/L	Πλήρης διατομή		Απομειωμένη (RBS)	
			$W_{el} (m^3)$	$W_{pl} (m^3)$	$W_{el,RBS} (m^3)$	$W_{pl,RBS} (m^3)$
S1	HEA100	0.76	7.276E-05	8.301E-05	4.444E-05	5.200E-05
S2	HEA100	0.66	7.276E-05	8.301E-05	4.444E-05	5.200E-05
S3	HEA120	0.76	1.063E-04	1.195E-04	6.409E-05	7.370E-05
S4	HEA120	0.66	1.063E-04	1.195E-04	6.409E-05	7.370E-05
S5	HEA140	0.76	1.554E-04	1.735E-04	9.424E-05	1.079E-04

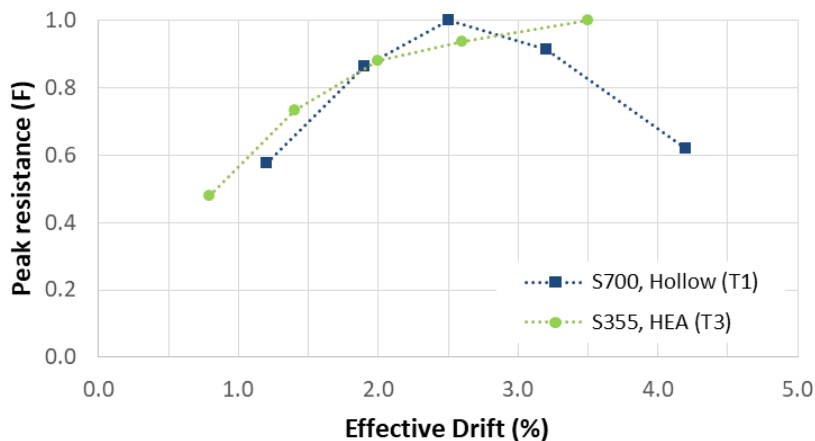
Με το πέρας των πειραμάτων παρατηρήθηκε ότι οι μετατοπίσεις των δοκών FUSEIS ήταν μικρότερες από τις αναμενόμενες βάσει των μετατοπίσεων του εμβόλου. Επιπλέον, σε ορισμένα πειράματα μετρήθηκαν σημαντικές παρασιτικές μετακινήσεις που σχετίζονταν με την πειραματική διάταξη (ανοχές οπών, κοχλιωτές συνδέσεις κλπ). Αυτό το φαινόμενο ήταν ιδιαίτερα έντονο στα πειράματα T3-T6 (FUSEIS με δοκούς HEA) στα οποία αφενός αναπτύχθηκαν μεγαλύτερες δυνάμεις και αφετέρου οι δοκοί επέδειξαν σημαντικές στρεπτικές παραμορφώσεις. Συνεπώς, έπρεπε να υπολογιστούν οι πραγματικές παραμορφώσεις των FUSEIS, λαμβάνοντας υπόψη τις προαναφερθείσες μετρήσεις. Στο Σχήμα 6 παρουσιάζονται οι βρόχοι υστέρησης των συστημάτων σε όρους φορτίου – πραγματικής γωνιακής παραμόρφωσης του φορέα (effective drifts).



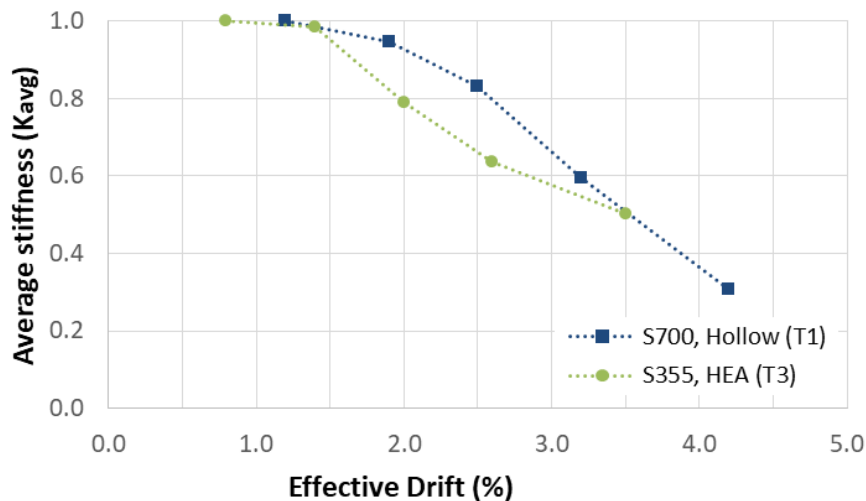


Σχήμα 6: Απόκριση εξεταζόμενων συστημάτων FUSEIS με δοκούς, πειράματα T1 έως T6

Τα πειραματικά αποτελέσματα αξιολογήθηκαν με όρους πλαστιμότητας, εξέλιξης της βλάβης, απομείωσης της αντοχής και της δυσκαμψίας κλπ. Όπως φαίνεται στο Σχήμα 7, το σύστημα με δοκούς από χάλυβα S355J2 ήταν πιο πλάστιμο καθώς δεν παρουσίασε βλάβες μέχρι να φτάσει σε γωνιακή παραμόρφωση ίση με 3,5%. Το σύστημα με δοκούς από S700MC έφτασε στη μέγιστη αντοχή του για γωνιακή παραμόρφωση ίση με 2,5%. Στο Σχήμα 8 δείχνεται η εξέλιξη της δυσκαμψίας των δύο συστημάτων για αυξανόμενες μετατοπίσεις. Και στις δύο περιπτώσεις, η μείωση της δυσκαμψίας κατά 20% συνέβη για γωνιακές παραμορφώσεις μεγαλύτερες του 2.0%. Δεδομένου ότι τα συστήματα είχαν διαφορετική αντοχή και δυσκαμψία, τα διαγράμματα των δυνάμεων και δυσκαμψιών είναι κανονικοποιημένα ως προς τις εκάστοτε μέγιστες τιμές τους ενώ για κάθε εύρος μετατόπισης έχει θεωρηθεί ο μέσος όρος στις δύο διευθύνσεις φόρτισης.



Σχήμα 7: Αντίσταση σε πλευρικό φορτίο για αυξανόμενες μετατοπίσεις (πειράματα T1, T3)



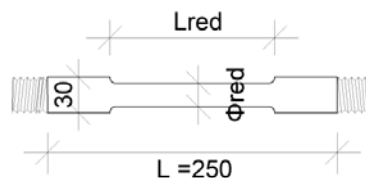
Σχήμα 8: Εξέλιξη δυσκαμψίας για αυξανόμενες μετατοπίσεις (πειράματα T1, T3)

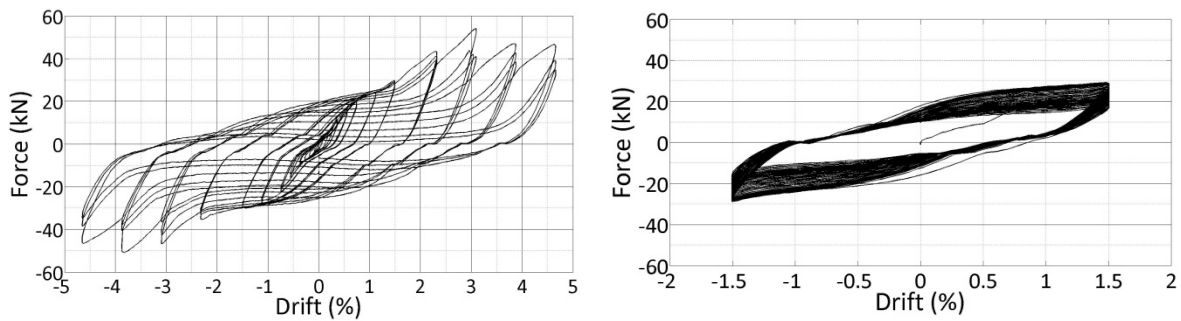
1.3.2 Πειράματα σε FUSEIS με πείρους

Ο Πίνακας 6 δίνει τις διαστάσεις των συνδέσμων πείρων που εξετάστηκαν. Για να προστατευτεί η περιοχή των συνδέσεων, οι πείροι είχαν απομειωμένες διατομές κατά μήκους του μέσου τους. Στο Σχήμα 9 δίνονται οι καμπύλες απόκρισης των συστημάτων για τα πειράματα T7 και T8. Σε αυτή την περίπτωση δεν παρατηρήθηκαν σημαντικές παρασιτικές μετατοπίσεις. Στο σύστημα με πείρους, αναπτύχθηκε λειτουργία καλωδίου (catenary action) με την αύξηση των μετατοπίσεων, η οποία αποτυπώνεται στους βρόχους μέσω ενός χαρακτηριστικού «μυτερού» σχήματος στην απόληξή τους. Αξίζει να σημειωθεί ότι στο πείραμα T7 οι πρώτες ρωγμές εμφανίστηκαν στα δοκίμια για γωνιακή παραμόρφωση περίπου ίση με 1.1%, επομένως οι μικρές ασυμμετρίες που παρατηρούνται στους τελευταίους κύκλους φόρτισης οφείλονται στο διαφορετικό ρυθμό εξάπλωσης των ρωγμών στις δύο διευθύνσεις φόρτισης.

Πίνακας 6: Διαστάσεις και γεωμετρία των πείρων από χάλυβα S500MC (πειράματα T7 και T8)

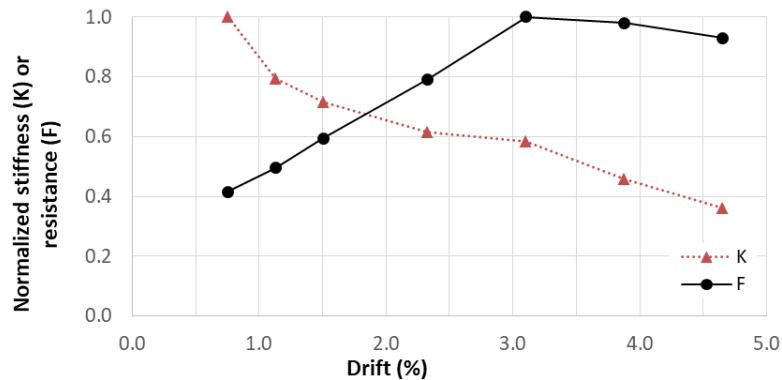
Δοκίμιο	Φred (mm)	Lred (mm)
S1	22	150
S2	20	130
S3	20	110
S4	15	130
S5	15	110





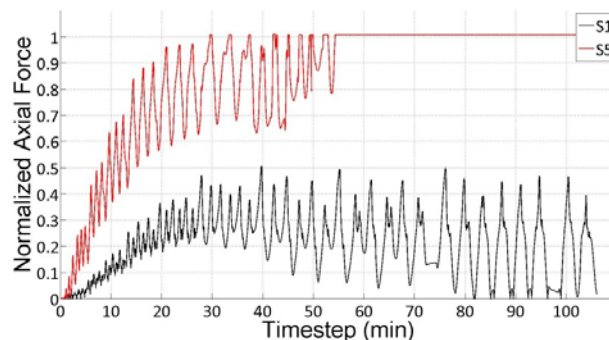
Σχήμα 9: Απόκριση εξεταζόμενων συστημάτων FUSEIS με πείρους, πειράματα T7 και T8

Στο Σχήμα 10 συνοψίζεται η εξέλιξη της πλευρικής αντίστασης (F) και της δυσκαμψίας (K) για αυξανόμενες επιβαλλόμενες μετατοπίσεις. Τα διαγράμματα είναι κανονικοποιημένα και αναφέρονται στις μέσες τιμές των F , K για τις δύο διευθύνσεις φόρτισης.



Σχήμα 10: Εξέλιξη αντίστασης (F) και δυσκαμψίας (K) για αυξανόμενες μετατοπίσεις (T7)

Όπως αναφέρθηκε, στα πειράματα με πείρους είχαν τοποθετηθεί μηχανοστάσιμα (strain gages) στις άνω και κάτω ίνες της μεσαίας διατομής ορισμένων δοκιμίων. Οι μετρηθείσες ανηγμένες παραμορφώσεις μετατράπηκαν σε τάσεις (κατά προσέγγιση) και κατόπιν υπολογίστηκαν οι αναπτυχθείσες αξονικές δυνάμεις. Στο Σχήμα 11 δίνονται οι αξονικές δυνάμεις των πείρων S1 και S5 κατά τη διάρκεια του πειράματος T7. Λόγω του διαφορετικού μεγέθους, οι δυνάμεις κανονικοποιήθηκαν ως προς την εφελκυστική αντοχή του εκάστοτε δοκιμίου. Όπως φαίνεται, ο πείρος S5 έφτασε στην εφελκυστική του αντοχή και αποκόπηκε.



Σχήμα 11: Κανονικοποιημένες αξονικές δυνάμεις στο μέσον των πείρων S1 και S5 κατά το πείραμα T7

Ο Πίνακας 7 συνοψίζει τις βλάβες κατά τη διάρκεια των πειραμάτων σε όρους έναρξης ρηγμάτωσης και πλήρους απότμησης, ανά κρίσιμη γωνιακή παραμόρφωση (ϕ), κύκλο φόρτισης (N) και πείρο (Si).

Πίνακας 7: Βλάβες (έναρξη ρηγμάτωσης και πλήρης απότμηση) στους πείρους FUSEIS για τα πειράματα T7, T8

Πείραμα	Μεγ. γωνιακή παραμόρφωση (ϕ)	Έναρξη ρηγμάτωσης (κρίσιμος πείρος Si)*	Απότμηση (κρίσιμος πείρος Si)*
T7	$\pm 4.7\%$ (I.A.)	$\phi_{cr} = 1.1\%$, $N_{cr} = 3$ (S5)	$\phi_s = 3.1\%$, $N_s = 2$ (S5) $\phi_s = 3.9\%$, $N_s = 1$ (S4)
		$\phi_{cr} = 1.5\%$, $N_{cr} = 1$ (S4)	
		$\phi_{cr} = 2.3\%$, $N_{cr} = 3$ (S2)	
T8	$\pm 1.5\%$ (C.A.)	$N_{cr} = 6$ (S5)	$N_s = 21$ (S5), $N_s = 31$ (S4)
		$N_{cr} = 9$ (S4)	
		$N_{cr} = 14$ (S2)	

1.3.3 Σύγκριση με παλαιότερες πειραματικές διερευνήσεις (με χάλυβα S235)

Το σύστημα FUSEIS αναπτύχθηκε πριν λίγα χρόνια, στα πλαίσια του ομώνυμου Ευρωπαϊκού ερευνητικού έργου (Vayas et al. 2013). Τότε είχαν διεξαχθεί πειράματα σε συστήματα με στοιχεία απορρόφησης ενέργειας (δοκούς ή πείρους) από χάλυβα S235. Στη διατριβή αυτή γίνεται – στο βαθμό που είναι εφικτό - σύγκριση μεταξύ των νεότερων και των παλαιότερων πειραματικών διερευνήσεων. Για το σύστημα με δοκούς, συγκρίθηκαν τα πειραματικά αποτελέσματα σε όρους παρεχόμενης πλαστιμότητας, με βάση μια απλοποιητική παραδοχή διγραμμικής προσέγγισης των καμπύλων απόκρισης. Ο Πίνακας 8 συνοψίζει τα αποτελέσματα και δείχνει ότι η αύξηση της πραγματικής τάσης διαρροής του υλικού συνεπάγεται μια αντίστοιχη μείωση της πλαστιμότητας (μ). Σημειώνεται ότι στα συστήματα με κοιλοδοκούς, η φέρουσα ικανότητα των FUSEIS με S235 ήταν αρκετά μεγαλύτερη του συστήματος με S700 και ότι δεν υπάρχουν δεδομένα για την αποτίμηση της επιρροής της διαφοράς μεγέθους (“size effect”). Η διάταξη του συστήματος με πείρους απλοποιήθηκε σε σχέση με την προηγούμενη εκδοχή της (αφαίρεση δοκών-υποδοχέων), επομένως η απευθείας σύγκριση αποτελεσμάτων δεν ήταν εφικτή. Ωστόσο, υπήρξαν ενδείξεις βελτίωσης της στροφικής ικανότητας των πείρων στη νεότερη/απλοποιημένη διάταξη με χάλυβα υψηλής αντοχής (S500), οι οποίες περιγράφονται στη διατριβή.

Πίνακας 8: Σύγκριση πλαστιμότητας από πειράματα σε FUSEIS με συνδέσμους δοκούς

Τύπος δοκού	Χάλυβας	Τάση διαρροής (MPa)	μ (μέση)
Κοίλες διατομές	S235	352	3.57
	S700MC	740	1.72
Διπλά ταυ	S235	344	4.88
	S355J2	440	3.63

1.4 Αναλυτική και αριθμητική προσέγγιση

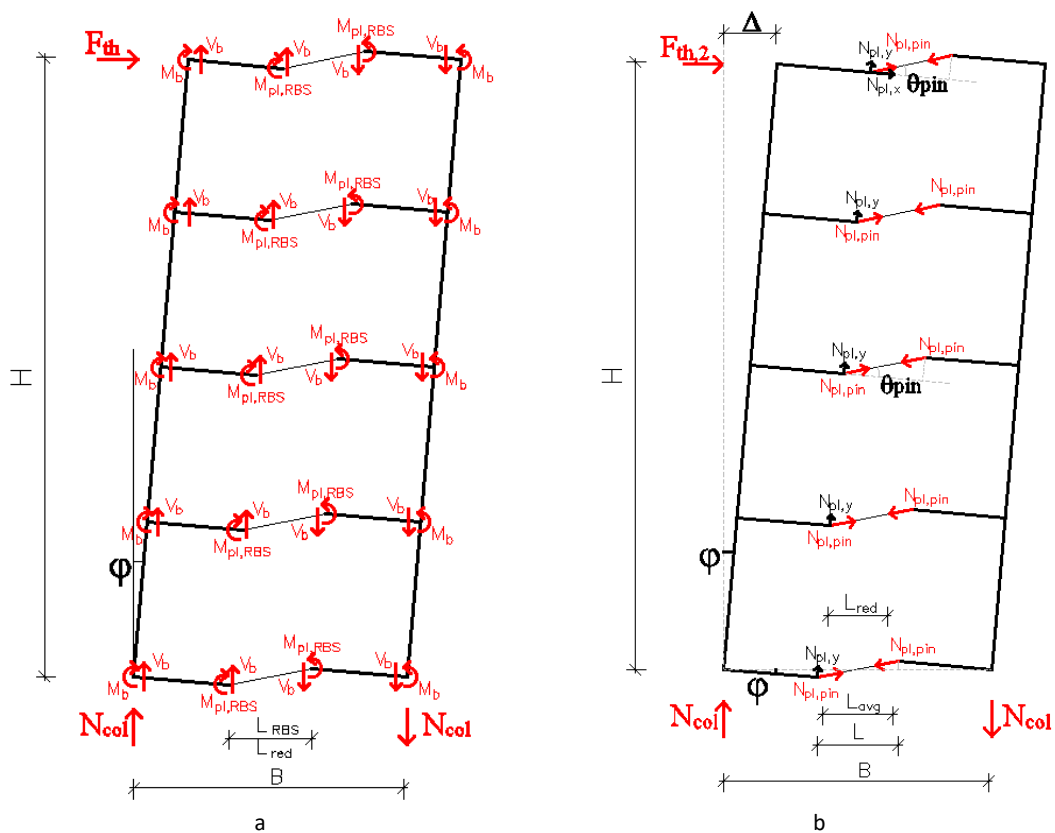
1.4.1 Θεωρητικές σχέσεις

Το σύστημα FUSEIS συμπεριφέρεται ως μια κατακόρυφη δοκός τύπου Vierendeel, καθώς παραλαμβάνει οριζόντια φορτία μέσω ενός συνδυασμού ανάπτυξης αξονικών δυνάμεων στα υποστυλώματα και κάμψης των δοκών (Σχήμα 12α). Βάση αυτού, η φέρουσα ικανότητα του συστήματος δίνεται από την παρακάτω εξίσωση:

$$F_{th} = 2 * \sum (M_{pl,RBS} * B) / (L_{RBS} * H) \quad \text{(FUSEIS δοκοί)} \quad \text{Eq. 1-1}$$

$$F_{th} = 2 * \sum (M_{pl,red} * B) / (L_{red} * H) \quad \text{(FUSEIS πείροι)}$$

Ο ορισμός των διαστάσεων B, L, H δίνεται στο Σχήμα 5.



Σχήμα 12: Θεωρητικές σχέσεις για τη λειτουργία των FUSEIS (α) σύστημα με δοκούς, τύπου κατακόρυφης Vierendeel (β) σύστημα με πείρους, λειτουργία καλωδίου

Όπως έχει αναφερθεί, στο σύστημα FUSEIS με συνδέσμους πείρους αναπτύσσεται επιπλέον λειτουργία καλωδίου για μεγάλες επιβαλλόμενες μετατοπίσεις (Σχήμα 12β). Σε αυτή την περίπτωση η φέρουσα ικανότητα του συστήματος περιγράφεται καλύτερα από τις παρακάτω εξισώσεις, που λαμβάνουν υπόψη τις αξονικές δυνάμεις στους πείρους και την παραμόρφωση του φορέα.

$$F_{th,2} = N_{col} * B / H \approx \sum N_{pl,y} * B / H = \sum (N_{pl,pin} * \sin \theta_{pin}) * B / H \quad \text{Eq. 1-2}$$

Σημειώνεται ότι ο όρος « θ_{pin} » αναφέρεται στην στροφή των πείρων ενώ ο όρος « ϕ » αναφέρεται στη γωνιακή στροφή του συστήματος. Ανάλογα με το αν θα θεωρηθεί ως μήκος του πείρου η συνολική απόσταση ανάμεσα στα πέλματα των υποστυλωμάτων FUSEIS (L) ή η μέση τιμή (L_{avg}) ανάμεσα στο L και το μήκος του απομειωμένου πείρου (L_{red}), μπορούν να χρησιμοποιηθούν οι παρακάτω σχέσεις:

$$F_{th,2} \approx \sum N_{pl,pin} * (\phi * B/L) * (B/H) \quad (a)$$

$$F_{th,2} \approx \sum N_{pl,pin} * (\phi * B/L_{avg}) * (B/H) \quad (b)$$

Eq. 1-3

Ο Πίνακας 9 συνοψίζει τις φέρουσες ικανότητες των FUSEIS που εξετάστηκαν και τις αντίστοιχες δυνάμεις που προκύπτουν από τις παραπάνω σχέσεις. Όπως παρατηρείται, στο σύστημα με δοκούς η θεώρηση της μέση τιμής μεταξύ των f_y , f_u για τον υπολογισμό του $F_{th(fy,fu)}$ μπορεί να οδηγήσει σε πολύ ακριβείς προσεγγίσεις. Εμφανώς η σχέση αυτή δεν επαρκεί για το σύστημα με πείρους, όπου οι εξισώσεις F_{th2} οδηγούν σε καλύτερες προσεγγίσεις.

Πίνακας 9: Σύγκριση μεταξύ πειραματικής (F_{exp}) και θεωρητικής (F_{th}) αντίστασης του συστήματος FUSEIS

Πείραμα	FUSEIS	f_y , f_u (MPa)	F_{exp} (kN)	$F_{th(fy,fu)}$ (kN)	F_{th2} (Eq. 1-3a)	F_{th2} (Eq. 1-3b)
T1, T2	Κοιλοδοκοί S700	$f_y = 740$ $f_u = 845$	117	114	-	-
T3,T4,T5,T6	HEA δοκοί S355	$f_y = 440$ $f_u = 605$	340	328	-	-
T7	Πείροι S500	$f_y = 510$	53	21	49	65
T8		$f_u = 660$	30		24	32

1.4.2 Προσομοιώσεις

Τα πειράματα προσομοιώθηκαν με τρία διαφορετικά λογισμικά αυξανόμενης πολυπλοκότητας, χρησιμοποιώντας δισδιάστατα ή τρισδιάστατα πεπερασμένα στοιχεία. Κάθε προσομοίωμα εξυπηρετεί διαφορετικό σκοπό. Αρχικά τα προσομοιώματα μορφώθηκαν στο εμπορικό λογισμικό SAP2000. Ο στόχος ήταν να προσεγγιστεί η περιβάλλουσα της απόκρισης των εξεταζόμενων φορέων και ο προσδιορισμός των παραμέτρων που περιγράφουν τις πιθανές πλαστικές αρθρώσεις (plastic hinges) για κάθε τύπο συνδέσμου. Στη συνέχεια, δημιουργήθηκαν επιπλέον προσομοιώματα με δισδιάστατα πεπερασμένα στοιχεία στο πρόγραμμα OpenSees που είναι πιο κατάλληλο για τη διεξαγωγή πολυάριθμων παραμετρικών δυναμικών αναλύσεων. Τέλος τα πειράματα προσομοιώθηκαν με χρήση τρισδιάστατων πεπερασμένων στοιχείων (solid elements) στο λογισμικό Abaqus. Βασικός στόχος ήταν η αξιολόγηση των καινοτόμων προσομοιωμάτων/υπορουτίνων υλικού που αναπτύχθηκαν από άλλους συνεργάτες στο ερευνητικό πρόγραμμα ως προς τη δυνατότητα πρόβλεψης της ρηγμάτωσης. Οι υπορουτίνες

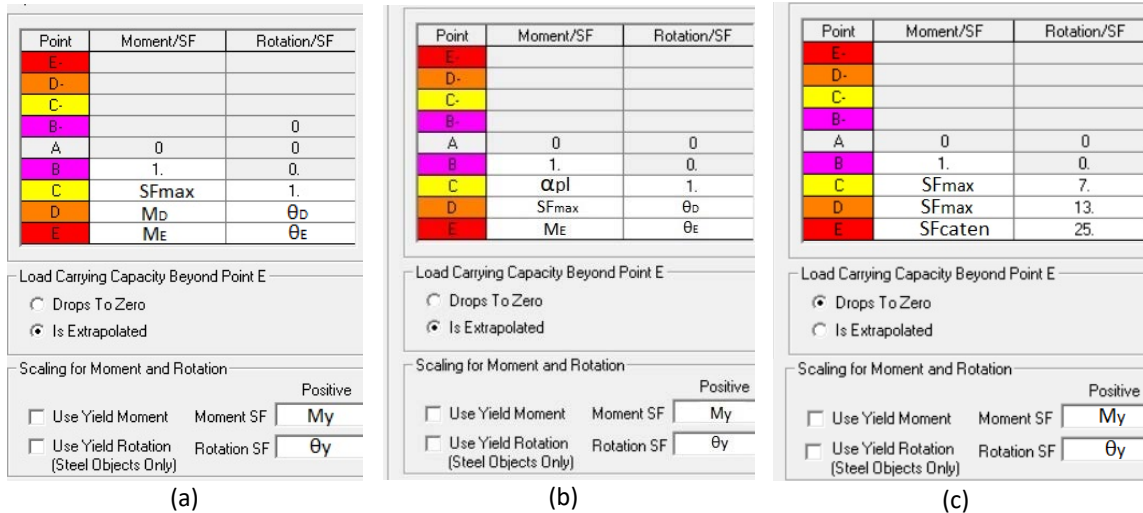
αυτές βασίζονται σε μια υβριδική προσέγγιση που συνδυάζει πειραματικά δεδομένα και αρχές της Μηχανικής Βλάβης.

Το Σχήμα 13 και ο Πίνακας 10 δείχνουν τις παραδοχές προσομοίωσης στο SAP2000 των εν δυνάμει πλαστικών αρθρώσεων για τα στοιχεία απορρόφησης ενέργειας που εξετάστηκαν. Για τους συντελεστές SF_{max} και α_{pl} ισχύουν οι παρακάτω σχέσεις:

$$SF_{max} = W_{pl} * f_u / (W_{el} * f_y) \quad (a) \quad \text{Eq. 1-4}$$

$$\alpha_{pl} = W_{pl} / W_{el} \quad (b)$$

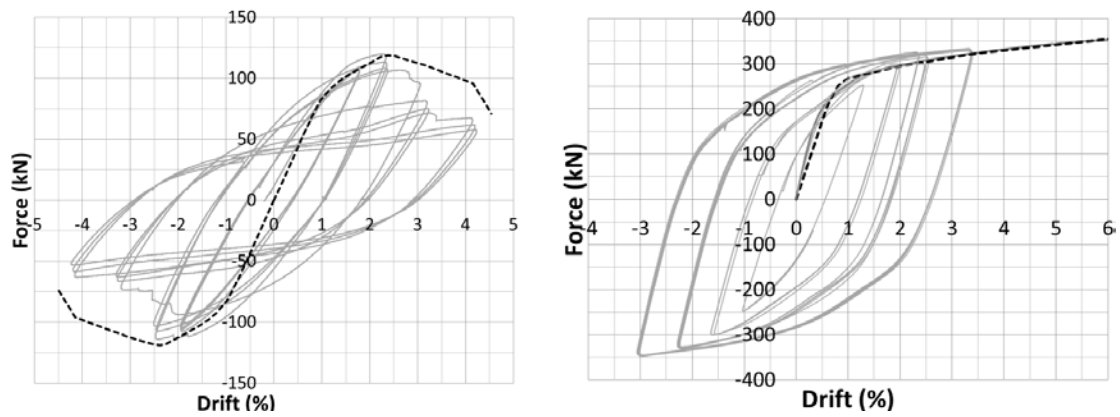
Τα αποτελέσματα των προσομοιώσεων ως καμπύλες απόκρισης των συστημάτων δίνονται στο Σχήμα 14 (FUSEIS με δοκούς) και στο Σχήμα 15 (FUSEIS με πείρους). Για την προσομοίωση της μη γραμμικής απόκρισης των πείρων, έγινε η απλοποιητική παραδοχή ότι η ίδια πλαστική άρθρωση μπορεί να χρησιμοποιηθεί για να περιγράψει διαφορετικές αλλά διαδοχικές εντατικές καταστάσεις (καμπτική λειτουργία και λειτουργία καλωδίου).



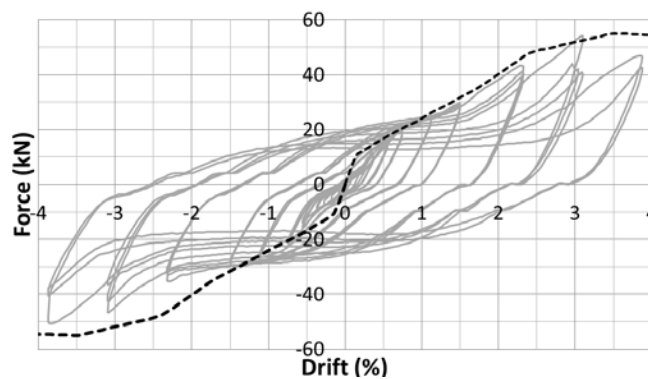
Σχήμα 13: Ορισμός πλαστικών αρθρώσεων σε συνδέσμους FUSEIS για (a) κοίλες διατομές S700 (b) διατομές HEA S355 (c) πείρους S500 (βλ. και Πίνακας 10)

Πίνακας 10: Παράμετροι προσομοίωσης πλαστικών αρθρώσεων συνδέσμων FUSEIS στο λογισμικό SAP2000

	S700 Κοίλες δοκοί		S355 δοκοί HEA		S500 πείροι	
	Moment	Rotation	Moment	Rotation	Moment	Rotation
C	$SF_{max} * M_y$	$1 * \theta_y$	$\alpha_{pl} * M_y$	$1 * \theta_y$	$SF_{max} * M_y$	$7 * \theta_y$
D	$1.0 * M_y$	$8 * \theta_y$	$SF_{max} * M_y$	$25 * \theta_y$	$SF_{max} * M_y$	$13 * \theta_y$
E	$0.1 * M_y$	$14 * \theta_y$	$0.8 * M_y$	$50 * \theta_y$	$5 * M_y$	$25 * \theta_y$

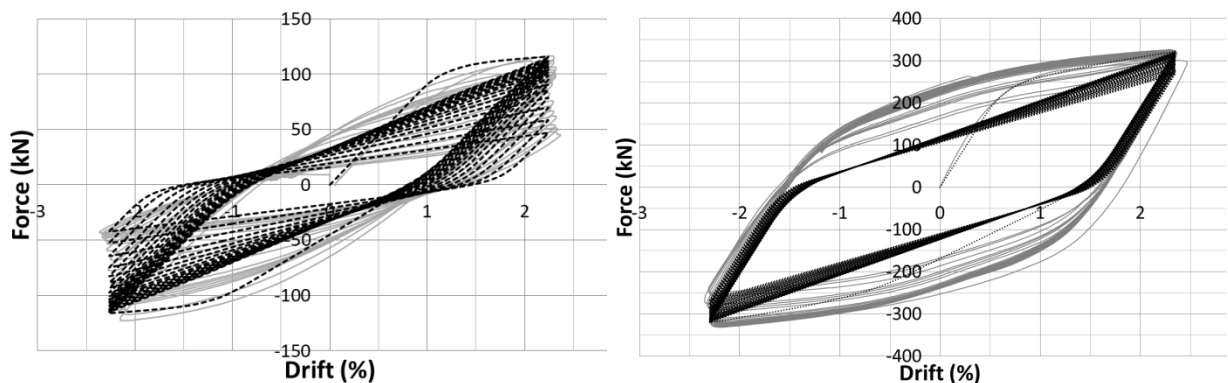


Σχήμα 14: Αποτελέσματα προσομοίωσης (μαύρο χρώμα) του συστήματος με δοκούς από χάλυβες (a) S700 και (b) S355 (πειραματικές καμπύλες σε γκρι χρώμα)



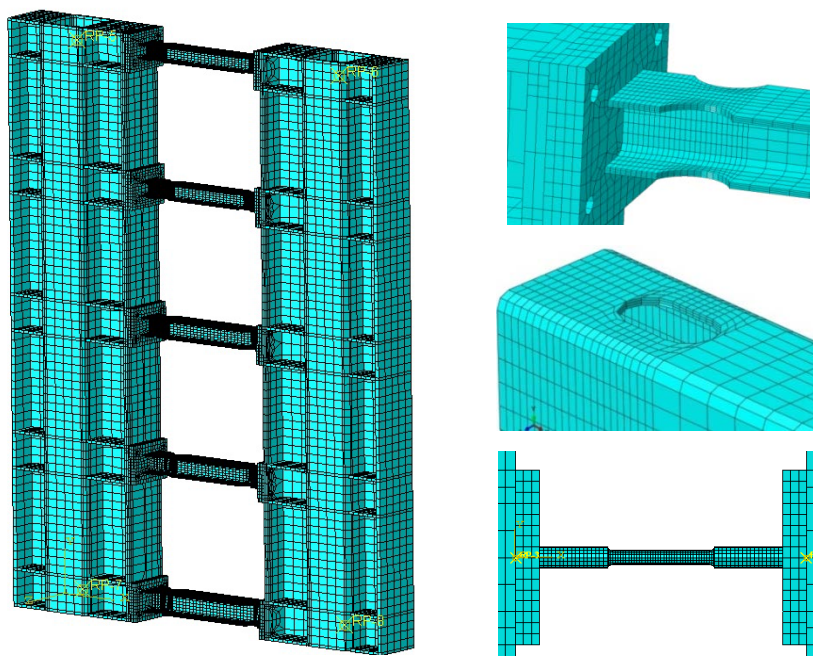
Σχήμα 15: Αποτελέσματα προσομοίωσης (μαύρο χρώμα) του συστήματος με πείρους S500 (πειραματικές καμπύλες σε γκρι χρώμα)

Στο Σχήμα 16 δίνονται τα αποτελέσματα της προσομοίωσης στο OpenSees για τα πειράματα ανακυκλιζόμενης φόρτισης σταθερού εύρους. Σε αυτή την περίπτωση, η μη-γραμμικότητα του υλικού προσεγγίστηκε με βάση την παραδοχή κατανεμημένης βλάβης (fiber elements) ενώ εκτιμήθηκαν παράμετροι για την προσομοίωση της βλάβης λόγω ανακυκλιζόμενης φόρτισης.



Σχήμα 16: Αποτελέσματα προσομοίωσης (μαύρο χρώμα) της βλάβης λόγω ανακυκλιζόμενου φορτίου στα FUSEIS δοκούς από χάλυβες (a) S700 και (b) S355 (πειραματικές καμπύλες σε γκρι χρώμα)

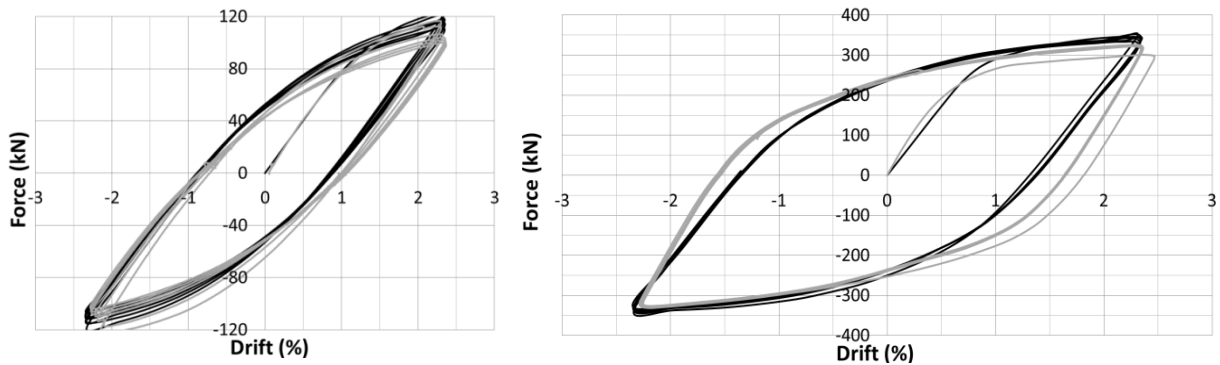
Η προσομοίωση στο Abaqus περιελάμβανε τη χρήση εξάεδρων πεπερασμένων στοιχείων (solid elements) και υπορουτινών υλικού βασισμένων στις Αρχές της Μηχανικής Βλάβης. Η δημιουργία των υπορουτινών υλικού έγινε από άλλους συμμετέχοντες στο πρόγραμμα “MATCH” (πανεπιστήμια Άαχεν και Θεσσαλίας) βάσει μιας υβριδικής αριθμητικής / πειραματικής προσέγγισης. Οι υπορουτίνες περιελάμβαναν ένα τμήμα που αναφερόταν στην μετελαστική συμπεριφορά του υλικού και ένα τμήμα που περιέγραφε τη διαδικασία συσσώρευσης βλάβης μέχρι τη ρηγμάτωση. Όπως φαίνεται στο Σχήμα 17 το πλέγμα των πεπερασμένων στοιχείων ήταν αρκετά πυκνότερο στις κρίσιμες περιοχές συγκέντρωσης της βλάβης. Αξίζει να σημειωθεί ότι λόγω των μεγάλων υπολογιστικών απαιτήσεων, η προσομοίωση όλων των κύκλων φόρτισης των πειραμάτων δεν ήταν εφικτή.



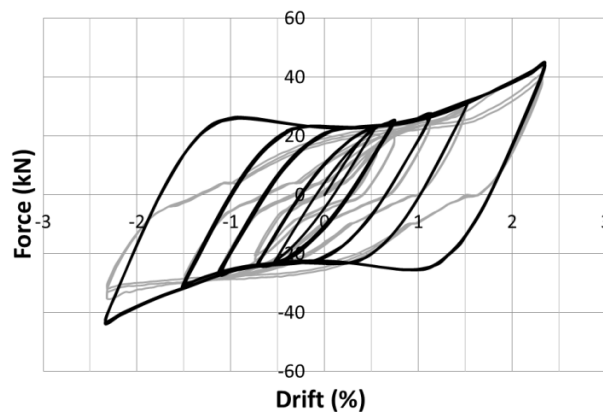
Σχήμα 17: Προσομοιώματα συστημάτων FUSEIS στο Abaqus

Στο Σχήμα 18 δίνονται τα αποτελέσματα της προσομοίωσης για τα πειράματα T2 (S700) και T5 (S355) σε FUSEIS με δοκούς. Το Σχήμα 19 δείχνει την προσομοίωση του πειράματος T7 σε FUSEIS με πείρους (S500). Όπως φαίνεται, το χαρακτηριστικό σχήμα των βρόχων υστέρησης (που σχετίζεται με την ανάπτυξη λειτουργίας καλωδίου) έχει προσομοιωθεί επαρκώς παρότι η προσέγγιση της συνολικής καταναλισκόμενης ενέργειας δεν είναι ιδιαίτερα ακριβής. Ένας από τους στόχους της προσομοίωσης στο Abaqus ήταν να αξιολογηθούν οι υπορουτίνες για τα τρία υλικά (S355, S500, S700) ως προς τη δυνατότητα να προβλέπουν την έναρξη της ρηγμάτωσης στα δοκίμια. Το Σχήμα 20 δείχνει πως προσομοιώθηκε η έναρξη της ρηγμάτωσης στα δοκίμια (με κόκκινο χρώμα) και παράλληλα συγκρίνει τα αριθμητικά αποτελέσματα με τα πειραματικά. Ο

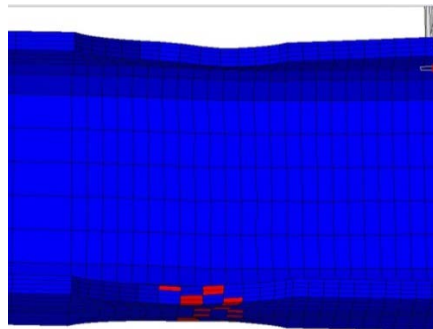
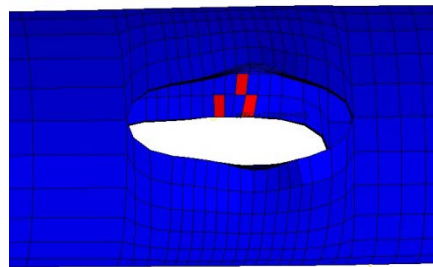
Πίνακας 11 συνοψίζει τους κρίσιμους κύκλους φόρτισης για την έναρξη ρηγματώσης σε κάθε σύστημα που προσομοιώθηκε. Όπως φαίνεται, η προσομοίωση ήταν πιο ακριβής για τα δοκίμια από χάλυβες υψηλής αντοχής και για τα πειράματα μεταβλητού εύρους.

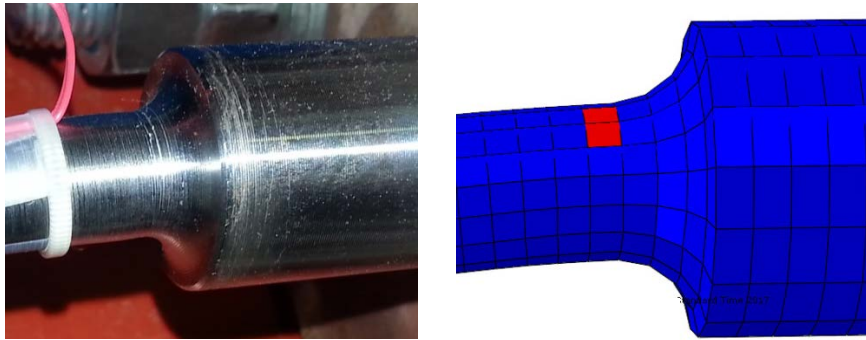


Σχήμα 18: Αποτελέσματα προσομοίωσης (μαύρο χρώμα) των 6 πρώτων κύκλων φόρτισης σε FUSEIS (a) με δοκούς S700 και (b) με δοκούς S355. Οι πειραματικές καμπύλες είναι σε γκρι.



Σχήμα 19: Αποτελέσματα προσομοίωσης (μαύρο χρώμα) δοκιμής T7 (γκρι χρώμα) σε FUSEIS με πείρους (S500)





Σχήμα 20: Έναρξη ρηγματώσης στα πειράματα και στα προσομοιώματα (κόκκινο χρώμα) σε δοκίμιο κυλινδρικής δοκού (S700), HEA (S355) και πείρο (S500)

Πίνακας 11: Σύγκριση πειραματικών και αριθμητικών αποτελεσμάτων ως προς την έναρξη ρηγματώσης

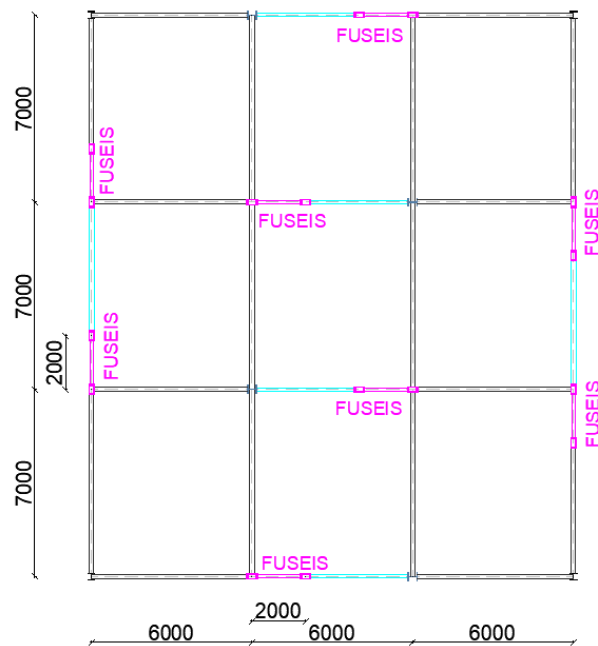
FUSEIS	Πείραμα	Φόρτιση	Έναρξη ρηγματώσης, πείραμα (σε δοκίμιο Si)*	Έναρξη ρηγματώσης, προσομοίωμα (σε δοκίμιο Si)*
S700 Κοίλες δοκοί	T1	Αυξαν. εύρος	$\phi_{exp} = 2.5\%$ (S1,S2) $N_{exp} = 9$ (S2)	$\phi_{sim} = 2.5\%$ (S1,S2) $N_{sim} = 3$ (S1)
	T2	Σταθ. εύρος	$N_{exp} = 10$ (S5) $N_{exp} = 15$ (S1)	$N_{sim} = 3$ (S5) $N_{sim} = 4$ (S2)
S355 Δοκοί HEA	T5	Σταθ. εύρος	$N_{exp} \leq 34$ (S3)	$N_{sim} = 4$ (S3)
			$N_{exp} = 38$ (S4) $N_{exp} = 43$ (S1) $N_{exp} = 45$ (S2)	$N_{sim} = 4$ (S1) $N_{sim} = 5$ (S2)
S500 Πείροι	T7	Αυξαν. εύρος	$\phi_{exp} = 1.1\%$ (S5) $\phi_{exp} = 1.5\%$ (S4) $\phi_{exp} = 2.3\%$ (S2) $N_{exp} = 6$ (S5)	$\phi_{sim} = 1.1\%$ (S5) $\phi_{sim} = 1.1\%$ (S4) $\phi_{sim} = 2.3\%$ (S2) $N_{sim} = 3$ (S5)
	T8	Σταθ. εύρος	$N_{exp} = 9$ (S4) $N_{exp} = 14$ (S2)	$N_{sim} = 3$ (S4) $N_{sim} = 7$ (S2)

* ϕ είναι η κρίσιμη γωνιακή παραμόρφωση και N είναι ο κρίσιμος κύκλος

1.5 Εφαρμογή σε κτίρια

1.5.1 Σχεδιασμός

Για την αποτίμηση της επιτελεστικότητας των δοκών FUSEIS από χάλυβα S700 σχεδιάστηκαν δύο κτίρια με δύο και πέντε ορόφους και την ίδια κάτοψη (Σχήμα 21). Το ύψος ορόφου θεωρήθηκε ίσο με 3,40 m. Όπως φαίνεται στο σχήμα, τα κτίρια διαθέτουν οκτώ συστήματα FUSEIS (μωβ χρώμα): τέσσερα σε κάθε διεύθυνση. Στο διώροφο η πλευρική ευστάθεια παρέχεται από τα FUSEIS αποκλειστικά ενώ στο πενταώροφο παρέχεται από συνδυασμένη δράση των FUSEIS με επιλεγμένα πλαίσια ροπής μέσω ισχυρών δοκών (γαλάζιο χρώμα).



Σχήμα 21: Κάτοψη κτιρίων

Ο Πίνακας 12 συνοψίζει τα φορτία που ελήφθησαν υπόψη κατά το σχεδιασμό, σύμφωνα με τους Ευρωκώδικες EN1991 και EN1998. Οι πλάκες και οι δευτερεύουσες δοκοί θεωρήθηκαν σύμμικτες.

Πίνακας 12: Φορτία σχεδιασμού (EN1991-1, EN1998-1)

Κατακόρυφα φορτία	(kN/m ²)
Dead (from composite slabs)	2.5
Additional dead	2.0
Imposed (category B, table 6.2 EN1991-1)	3.0
Σεισμικές παράμετροι	
Spectrum type	1
Peak ground acceleration	0.25g
Importance class/ factor	II/ $\gamma=1.00$
Ground type / Soil factor	B/ $S=1.2$
Period parameters T_B, T_C, T_D (sec)	0.15, 0.5, 2.0
Factor ϕ for variable actions in seismic combinations (for 5-story case study):	
- Roof	1.00
- Stories with correlated occupancies	0.80
Behavior factor q_{des}	3.50

Ο Πίνακας 13 συνοψίζει τις διατομές των μελών, όπως προέκυψαν από τους ελέγχους που προβλέπονται στους Ευρωκώδικες EN1993 και EN1998. Σε αρκετές περιπτώσεις, κρίσιμος ήταν ο έλεγχος περιορισμού βλάβης όπως εκφράζεται στον περιορισμό σχετικής παραμόρφωσης ορόφου. Όσον αφορά στα υλικά, χάλυβας υψηλής αντοχής χρησιμοποιήθηκε μόνο στις δοκούς FUSEIS οι

οποίες αποτελούνταν από κοίλες διατομές κατ' αντιστοιχία με τα πειραματικά δοκίμια. Σημειώνεται ότι η χρήση χάλυβα υψηλής αντοχής στα στοιχεία απορρόφησης ενέργειας ενός σχετικά εύκαμπτου αντισεισμικού συστήματος φαίνεται παράδοξη, καθώς ο συνδυασμός των απαιτήσεων δυσκαμψίας με την υψηλή αντοχή του υλικού οδηγεί σε χαμηλούς συντελεστές εκμετάλλευσης των FUSEIS. Επιπλέον αυτό αυξάνει τους συντελεστές των δράσεων κατά τον ικανοτικό έλεγχο. Ωστόσο κύριος στόχος αυτής της διερεύνησης είναι να εξετάσει κατά πόσο αυτά τα στοιχεία απορρόφησης ενέργειας μπορούν να έχουν αποδεκτή σεισμική συμπεριφορά, ανεξάρτητα από το αν η σχεδιαστική προσέγγιση παρέχει ουσιαστικά οικονομικά οφέλη.

Πίνακας 13: Διατομές μελών

Μέλος	Χάλυβας	Πενταώροφο	Διώροφο
FUSEIS columns	S355	RHS 400x200x14.2 / RHS 300x200x10.0	RHS 400x200x12.5
FUSEIS beams (for i story)	S700	RHS250x100x8 (1) RHS220x120x7.1 (2) RHS180x120x6 (3) RHS160x80x7.1 (4) RHS140x80x5 (5)	RHS180x120x6 (1) RHS180x120x6 (2)
Columns	S355	HEB360/HEB340 (internal) HEB260/HEB180 (corners)	HEB260
Strong Beams	S355	IPE450/IPE400	-
Main Beams	S355	IPE 300 (perimeter) IPE 330, 360 (X,Y)	IPE 300 (perimeter) IPE 330, 360 (X,Y)
Secondary Beams	S355	HEA140 (composite)	HEA140 (composite)

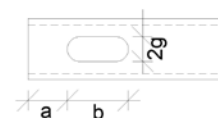
Οι δοκοί FUSEIS σχεδιάστηκαν με απομειωμένες διατομές (RBS) σύμφωνα με τις προδιαγραφές των EN1998-3 και FEMA350. Ο Πίνακας 14 συνοψίζει τα γεωμετρικά και αδρανειακά χαρακτηριστικά τους καθώς και ελέγχους σε σχέση με τις μέγιστες αναπτυσσόμενες καμπτικές ροπές και τέμνουσες δυνάμεις στο άκρο της εκάστοτε δοκού.

Ο Πίνακας 15 δίνει τα αποτελέσματα του ελέγχου περιορισμού βλαβών για τα δύο κτίρια σε κάθε διεύθυνση. Με βάση τον EN1998-1 το όριο της μέγιστης γωνιακής παραμόρφωσης για τον ελαστικό σεισμό σχεδιασμού είναι ίσο με 1,50%. Σημειώνεται ότι επειδή οι φορείς ήταν σχετικά εύκαμπτοι, τα φαινόμενα δευτέρας τάξης έπρεπε να ληφθούν υπόψη θεωρώντας τον συντελεστή προσαύξησης $1/(1-\theta)$ στα σεισμικά εντατικά μεγέθη, βάσει του EN1998-1.

Πίνακας 14: Σχεδιασμός απομειωμένων διατομών στις δοκούς FUSEIS (RBS)

	FUSEIS δοκός (όροφος)	Πλήρης διατομή W_{pl} (x1000 mm ³)	Διατομή RBS W_{plRBS} (x1000 mm ³)	2g (mm)	a (mm)	b (mm)	M_c/M_{plRdb}	$V_{Ed,max}/V_{plRd}$
5 όροφοι	RHS250x100x8 (1)	385.4	298.3	44.0	60	175.0	0.95	0.22
	RHS220x120x7.1 (2)	312.8	222.1	60.0	60	143.0	0.85	0.20
	RHS180x120x6 (3)	201.7	139.1	60.0	60	129.6	0.82	0.18
	RHS160x80x7.1 (4)	148.6	108.7	46.0	48	120.0	0.85	0.13
	RHS140x80x5 (5)	91.8	67.0	38.4	48	105.0	0.83	0.13
2 ορ.	RHS180x120x6 (1)	201.7	151.6	48	60	129.6	0.89	0.19
	RHS180x120x6 (2)	201.7	139.1	60	60	129.6	0.82	0.18

Διαστάσεις a, b, 2g όπως στο σχήμα:



Πίνακας 15: Έλεγχος γωνιακών παραμορφώσεων (%)

Όροφος	Πενταώροφο κτίριο		Διώροφο κτίριο	
	Διεύθυνση Χ	Διεύθυνση Υ	Διεύθυνση Χ	Διεύθυνση Υ
1	0.99 %	0.99 %	1.48 %	1.48 %
2	0.82 %	0.92 %	1.16 %	1.17 %
3	0.82 %	0.99 %	-	-
4	0.84 %	1.11 %	-	-
5	0.66 %	1.01 %	-	-

Για να διασφαλιστεί η κατά το δυνατόν ομοιογενής κατανάλωση ενέργειας μέσω των FUSEIS, έπρεπε να ελεγχθεί ότι ο μέγιστος συντελεστής υπεραντοχής Ω δεν υπερβαίνει τον ελάχιστο κατά περισσότερο από 25%, όπως περιγράφεται στην παρακάτω εξίσωση:

$$\Omega_i = M_{pl,Rd,i} / M_{Ed,i}$$

$$\max \Omega_i / \min \Omega_i < 1.25$$

Eq. 1-5

Ο Πίνακας 16 και ο Πίνακας 17 συνοψίζουν τα αποτελέσματα των ελέγχων για τους δύο φορείς. Σημειώνεται ότι για τον ικανοτικό έλεγχο σε κάθε κτίριο έχουν ληφθεί υπόψη οι εκάστοτε ελάχιστοι συντελεστές Ω .

Πίνακας 16: Συντελεστές υπεραντοχής Ω των συνδέσμων FUSEIS ανά όροφο (5)

Όροφος	FUSEIS	max (1/ Ω)	Ω_i	($\Omega_i - \Omega_{min}$)/ Ω_{min} (%)
1	RHS250x100x8	0.41	2.45	0.0
2	RHS220x120x7.1	0.33	3.06	24.8
3	RHS180x120x6	0.33	3.03	23.6
4	RHS160x80x7.1	0.37	2.70	10.3
5	RHS140x80x5	0.35	2.86	16.6

Πίνακας 17: Συντελεστές υπεραντοχής Ω των συνδέσμων FUSEIS ανά όροφο (2)

Όροφος	FUSEIS	max (1/ Ω)	Ω_i	($\Omega_i - \Omega_{min}$)/ Ω_{min} (%)
1	RHS180x120x6 (1)	0.49	2.06	0.0
2	RHS180x120x6 (2)	0.40	2.48	20.4

Ο Πίνακας 18 δίνει τους μέγιστους συντελεστές εκμετάλλευσης ανά τύπο μέλους. Στα υποστυλώματα έγιναν έλεγχοι διατομής και μέλους υπό αξονική δύναμη με διαξονική κάμψη σύμφωνα με τον EN1993, θεωρώντας τα εντατικά μεγέθη από τον ικανοτικό έλεγχο. Ο Πίνακας 19 συνοψίζει τα αποτελέσματα της ιδιομορφικής ανάλυσης.

Πίνακας 18: Συντελεστές εκμετάλλευσης μελών

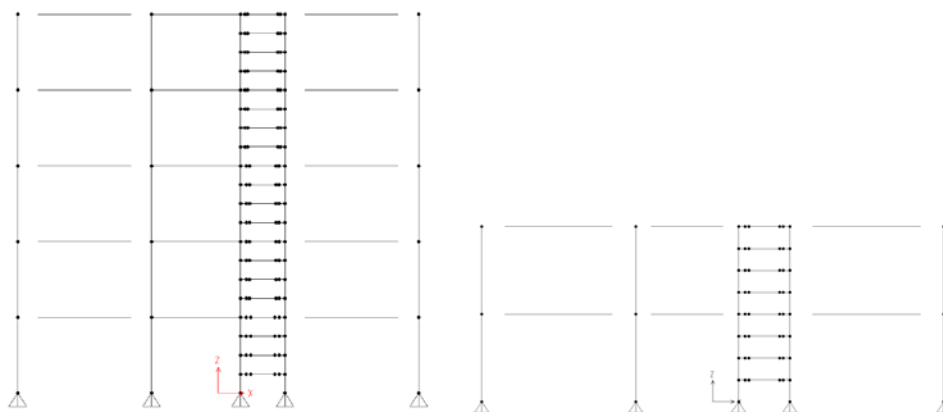
Μέλος	Πεντάωροφο κτίριο		Διώροφο κτίριο	
	Διατομή	Συντελ.	Διατομή	Συντελ.
Beams	IPE300	0.64	IPE300	0.64
	IPE330	0.68	IPE330	0.68
	IPE360	0.63	IPE360	0.63
Strong beams	IPE450	0.99	-	-
	IPE400	0.69	-	-
Columns	HEB360	0.77	HEB260	0.27
	HEB340	0.65		
Columns (corner)	HEB260	0.20		
	HEB180	0.29		
FUSEIS columns	RHS400x200x14.2	0.90	RHS400x200x12.5	0.66
	RHS300x200x10.0	0.90		

Πίνακας 19: Αποτελέσματα της ιδιομορφικής ανάλυσης

Ιδιομορφή	Πεντάωροφο κτίριο			Διώροφο κτίριο		
	Περίοδος (sec)	Συμμετοχή μάζας (X)	Συμμετοχή μάζας (Y)	Περίοδος (sec)	Συμμετοχή μάζας (X)	Συμμετοχή μάζας (Y)
1	1.30	0.00	0.80	0.80	0.92	0.00
2	1.10	0.84	0.80	0.80	0.92	0.92
3	0.85	0.84	0.80	0.57	0.92	0.92
4	0.47	0.84	0.94	0.25	0.92	0.92
5	0.39	0.96	0.94	0.25	0.92	0.92

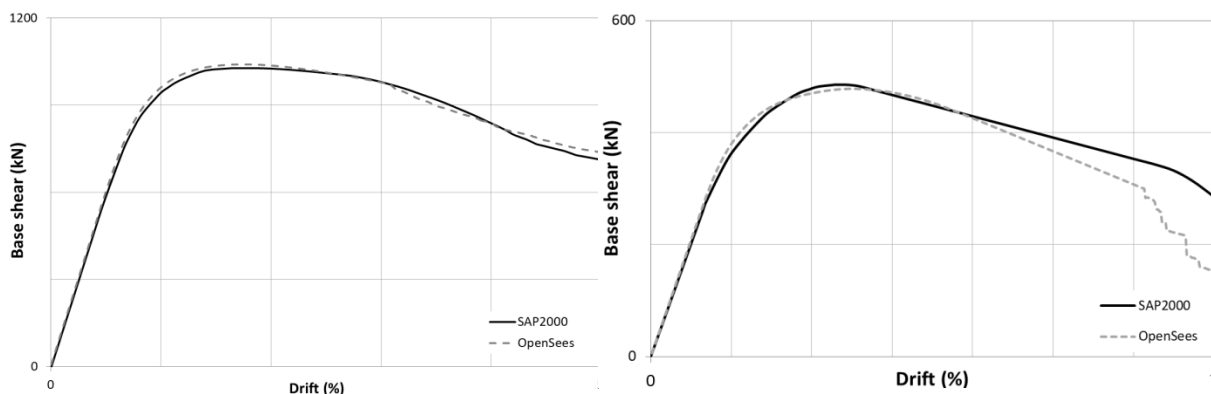
1.5.2 Δισδιάστατα προσομοιώματα και μη γραμμικές στατικές αναλύσεις

Δισδιάστατα προσομοιώματα των φορέων μορφώθηκαν για τη διευκόλυνση των μη γραμμικών στατικών και δυναμικών αναλύσεων. Όπως φαίνεται στο Σχήμα 22, εξετάστηκε ένα πλαίσιο κατά τη διεύθυνση X. Τα αποτελέσματα της ιδιομορφικής ανάλυσης στα δισδιάστατα μοντέλα ήταν σχεδόν ίδια με αυτά που παρουσιάστηκαν στον Πίνακα 19 για τη διεύθυνση X.



Σχήμα 22: Αντιπροσωπευτικοί δισδιάστατοι φορείς

Τα δισδιάστατα προσομοιώματα μορφώθηκαν σε δύο λογισμικά: αρχικά στο SAP2000 το οποίο είχε χρησιμοποιηθεί κατά τον σχεδιασμό και στη συνέχεια στο OpenSees, που είναι καταλληλότερο για αυξημένο αριθμό μη γραμμικών δυναμικών αναλύσεων. Το Σχήμα 23 δείχνει τη συμφωνία μεταξύ των δυο διαφορετικών προσομοιωμάτων, όπως φαίνεται από τα αποτελέσματα αναλύσεων pushover. Σημειώνεται ότι η προσέγγιση της μη γραμμικότητας του υλικού ήταν διαφορετική στις δύο περιπτώσεις: στο SAP2000 θεωρήθηκαν θέσεις πιθανών πλαστικών αρθρώσεων (συγκεντρωμένη βλάβη) ενώ στο OpenSees υιοθετήθηκε η προσέγγιση της κατανεμημένης βλάβης (διακριτοποίηση μελών με ίνες). Οι παραδοχές για μη γραμμικότητα βασίστηκαν στα αποτελέσματα της βαθμονόμησης των προσομοιωμάτων των πειραμάτων.



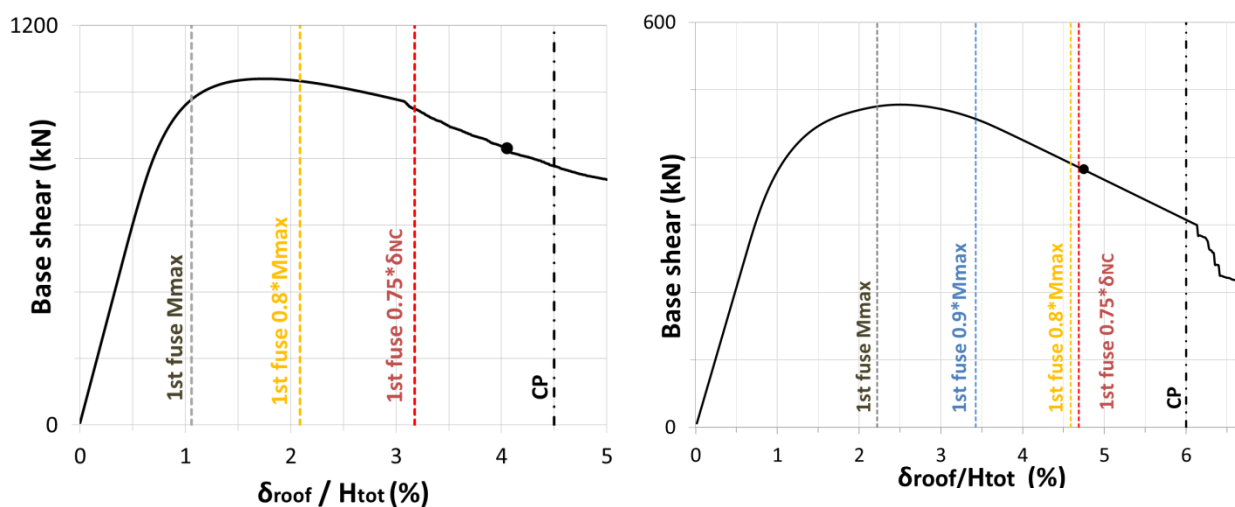
Σχήμα 23: Συμφωνία μεταξύ διαφορετικών προσομοιωμάτων (α) πενταώροφο και (β) διώροφο

Τα αποτελέσματα των μη γραμμικών στατικών αναλύσεων (pushover) αξιοποιήθηκαν για τη διερεύνηση των πλαστικών μηχανισμών και των γωνιακών παραμορφώσεων αναφοράς στη μετέπειτα φάση της αξιολόγησης, αλλά και για την προκαταρκτική αξιολόγηση του συντελεστή q . Ο Πίνακας 20 δείχνει ότι οι τιμές των συντελεστών συμπεριφοράς q με βάση την pushover είναι αρκετά μεγαλύτερες από την τιμή σχεδιασμού που ήταν ίση με 3,50.

Πίνακας 20: Υπολογισμός του συντελεστή συμπεριφοράς q_{st} από την pushover ανάλυση

	πενταώροφο	διώροφο
Overstrength ratio a_u/a_1	1.7	1.7
Ductility μ	4.3	4.6
Factor q_{st}	7.4	7.7

Ο Πίνακας 21 συνοψίζει τις οριακές τιμές για τις στάθμες επιτελεστικότητας “Προστασία ζωής – Life safety (LS)” και “Αποφυγή κατάρρευσης - Collapse prevention (CP)” σε όρους μέγιστης γωνιακής παραμόρφωσης (max. interstorey drift) και γωνιακής παραμόρφωσης όροφής (δ_{roof}/H_{tot}). Όπως φαίνεται στο πενταώροφο κτίριο οι τιμές αυτές διαφέρουν αρκετά καθώς με την αύξηση των μετατοπίσεων όροφής κατά την ανάλυση άρχισε να σχηματίζεται σταδιακά «μαλακός όροφος». Για την επιλογή των οριακών τιμών που δίνονται στον πίνακα, ακολουθήθηκε η μέθοδος INNOSEIS όπως περιγράφεται στο (Vamvatsikos et al. 2017). Για το πενταώροφο, καθοριστικό ρόλο ως προς της στάθμη LS έπαιξε η πτώση κατά 20% της αντοχής της δυσμενέστερης δοκού FUSEIS, ενώ η στάθμη CP καθορίστηκε από την απόκριση του δυσμενέστερου υποστυλώματος που συνδεόταν με τα FUSEIS μέσω ισχυρής δοκού (Σχήμα 24α). Για το διώροφο, η στάθμη LS καθορίστηκε από την πτώση κατά 10% της αντοχής της δυσμενέστερης δοκού FUSEIS, ενώ το όριο CP τέθηκε πριν από την απότομη πτώση της φέρουσας ικανότητας όπως φαίνεται στο Σχήμα 24β.



Σχήμα 24: Καμπύλες ικανότητας και στάθμες επιτελεστικότητας (α) πενταώροφο (β) διώροφο

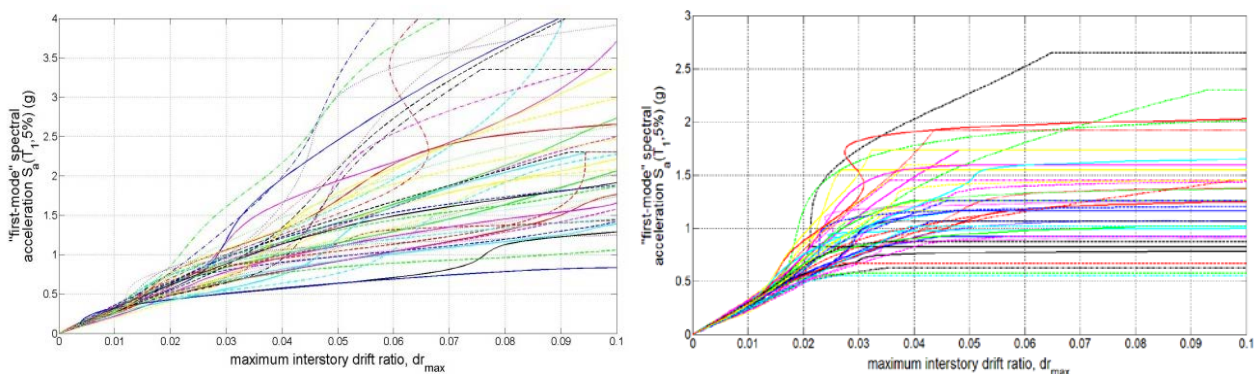
Πίνακας 21: Στάθμες επιτελεστικότητας για αποτίμηση συμπεριφοράς

Στάθμη επιτελεστικότητας	Πενταώροφο		Διώροφο	
	LS	CP	LS	CP
Μέγιστη γωνιακή παραμόρφωση (%)	4.2	8.0	3.8	6.3
$\delta_{\text{roof}}/H_{\text{tot}}$ (%)	2.1	4.5	3.4	6.0

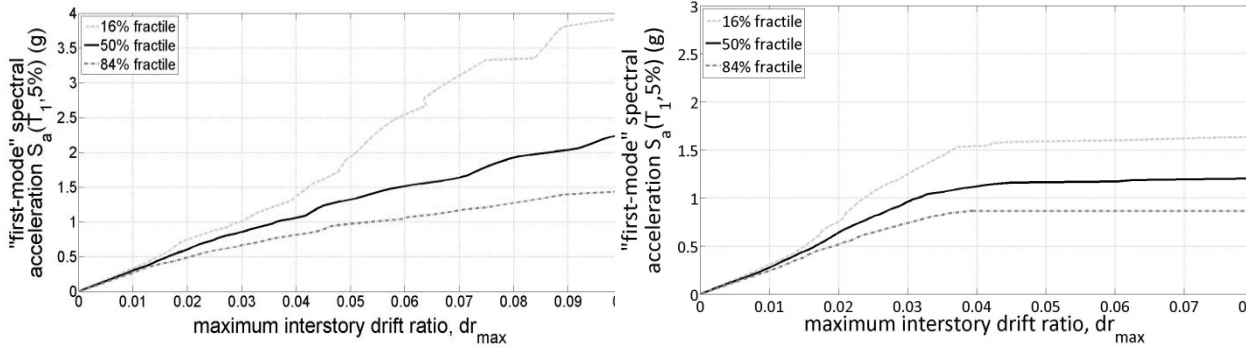
1.5.3 Μη γραμμικές δυναμικές αναλύσεις

Η αποτίμηση της απόκρισης των δύο φορέων για τις στάθμες επιτελεστικότητας LS και CP έγινε μέσω μη γραμμικών επαυξητικών δυναμικών αναλύσεων (Incremental Dynamic Analyses - IDA). Στις αναλύσεις αυτές, θεωρήθηκε ως δείκτης έντασης η φασματική επιτάχυνση (λαμβάνοντας υπόψη την πρώτη ιδιοπερίοδο, $S_a(T_1)$) και ως δείκτης «βλάβης» η μέγιστη (κατά απόλυτη τιμή) γωνιακή παραμόρφωση ορόφου. Η αποτίμηση έγινε με βάση δύο μεθοδολογίες: την ευρέως διαδεδομένη FEMA 695 και την INNONSEIS, η οποία αναπτύχθηκε πρόσφατα στα πλαίσια ενός ευρωπαϊκού ερευνητικού προγράμματος. Στόχος και των δύο μεθόδων είναι να επιβεβαιώσουν ή να απορρίψουν την τιμή του συντελεστή συμπεριφοράς q που θεωρήθηκε κατά τον σχεδιασμό. Ωστόσο, η διαδικασία επαλήθευσης καθώς και το σύνολο των επιταχυνσιογραφημάτων που κλιμακώνονται κατά τις αναλύσεις, διαφέρουν. Για τη μέθοδο FEMA695 χρησιμοποιήθηκε το σύνολο «Μακρινού πεδίου» (Far-Field Record set). Για τη μέθοδο INNONSEIS χρησιμοποιήθηκε το σύνολο που αντιστοιχεί σε υψηλή σεισμικότητα (high seismicity record set), διαθέσιμο στην ιστοσελίδα <http://innoseis.ntua.gr/>.

Στο Σχήμα 25 δίνονται οι καμπύλες IDA για το πενταώροφο και το διώροφο κτίριο και στο Σχήμα 26 τα αποτελέσματα συνοψίζονται με τις ποσοστιαίες καμπύλες 16%, 50% και 84%.



Σχήμα 25: Καμπύλες IDA για πενταώροφο και διώροφο φορέα (μέθοδος FEMA 695)



Σχήμα 26: Ποσοστιαίες καμπύλες για πεντάώροφο και διώροφο φορέα

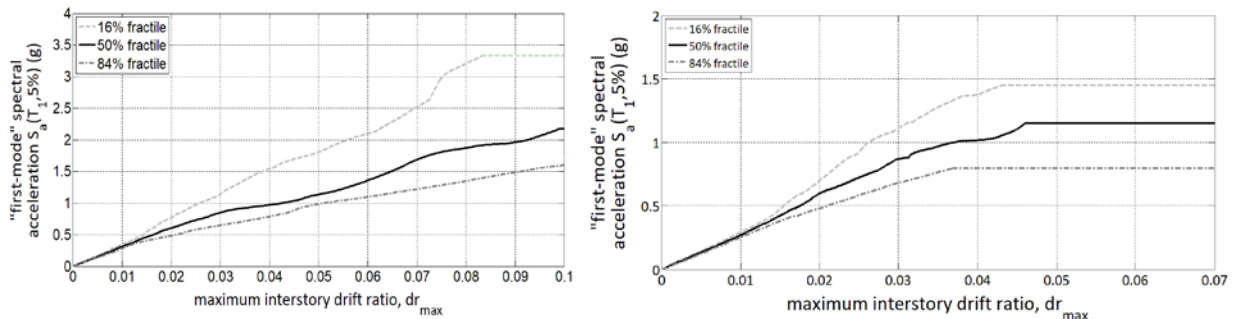
Ο Πίνακας 22 συνοψίζει τα αποτελέσματα της αποτίμησης για τους δύο φορείς και τις δύο στάθμες επιτελεστικότητας LS και CP. Ο συντελεστής η είναι αποδεκτός, εφόσον το «προσαρμοσμένο περιθώριο ασφαλείας» (ACMR) είναι μεγαλύτερο από την οριακή τιμή ACMR10%.

Πίνακας 22: Επαλήθευση συντελεστή η (μέθοδος FEMA 695)

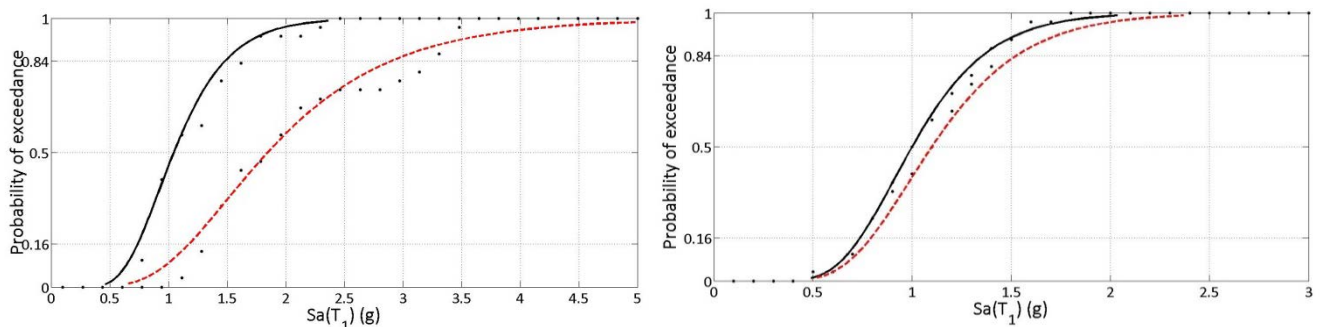
Limit State	Πεντάώροφο		Διώροφο	
	LS	CP	LS	CP
Median Value (S_{CT}) – g units	1.10	1.90	1.15	1.24
Intensity of MCE (S_{MT}) – g units	0.595	0.595	0.80	0.80
Collapse margin ratio (CMR)	1.85	3.19	1.44	1.55
Spectral Shape factor (SSF)	1.19	1.19	1.16	1.16
Adjusted Collapse margin ratio (ACMR)	2.20	3.80	1.67	1.80
Total uncertainty β_{TOT}	0.50	0.60	0.40	0.45
Limit ACMR10%	1.90	2.16	1.67	1.78
Check (ACMR > ACMR10%)	ok	ok	ok	ok

Το Σχήμα 27 συνοψίζει τα αποτελέσματα της ανάλυσης IDA με τη μέθοδο INNOSEIS σε όρους ποσοστιαίων καμπύλων. Το Σχήμα 28 απεικονίζει τις καμπύλες τρωτότητας για το κάθε κτίριο και την κάθε στάθμη επιτελεστικότητας (προστασία ζωής σε μαύρο χρώμα και αποφυγή κατάρρευσης σε κόκκινο). Στη μέθοδο αυτή, οι καμπύλες τρωτότητας συνδυάζονται με τις «καμπύλες σεισμικού κινδύνου» (hazard curves) ορισμένων κρίσιμων και αντιπροσωπευτικών (σε όρους σεισμικότητας) περιοχών, με στόχο να προκύψει η μέση ετήσια συχνότητα υπέρβασης της εκάστοτε στάθμης επιτελεστικότητας (τιμές λ ή αλλιώς mean annual frequency – MAF). Οι κρίσιμες περιοχές που προτείνονται σε συνδυασμό με το σύνολο υψηλής σεισμικότητας είναι οι: Αθήνα (GR), Perugia (IT) και Foscani (RO). Ο Πίνακας 23 συνοψίζει τα αποτελέσματα της αποτίμησης. Οι τιμές λ_x που προκύπτουν για κάθε στάθμη επιτελεστικότητας συγκρίνονται με τις οριακές τιμές λ_{lim} που αντιστοιχούν σε 10% πιθανότητα υπέρβασης σε 50 χρόνια για τη στάθμη LS και 2% πιθανότητα

υπέρβασης σε 50 χρόνια για τη στάθμη CP. Όπως φαίνεται, ο συντελεστής η είναι αποδεκτός καθώς τα περιθώρια ασφαλείας $\lambda_{lim} / \lambda_x$ είναι αρκετά μεγάλα. Ωστόσο, σημειώνεται ότι τα περιθώρια αυτά μπορεί να μειωθούν σημαντικά εάν στη διαδικασία αποτίμησης συμπεριληφθούν επιπλέον αβεβαιότητες (πέραν της διασποράς των αποτελεσμάτων), όπως δείχνει ο Πίνακας 24.



Σχήμα 27: Ποσοστιαίες καμπύλες IDA για πεντάωροφο και διώροφο φορέα (INNOSEIS)



Σχήμα 28: Καμπύλες τρωτότητας για πεντάωροφο και διώροφο φορέα

Πίνακας 23: Επαλήθευση συντελεστή η (μέθοδος INNOSEIS)

Limit State	5-story		2-story		
	LS	CP	LS	CP	
MAF of limit state λ_{lim}	2.107	0.404	2.107	0.404	
Uncertainty β	0.351	0.453	0.306	0.330	
Athens	MAF from IDA, λ_x (‰)	0.064	0.017	0.118	0.096
	Margin Ratio ($\lambda_{lim} / \lambda_x$)	33.1	23.2	17.93	4.21
	check ($\lambda_{lim} > \lambda_x$)	ok	ok	ok	ok
Perugia	MAF from IDA, λ_x (‰)	0.044	0.012	0.092	0.076
	Margin Ratio ($\lambda_{lim} / \lambda_x$)	47.42	32.98	22.85	5.34
	check ($\lambda_{lim} > \lambda_x$)	ok	ok	ok	ok
Foscani	MAF from IDA, λ_x (‰)	0.030	0.004	0.086	0.064
	Margin Ratio ($\lambda_{lim} / \lambda_x$)	71.07	100.21	24.50	6.28
	check ($\lambda_{lim} > \lambda_x$)	ok	ok	ok	ok

Πίνακας 24: Επαλήθευση συντελεστή q (μέθοδος INNOSEIS) με αυξημένες αβεβαιότητες

Limit State	5-story		2-story		
	LS	CP	LS	CP	
MAF of limit state λ_{lim} (‰)	2.107	0.404	2.107	0.404	
Uncertainty β_{tot}	0.43	0.54	0.39	0.45	
Athens	MAF from IDA, λ_x (‰)	0.073	0.024	0.139	0.127
	Margin Ratio ($\lambda_{lim} / \lambda_x$)	28.8	16.6	15.1	3.2
	check ($\lambda_{lim} > \lambda_x$)	ok	ok	ok	ok
Perugia	MAF from IDA, λ_x (‰)	0.053	0.017	0.107	0.097
	Margin Ratio ($\lambda_{lim} / \lambda_x$)	39.7	23.9	19.7	4.2
	check ($\lambda_{lim} > \lambda_x$)	ok	ok	ok	ok
Foscani	MAF from IDA, λ_x (‰)	0.050	0.011	0.128	0.122
	Margin Ratio ($\lambda_{lim} / \lambda_x$)	42.3	36.6	16.4	3.3
	check ($\lambda_{lim} > \lambda_x$)	ok	ok	ok	ok

1.6 Σύνοψη και προτάσεις για περαιτέρω έρευνα

Στη διατριβή διερευνάται η χρήση χαλύβων υψηλής αντοχής σε στοιχεία απορρόφησης ενέργειας του καινοτόμου αντισεισμικού συστήματος FUSEIS. Η διάταξη της εργασίας είναι η εξής: (i) βιβλιογραφική έρευνα, (ii) περιγραφή και ανάλυση πειραματικών διερευνήσεων, (iii) αναλυτικές και αριθμητικές προσεγγίσεις των πειραμάτων και (iv) σχεδιασμός και αποτίμηση της επιτελεστικότητας σχετικών κτιριακών φορέων.

Τα πειραματικά δοκίμια αποτελούνταν από συνδέσμους FUSEIS διαφορετικών τύπων, διατομών και υλικών (S355, S500, S700). Τα πειραματικά αποτελέσματα αξιολογήθηκαν με όρους πλαστιμότητας, εξέλιξης της βλάβης, απομείωσης της αντοχής και της δυσκαμψίας κλπ. Το σύστημα FUSEIS με δοκούς HEA από χάλυβα S355J2 ήταν πιο πλάστιμο, καθώς δεν παρουσίασε βλάβες μέχρι να φτάσει σε γωνιακή παραμόρφωση ίση με 3,5%. Το σύστημα με κοιλοδοκούς από S700MC έφτασε στη μέγιστη αντοχή του για γωνιακή παραμόρφωση ίση με 2,5%. Το σύστημα με κυλινδρικούς πείρους από S500MC έφτασε στη μέγιστη αντοχή για γωνιακή παραμόρφωση ίση με 3,1% (αντίστοιχη στροφή πείρων περίπου ίση με 174 mrad) και παράλληλα ανέπτυξε λειτουργία καλωδίων (catenary action). Σύγκριση με προηγούμενα πειραματικά δεδομένα σε συστήματα με συνδέσμους από χάλυβα S235, έδειξε ότι στην περίπτωση των δοκών FUSEIS, η αύξηση της αντοχής του χάλυβα οδήγησε σε αντίστοιχη μείωση της πλαστιμότητας. Δεδομένου ότι δεν υπάρχουν ακόμη κανονιστικές προδιαγραφές για τα αποδεκτά όρια παραμορφώσεων των FUSEIS, παρατέθηκαν ορισμένες τιμές αναφοράς (ως τάξη μεγέθους) για συμβατικά συστήματα πλευρικής ευστάθειας, όπως τα πλαίσια ροπής και τα πλαίσια με διαγώνιους συνδέσμους. Με βάση αυτά τα

στοιχεία (και παρότι το πλήθος των πειραμάτων που εκπονήθηκαν είναι σχετικά μικρό), φαίνεται πως τα συστήματα που εξετάστηκαν επέδειξαν ικανοποιητική (S355, S500) ή αποδεκτή σεισμική απόκριση (S700).

Η αναλυτική προσέγγιση των πειραμάτων κατέληξε σε προτεινόμενες εξισώσεις για τον υπολογισμό της φέρουσας ικανότητας των FUSEIS είτε με δοκούς είτε με πείρους. Οι αριθμητικές προσομοιώσεις των πειραμάτων έγιναν με χρήση διαφορετικών λογισμικών και κατέληξαν σε προτάσεις και παραμέτρους που μπορούν να αξιοποιηθούν σε μελλοντικές διερευνήσεις.

Τέλος, ο σχεδιασμός παραδειγμάτων κτιρίων με συστήματα FUSEIS με στοιχεία κατανάλωσης ενέργειας από χάλυβα S700, κατέδειξε τις δυσκολίες που μπορεί να δημιουργηθούν από αυτή την επιλογή υλικών κατά τους αντισεισμικούς ελέγχους. Ωστόσο, η διερεύνηση της απόκρισης των φορέων μέσω μη-γραμμικών στατικών και δυναμικών αναλύσεων, έδειξε ότι η θεώρηση συντελεστή συμπεριφοράς q ίσο με 3.5 για τα FUSEIS με δοκούς από S700, είναι αποδεκτή.

Ως γνωστόν, ο σχεδιασμός πειραμάτων μεγάλης κλίμακας υπόκειται σε ένα πλήθος αντικειμενικών περιορισμών που σχετίζονται με τις δυνατότητες των εμπλεκόμενων Εργαστηρίων (χωροθέτηση, δυνατότητες εμβόλων, λοιπές υποδομές, οικονομικοί πόροι για την αγορά των δοκιμίων κοκ). Οι περιορισμοί αυτοί καθορίζουν το πλήθος των πειραμάτων, ενώ είναι ευρέως αποδεκτό ότι αυξημένος αριθμός πειραμάτων μπορεί να οδηγήσει σε μεγαλύτερη ακρίβεια. Η εκπόνηση περισσότερων αντίστοιχων πειραμάτων προτείνεται για το μέλλον. Επιπλέον, προτείνεται να διερευνηθεί η επιρροή του μεγέθους (size effect) των συνδέσμων FUSEIS στην απόκριση του συστήματος καθώς και μια εναλλακτική διάταξη που θα περιλαμβάνει συγκολλητές αντί για κοχλιωτές συνδέσεις τους με τα υποστυλώματα, προς αποφυγή των - ενίοτε μεγάλων - παρασιτικών μετατοπίσεων. Τέλος προτείνεται στις μελλοντικές διερευνήσεις να περιοριστεί το πλήθος των υπό εξέταση παραμέτρων (σε σχέση με την παρούσα έρευνα) προς διευκόλυνση της επεξεργασίας των αποτελεσμάτων και της εξαγωγής συμπερασμάτων.

1.7 Συμπεράσματα και πρωτότυπη συμβολή

Ο βασικός στόχος αυτής της διατριβής είναι να συμβάλει στην υπό εξέλιξη διεθνή συζήτηση πάνω στις πιθανές εφαρμογές των δομικών χαλύβων υψηλής αντοχής σε αντισεισμικά συστήματα. Μέχρι στιγμής, η διαθέσιμη βιβλιογραφία για πειράματα σε φορείς με χάλυβες υψηλής αντοχής υπό ανακυκλιζόμενη φόρτιση είναι αρκετά περιορισμένη. Στα πλαίσια αυτής της έρευνας, πραγματοποιήθηκαν πειράματα σε συστήματα FUSEIS με συνδέσμους από χάλυβες S500 και S700.

Επιπλέον, με τη διατριβή αυτή διευρύνεται η διαθέσιμη βάση δεδομένων για τα καινοτόμα συστήματα FUSEIS, τα οποία είχαν μελετηθεί στο παρελθόν με συνδέσμους (δοκούς ή πείρους) από χάλυβα S235. Πιο συγκεκριμένα, μελετήθηκαν ως στοιχεία απορρόφησης ενέργειας: κυλινδρικοί πείροι από S500, δοκοί HEA από S355 και κοίλες δοκοί από S700. Κατόπιν προτάθηκαν παράμετροι για την προσομοίωση της μη-γραμμικής συμπεριφοράς κάθε ενός από τους παραπάνω συνδέσμους. Τέλος, η διάταξη του συστήματος με πείρους απλοποιήθηκε.

Αναφορικά με τη διερεύνηση της απόκρισης σχετικών κτιριακών φορέων, προτάθηκε ο συνδυασμός της δράσης των FUSEIS είτε με γειτονικά συστήματα είτε με γειτονικά πλαίσια ροπής μέσω ισχυρών δοκών. Η προσέγγιση αυτή δείχνει να αντιμετωπίζει σε ένα βαθμό προβλήματα που απορρέουν από τη σχετική ευκαμψία του συστήματος και να επιτρέπει τη μείωση των διατομών των FUSEIS με ταυτόχρονη διατήρηση της απαιτούμενης δυσκαμψίας.

Συνοψίζοντας, ο αντισεισμικός σχεδιασμός με χάλυβες υψηλής αντοχής μπορεί να οδηγήσει σε αποδεκτά αποτελέσματα. Ωστόσο, για να είναι αποτελεσματική και επικερδής μια τέτοια σχεδιαστική προσέγγιση στο μέλλον, μάλλον θα πρέπει να συμπεριλαμβάνει υβριδικές λύσεις με χάλυβες υψηλής αντοχής και συστήματα που να συνδυάζουν τα πλεονεκτήματα των διαφορετικών υλικών.

Table of Contents

Chapter 1: Introduction	1
1.1 Prologue.....	1
1.2 Research objectives and framework	2
1.3 Thesis outline.....	3
Chapter 2: Literature review.....	5
2.1 Introduction.....	5
2.2 Material properties for design of steel structures.....	6
2.2.1 Basic terms	6
2.2.2 Eurocodes' material requirements and discussion	9
2.3 Development, research and applications of high-strength steels (HSS).....	12
2.4 Conventional seismic resistant systems	20
2.4.1 Moment Resisting Frames (MRF)	20
2.4.2 Braced frames	22
2.5 Innovative anti-seismic systems incorporating reparability	25
2.5.1 FUSEIS with beam or pin links	25
2.5.2 FUSEIS with splices	27
2.5.3 INERD connections	28
2.6 Innovative self-centering systems	29
2.6.1 Posttensioned Energy Dissipating Connection (PTED)	29
2.6.2 Self-Centering Energy Dissipative Bracing System (SCED).....	30
Chapter 3: Experimental investigations.....	32
3.1 Introduction.....	32
3.2 Test setup	32
3.3 Material properties.....	36
3.4 Measurements and kinematics	39
3.5 Loading protocols	41
3.6 Tests on FUSEIS with beam links.....	43
3.6.1 FUSEIS beam specimens.....	43
3.6.2 Cyclic response of FUSEIS with hollow-section beams of S700MC	46
3.6.3 Cyclic response of FUSEIS with HEA beams of S355J2	48
3.6.4 Correction of experimental data	51

3.6.5	Peak resistance and stiffness degradation	55
3.6.6	Overstrength and ductility of tested system	56
3.6.7	Energy dissipation	58
3.6.8	FUSEIS beams component tests	60
3.6.9	Comparison with previous research on FUSEIS beams with S235	63
3.7	Tests on FUSEIS with pin links.....	65
3.7.1	FUSEIS pin specimens	65
3.7.2	Cyclic response of FUSEIS with S500MC pin links	67
3.7.3	Investigation of pins' internal forces, strain gage measurements	69
3.7.4	Peak resistance and stiffness degradation	72
3.7.5	Energy dissipation	73
3.7.6	Overstrength, rotation capacity and ductility of tested system.....	73
3.7.7	Cyclic component tests on S500MC pin links	75
3.7.8	Previous research on FUSEIS with S235 pins.....	77
3.8	Conclusions.....	79

Chapter 4: Analytical and Numerical Investigations 82

4.1	Introduction.....	82
4.2	Theoretical model for lateral resistance.....	82
4.3	Simulation of FUSEIS systems using beam elements.....	85
4.3.1	Basic assumptions	85
4.3.2	Simulation of FUSEIS systems using SAP2000	87
4.3.3	Simulation of FUSEIS with beams using OpenSees	91
4.4	Simulation using solid elements	92
4.4.1	Theoretical background of material simulation	92
4.4.2	Description of models	96
4.4.3	Response of FUSEIS with beams models.....	97
4.4.4	Response of FUSEIS with pins models.....	98
4.4.5	Evaluation of damage prediction	99
4.5	Conclusions.....	101

Chapter 5: Case studies and performance evaluation..... 102

5.1	Introduction.....	102
5.2	Design of the case studies	103
5.2.1	Configuration, loads and selection of profiles.....	103
5.2.2	Modal analysis.....	107

5.2.3	Design checks	108
5.3	Nonlinear models	113
5.4	Performance based assessment	116
5.4.1	Pushover analysis	116
5.4.2	Limit states for performance evaluation	117
5.4.3	Incremental Dynamic Analysis (IDA)	119
5.4.4	Time-history analysis for evaluation of residual deformations	129
5.5	Conclusions	130
Chapter 6: Conclusions		132
6.1	Research overview	132
6.2	Research limitations and suggestions for future investigations	134
6.3	Overall conclusion and contribution	136
Chapter 7: References		138

Chapter 1: Introduction

1.1 Prologue

The devastating effects of earthquakes over the centuries have earned them numerous mythological explanations around the world. In Greek mythology, earthquakes were triggered by angry Poseidon (god of the sea) striking the ground with his trident. In Japan, earthquakes were caused by Namazu, a giant mischievous catfish living beneath the earth. In ancient Peru earthquakes were believed to be caused by the footsteps of gods who visited earth to count the people. The list of myths is extensive, however the less dramatic explanation related to tectonic activity of the earth's crust is nowadays common knowledge. Earthquakes constitute a life threatening situation worldwide, with an average of 200 large-magnitude earthquakes occurring per decade. During the twentieth century more than 1248 lethal earthquakes with over 1.68 million fatalities were officially reported, while a small number of strong earthquakes are the main contributors to the death toll. Although the statistics usually consider a wide range of seismic-induced causes of death (fires, tsunamis, landslides etc.), the principal cause was building collapse (mostly of older masonry structures) (Coburn and Spence, 2002). The damage caused by an earthquake depends on its location, its intensity, its focal depth and the vulnerability of structures in the occasionally affected area. Although improvements in construction practices and seismic design reduce the average vulnerability of the building stock, this does not yet sufficiently counteract the increase of population at risk due to the rate of the global population's growth.

The evolution of seismic design codes understandably follows major seismic events. The earthquake of Messina in 1908, the most destructive in Europe, almost leveled the city and killed approximately 80000 people. As a result, a report was published describing - for the first time - a procedure of applying seismic forces on structures as a percentage of their weight. This was the seismic coefficient method, widely applied in many countries thereafter. Similarly, the first seismic design code was issued in Japan in 1924, following the Great Kanto earthquake (1923). In Greece, the first seismic provision for local application was conducted in 1928 following a destructive earthquake in Corinth. A series of strong fatal earthquakes in Greece followed in the next years gradually leading to updates and expansion of the application field of these guidelines. Eventually the National Seismic Code was applied in 1959. Starting from 1975 a program of common Codes for all European countries has been developed, the Eurocodes. Modern seismic design approaches have shifted from the constant values of seismic coefficients to using response spectra. Furthermore they incorporate concepts such as inelastic response, ductility and acceptable levels of

damage at selected zones of a structure. As technological research proceeds, our knowledge broadens and so do the requirements for safe, economic, environmentally friendly structural solutions. In this direction innovative seismic resistant systems like those promoting reparability or self-centering behavior are developed. FUSEIS is such an innovative system for steel buildings consisting of replaceable dissipative links.

Steel offers high resistance-to-weight ratio, ductility, high connectivity and recyclability that render it possibly the most suitable building material. Recent advances have led to the creation of high-strength steels (HSS) the application of which could lead to significant advantages although its efficiency in building structures, especially in seismic prone areas, is still under consideration. This study focuses on the performance of FUSEIS systems consisting of HSS dissipative elements. Current seismic guidelines would not possibly allow such an application, as HSS members exhibit reduced inelastic deformation capacity compared to conventional steels while no sufficient data on the seismic performance of HSS are available yet. Extensive research is required to introduce such a possibility in the future.

1.2 Research objectives and framework

The main objective of this study is to examine the application of high-strength steels (HSS) in energy dissipating elements via experimental and numerical investigations. Up to date, research on the cyclic response of systems incorporating HSS members is still limited. Aiming to contribute in an ongoing international discussion on the relevance of HSS to seismic design, the question posed is not whether HSS is preferable to conventional steel but whether its ductility and hysteretic behavior is sufficient for using it in dissipative zones.

The selected seismic resistant system in this study is FUSEIS, a system consisting of two strong columns rigidly connected by multiple links through which seismic energy may be dissipated protecting the rest structural members from damage. The main advantage of the system is reparability: the dissipative links are easily replaceable, reducing interruption of building use and repair costs that usually follow a strong seismic event. As the system is relatively new, another objective of this study is to provide additional data on the system's performance, supplementing the existing design guides. Hence, the presented experimental campaign includes different types of FUSEIS links (beams and pins) and steel grades (S355, S500 and S700).

Part of the research hereby discussed was conducted in the framework of the European research project "Material Choice for seismic resistant structures (MATCH)" (RFSR-CT-2013-00024) partly funded by the Research Fund for Coal and Steel (RFCs). The main objective of "MATCH" was to

define a method for material choice related to toughness values for seismic design. Therefore different steel materials were tested in different configurations (coupons, components and different seismic resistant systems). A focal point for the experiments was damage initiation, so relevant data were collected and used for the calibration of numerical models that could serve for damage prediction. Although this is not in the scope of the current thesis, it is mentioned as the project's objective largely affected the selection of the specimens and test monitoring. The other participants in the project were: RWTH Aachen in Germany (coordinator), University of Pisa in Italy, University of Thessaly in Greece, RUUKKI (SSAB-Europe Oy) in Finland and ILVA SPA in Italy.

1.3 Thesis outline

Chapter 1 is an introductory chapter, highlighting research objectives and framework of the current study. Chapter 2 consists of a bibliographic review considering three topics: (i) material requirements for design of steel structures, (ii) development of high-strength steel (HSS) and relevant research focusing on experimental campaigns and (iii) conventional and innovative steel seismic resistant systems.

Chapter 3 includes experimental investigations. Eight large scale tests on FUSEIS systems with different types of links (hollow-section beams, HEA beams, pins) and materials (S700, S355, S500) are presented. Their results are discussed with respect to damage, ductility, stiffness and load degradation and energy dissipation. These tests were conducted in the Institute of Steel Structures in NTUA. In addition, the results of relevant component tests on FUSEIS beam and pin links are outlined. The component tests were conducted in Aachen University. Finally, the test results are juxtaposed with previous investigations on FUSEIS with various types of S235 links.

In Chapter 4 the aforementioned tests are approached analytically and numerically. The theoretical model of a vertical Vierendeel beam is verified for the FUSEIS with beam links. For the capacity of the system with pin links, additional formulas are given considering the effects of catenary action that develops in the links at large deformations. The tests are simulated with either 2D or 3D elements using different software to address different purposes. Some basic parameters to capture the actual systems' performance and material non-linearity in the beam-element models are suggested. Simulation using solid elements is presented along with the basic features of the accompanying material subroutines based on a hybrid experimental/numerical approach and damage mechanics. The material subroutines were developed by other academic partners.

Chapter 5 includes the design and performance evaluation of two relevant case studies subjected to non-linear static (pushover) and Incremental Dynamic Analysis (IDA). The case studies consist of

a two-story and a five-story building including FUSEIS systems with S700 beam links. The structures are designed to comply with the current Eurocodes although the application of HSS in dissipative members is not yet prescribed. The objective is to examine whether the seismic performance of HSS dissipative members may be acceptable. The models' response was assessed for two performance levels (Life Safety and Collapse Prevention) based on two different methodologies: FEM695 and INNOSEIS. Finally, the extent of the models' residual deformations after design-level ground motions is investigated, as related to the system's reparability.

Chapter 6 summarizes the results of this research. Concluding remarks and few suggestions for future research are given.

Chapter 2: Literature review

2.1 Introduction

The evolution of structural steel follows the development of the industrialized world. The Industrial Revolution (1760 to 1840) marked the transition to new manufacturing processes related to machines, steam power and iron production. By 1830 wrought iron had become a major structural material while steel - being very expensive - was reserved for cutting tools, watches and swords. The invention of the “Bessemer process” in 1855 increased the scale and speed of steel production through iron conversion, while in 1865 the development of the Siemens-Martin steelmaking process based on the application of “open-hearth” furnaces, complemented the Bessemer process and led to mass steel production. The large-scale production of steel was one of the pillars of the Second Industrial Revolution (1870 to 1914), characterized by rapid industrialization. Inversely, the concurrent wide-scale urbanization served as a driving force for the steel industry. The pursuit of increasing profit in limited spaces led to a tendency to develop buildings upwards and resulted in the first skyscrapers. Requirements on larger spans and smaller erection times also grew, leading to increasing use of truss girders. Innovation in steel industry and construction continued ever since. Today steel is either produced by the basic oxygen process (using pig iron) or in electric arc furnaces (using scrap). The first method currently dominates but there is a tendency to shift to the second one, which is regarded more efficient and environmentally friendly. Structural steel has undergone significant changes since its initial applications, partly driven by demands for higher strength and economy and thanks to technological developments related to its manufacturing. This study focuses on - relatively recent - high-strength steel (HSS). This is usually produced by appropriate alloying and thermo-mechanical treatment leading to fine grain material as outlined later.

The basic function of a structural system is to withstand and transfer vertical loads to the foundations. In addition, it has to resist and safely transfer lateral forces resulting from seismic action, wind and constructional imperfections. In concrete buildings, the monolithic beam-to-column joints ensure the development of frame action and hence lateral stability. In steel and composite buildings, where joints may vary from rigid to simple, design must incorporate lateral stability systems. Such widely used systems are Moment Resisting Frames (MRF) and Concentric or Eccentric Braced Frames (CBF or EBF), the properties of which are outlined in this chapter. In general, steel structures in seismic zones must be designed to provide stiffness, strength and ductility. Stiffness limits damage of nonstructural elements and reduces second order effects. Strength is required for a safe transmission of the acting forces and moments. Ductility serves for

the dissipation of the input seismic energy. Balance between these properties is not always easy to achieve. For example, MRF can be very ductile but lack in stiffness and may lead to heavier solutions while CBF are more stiff but less ductile. To address this issue, along with notions such as reparability or resilience, innovative lateral stability systems have been proposed in the last years, mostly as the result of international research programs. Some of these systems are presented in this chapter.

The contemporary approach for seismic design of buildings allows for substantial inelastic behavior in the case of the design earthquake. Frames are designed to withstand intense ground shaking without collapse, but with limited structural damage. Therefore, the application of ductile materials and systems is encouraged, while sufficient redundancy should be provided to compensate for contingent failures. As steel structures are generally ductile, they are very suitable for inelastic design. However, steel members are susceptible to buckling while their plastic deformation capacity strongly depends on the material's stress-strain characteristics. Overall, material and geometric characteristics such as for example the yield-to-strength ratio (or inversely f_u/f_y) and the classification or else compactness of a cross-section strongly affect the methods used for analysis and design of steel structures. In this chapter, material requirements for the steel structures' design are discussed.

2.2 Material properties for design of steel structures

2.2.1 Basic terms

Fracture is a complex phenomenon influenced by many factors such as the material's composition and microstructure, the type and rate of loading, the temperature, the member's geometry etc. In steel members there are three main causes of fracture: (i) elastic instability (buckling), (ii) plastic instability (plastic strain leads to "necking" where stress increases) and (iii) crack instability (flaw or crack creates stress concentration leading to fracture). The most common fracture mechanisms are ductile fracture and fatigue mechanism. Ductile fracture is a process of three stages: nucleation, growth and coalescence of voids inside the material due to large plastic deformation. The voids may initiate at material defects (mostly inclusions) or preexist in the material. Depending on the stress state, the final phase of ductile fracture may follow two different mechanisms: (i) internal necking of significantly enlarged voids (primary inclusions) or (ii) internal shear link-up voids that experienced limited growth (secondary inclusions). These mechanisms may co-operate or compete. Voids' coalescence leads to the formation of microcracks and eventually macroscopic failure. Fatigue cracks may initiate around inclusions via particle fracture, particle decohesion and slip-

driven nucleation. Dislocations (linear defects in the crystal structure) play an important role as it has been observed that after a number of loading cycles dislocations pile up into slip bands that eventually lead to the formation of stress raisers.

When steel structures are subjected to seismic loads, their failing components experience ultra-low cycle fatigue (ULCF). This fatigue regime involves a few (generally less than twenty) cycles of large plastic strains, while its underlying micro-mechanisms are similar to those of ductile fracture under monotonic loading. More specifically, the damage mechanism during ULCF is a combination of the aforementioned ductile fracture process and fatigue mechanism.

Ductility is a measure of a material's capability to withstand large inelastic deformations before fracture, while toughness is related to its ability to absorb energy before fracture. Toughness thus requires a balanced combination of strength and ductility and can be given by the area enclosed by the stress-strain curve of a tensile test (in units of energy per volume) as shown in Fig. 2.1. Toughness is strongly influenced by the rate of loading (strain rate), temperature and the notch effect (related to stress distribution). In general, increased rate of loading, lower temperatures and the presence of a notch cause decreased toughness.

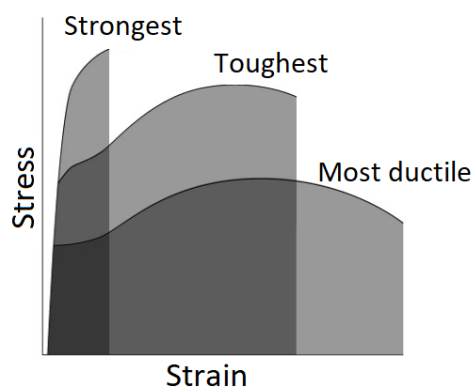


Fig. 2.1 Definition of toughness in stress-strain curve

There are different types of tests regarding toughness. The most common is the Charpy (V-notch) test that defines impact toughness (K_v). Multiple Charpy tests in different temperatures must be conducted to produce the impact energy vs. temperature diagram of a material as shown in Fig. 2.2. The graph is generally divided in three regions: the lower shelf region corresponding to more brittle behavior, the upper shelf region in which “steel elements exhibit elastic-plastic behavior with ductile modes of failure irrespective of the presence of small flaws and welding discontinuities from fabrication” (EN1993-1-10) and the transition region between the two. Steel product standards generally specify that test specimens should not fail at an impact energy lower than 27J at a specified test temperature (T_{27J}).

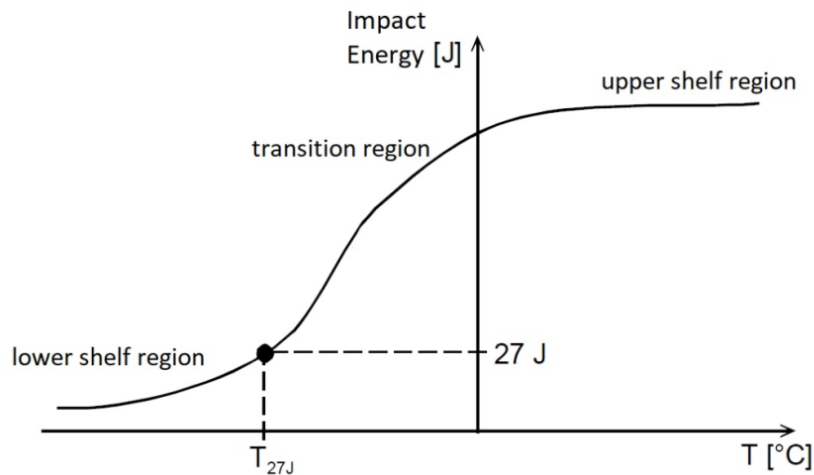


Fig. 2.2 Relationship between impact energy and temperature

Fracture toughness is a generic term for different measures of the amount of energy required for crack propagation. Fracture mechanics is the field of mechanics concerned with propagation of existing cracks, defined in terms of size and location. Different kinds of flaws such as material voids, inclusions or weld defects may be considered as cracks. Basic parameters of fracture mechanics are the stress-intensity factor K (or else elastic fracture toughness value), the J-integral and the CTOD (Crack Tip Opening Displacement). The stress-intensity factor describes the stress required to propagate a crack and is indicated as K_I , K_{II} or K_{III} depending on the type of fracture mode (opening, in-plane shear and out-of-plane shear). J-integral is also a toughness measure and is more suitable in case of intense material plastification compared to K parameter. It is defined as a line or surface integral that encloses the crack front from one crack surface to the other. CTOD is defined as the distance between the opposite faces of a crack tip at the 90° intercept position. In general the assessment of K and J parameters is expensive and difficult. As a result material delivery standards such as EN10025 refer to impact toughness since Charpy test are simpler and economic. Although impact toughness is not directly related with fracture mechanics, correlations between the Charpy energy and fracture toughness have been developed (Amlung et al. 2009).

Contrary to fracture mechanics, damage mechanics is engaged with investigating and simulating crack initiation and propagation through a material without pre-assumption of a crack-like defect. Damage mechanics models introduce parameters to describe damage evolution within the material, based on either a microscopic or a macroscopic/phenomenological approach. Damage mechanics models are further discussed in Chapter 4, where the material models for the simulations of the tests are presented.

2.2.2 Eurocodes' material requirements and discussion

EN1993 includes provisions for material selection regarding ductility and toughness and provides Ultimate Limit State (ULS) verifications considering different partial safety factors and material strength (f_y or f_u) depending on the ductile failure mode as shown in Fig. 2.3. These rules are partly based on tests conducted at room temperature where the components' behavior is presumably governed by the upper shelf toughness (Geradin et al. (Eds, 2008)). Brittle fracture (that may occur in low temperatures) is deemed excluded via appropriate material choice according to its toughness and EN1993-1-10.

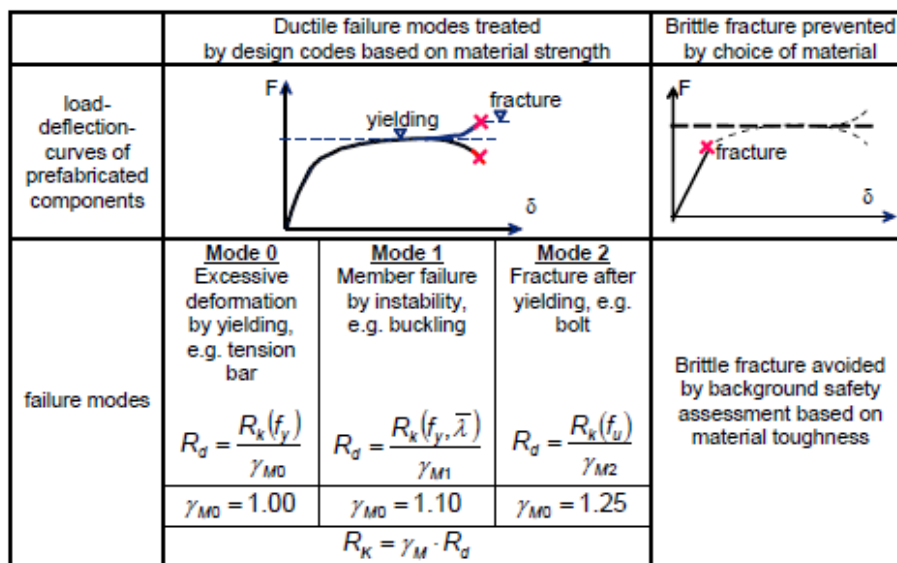


Fig. 2.3 Resistance functions based on f_y , f_u for different failure modes (Geradin et al. 2008)

EN1993-1-10 provides maximum allowable element thickness values as a function of the stress level and the reference temperature (ranging from -50°C to 10°C and covering S235 to S690). It also allows for alternative methods to express toughness requirements for numerical evaluation involving fracture mechanics (using CTOD, J-integral, or K_I). However the seismic design load combinations are not included in EN1993-1-10 while the European delivery standards for steel such as EN 10025 refer to the lower-shelf region instead of specifying minimum toughness requirements for the upper-shelf. Since toughness is fundamental for avoiding brittle behavior, the establishment of minimum upper shelf requirements could provide a useful tool for material selection regarding plastic design. In this direction, experimental and numerical studies to determine the material demand using fracture and damage mechanics approaches have been conducted. Some of them can be found in (Amlung et al. 2009, Feldmann et al. 2011, Feldmann and Schaffrath 2017, Feldmann et al. 2018).

The EN1993 requirements for resistance, serviceability and stability of steel structures also rely on a certain degree of material ductility that is expressed in terms of minimum ultimate to yield strength

ratio, elongation at failure on a specified gauge length and uniform elongation (ϵ_u), as summarized in Table 2.1. Although different limits apply for conventional and high-strength steel (HSS), still the current requirements seem rather restrictive for HSS while their appropriateness is often debated. Especially the ϵ_u criterion is mostly doubted as it is not explicitly specified in material codes, while ϵ_u values have high variation and strongly depend on the geometry of the coupon specimens (Schillo et al. 2018). In addition, the limitation of ϵ_u leads to a steel grade limitation, as ϵ_u decreases when f_y increases. This is illustrated in Fig. 2.4a with the schematic true stress-strain curves of materials with increasing yield (practically parallel), the curve representing the necking (or else Considère) criterion and the resulting ϵ_u points in the engineering σ - ϵ curves. Fig. 2.4b quantifies the above and plots them in a timeline of steel development. Feldmann and Schaffrath (2017) suggest that a fracture strain criterion could be used as a substitute for a minimum upper-shelf toughness requirement. More specifically, for HSS a limit of 12% is proposed instead of the 10% that currently applies.

Table 2.1: Material ductility requirements according to Eurocode 3

Criterion	EN1993-1-1	EN1993-1-12
	Steel grades S235-S460	Steel grades S500-S700
f_u/f_y	≥ 1.10	≥ 1.05
elongation at failure	$\geq 15\%$	$\geq 10\%$
ultimate strain ϵ_u	$\geq 15 \cdot f_y/E$	$\geq 15 \cdot f_y/E$

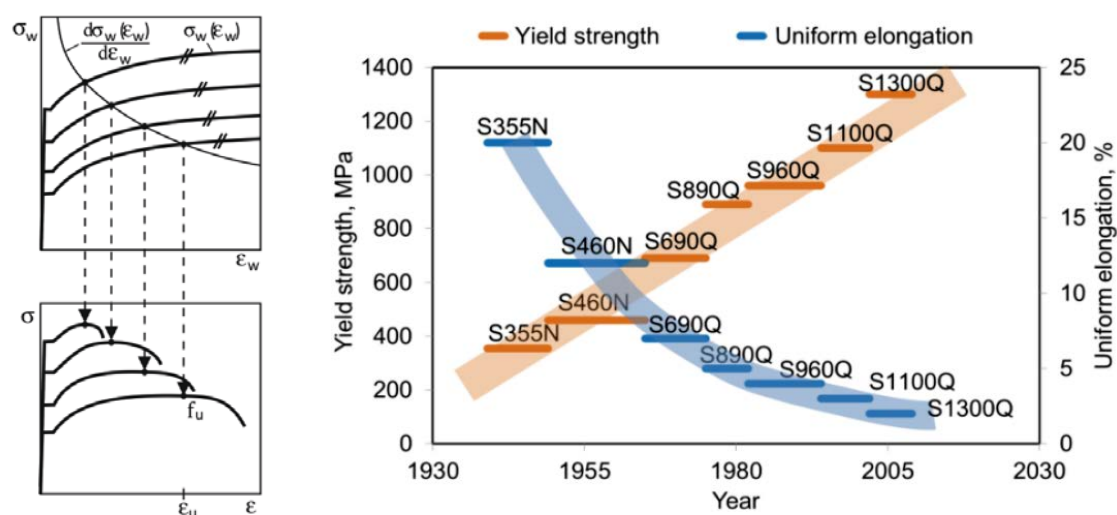


Fig. 2.4 Reduction of uniform elongation for increasing yield stress (a) according to necking (Considère) criterion (b) following the development of HSS (Feldmann and Schaffrath (2017))

The ratio of f_u/f_y is regarded relevant with the ability of stress redistribution near stress raisers such as holes or welds. EN1993-1-1 states that for members under tension the gross cross-section resistance to tension is associated with yielding and is given by Eq. 2-1(a) while the net cross-section resistance is associated with fracture and is given by Eq. 2-1(b). For ductile design of tension members, capacity design requires $N_{u,Rd} > N_{pl,Rd}$ which eventually leads to $f_u/f_y > 1.39$. This practically excludes all steel grades above S355 as shown in Fig. 2.9. The applicability of Eq. 2-1(b) for net section resistance in HSS is examined experimentally and numerically in Feldmann et al. (2016) and Feldmann and Schaffrath (2017) where it is suggested that if the existence of cracks can be excluded, the factor 0.9 may be omitted. In addition, parametric studies in Feldmann et al. (2016) suggest that lower than the current limits for f_u/f_y ratio for HSS could be applied if sufficient material toughness was provided. Investigations on the relationship between f_u/f_y ratio and yield strength and its effect on deformation capacity are presented in the following paragraph.

$$\begin{aligned} N_{pl,Rd} &= A \cdot f_y / \gamma_{M0} & (a) \\ N_{u,Rd} &= 0.9 \cdot A_{net} \cdot f_u / \gamma_{M2} & (b) \\ \gamma_{M0} &= 1.00, \gamma_{M2} = 1.25 \end{aligned} \quad \text{Eq. 2-1}$$

EN1998-1 lacks additional requirements for material properties under seismic loading, making reference to the aforementioned basic guidelines of EN1993. More specifically, it states that the distribution of material properties in the structure should ensure that dissipative zones will be formed where intended, suggesting as a common design approach the application of S355 for non-dissipative members and S235 for the dissipative ones.

To identify whether local buckling may limit the resistance and rotation capacity of cross sections, EN1993-1-1 prescribes cross-section classification, depending on geometric properties and f_y . Local buckling may occur in all classes but at different imposed strains: For class 1 sections, it appears at high strains following considerable strain hardening while for class 4 it appears at significantly smaller elastic strains. The classification thus translates to different extents of plastic strain development within a member ranging from localized in parts of a cross-section (class 3) to full plastification at more than one cross-sections (class 1). Cross-section classification has implications in analysis and design: plastic methods for both are allowed only for elements consisting of class 1 cross-sections, while in the case of class 2 plastic design may be applied but the analysis must be elastic. The applicability of the classification limits to HSS has often been investigated and some relevant publications are presented in the next paragraph. EN1998-1 dictates that in high ductility class structures (DCH) the dissipative elements should belong to cross-section class 1, while for medium ductility class (DCM) with $q > 2$ they should belong to class 1 or 2.

Apart from the material and cross-section demands mentioned, EN1998-1 and EN1993-1-8 provide general (global) performance requirements such as minimum rotation capacities of members and connections which are not hereby discussed. The requirements for ductility and deformation capacity are stricter for structures subjected to seismic actions, particularly in the energy dissipation zones where plastic hinges develop. Overall, the requirement for satisfactory inelastic response without brittle fractures and significant strength degradation is paramount for the design of steel structures especially under seismic conditions. This issue is even more pronounced in HSS structures, raising concern over the sufficiency of the current code provisions. The formulation of material requirements related to upper-shelf region could be efficient for safe plastic design while covering conventional and high-strength steels.

2.3 Development, research and applications of high-strength steels (HSS)

The development of new steel grades is driven by the incessant demand for materials with enhanced mechanical characteristics and fabrication properties. The two main techniques for increasing the steel's yield strength are: alloying and heat-treatment. The first consists in increasing elements such as carbon and manganese and usually results in deteriorating the fabrication properties. Heat treatment affects the microstructure and grain size and its main advantage is that it results in fine-grained steels with higher strength and toughness. The most recent historical development of production processes is given in Fig. 2.5. Until the 1950s the steel today known as S355J2 was regarded as high strength steel. It was produced by conventional hot rolling followed by normalizing heat treatment and then slow cooling. In the 1960s the quenching and tempering (QT) process began, consisting of rolling followed by heating and rapid cooling (quenching) and a subsequent tempering (heating below a critical point and then cooling in still air). This treatment combined with the addition of micro-alloying elements (niobium, vanadium, titanium) creates steel with good balance of strength and toughness and to date can give steel grades with yield strength (f_y) up to 1100MPa. In the 1970s the thermo-mechanical (TM) rolling process was developed, in which final deformation is carried out in certain temperature range leading to properties that cannot be achieved by heat treatment alone. The addition of micro-alloying elements is also usual. The TM process results in steels with fine micro-structure, high strength and toughness, low carbon content and improved weldability while it is more economic compared to QT.

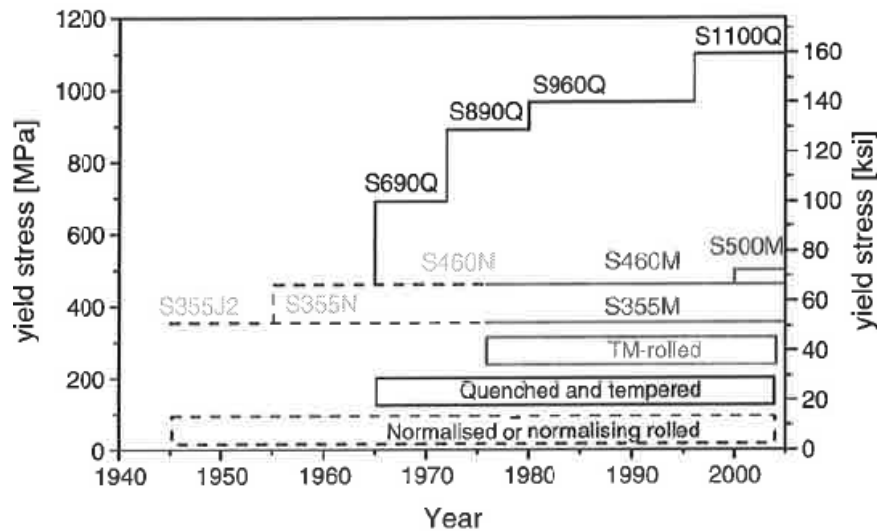


Fig. 2.5 Historical development of production processes for rolled steel products (Gunther et al. (Eds) 2005)

The term high-strength steel (HSS) nowadays refers to steel grades with yield strength $f_y \geq 460$ MPa. The application of HSS reduces member sizes and workload of transportation and construction (including reduced welding and painting), and thus may provide significant economic, architectural and environmental advantages. So far the advantages of HSS are mostly prominent in bridge construction, as the design of buildings is largely controlled by stiffness demands and hence governed by the modulus of elasticity, which is the same in all steel grades. The aforementioned recent advances in steel making technologies have led to the creation of HSS with improved properties referred as high-performance steel (HPS). HPS exhibits better performance in terms of strength, toughness, weldability, cold formability and corrosion resistance compared to the conventional mild steel grades. Galambos et al. (1997) conducted a report on the properties of HPS and the technical feasibility of its structural application. Gunther et al. (Eds, 2005) give an overview of development and application of HPS at an international level, mainly in bridge construction. Bjorhovde (2004, 2010) gives a historical review of steel production techniques focusing on HPS and examines its structural application with respect to practical and design issues. Some applications of HSS in buildings and bridges around the world are listed below (Fig. 2.6):

- Germany: the Nesenbachtal bridge in Stuttgart (S690), the Rhine bridge at Dusseldorf-Ilverich (S460), the roof truss of the Sony Centre in Berlin (S460, S690), the composite bridge near Ingolstadt (S690QL)
- France: the Millau viaduct (S460ML)
- Sweden: the hybrid girder bridge in Mittadalen (S690), the Fast Bridge 48 -military bridge (S960, S1100)

- China: the National Stadium, the Phoenix International Media Center, the Shenzhen Bay Sports Center, CCTV headquarters (Q460, $f_y = 460\text{MPa}$)
- Japan: the Landmark tower in Yokohama ($f_y = 600\text{MPa}$)
- Australia: the Star City and the Latitude Building in Sydney (steels with f_y 650 and 690 MPa)
- South Korea: the SNU Kwanjeong Library and the Lotte World Tower in Seoul ($f_y = 650\text{MPa}$)



Fig. 2.6 Structural applications of HSS (Millau viaduct, Chinese National Stadium, Lotte World Tower)

The mechanical properties of HSS and hence the behavior of HSS members are different from those of mild steel, while the most striking drawback of HSS - under the current steel processing conditions- is its reduced ductility compared to lower steel grades. Although high-strength Steels have been available for a few decades, their structural application is still limited and will probably remain so until HSS is fully implemented in the relevant Codes. Eurocode 3 has currently additional rules for extension of the code up to steel grade S700 (EN1993-1-12) while the American specification for structural steel buildings (ANSI/AISC 360-16) includes rules for steel grades with yield strengths up to 690 MPa (A514). However, the application of HSS in seismic design is restricted by current codes while no systematic design methods for HSS are provided yet. The American provisions set an upper limit of yield strength for steel members subject to plastic hinging at 450 MPa (65 ksi) while capacity checks described in Eurocodes practically exclude the application of HSS. In China, the code for design of steel structures (GB 50017-2017) covers steels with yield strength up to 460 MPa (Q460) while the code for seismic design (GB50011-2010) sets stricter ductility requirements for steel compared to the Eurocodes (as given in Table 2.1), that are hardly met by HSS. This is expected to change in the next versions of the codes, in light of the technological developments and the possible benefits from HSS applications. The next generation of EC3 is being prepared and will incorporate design rules for steel grades up to S700 while the design rules for a Chinese specification for HSS structures will be published soon. To provide a basis

for relevant design rules, extensive pre-normative research on the performance of HSS structures is needed, including full-scale experimental studies. So far, research on HSS materials and members has generally showed that the direct extension of conventional design methods to HSS would not be justified due to the different mechanical properties of the materials beyond yield. Although these differences may challenge the applicability of plastic design in HSS structures, they do not necessarily mean that HSS cannot provide acceptable inelastic performance.

Research on HSS has been carried out since the 1960s. Amongst the earliest publications, Haaijer (1961) discussed the economic benefits of HSS application by analyzing different types of structural members, while McDermott (1969a,b) conducted experimental campaigns on HSS members. Overviews of research on HSS are given in Shi et al. 2014, Ban et al 2017 and Shi et al 2018. They provide extensive literature review of the earliest studies on HSS and a synopsis of experimental and numerical investigations on HSS in China with respect to the codification of a new specification, the “Standard for Design of high-strength steel Structures”. In addition they give tables of experimental campaigns regarding fire resistance, residual stresses, beam-to-column connections etc. and suggestions for buckling curves for columns of grades ranging from 420 to 960. The applicability of current (at time) design methods on HSS structures is discussed, indicating some rules that seem too conservative and others that lack safety.

A major difference between HSS and mild steels lies in their strain hardening region. Low steel grades develop a significant yield plateau and usually profit from large f_u/f_y ratios whereas HSS with $f_y > 500$ MPa do not exhibit a distinctive yield point (Fig. 2.7a) and have significantly smaller f_u/f_y ratios. In the latter case the yield strength is usually assessed using the 0.2% strain criterion. Kato in (1990a,b) investigated the role of steel's strain hardening on its structural performance, by separately examining the influence on the rotation capacity of parameters such as yield strength f_y , yield ratio f_y/f_u , ϵ_{st}/ϵ_y and E_{st}/E_y (Fig. 2.7b), using various steel grades. He demonstrated that the increase of f_y (for given values of the remaining parameters) has a small effect, as it gradually reduces rotation capacity, while the influence of the yield ratio $Y = f_y/f_u$ on the rotation capacity is very strong. The negative impact of the increasing yield ratio on ultimate strength and plastic deformation capacity was verified in different types of structural members. Regarding beams consisting of steels with yield plateau, he showed that the complementary energy of the stress-strain relationship (C_1 , C_2 and C_3 in Fig. 2.7b) largely determines rotation capacity. Additionally, he studied the effects of flange and web slenderness on deformation capacity and suggested formulae to consider interaction between them. Steenbergen et al. (1996) also conducted a numerical investigation of the influence of the f_u/f_y ratio on the ability of I-section beams to form a plastic hinge and allow redistribution of forces. They suggested that a decrease in the f_u/f_y ratio results in a decrease in the plastic hinge length and the available rotation capacity, while for a given f_u/f_y ratio

the rotation capacity decreases with the increase of yield strength, as shown in Fig. 2.8. Fig. 2.9 shows the comparison of f_u/f_y ratios for different steel grades based on their delivery standards (van Es et al. 2018).

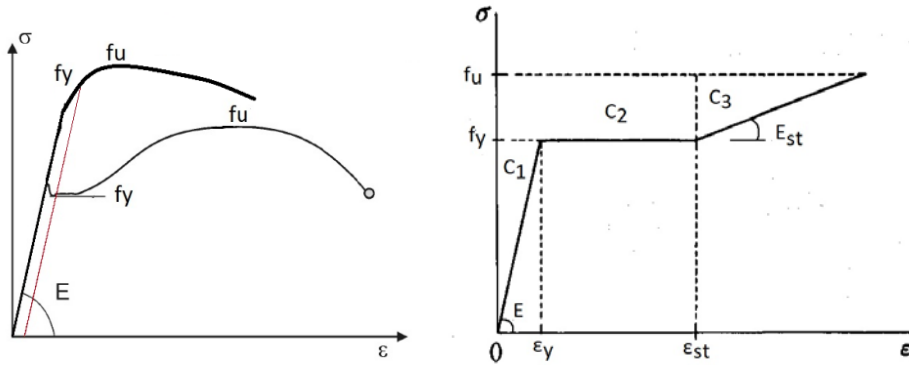


Fig. 2.7 Generic stress-strain curves for (a) HSS and mild steel (b) definition of basic parameters in steels with distinct yield plateau

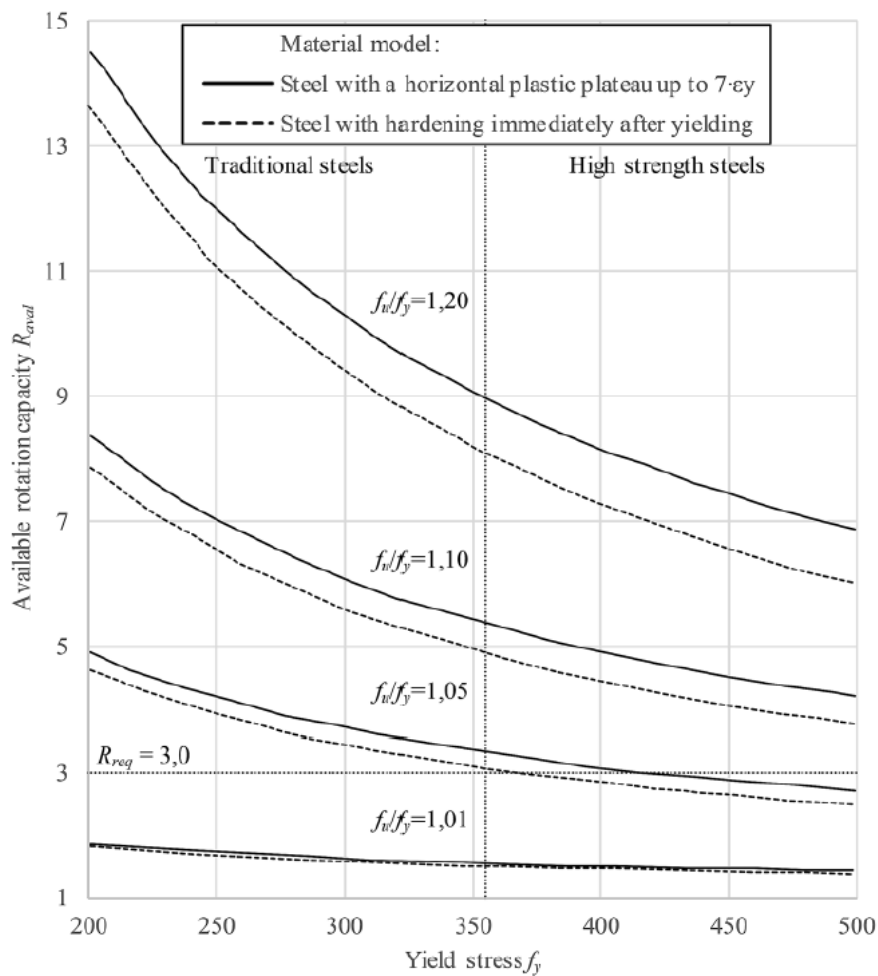


Fig. 2.8 Influence of f_u/f_y ratio as a function of f_y on beams' rotation capacity (Steenbergen et al. 1996)

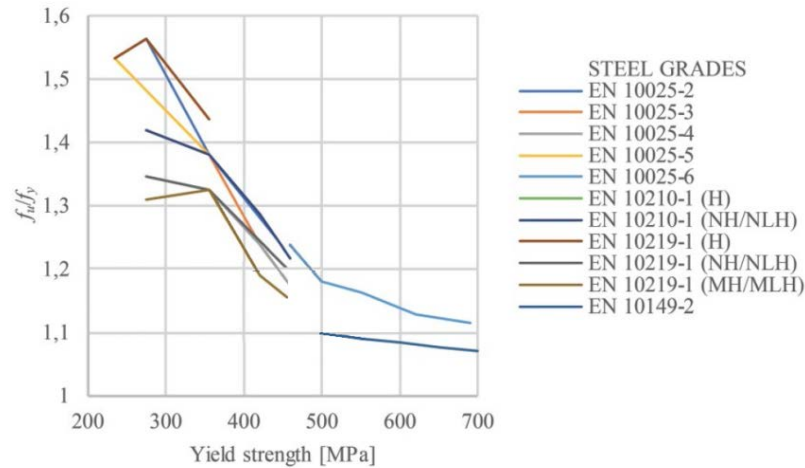


Fig. 2.9 Comparison of f_u/f_y ratio for different steel grades based on their delivery standards (van Es et al. 2018)

Regarding HSS material tests, Fukumoto (1996) assembled and statistically evaluated hundreds of coupon tests to investigate the relationship between yield strength f_y , yield ratio f_y/f_u and uniform strain ϵ_u . Ban et al. (2011) also reviewed the available coupon tests' data from steels with f_y 420, 460, 690 and 960 MPa and compared them in terms of yield ratio f_y/f_u , elongation at failure (A) and uniform elongation (ϵ_u) with the limits set by Codes in Europe, North America, Australia, Japan and China (Fig. 2.10). Shi et al. (2013) and Wang et al. (2015) present a series of cyclic tests on Q460C base metal and welded connection specimens ($f_y = 460$ MPa) subjected to various loading patterns and describe relevant constitutive models for numerical analysis.

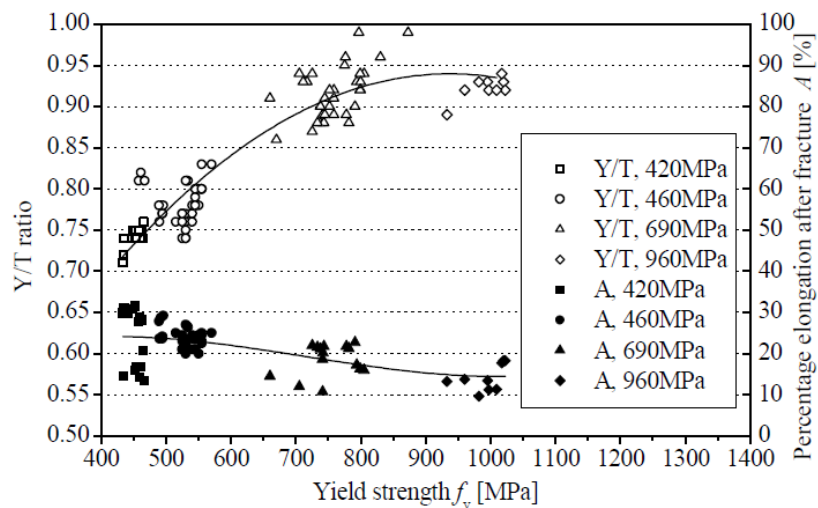


Fig. 2.10 Overview of material tests' in terms of yield ratio and elongation at failure (Ban et al. 2011)

Regarding investigations on HSS structural members, the current literature review focuses mainly on bending tests on beams and axial or combined axial with transverse loading tests on columns. In both cases, the effect of flange and web slenderness was often investigated, as the classification of a cross-section is a measure of its susceptibility to local buckling (Fig. 2.11). Providing sufficient

cross-section compactness, research on beams subjected to bending often focuses on their rotational capacity as certain plastic rotations are necessary to reach plastic bending moment M_{pl} and form plastic hinges. In this case, the rotation capacity R is given by Eq. 2-2. Apart from cross-section properties, the required rotation capacity R depends on the structural system (frame, continuous beam etc) and the loading conditions (moment gradient). Fig. 2.12 shows few relevant examples. An often used benchmark value for rotation capacity is $R = 3$.

$$R = \frac{\phi_u - \phi_{pl}}{\phi_{pl}} = \frac{\phi_u}{\phi_{pl}} - 1 \quad \text{Eq. 2-2}$$

Where ϕ_{pl} denotes the hypothetical rotation at which M_{pl} would be reached if the beam remained completely elastic to that point and ϕ_u is rotation at which moment resistance is reduced back to M_{pl} (Fig. 2.11).

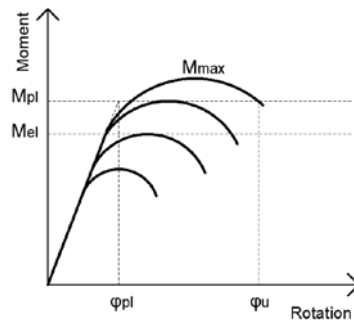


Fig. 2.11 Rotation capacity of beams with different cross-section classes subjected to bending

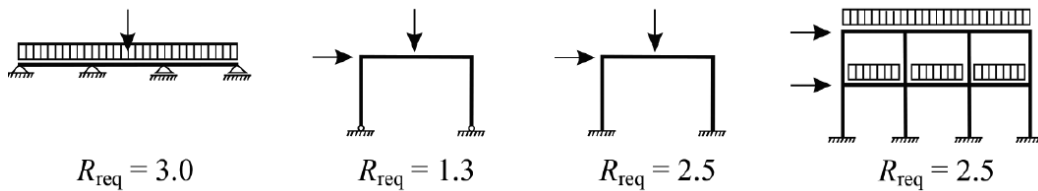


Fig. 2.12 Average required rotation capacity depending on structural system (Spangemacher 1992)

As mentioned, McDermott (1969a,b) was amongst the first to publish experimental investigations on HSS members (using A514 steel, with $f_y = 690$ MPa) and his results have been widely used by other researchers in the following decades. He conducted bending tests on I-shaped beams and axial compression tests on cross-shaped columns and investigated their ability to fulfill requirements for plastic design. Rasmussen and Hancock in (1992) carried out a test program including stud columns (sufficiently short to exclude overall instability yet long enough to allow local buckling) made of HSS ($f_y = 690$ MPa) with box-, cruciform and I-sections. Their scope was to determine whether the same slenderness limits apply for mild steel and HSS and concluded that the slenderness demarcating a slender and semi-compact flange was the same. In this direction, Beg

and Hlandik (1996) conducted 4-point bending tests on welded I-section beams made of HSS ($f_y = 700$ MPa) with different flange slenderness to examine the limit between Class 4 and Class 3. They concluded that the ultimate carrying capacity of cross-sections is greatly influenced by the flange and web interaction. Ricles et al. (1998) investigated the inelastic behavior of beams made of HSLA-80 ($f_y = 550$ MPa) with respect to the effects of stress-strain characteristics, web and flange slenderness and moment gradient on the rotation capacity R . They concluded that the f_u/f_y ratio has a major impact on R and that the extrapolation of the current (at time) AISC compactness criteria of conventional steels to HSS members does not guarantee the expected rotation capacity. They also suggested slenderness limits for compact sections (relevant to AISC provisions) in order to obtain $R > 3$ or $R > 7$ (valid for non-seismic or seismic conditions respectively). As part of the same research, Green et al. (2002) presented cyclic and monotonic tests on welded I-shaped beams of HSLA80 and conventional A36 steel and discussed the effects of material parameters, slenderness and loading conditions on rotation capacity. Sauce and Fahnestock (2001) conducted 3-point bending tests on I-girder using 100W steel grade ($f_y = 690$ MPa) and compared results with reliable previous research using different steel grades. They showed that their specimens exhibited satisfactory flexural strength (reached M_{pl}) but reduced rotational capacity ($R < 3$). They also indicated that similar specimens fabricated from conventional steels did not consistently provide $R > 3$ either. Lee et al. (2013) also conducted 3- or 4- point bending tests on HSS I-shaped beams (HSB800 and HSA800, $f_y > 650$ MPa) with varying web and flange slenderness. They discussed the effect of material stress-strain characteristics on the members' flexural behavior focusing on the yield ratio (f_y/f_u) and the absence of yield plateau, showing how they can significantly reduce rotation capacity. Their specimens exceeded M_{pl} but most of them did not develop rotations corresponding to $R > 3$. Schillo and Feldmann (2018) investigated the rotational capacity of class-1 I-section beams made of S700 and S960, by performing 3- and 4-point bending tests. They found that all S700 specimens exhibited rotation capacity $R > 3$ while all S960 specimens provided smaller capacities. They suggest that for S700 the current cross-section classification limits for parts in bending are applicable while the EN1993-1-12 restrictions for plastic design might be conservative. Concerning investigations on HSS columns buckling behavior, Ban et al. (2012) and Li et al. (2016 a,b) and Shi et al. (2012) conducted tests and relevant parametric numerical studies on welded hollow and I-section columns using steels with yield strength 460, 690 and 960 MPa. They compared results with current American, Chinese and European codes and found that the non-dimensional buckling strength of HSS is often underestimated while the effects of residual stresses and geometric imperfections were reduced compared to conventional steels. In addition, Wang et al. (2014) and Chen et al. (2016) performed tests of combined axial and cyclic lateral loading on

columns with f_y 460 and 690 MPa respectively. Their specimens exhibited good hysteretic performance and satisfactory rotation capacity according to FEMA 356 and Chinese codes (GB50011-2010). In spite of the numerous investigations on HSS members, rather few studies are available regarding the seismic behavior of systems with HSS. Hu et al. (2017) conducted cyclic loading tests on frames using combinations of Q345 ($f_y = 345$ MPa), Q460 ($f_y = 460$ MPa) and Q890 ($f_y = 890$ MPa) steels for the beams and columns. They concluded that the frames consisting of Q460 were capable of accommodating rotation capacities (R) larger than 10 and overall drifts up to 4% while the frame with Q890 columns exhibited reduced deformation capacity but still accommodated 2.6% drift. Hai et al. (2019) conducted cyclic tests on Q690 ($f_y = 690$ MPa) H-section beam-columns. They concluded that plastic local buckling dominated the specimens' failure mechanisms, while all columns exhibited very good energy dissipation capacity and sustained drifts up to 5% before reaching a failure state. Obviously, extensive further research including cyclic tests on structural systems made of HSS is required.

Another approach towards the application of HSS in seismic resistant structures is described by the concept of "dual-steel" structures, as presented in Dubina et al. (Eds, 2013). According to this, mild carbon steel is used for the dissipative members while HSS for the non-dissipative ones. An efficient dual system consists of a rigid and ductile sub-system combined with a flexible one. To compensate for the loss of stiffness due to cross-section reduction, composite columns with HSS are suggested. The performance of a dual system incorporating replaceable dissipative links that could be used in eccentrically braced frames (EBF) is investigated in Dubina et al. (2008). Tenchini et al. (2011) numerically investigates the seismic behavior of dual concentrically braced frames (CBF) using S460 or S690.

2.4 Conventional seismic resistant systems

2.4.1 Moment Resisting Frames (MRF)

Steel Moment resisting frames (MRF) have been used since the beginning of the 20th century and evolved during the years to their present form which entails heavy rolled, or welded, sections for beams and columns that connect in welded or bolted, rigid or semi-rigid joints (FEMA 355D, 355E). Structures with MRF are usually flexible. It is common American practice to position MRF in the buildings' perimeter and form all other connections as simple. Lateral stability is thus provided exclusively by these 2D frames, while horizontal actions are transferred to them through the floor diaphragms. Their members are usually made of open-sections and the beams may have composite action with the concrete slabs. Another possible configuration is to form rigid beam-to-column

joints in both column axes thus creating 3D frames, as is common in Japan. These frames have increased redundancy, and thus possibilities of load redistribution. The most appropriate profiles for the columns are hollow sections or crossed double I-sections with similar stiffness in both principal axes.

Starting from the 1960s, welded steel MRF were regarded as the most ductile system. The earthquakes in Northridge, USA (1994) and Kobe, Japan (1995) challenged this belief. In Northridge, numerous steel moment-frame buildings experienced brittle fractures of joints. The damaged buildings had a wide range of stories (1-26), ages (30-years-old to new) and were geographically spread. Although the buildings meeting the codes did not collapse, their inspection and repair were rather costly as they often did not display obvious signs of “architectural” damage. Investigations showed that most brittle fractures initiated at the weld between the beam bottom flange and column flange, at low levels of plastic demand. These discoveries raised concern that undetected damage may have been caused by past earthquakes. Indeed, later investigations confirmed such damage caused by the 1992 Landers, 1992 Big Bear and 1989 Loma Prieta earthquakes. It is now known that the typical connection detail employed prior to the Northridge earthquake had some features that rendered it susceptible to brittle fracture, as presented in (FEMA 350, FEMA 351, FEMA 355D, FEMA 355E). In Japan, investigations conducted after the Kobe earthquake, determined that approximately 1/3 of the examined modern steel buildings in the heavily shaken area underwent severe damage or collapse. Amongst them, the main damage types were fracture of the welded joints of the 1st story column top and fracture of the column bases’ anchors (BRI 1996, Kuwamura 1998). The aforementioned fractures raised concern over the cyclic response of MRF joints and triggered extensive research on its improvement. In USA, emphasis was placed on improving the connection details, while in Japan the research also focused on material toughness. In Europe, the studies carried out resulted in amendments to the existing design rules (Mazzolani 2000).

According to modern seismic codes, in case of a strong earthquake MRF should develop a reliable plastic mechanism by forming a number of plastic hinges. Any failure should be avoided before this mechanism, while the members or connections adjacent to possible plastic hinges should be designed with sufficient overstrength. EN1998 states that plastic hinges are to be formed in the beams (or in the connections if special connections are used). To achieve this, a strong-column-weak-beam design must be incorporated. Furthermore, moment resisting connections should be configured to shift plastic hinge formation away from the column face. This can be done either by local reinforcement of the beam flanges in the connection area (haunched or cover plate connections) or by locally reducing the beam flanges at a distance away from the connection

(Reduced Beam Sections – RBS), as shown in Fig. 2.13. The concept of RBS connections was proposed by Plumier in 1990 and was extensively investigated after the Northridge earthquake using different types of reduction such as straight-cut, tapered-cut and radius-cut sections (Popov et al. 1996, Chen et al. 1996, Engelhardt et al. 1996, Moore et al. 1999, FEMA 355D). The latter exhibited more satisfactory ductile behavior and was introduced in FEMA 350 and EN1998-3. The length of plastic hinges in steel beams is typically on the order of half its depth and their location should be shifted at least that distance away from the face of the column. These improvements of MRF connection configurations are considered effective in preventing brittle fractures - which may compromise life safety - but do not generally prevent structural damage. Plastic hinge formation within a beam translates to significant plastic rotations and may cause localized damage to floor slabs and other elements, the repair of which could be both costly and difficult. Hence, the need to investigate stability systems that favor reparability rises.

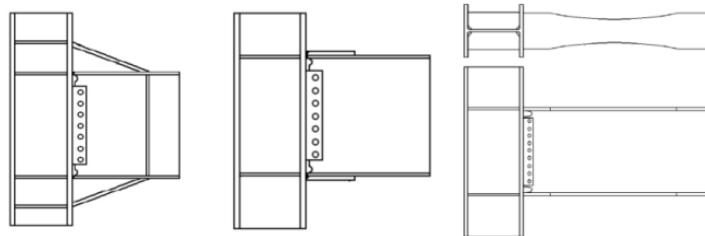


Fig. 2.13 Improvement of moment resisting connections using haunches, cover plates or reduced beam sections (RBS) (drawings from FEMA 355D)

2.4.2 Braced frames

Steel braced frames develop seismic resistance primarily through axial forces in the components. They behave as vertical trusses where the columns represent the chords. The bracings may be concentric or eccentric and their optimum angle is about 45° . Braced frames are generally stiffer than moment resisting frames (MRF).

2.4.2.1 Frames with concentric bracings

Concentric braced frames (CBF) are those systems where component centerlines practically intersect at a single point in a joint. The most common type is the X-bracing but other types are applicable depending on architectural demands. Fig. 2.14 shows alternatives of CBF. Horizontal forces are undertaken mainly via the development of axial forces in the diagonals and energy is dissipated through their cyclic response. Seismic design must ensure that they will yield before any other type of failure occurs. Types of bracing associated with brittle failures (such as V- and especially K-type) are to be avoided in seismic areas (Vayas et al. 2019). In general the CBF are very effective in providing stiffness but their performance is governed by buckling of the diagonals, and

hence their hysteretic behavior is relatively poor. A typical CBF problem is that under increasing lateral displacement, buckling of the compression braces leads to unbalanced vertical forces on the intersecting beams eventually leading to damage concentration in a single story (Fig. 2.15a).

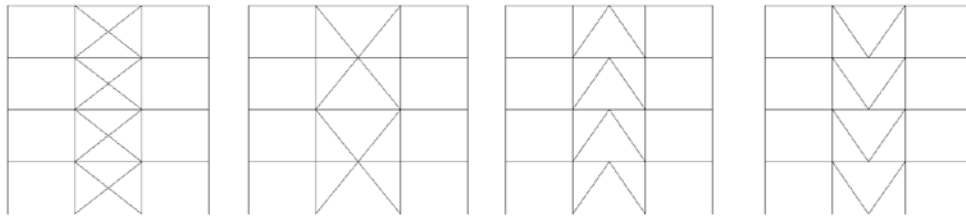


Fig. 2.14 Types of Concentric Braced Frames (CBF)

Extensive damage was reported in CBF following earthquakes such as the 1985 Mexico City, 1989 Loma Prieta, 1994 Northridge and 1995 Kobe events leading to updates of the seismic codes' provisions (Uriz and Mahin 2008). Still, the conventional CBF have limited ductility and are prone to low-cycle fatigue and soft-story mechanism. Numerous investigations have been carried out to improve their performance by introducing new structural elements or using special bracing elements etc. Two such examples are shortly presented: the zipper braced frames and the Buckling Restrained Braces (BRB).

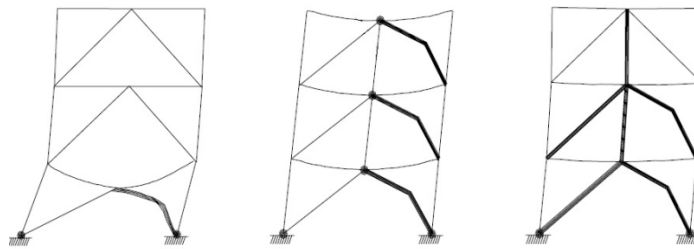


Fig. 2.15 (a) Failure mechanism of Λ -braced frame (soft story) (b) Full-height zipper mechanism (c) Partial-height zipper mechanism (Leon and Yang 2003)

The zipper braced frame configuration was first proposed by Khatib et al. (1988). Its configuration is similar to the conventional inverted-V (or else Λ -) type except that a vertical element - the zipper column - is added at the beam midspan points from the second to the top story. The zipper columns tie all brace-to-beam intersection points together, forcing all compression members to buckle almost simultaneously. In the event of a strong earthquake, the braces in the first story buckle and cause unbalanced forces at the midspans of the first-floor beams. Via the zipper columns, these forces are transmitted to the midspan of the above stories causing their diagonals to buckle as well, preventing the formation of soft-story mechanism. However, instability may eventually occur once the full-height mechanism is formed (Fig. 2.15b). Leon and Yang (2003) modified this system by increasing the member sizes of the diagonals at selected stories so that

they remain elastic and prevent formation of the complete zipper mechanism (partial-height zipper mechanism Fig. 2.15c). This configuration has improved ductility and is called the suspended zipper braced frame. Its main disadvantage is that as the number of stories increases, so does the magnitude of the unbalanced vertical forces, making difficult the design of the braces in the top stories (Yang et al. 2008a,b, 2009)

An improved version of the CBF with regard to diagonal buckling, are the buckling restrained braces (BRB) whose typical configuration is shown in Fig. 2.16a. They consist of a steel core that fully resists the axial force developed in the braces, a buckling restraining unit (usually concrete casing) and a separation unit (usually a debonding material such as resins, Teflon etc or a gap) that allows for sliding and Poisson effects of the core. Fig. 2.16b shows different cross-sections of BRB consisting of mortar-infilled tubes, precast concrete panels, steel tubes etc. Due to restraining of the buckling, the BRB exhibit same hysteretic behavior in both loading directions. BRB were developed and applied first in Japan in the end of the 1980s while their popularity increased internationally in the 2000s (Xie 2005, Takeuchi 2018). To prevent inelastic deformations at the ends of the braces (connection zones) which are not restrained, reinforcement via stiffeners is usually applied.

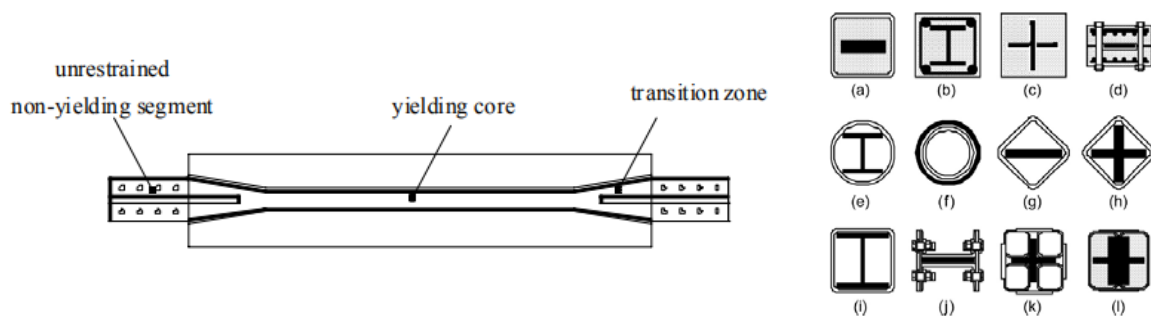


Fig. 2.16 (a) Configuration of typical BRB (Bosco et al. 2012) and (b) Cross-sections of BRB (Xie 2004)

2.4.2.2 Frames with eccentric bracings

In eccentric braced frames (EBF), diagonal elements are placed eccentrically in respect to the adjoining beams or columns. The component between two diagonals, between a diagonal and the column, or between the diagonals and the beam is called seismic link and can be either horizontal or vertical (Fig. 2.17). Beam-to-column joints are simple when the seismic links are away from the beam ends, otherwise they must be rigid. The connections between the braces and the beams may be either rigid or simple. The dissipative members are the links which develop plastic deformations due to shear or bending, depending on their length. In EN1998-1, different limits apply for the

plastic rotations of long and short links. The links are reinforced with web stiffeners to avoid local instabilities. Seismic links are usually not connected to the concrete slab through studs to avoid composite behavior and concrete cracking due to large deformations. EBF have been employed for many decades worldwide and could be considered as a hybrid between MRF and CBF, representing an attempt to combine their advantages while restrain their disadvantages (Hjelmstad and Popov 1984, Popov and Engelhardt 1988). Hence, EBF are stiff similarly to CBF and ductile alike MRF.

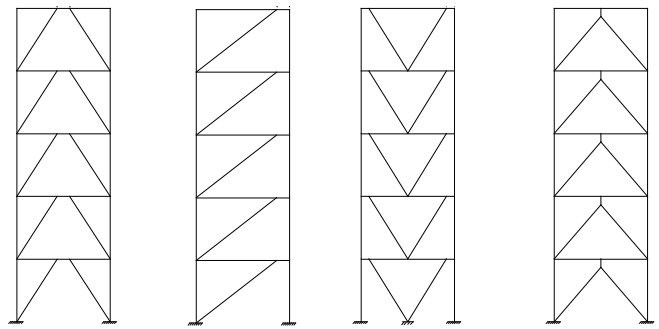


Fig. 2.17 Eccentrically Braced Frames (EBF)

2.5 Innovative anti-seismic systems incorporating reparability

The most important drawback of the aforementioned conventional seismic resistant systems is their lack of reparability. After a strong seismic event, replacement of beams in a MRF would be rather difficult, as they resist gravity loads. Similarly in EBF, concentration of damage in the links would involve replacement of beams' parts. In the case of CBF, replacement of the braces would be laborious due to their size and weight. To address this issue, research on the development of lateral stability systems that can be simple to repair, by having easily exchangeable dissipative members has been carried out in the past years. The European funded INNOSEIS project (Vayas (Ed.) 2017) summarizes the results of some of these investigations and provides relevant design guides for the respective innovative systems. Few such systems are hereby presented, one of them being the FUSEIS system, investigated in this thesis.

2.5.1 FUSEIS with beam or pin links

FUSEIS is an innovative seismic resistant system consisting of two closely spaced strong columns rigidly connected via multiple horizontal links which can be either beams or pins (Fig. 2.18). The number of links depends on overall stiffness requirements and geometric limitations such as provision for sufficient vertical spacing. Assuming a typical floor height of 3.4m, the use of four or

five links per story is suggested. The FUSEIS system resists horizontal loads as a vertical Vierendeel beam (Wickersheimer 1976, Verswijver et al. 2009) combining axial force in the columns and bending of the links. When a horizontal force is applied, the system deforms and the links are subjected to bending until they reach their moment capacity and plastic hinges are formed. In the FUSEIS with pin links, catenary action develops when the applied deformations increase beyond the bending capacity of the links. The system's resistance is then controlled by the links' axial forces. The system is capacity designed, so in case of a strong seismic event damage is concentrated in the exchangeable fuses. Repair -if needed- is limited to replacing them.

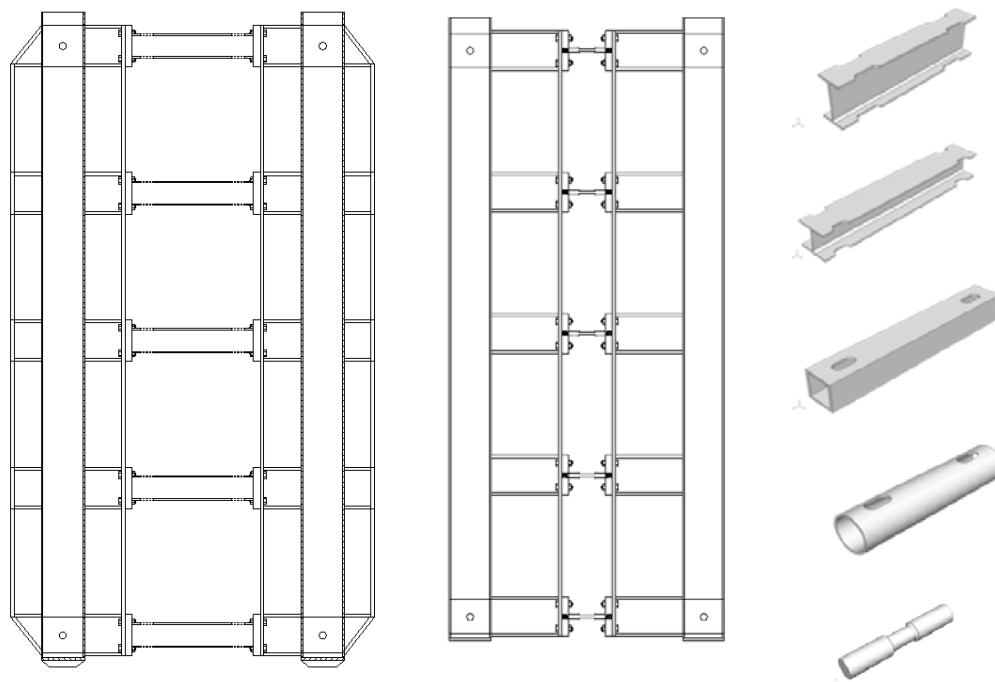


Fig. 2.18 FUSEIS systems with (a) beam and (b) pin links and (c) types of FUSEIS links

FUSEIS may provide lateral stability alone or in combination with moment resisting frame action, depending on whether the building's beam-to-column connections are formed as simple or as rigid/semi-rigid. The FUSEIS links are generally not subjected to gravity loads as they are mostly placed between floor levels. The FUSEIS system also serves architectural versatility as it allows for more unobstructed surfaces for various openings, fenestration etc.

The beam links may have I-shaped open cross-sections or hollow-sections (Fig. 2.18c). The depth of the cross-sections may vary between floors, to accommodate the increase of story shear along the building's height. In order to shift the location of the plastic hinges away from the connection area, reduced beam sections (RBS) can be used at a distance from the beam ends. Similarly to the RBS concept, for the protection of the connection areas of the pins, their sections are weakened along a length around their middle. The FUSEIS columns may have open or hollow cross-sections. The first

are more practical in forming the connections while the latter are beneficial against buckling. A synthetic approach of closed sections welded with T-sections can also be applied. In order to restrict damage from the foundations, pinned connections of the columns bases are generally proposed, however fixed supports may also be applied in multi-story buildings.

The system was initially investigated during the European Research Project “FUSEIS-Dissipative Devices for Seismic Resistant Steel Frames” using links of S235 steel (Vayas et al. 2013, Dimakogianni et al. 2012, Dougka et al. 2014, Dimakogianni et al. 2015). It was further investigated during the MATCH Research Project (Feldmann et al. 2017, Avgerinou et al. 2020a,b) using materials with higher strength (S355, S500, S700) and a modified version of the system with links. More specifically, in the previous version the link consisted of two receptacle beams connected through a short pin, whereas in the current version the receptacle beams are omitted (Fig. 2.19). Few dissertations on FUSEIS with beams and pins links may be found in the literature (Karydakis 2011, Dougka 2016, Dimakogianni 2017). FUSEIS systems with beam links were recently applied in a composite one-story irregular building in the German School of Athens (Vayas et al. 2014). The system provided lateral stability alone as the beam-to-column connections of the structure were formed as simple.

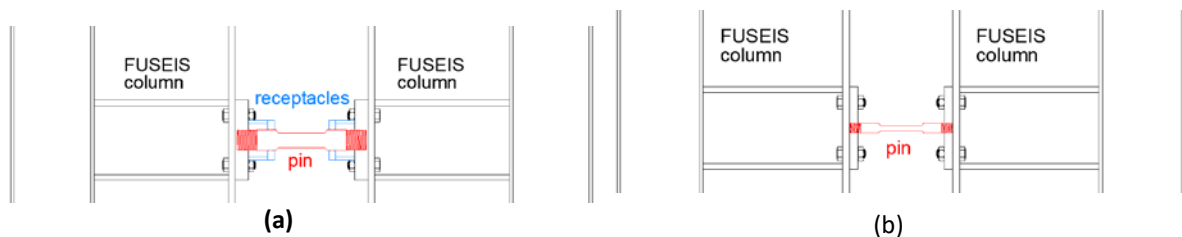


Fig. 2.19 Details of FUSEIS with pin links: (a) previous version with receptacle beams and (b) simplified current version

2.5.2 FUSEIS with splices

FUSEIS with splices is an innovative beam-to-column connection type achieved by introducing a discontinuity in the beams of a moment resisting frame and splicing the two parts through steel plates bolted to the web and flange of the beam (Valente et al. 2016, Kanyilmaz et al. 2019). Fig. 2.20 shows the configuration of such a connection. The system was developed in the framework of European research project FUSEIS (Vayas et al. 2013). The part of the column near the connection is reinforced in order to have sufficient over-strength. In case of a strong seismic event, the configuration of the splice promotes buckling and hence energy dissipation in the replaceable web and flange steel plates, without damage in the rest of the elements. As can be seen, the steel reinforcement bars are not interrupted at the gap, to avoid the damage to the concrete slab, the

floor finishes, hydraulic piping etc. In practice, the gap can be filled with low stiffness foams made of polymers which would not affect the structural performance. Component and large-scale experimental investigations showed very good performance of the system in terms of stiffness, ductility, energy dissipation and resistance while the structural fuses proved to be easily replaceable (Castiglioni et al. 2012, Calado et al. 2013).

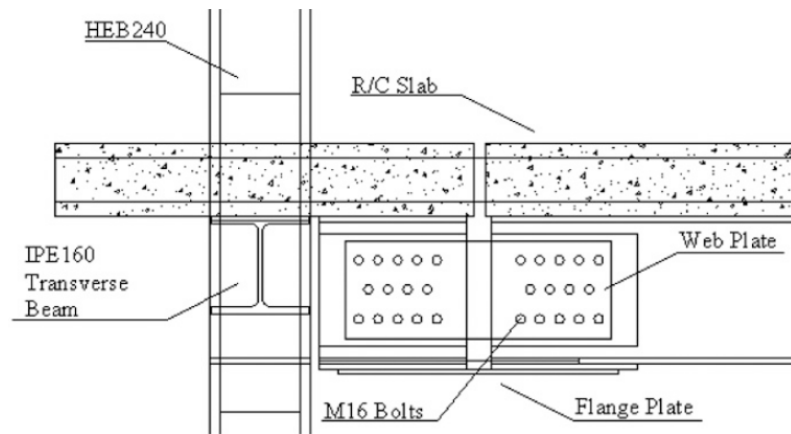


Fig. 2.20 Detail of FUSEIS with splices, exterior joint (Kanyilmaz et al. 2019)

2.5.3 INERD connections

INERD connections are dissipative connections that can be placed between the vertical brace of a building and the adjacent column. They were developed in the frame of European Research program “INERD” (Plumier et al. 2004, Vayas and Thanopoulos 2005, Drei et al. 2006, Thanopoulos 2006) while design guide is provided in (Vayas (Ed.) 2017). Two types of INERD connections were proposed: pin connections and U-shape connections. The pin connection (Fig. 2.21a) consists of two external plates (bolted or welded to the column flanges), one or two internal plates (welded to the brace) and a pin that passes through them. The pin may have rectangular, rounded or circular cross section and is subjected to 3- or 4-point bending by transferring the brace’s axial force. As the connection’s response is governed by bending, it is similar for both tension and compression of the diagonals. The U-connection consists of a bent U-shaped thick plate that is bolted to the brace and to the column (Fig. 2.21b).

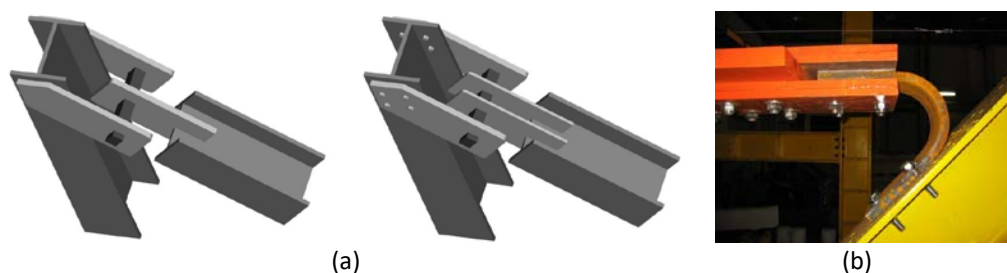


Fig. 2.21 INERD connections consisting of (a) pins and (b) U-shaped plates

In both cases, the resistance of the INERD connection is designed to be smaller than the buckling resistance of the braces. The diagonals are thus protected and can remain active regardless of their axial force direction. In case the design earthquake occurs, significant axial forces develop in the braces leading the INERD connections to deform inelastically and dissipate energy. Plasticification is limited at the connections' pins or U-plates, whose location allows for immediate inspection and, if necessary, replacement. In that case, the weight of the replaceable member is rather small, resulting in reduced requirements in terms of cost, time and equipment.

2.6 Innovative self-centering systems

As discussed, current seismic design codes encourage the application of ductile materials and systems, aiming at inelastic structural response involving energy dissipation in selected zones. However, repairs following small or moderate earthquakes require downtime and possibly disturbance to business operation that may not always be tolerated. Therefore investigations have been carried out on systems that exhibit self-centering capabilities, and thus reduce post-earthquake residual deformations. Two such systems are presented, constituting “upgrades” of conventional moment resisting and braced frames.

Regarding residual drifts, correlation between their extent and their consequences is not strictly defined, although some quantification is available. According to AISC specifications (2016), residual drifts less than 0.2% can be considered as insignificant since this is the acceptable erection tolerance. For residual drifts between 0.5% and 1.0%, assessment by a structural engineer should be required before the building may be reoccupied. Residual drifts between 1.0% and 1.5% would require interventions as they would cause occupancy issues apart from the structural aspect. The cost of such interventions would be high. Lastly, residual drifts greater than 1.5% would likely be a total loss from an economic point of view (Choi et al. 2008).

2.6.1 Posttensioned Energy Dissipating Connection (PTED)

The Posttensioned Energy Dissipating (PTED) connection provides an improvement of steel moment resisting connection based on the concept of precast concrete connections. The system consists of posttensioned high-strength steel bars that are designed to remain elastic and provide a self-centering response along with buckling-restrained energy dissipating bars that are able to yield in tension and compression. Numerical and experimental investigations of the connections are available in (Chistopoulos 2002a,b). Fig. 2.22 shows the geometric configuration of a frame

incorporating PTED connections. Each beam-to-column joint includes four symmetrically placed energy dissipating bars (ED) and two high-strength posttensioned bars (PT) located at mid-depth of the beam, on each side of the web. Experimental research has shown that the connection can undergo large deformations while dissipating energy, without introducing inelastic deformations in the beams or columns and without residual drifts.

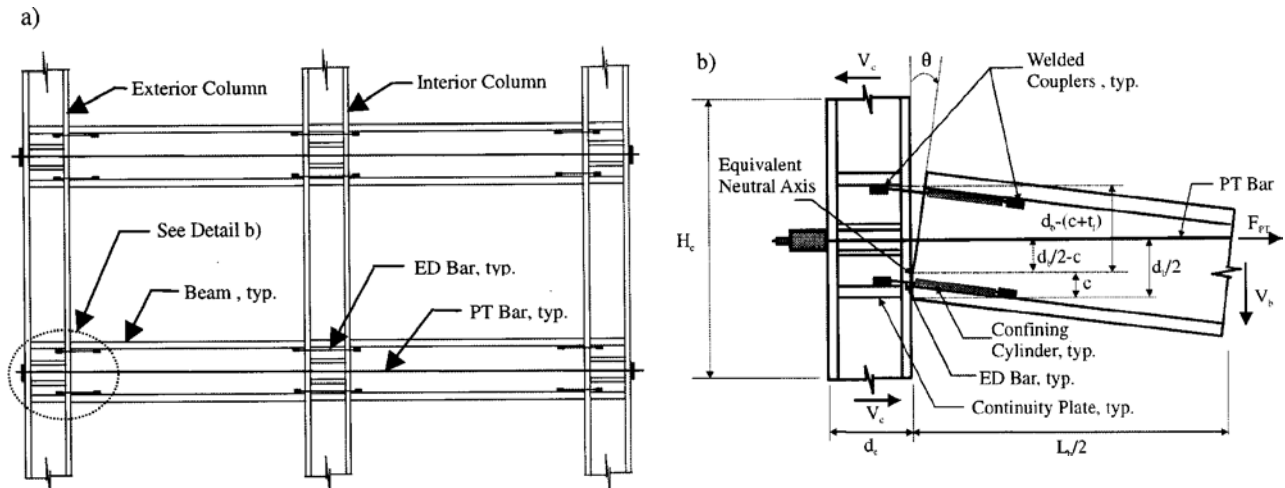


Fig. 2.22 Exterior Posttensioned Energy Dissipating Connection (PTED) and detail (Christopoulos 2002)

2.6.2 Self-Centering Energy Dissipative Bracing System (SCED)

The Self-centering Energy Dissipative (SCED) brace is a cross-bracing system consisting of traditional steel bracing elements interconnected by a dissipative mechanism and a self-centering mechanism comprised of pretensioned fiber tendons (Tremblay and Christopoulos 2005 (patent), Christopoulos et al. 2008). The brace is assembled in a way that the tendons are elongated regardless of the direction of axial deformation. The system reduces or eliminates residual building deformations after major seismic events, leaving the main structural components of the building intact. Fig. 2.23 illustrates the function of the SCED brace.

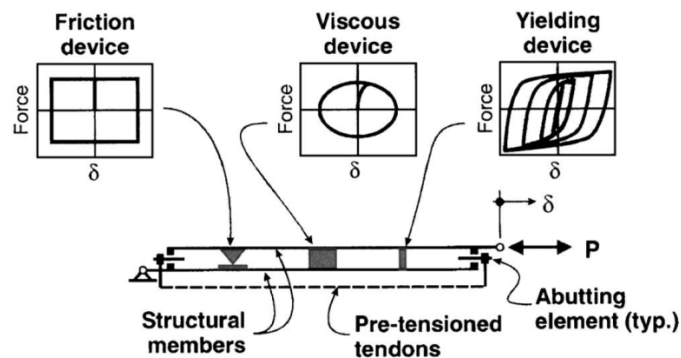


Fig. 2.23 Concept of SCED System (Christopoulos et al. 2008)

Numerical comparison of building case studies with varying number of floors using MRF, Buckling Restrained Braced frames (BRB) and SCED braced frames subjected to time-history analysis is given in (Tremblay et al. 2008, Choi et al. 2008). For the considered record set scaled at design level, the SCED braced and the BRB frames exhibited similar response. However, the SCED braced frames experienced negligible residual drifts (less than 0.7 %), while the BRB frames and the MRF experienced significant residual drifts with an average magnitude around 1.2%, translating to expensive repair.

Chapter 3: Experimental investigations

3.1 Introduction

This chapter presents the experimental campaign conducted in the frame of this research. Eight large scale tests on FUSEIS systems were performed in the Institute of Steel Structures at NTUA: two tests on FUSEIS with S700 beam links, four tests on system with S355 beam links and two tests on FUSEIS with S500 pin links. The tests configuration is described and their results are discussed in terms of ductility, damage, load and stiffness degradation, energy dissipation etc. In addition, component tests on similar FUSEIS links were conducted in the University of Aachen and are hereby outlined. Given that the FUSEIS systems with S235 beam and pin links have been investigated in the past, comparison - where applicable - is made between the previous and the current test results.

3.2 Test setup

Eight large scale tests on FUSEIS subjected to cyclic or monotonic loading were conducted in NTUA in the frame of the RFCS-supported project "MATCH" (Feldmann et al. 2017). Six of them were with beam links (either hollow or open sections) and two with pin links. The examined systems consisted of two strong columns connected via five links that acted as fuses. The parameters differentiating the experimental investigations were the type and profile of the fuses, the steel grades and the loading procedures. The beam fuses were welded on end-plates that were bolted to the columns in order to facilitate the replacement of the fuses after tests. In most cases the beams had RBS areas to protect the welded joints from fracture. The pin fuses were bolted via reverse threads onto the plates allowing for adjustments during installation, and the assembly was then bolted to the column flanges. In this case, the connection areas were protected by means of weakening the sections of the pins along their middle parts.

The dimensions of the examined systems corresponded to one floor of a real building frame: Height (H) 3.4 m and axial distance between columns (B) 1.50 m for the beam links or 1.40 m for the pin links (Fig. 3.1). Table 3.1 gives an overview of the tests.

The experimental setup included a rigid frame test rig, a computer controlled hydraulic cylinder and the FUSEIS strong columns. The Laboratory of Steel Structures is equipped with two rigid test rigs in order to accommodate different test configurations. For this experimental campaign, both test rigs were used as two different sets of FUSEIS columns were available from a previous research project

(Vayas et al. 2013; Dougka et al. 2014; Dimakogianni et al. 2012), facilitating the testing of systems with similar widths but significantly different lengths of dissipative elements (Fig. 3.2 and Fig. 3.3).

Table 3.1 Overview of tests on FUSEIS systems

Test	Link type	Steel	B (mm)	L (mm)	Loading type
T1	Hollow-section beams	S700	1500	722	Cyclic (I.A)*
T2					Cyclic (C.A)**
T3	HEA beams	S355	1500	702	Cyclic (I.A)
T4					Cyclic (C.A)
T5					Cyclic (C.A)
T6					Monotonic
T7	Pins	S500	1400	296	Cyclic (I.A)
T8					Cyclic (C.A)

* I.A.: increasing amplitude
**C.A.: constant amplitude

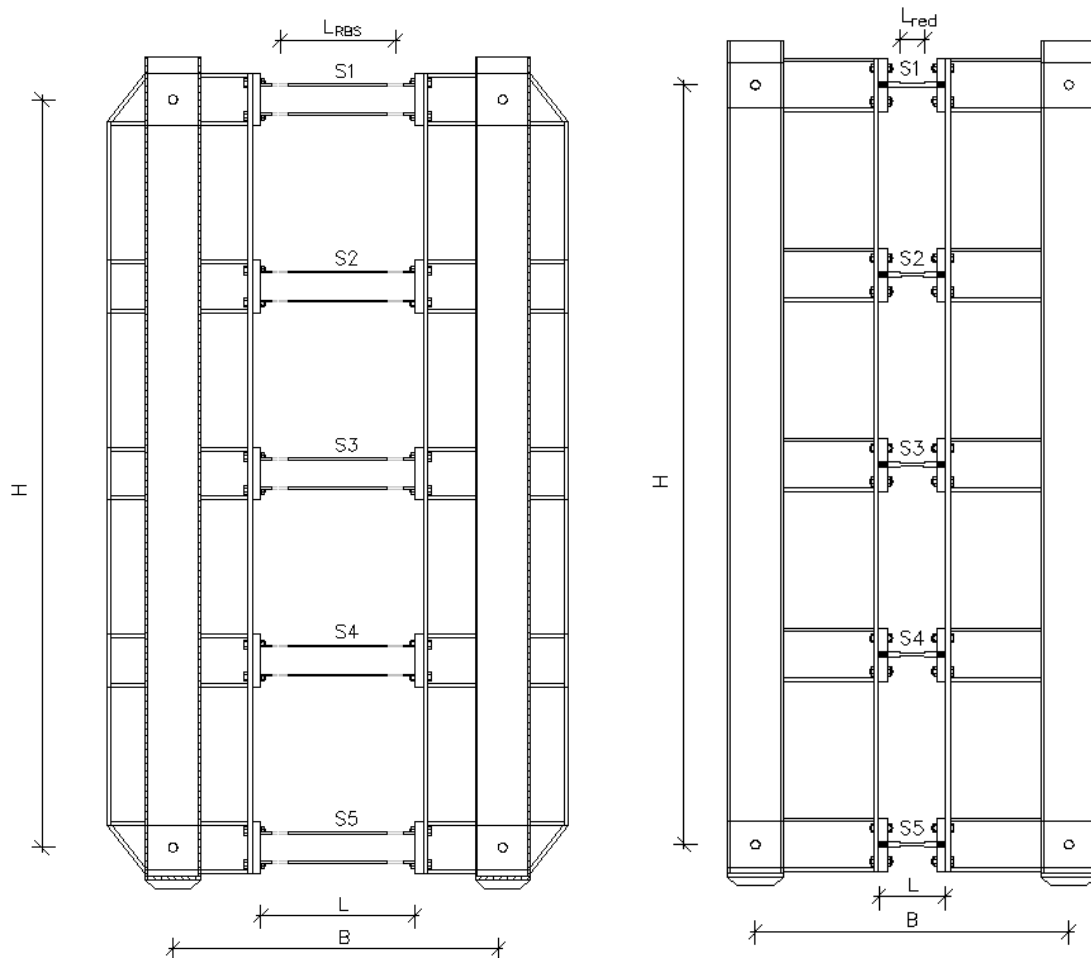


Fig. 3.1 Overall dimensions and numbering of specimens (a) beam links (b) pin links

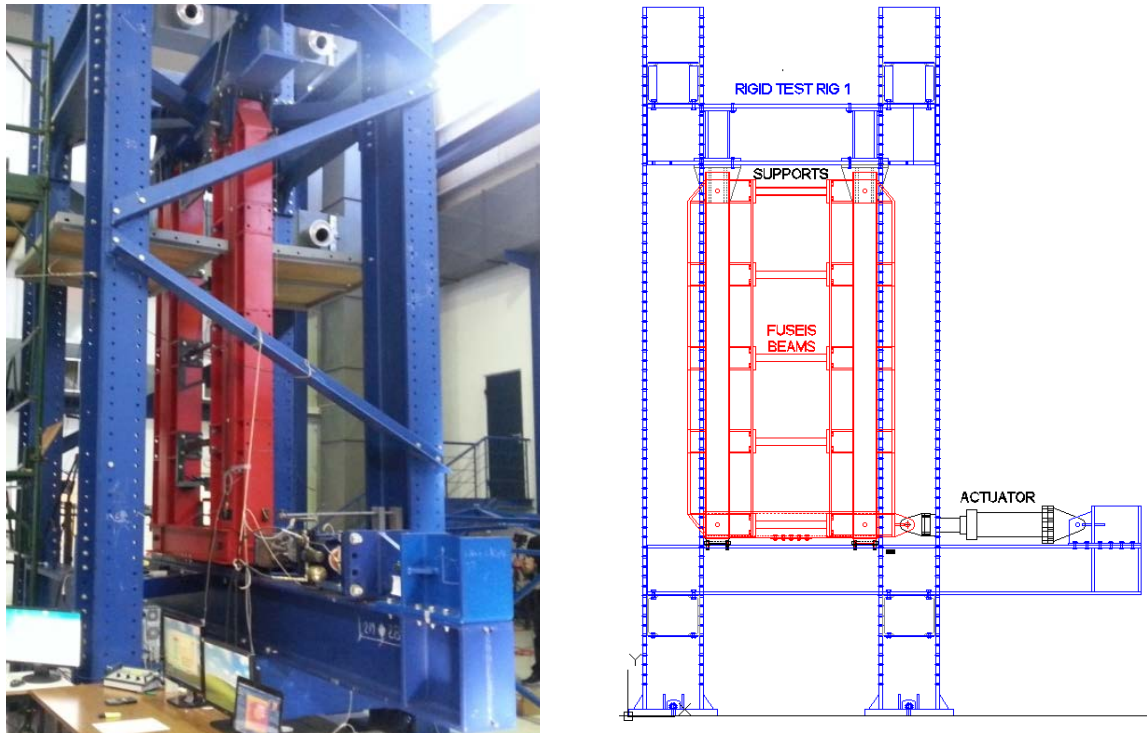


Fig. 3.2 General layout of test setup for FUSEIS with beams (a) photo (b) drawing

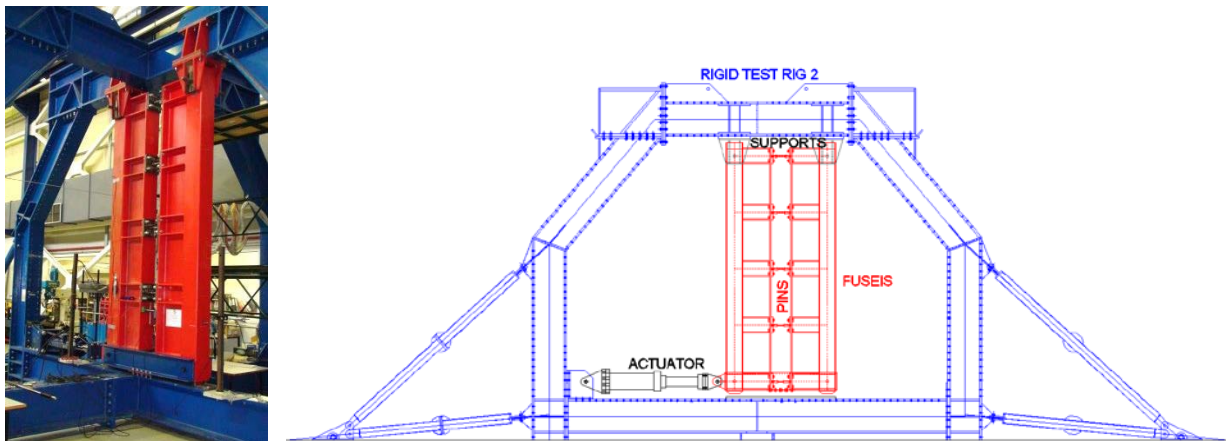


Fig. 3.3 General layout of test setup for FUSEIS with pins (a) photo (b) drawing

Contrary to previous experimental campaigns, all specimens of the same type had the same length and were welded on identical plates at both ends. The FUSEIS strong columns were designed to have adequate stiffness to accommodate various experimental investigations with different types of links. Their profiles consisted of a hollow-section on which T-profiles were welded (Fig. 3.4). Thus the advantage of hollow-sections against buckling was combined to that of open-sections in terms of connectivity. Plate stiffeners were used to reinforce the columns' webs at the levels of the connections with the links.

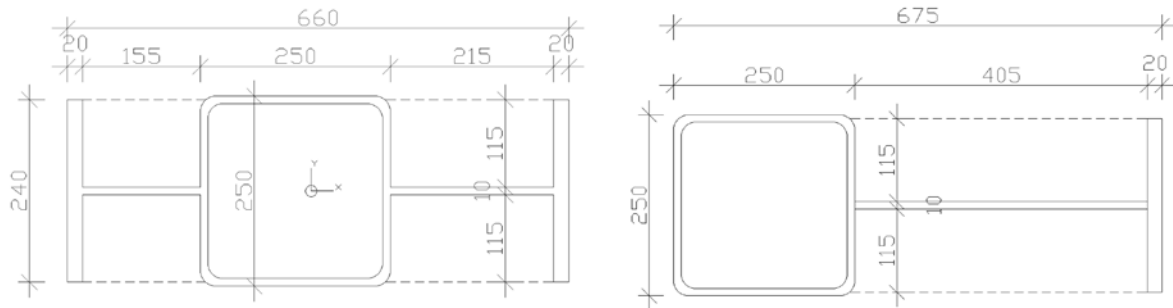


Fig. 3.4 Cross-section of FUSEIS columns for system with (a) beam and (b) pin links (dimensions in mm)

The columns were connected to the test rig at their top by M38 pins (Fig. 3.5a). Loading was applied through a hydraulic actuator positioned horizontally between the bottom of the columns and a rigid lateral support (Fig. 3.5b). The actuator was hinged at both ends in order to transfer only axial loads to the test frames. At each side of the bottom of the columns a pair of simply supported horizontal beams of UPN260 profile was used, simulating the floor diaphragm action (Fig. 3.6a). Thus, equal displacements of the columns were ensured while the links of this level were protected from the axial load applied by the adjacent actuator. As can be observed in Fig. 3.6a, the UPN beams were connected to each other at their bottom flanges via a bolted plate, hence constraining the columns' torsional deformations at the level of load application. Fig. 3.6b shows how out-of-plane displacement of the test frame was restricted via steel plates/leaders. Mounting of the test configuration was carried out with a crane due to the size and weight of the parts involved. First the columns were pinned to the test rigs and then, at each level at a time, a beam specimen was bolted to the FUSEIS columns using provisionally steel rods as spacers. The bolts were preloaded using a torque wrench and double nuts were used.

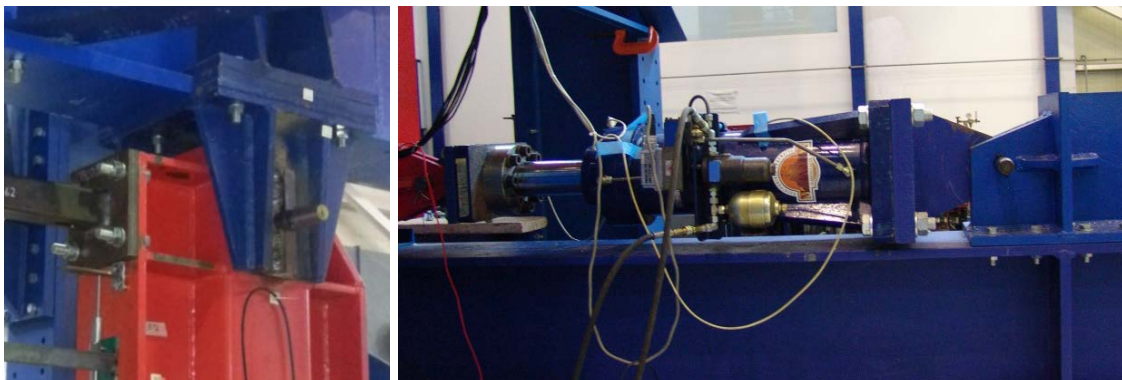


Fig. 3.5 Details of the setup (a) pin supports of the columns and (b) hydraulic actuator pinned at both ends



Fig. 3.6 (a) UPN beams providing “diaphragm” action and (b) steel members as “leaders” to prevent out-of-plane displacements

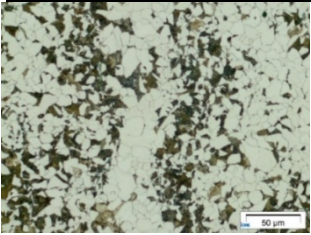
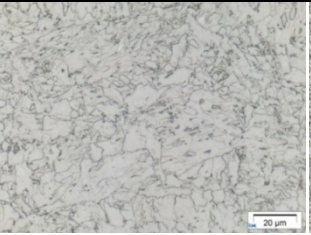
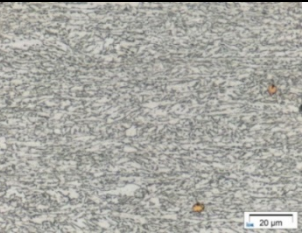
3.3 Material properties

Three types of steel were examined in this research. Steel grade S355J2 was used in the HEA beam links, S700MC was used for the hollow-section beam links while the pin links were made of S500MC steel. Macroscopic and microscopic material data were provided by RWTH and UTH, which were the participants of the MATCH project engaged with the conduction of the small-scale tests and the development of the material models for the numerical simulations (Feldmann et al. 2017). The materials for the small-scale tests were delivered in different forms, thus determining the geometry of the samples and occasionally influencing the testing conditions. The chemical composition of the materials was obtained by spectroscopic analysis and is demonstrated in Table 3.2, while the microstructure configuration was achieved via Light Optical Microscopy (LOM) and is summarized in Table 3.3.

Table 3.2 Chemical composition of materials (%)

S355J2	C	Si	Mn	P	S	Cr	Mo	Ni	Al	Cu	N	Sn	Ti
	0.197	0.21	1.33	0.022	0.015	0.18	0.01	0.07	0.021	0.23	0.0085	0.02	0.01
S500MC	C	Si	Mn	P	Cr	Mo	Ni	Al	Ca	Co	N	Nb	V
	0.02	0.21	1.57	0.008	0.20	0.19	0.54	0.03	0.02	0.02	0.0068	0.03	0.01
S700MC	C	Si	Mn	P	Cr	Mo	Ni	Al	Co	N	Nb	V	
	0.05	0.45	1.42	0.006	0.003	0.01	0.04	0.03	0.01	0.0089	0.05	0.05	

Table 3.3 Microstructural configuration and analysis of delivered materials

S355J2		S500MC	S700MC
			
Pearlite 25%	Ferrite 75%	Bainite 100%	Bainite 100%

The strength properties were determined by tensile tests at room temperature using round bar samples (S500MC) or flat samples (S355J2, S700MC), depending on the geometry of the delivered material. Table 3.4 gives the results in terms of yield and tensile strength.

Table 3.4 Experimentally defined yield and tensile strength of specimens' steel

Steel grade	f_y (MPa)	f_u (MPa)	f_u / f_y
S355J2	440	605	1.38
S500MC	510	660	1.29
S700MC	740	845	1.14

In order to determine the mechanical behavior of the links' materials within the inelastic regime under cyclic loading, cyclic tests on material specimens were performed under either stress or strain control. In total, twenty eight (28) small-scale tests were conducted in UTH for the three steel grades using a servo-hydraulic testing machine (Instron) and an anti-buckling guide. The thickness of the specimens was 3.9 mm for S700MC and 3 mm for S500MC and S355J2. The results of these tests were used to determine the cyclic plasticity parameters of the material model incorporated in the finite element (FE) simulations discussed in the next chapter. For the strain controlled tests, at least two levels of strain amplitude were examined using one or two specimens for each material. The objective of these tests was to investigate the Bauschinger effect and the cyclic hardening or softening of the material and to obtain numerous hysteresis cycles for the material calibration. Regarding the stress controlled tests, they were conducted for two different loading ratios $\sigma_{\min} / \sigma_{\max}$ (-1/3 and -2/3) allowing for observations on the ratcheting effect (accumulation of plastic strain).

A series of Charpy-tests was conducted for each material in RWTH under different temperatures, aiming to cover the lower and upper shelf temperatures. The V-notch specimens were manufactured according to the standard DIN EN ISO 148-1, while their thickness varied due to the geometry of the delivered material (10 mm for S500MC, 2.5 mm for S700MC and 7.5 mm for S355J2). The transition curves are illustrated in Fig. 3.7, where the markers refer to experiments while the curves were fitted according to Wallin's method (Wallin, 2011). It may be seen that the upper shelf region for S355J2 was achieved at higher temperature compared to HSS.

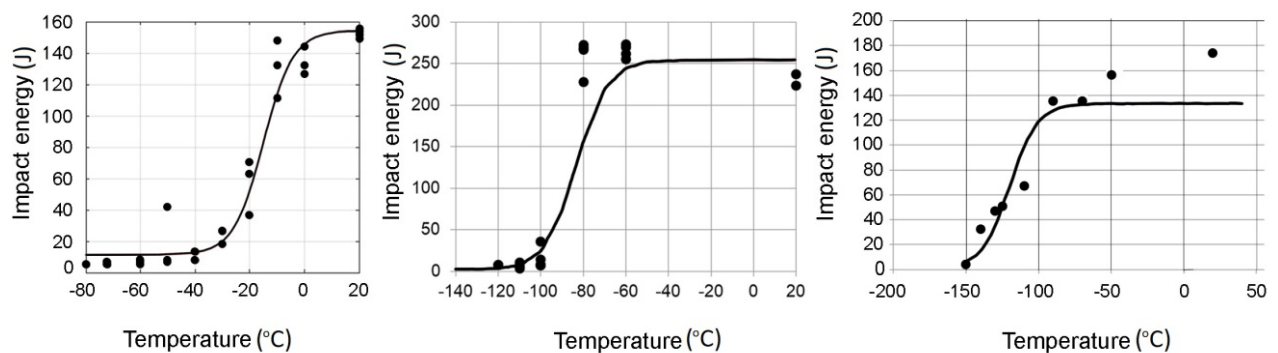


Fig. 3.7 Transition curves for (a) S355J2, (b) S500MC, (c) S700MC

The specimens were fabricated using S355J2 according to delivery standard EN10025-2 and S500MC, S700MC meeting the requirements of EN10149-2. However, EN10149-2 does not suggest minimum impact energies, so alternatively the recommendations related to S460ML (EN10025-4) and S690QL (EN10025-6) are used as a reference. Table 3.5 presents the minimum impact energy at -20°C temperature according to the delivery standards for the above steel grades. Comparing the transition curves of Fig. 3.7 with the Code provisions of Table 3.5, it may be seen that the actual material toughness was significantly higher than the reference values.

Table 3.5 Minimum impact energy at -20°C , according to delivery standards and relevant measured values

Steel grade	Standard	Impact energy at -20°C	Steel tested	Measured impact energy at -20°C
S355J2	EN 10025-2	27 J	S355J2	55 J
S460ML	EN 10025-4	47 J	S500MC*	260 J
S690QL	EN 10025-6	40 J	S700MC*	135 J

*Complying with EN10149-2, which does not specify impact energies

3.4 Measurements and kinematics

The following measurements were conducted during the tests (Fig. 3.8):

- The applied displacement and force (actuator)
- The horizontal displacements of the columns at different levels (LVDTs, Fig. 3.9)
- The differential displacement of the fuse ends (LVDTs, Fig. 3.10)
- The columns' inclination (inclinometers, cyan in Fig. 3.8)
- The slippage of some links' endplates (LVDTs, Fig. 3.9 and Fig. 3.11)
- The strains at top and bottom of middle section in the pin links (strain gages, Fig. 3.11)

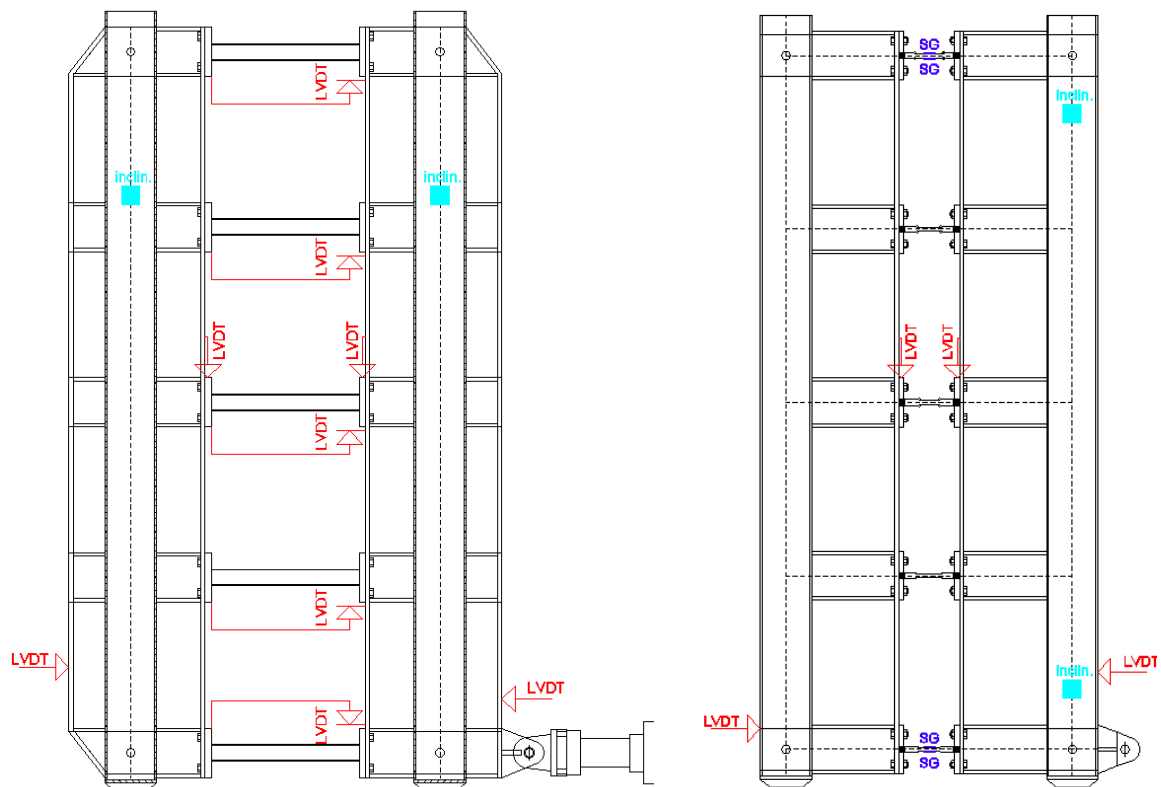


Fig. 3.8 Overview of measuring instrumentation for FUSEIS with (a) beams and (b) pins



Fig. 3.9 LVDTs for measuring horizontal displacements of FUSEIS system and plate slippage

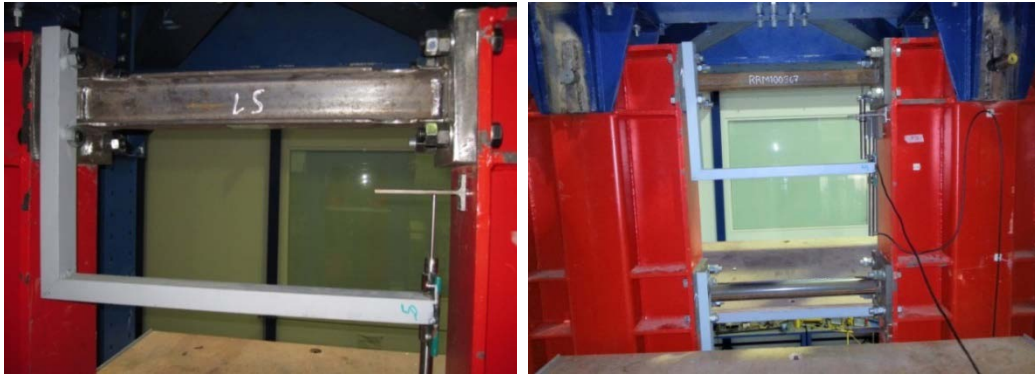


Fig. 3.10 LVDTs for measuring differential displacements of link's ends



Fig. 3.11 Strain gages at middle of pin's reduced section and LVDTs for measuring plate slippage

Fig. 3.12 illustrates the system's kinematics. The initial state is in black while the deformed in red. A similar graph for the FUSEIS with pins is in Fig. 3.45. The overall rotation (drift) of the system is denoted as ϕ and given by Eq. 3-1:

$$\phi = \Delta/H \tag{Eq. 3-1}$$

where Δ is the total horizontal displacement of the system (at the level of the actuator) and H is the system's height.

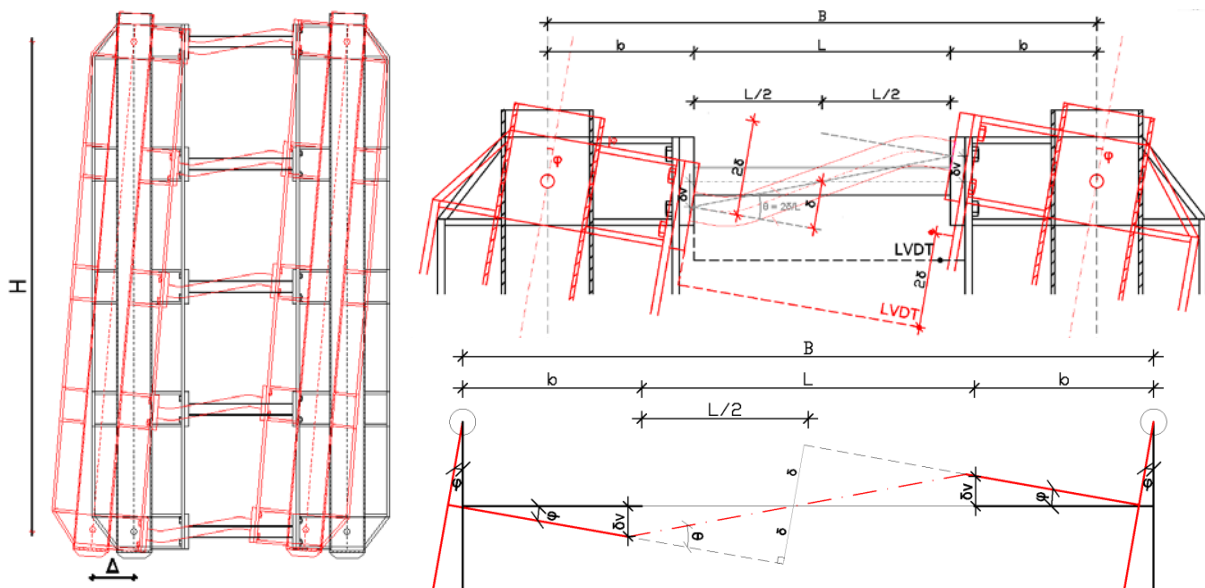


Fig. 3.12 Correlation between drift ϕ , link rotation θ and differential displacement of links 26

The differential displacement of the fuse ends measured by the LVDTs is denoted as 2δ (Fig. 3.12). As can be seen δ is the link's deflection at midspan, while δv is the vertical displacements of the link's endpoints, given by Eq. 3-2. The rotation of the link in its local system is θ , given by Eq. 3-3.

$$\delta v = b \cdot \tan \phi \approx b \cdot \phi \quad \text{Eq. 3-2}$$

$$\theta = \delta / 0.5L = 2\delta / L \quad \text{Eq. 3-3}$$

As can be seen in the simplified drawing in Fig. 3.12 there are two triangles that share the same base δ for which the following equations apply:

$$\delta = \sin \phi \cdot (b + L/2) \approx \phi \cdot (B/2) \quad \text{Eq. 3-4}$$

$$\delta = \sin \theta \cdot (L/2) \approx \theta \cdot (L/2) \quad \text{Eq. 3-5}$$

Combination of Eq. 3-4 and Eq. 3-5 leads to the above leads to Eq. 3-6:

$$\phi = \theta \cdot L/B \text{ or else } \theta = \phi \cdot B/L \quad \text{Eq. 3-6}$$

Combination of Eq. 3-4 and Eq. 3-1 leads to Eq. 3-7, which correlates the measured differential displacements of the beams (2δ) and the applied horizontal displacement Δ :

$$2\delta = \phi \cdot B = \Delta \cdot B/H \quad \text{Eq. 3-7}$$

Given the dimensions of the system with beams, Eq. 3-7 is approximately $2\delta = 0.44 \cdot \Delta$.

3.5 Loading protocols

The tests were performed under displacement control. The required displacements were input in the computer and then applied via the actuator with constant velocity 1.5 mm/s. For each type of fuse at least one cyclic test with increasing amplitude (I.A.) and one with constant amplitude (C.A.) was performed, as can be seen in the Test matrix of Table 3.6. Processing of the experimental data indicated that there were divergences between the input displacements (actuator data) and the specimens' resulting deformations. This was mainly attributed to hole allowances and slips in the pinned and bolted connections. As discussed later in detail, the divergence varied depending on the type of the specimen and the forces developed during each test. Therefore Table 3.6 presents the maximum drifts according to data obtained by i) the actuator, ii) the FUSEIS columns and iii) the links (referred as effective drifts).

The applied drifts in the increasing amplitude cyclic tests were selected according to a modified version of ECCS provisions (ECCS 1986). The modification of the ECCS load protocol involved the application of smaller loading steps beyond the assumed elastic range. More specifically, in the standard ECCS version, the amplitude of the loading cycles in the plastic range increases by a step of $2 \cdot e_y$ (where e_y is the displacement corresponding to a conventional limit of the elastic range), translating to a loading sequence of: $\pm 0.25 \cdot e_y$, $\pm 0.50 \cdot e_y$, $\pm 0.75 \cdot e_y$, $\pm 1.00 \cdot e_y$, $\pm 2.00 \cdot e_y$, $\pm 4.00 \cdot e_y$,

$\pm 6.00 \cdot e_y$, $\pm 8.00 \cdot e_y$ etc. The reference yield displacement e_y was based on preliminary numerical studies instead of previous monotonic tests as foreseen in the specification. In the current tests the loading protocol was modified to $\pm 0.25 \cdot e_y$, $\pm 0.50 \cdot e_y$, $\pm 0.75 \cdot e_y$, $\pm 1.00 \cdot e_y$, $\pm 1.50 \cdot e_y$, $\pm 2.00 \cdot e_y$, $\pm 3.00 \cdot e_y$, $\pm 4.00 \cdot e_y$, $\pm 6.00 \cdot e_y$, $\pm 8.00 \cdot e_y$, $\pm 10.00 \cdot e_y$ and $\pm 12.00 \cdot e_y$. When the amplitude corresponding to $\pm 12.00 \cdot e_y$ (or else 163mm actuator stroke) was reached, the loading cycles maintained the same amplitude upon test completion. Pauses were made between triplets of cycles to ease data processing. For comparison reasons the same loading protocol was used in the increasing amplitude (I.A.) tests T1, T3 and T7. Fig. 3.13 shows two of the applied Load Protocols. The illustrated number of cycles at maximum amplitude is schematic.

Table 3.6 Test matrix

Test	FUSEIS link	Load Protocol	Max. drift (actuator)	Max. drift (columns)	Max. effective drift (links)	Cycles at max. drift
T1	Hollow beams	Cyclic with I.A.	4.8 %	4.5 %	4.2 %	3
T2		Cyclic with C.A.	3.0 %	2.8 %	2.3 %	18
T3		Cyclic with I.A.	4.8 %	4.4 %	3.5 %	15
T4	HEA beams	Cyclic with C.A.	(1.6 %) 3.0 %	(1.4 %) 2.7 %	(0.5%) 1.7 %	(261) 111
T5		Cyclic with C.A.	4.0 %	3.7 %	2.5 %	45
T6		Monotonic	8.0 %	7.6 %	6.2 %	-
T7	Rods	Cyclic with I.A.	4.8%	4.7 %	-	3
T8		Cyclic with C.A.	1.6 %	1.5 %	-	36

Note: I.A. stands for increasing amplitude, C.A. stands for constant amplitude

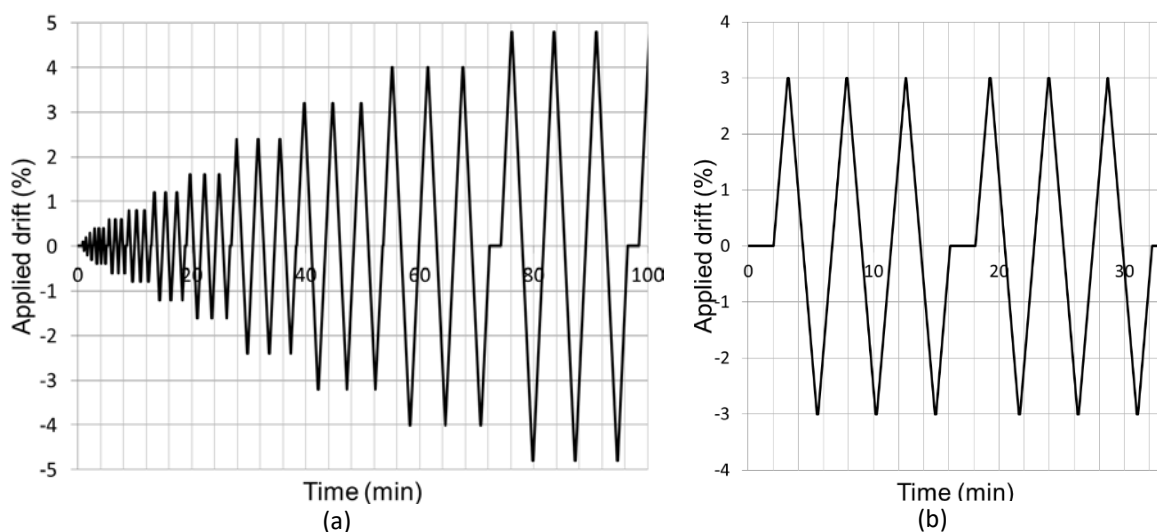


Fig. 3.13 Load protocols input for tests (a) T1, T3, T7 and (b) T2, T4

For each FUSEIS system, the I.A. test was performed prior to the C.A. test, to facilitate the selection of suitable amplitude for each case. The selection was dependent on the experimentally defined yield displacement of each system while allowing for investigation of an ultra-low cycle fatigue (ULCF) regime. In the system with HEA beam links, test T4 was initially subjected to constant cycles of small magnitude (1.6% nominal drift). After many hours of testing no sign of damage was given, and hence the applied drift was increased in order to cause failure of the specimens (Table 3.6).

Regarding the order of magnitude of the imposed deformations, it is noted that the maximum applied drifts were between 2% and 5%, which are the maximum expected drifts for braced frames and for MRF respectively at the Collapse Prevention performance level according to FEMA 356. The Eurocodes do not provide requirements in terms of overall drifts but refer to local rotation capacities of joints and plastic hinges. According to EN1998-1, the beam-to-column connection design should be such that the minimum rotation capacity of the plastic hinge region is 35 mrad for structures of high ductility class (DCH) or 25 mrad for medium ductility class (DCM). This rotation capacity should be ensured under cyclic loading without stiffness or strength degradation greater than 20%. Moreover, for braced frames with horizontal seismic links, the maximum link rotation angle should be 20 mrad for long links or 80 mrad for short links. A link is categorized as long or short depending on its length and its relationship to the $M_{p,link}/V_{p,link}$ ratio where $M_{p,link}$ and $V_{p,link}$ are the plastic moment and shear capacities of the link. For the FUSEIS system the link rotation is given by Eq. 3-6. According to this, a drift applied in the tests equal to 4.8%, would correspond to approximately 100 mrad rotation of beam links and 268 mrad rotation of the pin links.

3.6 Tests on FUSEIS with beam links

3.6.1 FUSEIS beam specimens

As shown in Table 3.1 amongst the six tests on FUSEIS with beam links, two were on FUSEIS with hollow-section beam links and four were on systems with HEA beam links. The hollow beam specimens were of S700MC steel and provided by SSAB-Ruukki, while the open-section beam specimens were of S355J2 and provided by ILVA SPA. Each system consisted of five links and was investigated under constant amplitude and increasing amplitude cyclic loading. The hollow-section specimens were fillet welded on the end plates, while the HEA beams were welded to the end plates by all around full penetration butt welds and additional sealing fillet welds. In order to shift the plastic hinge formation away from the connection zones most of the specimens had reduced beam sections (RBS) at their ends.

Aiming to investigate damage initiation in different materials and profiles, the specimens had different cross sections and reduced lengths (L_{RBS} , Fig. 3.1). Thus, sequential yielding was achieved, facilitating monitoring and model calibration. Table 3.7 summarizes the cross sections and the L_{RBS} of the specimens for each test. The section moduli of the specimens' full and reduced sections are given in Table 3.8 and Table 3.9.

Table 3.7 General properties of FUSEIS beam link specimens (see Fig. 3.1)

Tests	T1, T2		T3, T4, T5, T6	
Steel	S700MC		S355J2	
Specimen	Profile	L_{RBS} (mm)	Profile	L_{RBS} (mm)
S1	SHS80*4	562	HEA100	532
S2	CHS76*3	572	HEA100	462
S3	CHS60*4	572	HEA120	532
S4	SHS60*3	no RBS	HEA120	462
S5	SHS100*4	562	HEA140	532
L (mm)	722		702	

Table 3.8 Hollow-section beams, properties of full and reduced sections (tests T1, T2)

Specimen	Profile	L_{RBS}/L	Full section		Reduced section (RBS)	
			W_{el} (m ³)	W_{pl} (m ³)	W_{el} (m ³)	W_{pl} (m ³)
S1	SHS80*4	0.78	2.776E-05	3.307E-05	1.882E-05	2.334E-05
S2	CHS76*3	0.79	1.280E-05	1.700E-05	8.620E-06	1.220E-05
S3	CHS60*4	0.79	9.340E-06	1.270E-05	6.178E-06	8.992E-06
S4	SHS60*3	-	1.171E-05	1.395E-05	-	-
S5	SHS100*4	0.78	4.527E-05	5.330E-05	2.936E-05	3.640E-05

Table 3.9 HEA links, properties of full and reduced sections (tests T3 to T6)

Specimen	Section	L_{RBS}/L	Full section		Reduced section (RBS)	
			W_{el} (m ³)	W_{pl} (m ³)	$W_{el,RBS}$ (m ³)	$W_{pl,RBS}$ (m ³)
S1	HEA100	0.76	7.276E-05	8.301E-05	4.444E-05	5.200E-05
S2	HEA100	0.66	7.276E-05	8.301E-05	4.444E-05	5.200E-05
S3	HEA120	0.76	1.063E-04	1.195E-04	6.409E-05	7.370E-05
S4	HEA120	0.66	1.063E-04	1.195E-04	6.409E-05	7.370E-05
S5	HEA140	0.76	1.554E-04	1.735E-04	9.424E-05	1.079E-04

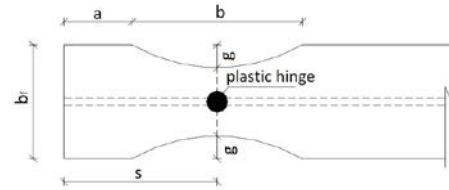
Table 3.10 summarizes EN1998-3 and FEMA 350 recommendations regarding the geometric characteristics of RBS on double-T profiles in terms of distance between the beginning of the RBS and the beam-end (a), the length of the reduced flanges (b) and the depth of the flange cut (g). As can be seen, the suggested values are proportional to the beams flange width (b_f) and the beam's height (h_b). In both cases the depth of the flange cut is determined by a capacity design check

where it is verified that the maximum bending moment developed at hinge formation (M_{cf}) is less than the plastic moment of the beam ($M_{pl,Rd,b}$).

Table 3.10 Eurocode and FEMA recommendations for the design of RBS sections

	Distance from end a (mm)	Reduction length b (mm)	Flange reduction 2g (mm)	Capacity check $M_{cf} / M_{pl,Rd,b}$
EN 1998-3	$0.60*b_f$	$0.75*h_b$	$< 0.50*b_f$	$0.85 \div 1.00$
FEMA 350	$(0.50 \div 0.75)*b_f$	$(0.65 \div 0.85)*h_b$	$< 0.50*b_f$	< 1.00

The definition of the distances a, b and g is given in Figure B.1 of EN 1998-3 as following:



According to EN1998-3, the formation of the intended plastic hinge can be assumed at the center of the RBS. For double-T cross sections, plastic modulus ($W_{pl,RBS}$) and plastic moment ($M_{pl,RBS}$) may be determined from:

$$W_{pl,RBS} = W_{pl} - 2*g*t_f*(h_b - t_f) \text{ and} \quad \text{Eq. 3-8}$$

$$M_{pl,RBS} = W_{pl,RBS} * f_y \quad \text{Eq. 3-9}$$

where t_f is the flange thickness and f_y is the yield stress.

The shear force $V_{pl,RBS}$ in the plastic hinge section is equal to:

$$V_{pl,RBS} = 2*M_{pl,RBS}/L_{RBS} + w*L_{RBS}/2 = 2*M_{pl,RBS}/L_{RBS} \quad \text{Eq. 3-10}$$

where $w=0$ due to the absence of uniform gravity load acting on the FUSEIS beams in the seismic design situation.

The bending moment that develops at the end of the fuse when a plastic hinge forms at the center of the RBS is:

$$M_{cf} = M_{pl,RBS} + V_{pl,RBS}*s \quad \text{Eq. 3-11}$$

where s is the distance of the hinge to the beam-end.

Table 3.11 and Table 3.12 give the geometry of the RBS on each specimen and the capacity check ratios for the FUSEIS with hollow and HEA beams respectively. For the circular hollow-sections (CHS), the external diameter of the profile is used instead of b_f and h_b . For technical reasons, in the case of HEA links not all RBS distances (a , b) complied with the recommendations, although the flange reduction ($2g$) and the capacity check did. In any case, these exceptions did not necessarily affect the failure modes, as later discussed.

Table 3.11 Hollow-section links, geometry of flange reduction and capacity design check

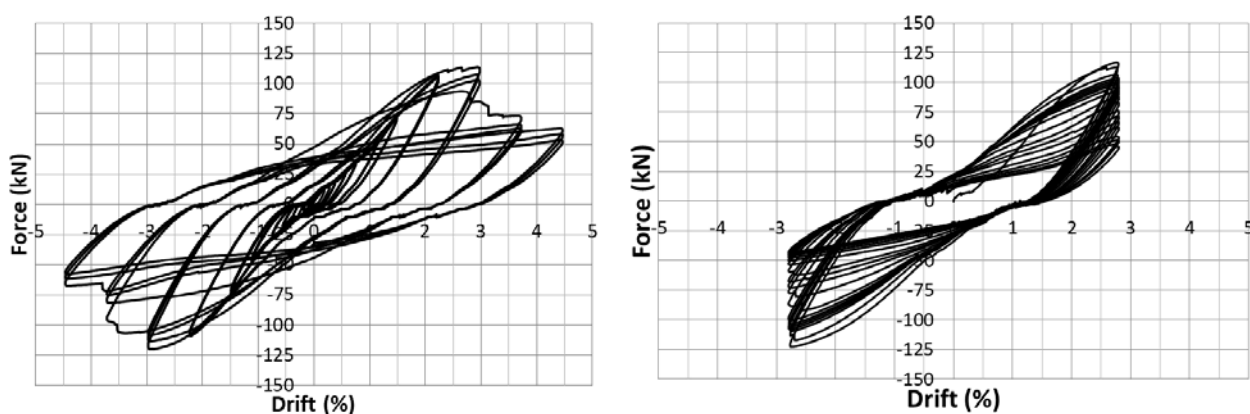
Specimen	Profile	a (mm)	b (mm)	2g (mm)	$M_{cf} / M_{pl,Rd,b}$
S1	SHS80*4	50	60	32	0.92
S2	CHS76*3	50	50	20	0.91
S3	CHS60*4	50	50	16	0.89
S5	SHS100*4	50	60	44	0.89

Table 3.12 HEA links, geometry of flange reduction and capacity design check

Specimen	Profile	a (mm)	b (mm)	2g (mm)	$M_{cf} / M_{pl,Rd,b}$
S1	HEA100	50	70	44	0.83
S2	HEA100	85	70	44	0.95
S3	HEA120	50	70	54	0.81
S4	HEA120	85	70	54	0.94
S5	HEA140	50	70	62	0.82

3.6.2 Cyclic response of FUSEIS with hollow-section beams of S700MC

Two cyclic tests were conducted on FUSEIS with hollow beams of S700MC: one with increasing amplitude (I.A.) and one with constant amplitude (C.A.) (Table 3.6). Both tests were loaded until the system's strength dropped to roughly 50% of its maximum value. Fig. 3.14 presents the response curves for the tests, referring to column deformations. Upon completion of both tests, cracks were extensive in most specimens.

**Fig. 3.14 Cyclic response for hollow-section tests T1 and T2 (data obtained from columns)**

As mentioned, the displacements applied via the actuator were not exclusively sustained by the FUSEIS links. For example, in the first cycle of T2 (Fig. 3.14) there are two softening segments (at approximately 0.2% and 0.5% drift) where the system deforms at practically no force. However, the slope of the unloading segments for the loading cycles prior to peak resistance remains constant and is the same in both tests. These “collateral” displacements are further discussed in paragraph 3.6.4. The differential displacements of the links were monitored via LVDTs and were practically

the same for the five specimens. Fig. 3.15 illustrates the response curves for tests T1 and T2 with respect to the measured link deformations. In the graph for T2 the deformations appear to increase slightly, although constant amplitude loading was applied. This could be related to crack propagation, bolt/end-plate slippage or dislocation of the monitoring equipment.

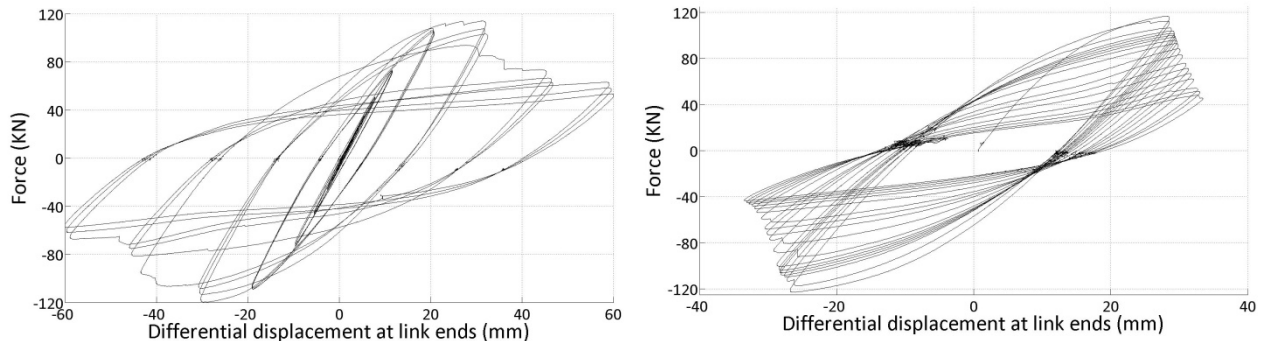


Fig. 3.15 Response curves based on links deformations tests T1 and T2

In both tests, plastic deformations took place in the fuses devices only, where yielding of most specimens started at the RBS areas eventually leading to ductile fractures. Load degradation occurred due to crack propagation and limited local buckling at the RBS areas, with the exception of specimen S4 (SHS 60) which had no RBS (Fig. 3.16, Fig. 3.17). However, one specimen (S1, with SHS 80 cross-section) failed differently in the two tests: in T1 cracks occurred in the RBS while in T2 in the heat affected zones (HAZ). This could be related with the fact that welds are more prone to fatigue failure.

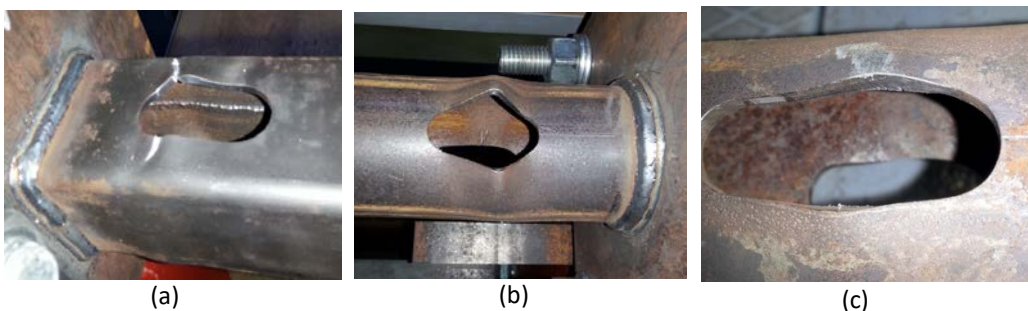


Fig. 3.16 Failure in test T1 on specimens: (a) S1 and (b) S2 and (c) S3

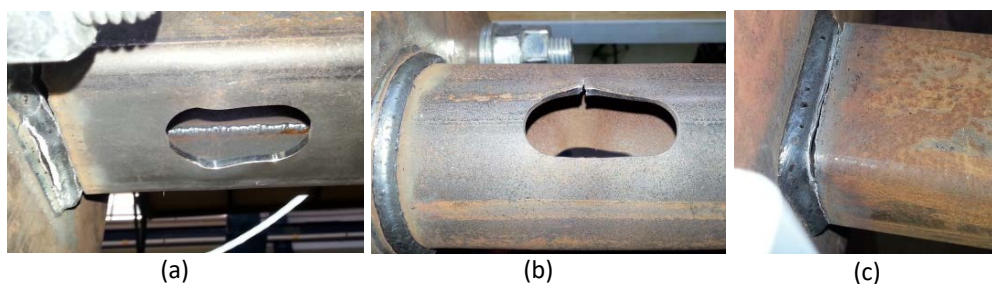


Fig. 3.17 Failure in test T2 on specimens: (a) S1 and (b) S2 and (c) S4

Fig. 3.18 shows for the C.A. test (T2) the increase of temperature in a specimen from the 3rd to the 10th loading cycle indicating the development of plastic deformations in the RBS.

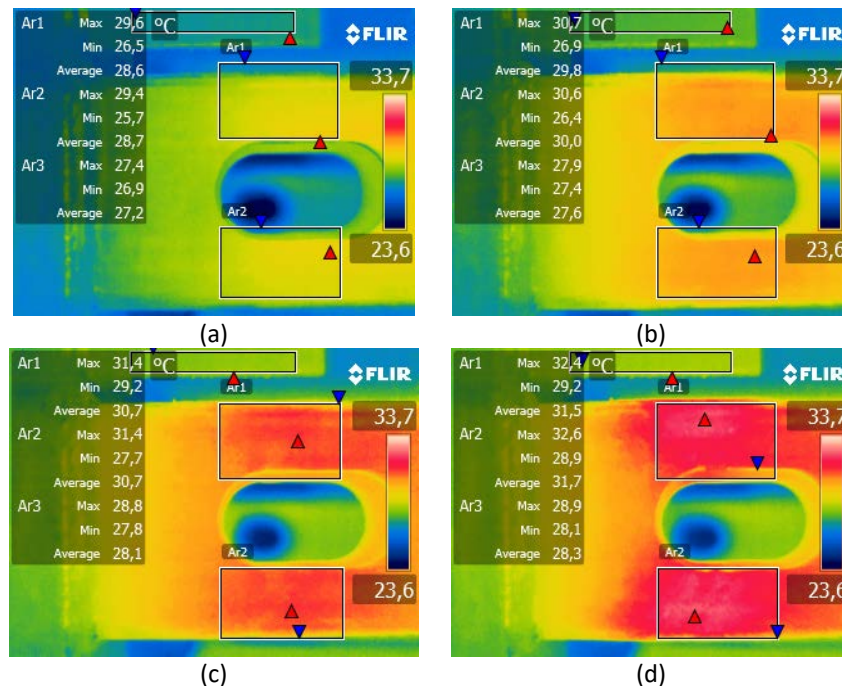


Fig. 3.18 Thermal camera snapshots of link S1 in test T2 for cycles (a) 3, (b) 5, (c) 9 and (d) 10

3.6.3 Cyclic response of FUSEIS with HEA beams of S355J2

The behavior of the system with HEA beams of S355J2 steel was more ductile compared to the system with HSS links and exhibited hardening at large deformations. In total, four tests were performed (Table 3.6): T3 with loading cycles of increasing amplitude (I.A.), T4 and T5 with cycles of constant amplitude (C.A.) and monotonic test T6. Tests T3 and T6 were completed without any signs of crack formation, for technical reasons. In all tests, load degradation process was slow.

In Fig. 3.19 the response curves for each test are presented in terms of force vs. drift as measured on the columns. Tests T4 and T5, where ductile fatigue cracks occurred, were completed when the system's strength was reduced by approximately 20%. In T3, load degradation (about 6% after 15 loading cycles at maximum amplitude) was attributed to limited local buckling in some link specimens. In most cases, cracks were formed in the RBS flanges and propagated in the web and towards the welds (Fig. 3.22, Fig. 3.23). Significant torsional deformations of the links were also observed. The fact that in some beams not all RBS dimensions complied with the Codes, did not unequivocally affect their failure. For example, some specimens exhibited different types of failures (in the RBS or in the heat affected zones) at different ends and in different tests. In any case, the links whose RBS complied with provisions, systematically failed in the RBS regions.

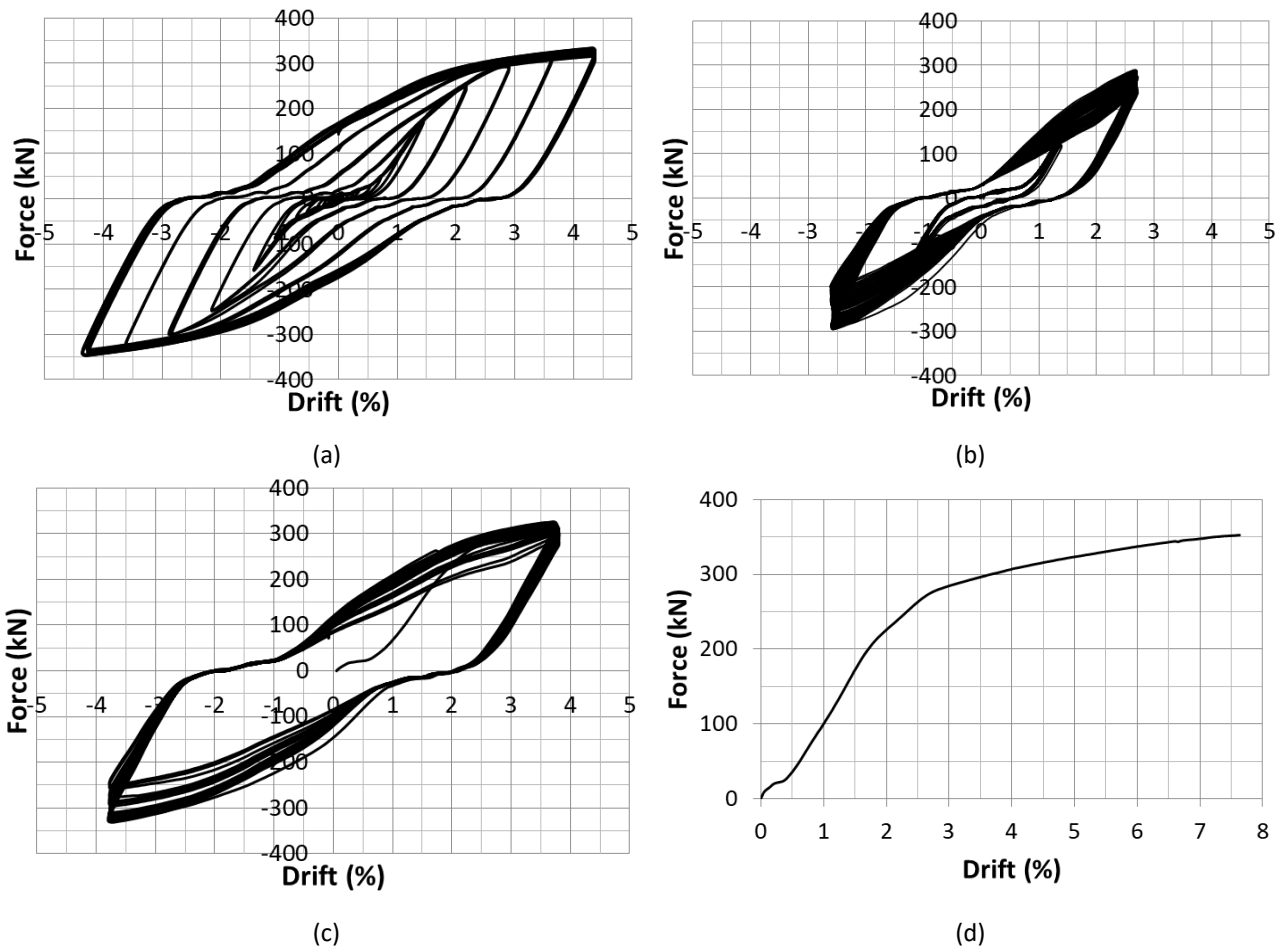


Fig. 3.19 Cyclic response for tests on FUSEIS with HEA beam links (a)T3, (b) T4, (c) T5 and (d) T6 (based on columns' data)

Fig. 3.20 shows the measured differential displacements of the links in the I.A. test. For unclear reason, the measurements for specimen S5 were rather smaller compared to the rest (which were practically the same).

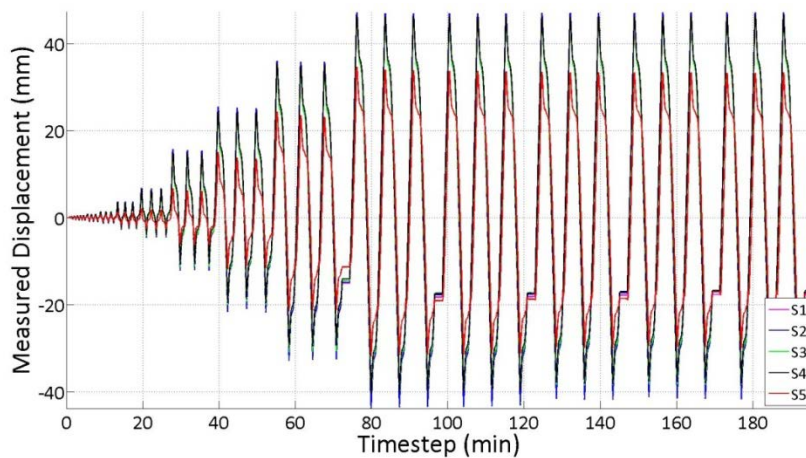


Fig. 3.20 Measured displacements of FUSEIS links in T3

Fig. 3.21 shows the response curves based on the links' deformations. The graphs illustrate the process of energy dissipation via plastic deformation of the links. For example, it is shown that in

the first part of test T4 (with small amplitude cycles, Table 3.6) no energy was absorbed by the beams. Limited slippage can be observed in the constant amplitude tests.

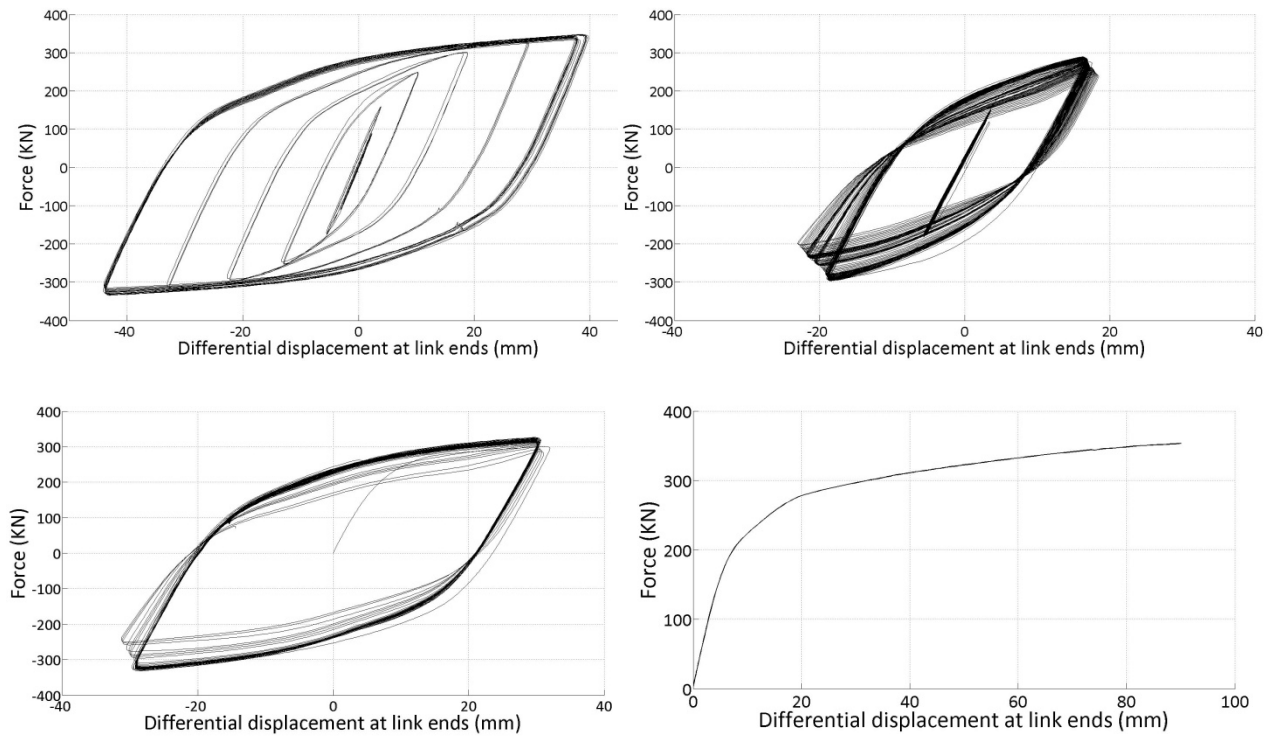


Fig. 3.21 Response of FUSEIS beam links in tests T3 to T6, based on average link deformations (26)



Fig. 3.22 Test T4, crack propagation on specimens: (a) S3, (b) S4, (c) S1



Fig. 3.23 Test T5, crack propagation on specimens (a) S3, (b) S4 (c) crack initiation on S1

Fig. 3.24 shows the increase of temperature in a C.A. test (T5) in specimen S4 from the 14th to the 40th loading cycle indicating the development of plastic deformations in the RBS.

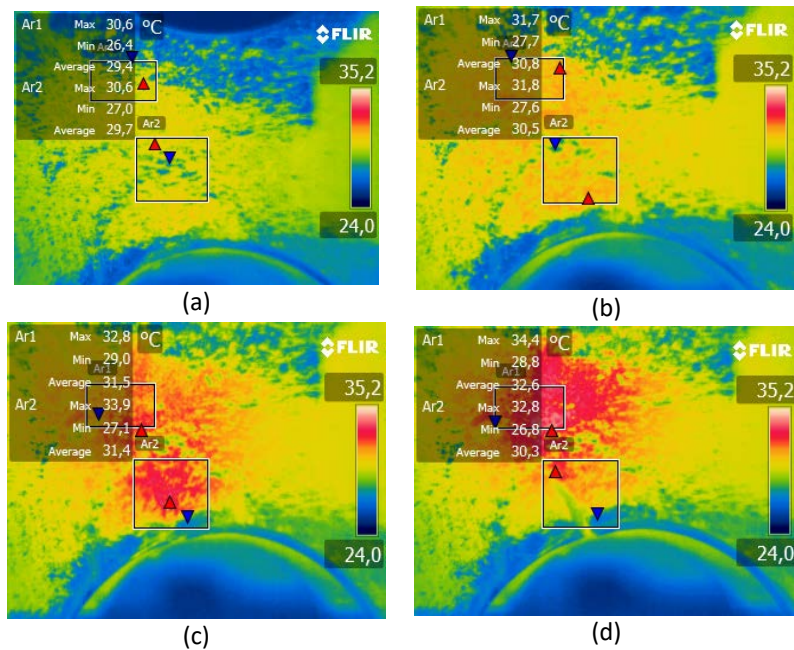


Fig. 3.24 Thermal camera snapshots during T5 for loading cycles (a) 14, (b) 24, (c) 38 and (d) 40

3.6.4 Correction of experimental data

As previously mentioned, the overall drift and the local link rotations were recorded independently, despite the fact that there exists a certain kinematic relation between them, expressed by Eq. 3-7. However, when checking this relation as shown in Fig. 3.25, it was found that according to the actuator's data, the links' differential displacements were smaller than expected. This is due to the fact that the actual overall drift, is a result not only of the link deformations but also of additional displacements and deformations not appearing in Eq. 3-7. Such displacements may be related to hole allowances in bolts and pins, hole ovalizations due to bearing, bolts slippage, inelastic deformations of the supporting pins or elastic deformations in the test setup etc. These "collateral" displacements resulted in the distortion of the system's initial elastic stiffness, as softening branches were formed at the beginning of the loading cycles. Nevertheless, the slope of the unloading segments for the cycles prior to load degradation remained constant in all tests within the same group and was used as a reference for the system's initial stiffness. The most important factors influencing the results are shortly discussed.

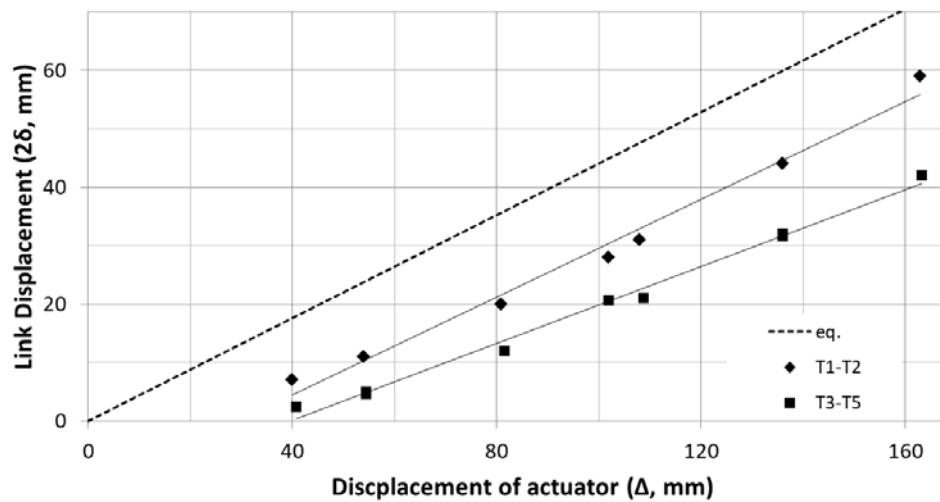


Fig. 3.25 Correlation between link deformation (2δ) and system's horizontal displacement (Δ), according to Eq. 3-7 and tests

- **Supports of FUSEIS columns and actuator**

The assembly for the restriction of the actuator's movement in the horizontal axis, shown in Fig. 3.2 and Fig. 3.5, involved numerous prestressed bolts. However in some tests, relative horizontal displacements of the involved parts were observed and tensioning of the bolts was relaxed. In addition, the pinned supports of the FUSEIS columns were realized with 2 mm tolerances. In case of combined adverse slippage (in opposite directions) of both pins, a differential vertical displacement equal to 4 mm would be imposed on the links' ends, translating to an overall drift equal to 0.27% according to Eq. 3-7. The effect of these factors was partly monitored via LVDTs and inclinometers placed on the columns. In general, the data obtained from the different instruments were in agreement with each other and verified that the actual horizontal displacements of the columns were smaller than those applied by the actuator (Fig. 3.26). The size of this divergence varied and reached values translating to 0.4% drift in the most adverse case.

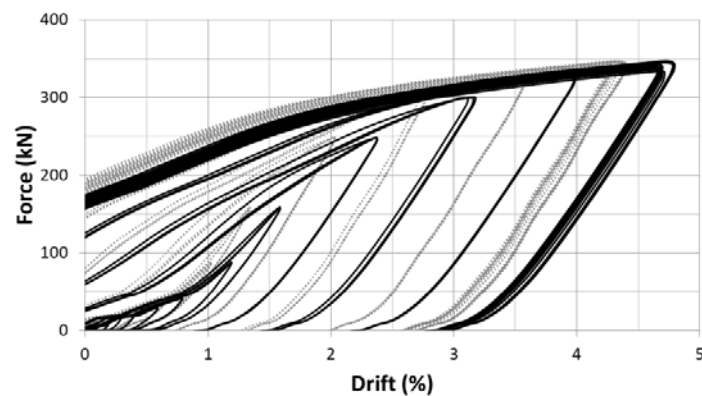


Fig. 3.26 Comparison between data obtained from the actuator (black) and the columns (grey) for test T3

- **Bolted connections of FUSEIS beams and end-plate slippage**

Fig. 3.27 gives a generic graph of the behavior of a bolted connection. Resemblance between this response and the aforementioned softening parts in the first cycles of the experimental curves can be easily observed. The deformation process of a bolted connection is the resultant of the following: (i) the shank's deformation due to bending and shear, (ii) the slippage of the bolt due to clearances and (iii) the deformations of the holes and/or the connected members. If the bolts are preloaded, as in this case, the slippage occurs when the applied force exceeds the static friction force (design slip resistance).

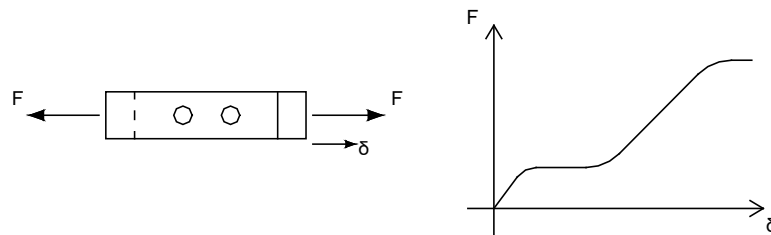


Fig. 3.27 Representation of force – deformation relationship of a bolted connection (Vayas, 2003)

As mentioned, an unforeseen gradual increase in the links' displacements was monitored in the constant amplitude tests (Fig. 3.15 and Fig. 3.21), attributed to slippage of the end-plates. Fig. 3.28 shows the data obtained from the LVDTs monitoring the end-plates of specimen S3 in tests T2 and T3. As can be seen, the relative displacement between the plates and the adjacent column flanges varied and reached values up to 3mm. In most cases the measured displacements increased with the number of cycles, although it is possible that after a certain point the support of the LVDTs was also sliding. The phenomenon was negligible in the monotonic test (T6). Regarding tolerances, the bolts connecting all FUSEIS specimens to the columns were M24 and their holes were designed with 2 mm tolerance. However, in some cases the delivered plates were found with larger clearances.

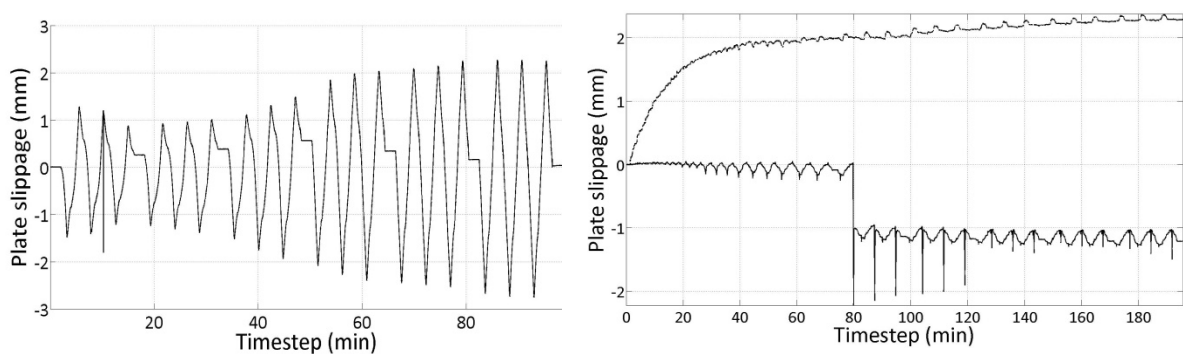


Fig. 3.28 Monitoring of bolt/end-plate slippage in tests T2 (one plate) and T3 (both end-plates)

To conclude, the data obtained from the links can be used for the correction of the experimental data. To do so, a conversion factor as that given by Eq. 3-7 is necessary, based on the system's kinematics. However, utilization of this theoretical factor occasionally resulted in significantly smaller overall drifts, larger initial stiffness and less absorbed energy. To balance this, an additional modification factor was applied, based on the assumption that the actual energy absorbed by the system is better approximated by the data obtained from the columns. Hence, this factor represented a ratio between the "actual" and the "reduced" energies for each group of similar loading cycles. Fig. 3.29 gives the adapted response curves of all tests on FUSEIS with beams, based on the above. To avoid confusion, the drifts presented in these graphs are referred as effective drifts (Table 3.6).

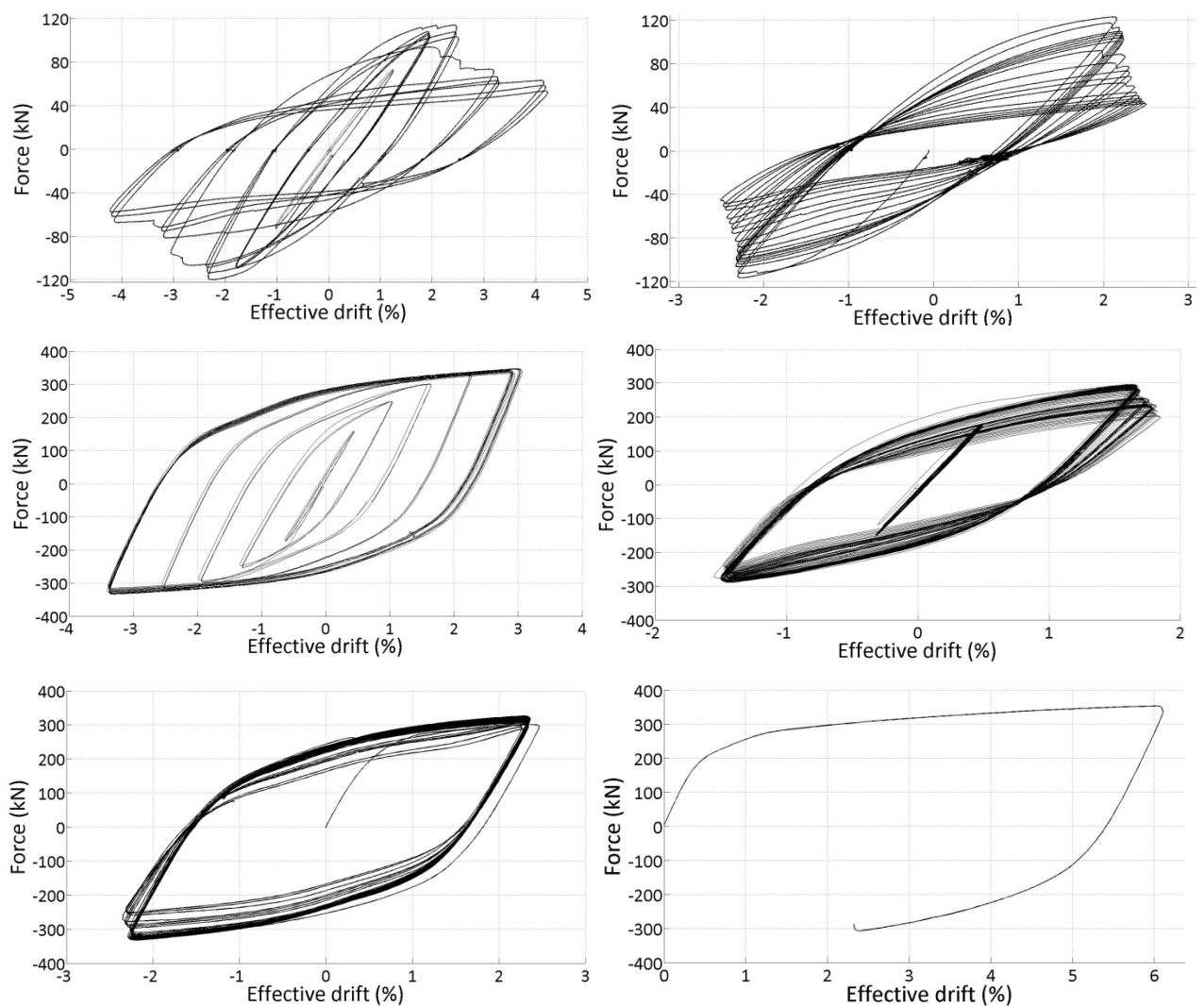


Fig. 3.29 Corrected response curves of FUSEIS systems in tests T1 to T6 (effective drifts)

3.6.5 Peak resistance and stiffness degradation

To assess the evolution of the system's lateral resistance and stiffness, the peak resistance and the peak-to-peak stiffness (Fig. 3.30) were calculated at the first loading cycle of each displacement in the I.A. tests. To account for occasional asymmetries in the two loading directions, the average stiffness (K_{avg}) and peak resistance were considered. Given the different capacities of the tested systems, the forces were normalized by the maximum obtained force during each test (Fig. 3.31) while the stiffness values were normalized by their initial elastic values (Fig. 3.32). For clarity reasons, the first elastic cycles of the tests were omitted. The horizontal axes refer to the effective drifts (Fig. 3.29).

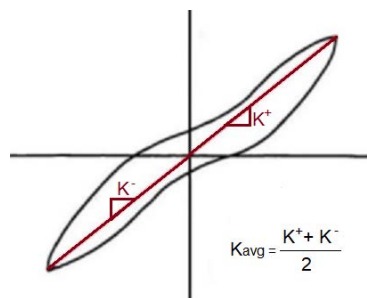


Fig. 3.30 Calculation of peak-to-peak stiffness for the two loading directions

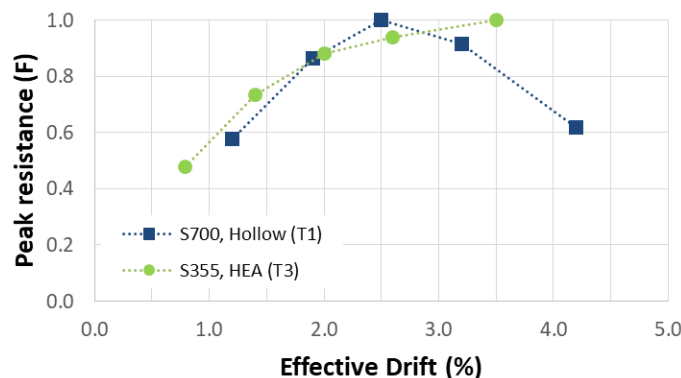


Fig. 3.31 Average peak resistance (normalized) in increasing amplitude cyclic tests (T1, T3)

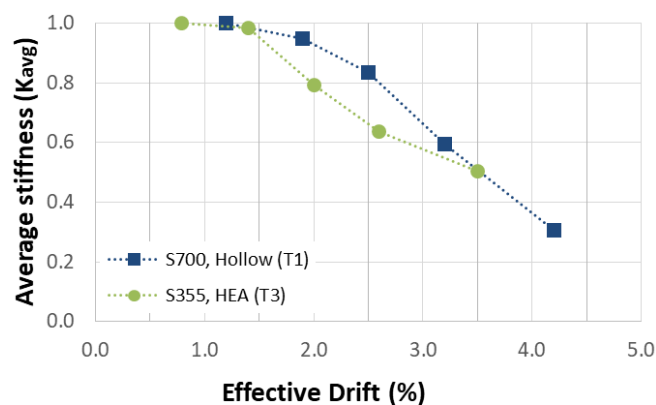


Fig. 3.32 Peak-to-peak (normalized) stiffness degradation in increasing amplitude cyclic tests (T1, T3)

The graphs show that in both cases the systems yielded at approximately 1% effective drift, while their resistance kept increasing until relatively high drifts (around 3%). More specifically, the FUSEIS with S700MC hollow-section beams yielded at 1.2% effective drift and reached its peak resistance at approximately 2.5%. The more ductile system with S355J2 HEA beams yielded at approximately 0.8% effective drift and kept its lateral resistance increasing until 3.5% drift, where its stiffness was reduced to almost 50%.

Assuming the two failure criteria of (a) 20% degradation in stiffness and (b) 20% degradation in resistance, it can be seen that both systems meet the stricter criterion (a) for effective drifts larger than 2.0%. As reference, it is noted that this is the limit for braced steel frames within the Collapse Prevention performance level according to FEMA 356. In addition, the FUSEIS with S700MC beams meets criterion (b) for effective drifts larger than 3.5% while the system with S355J2 links does not. The above estimations are based on cyclic tests, and thus the specimens were also subjected to fatigue (affecting the process of crack propagation).

Table 3.13 gives an overview of observations regarding crack initiation on the links. The effective drift is denoted as ϕ and N refers to the number of loading cycles. The constant amplitude tests are indicated with "C.A.". In case of uncertainty on the specific cycle of crack initiation, an inequality symbol (\leq) is used.

Table 3.13 Observations on crack initiation during tests

Test	Steel	Max. Effective drift (ϕ_{\max})	Cycles N at ϕ_{\max}	Crack initiation: critical drift ϕ_{cr} or cycles N_{cr} (in Si link)
T1	S700MC	$\pm 4.2\%$	3	$\phi_{cr} = 2.5\%$ (S4, S2, S1), $\phi_{cr} = 3.2\%$ (S5)
T2		$\pm 2.3\%$ (C.A.)	18	$N_{cr} = 6$ (S4), $N_{cr} = 9$ (S2), $N_{cr} = 10$ (S5), $N_{cr} = 15$ (S1)
T3	S355J2	$\pm 3.5\%$	15	No cracks
T4		$\pm 1.7\%$ (C.A.)	111	$N_{cr} = 60$ (S4), $N_{cr} = 68$ (S2), $N_{cr} = 78$ (S3), $N_{cr} = 105$ (S1)
T5		$\pm 2.5\%$ (C.A.)	45	$N_{cr} \leq 34$ (S3), $N_{cr} = 38$ (S4), $N_{cr} = 43$ (S1), $N_{cr} = 45$ (S2)
T6		6.2%	-	No cracks

3.6.6 Overstrength and ductility of tested system

Table 3.14 summarizes the over-strength (Ω), ductility (μ) and behavior factors ($q = \mu \cdot \Omega$) of each system on the basis of experimental results. Regarding overstrength, it was defined as:

$$\Omega = F_{\max} / F_1 \quad \text{Eq. 3-12}$$

where F_{\max} is the peak resistance of each system (average for the two loading directions) and F_1 is the base shear at first yield of the experimental curves.

For the estimation of systems' ductility, the experimental response curves were idealized as bilinear, as shown in Fig. 3.33, according to FEMA 356 recommendations. The line segments on the idealized curves were defined using an iterative procedure that balanced the areas above and below the curve (equal energy concept). Ductility was defined as:

$$\mu = \delta_u / \delta_y \quad \text{Eq. 3-13}$$

where δ_u refers to a displacement at an ultimate limit state and δ_y refers to the yield displacement of the bilinear graph.

Regarding δ_u , it is normally specified via pushover procedures and is defined as the displacement at which 20% load degradation occurs (FEMA 695) or when a plastic mechanism forms (EN 1998-1). However, the 20% load degradation criterion was not applicable in the case of FUSEIS with HEA beams. In order to use a uniform criterion, δ_u was conservatively assumed to represent the displacement at peak resistance of each increasing amplitude cyclic test. Table 3.14 gives the ductility and overstrength of the systems based on cyclic tests, Eq. 3-12 and Eq. 3-13. As can be seen, the tested FUSEIS with S355J2 links was twice as ductile compared to the system with S700MC beams. Comparison is made without considering the different system capacities or the beam section type.

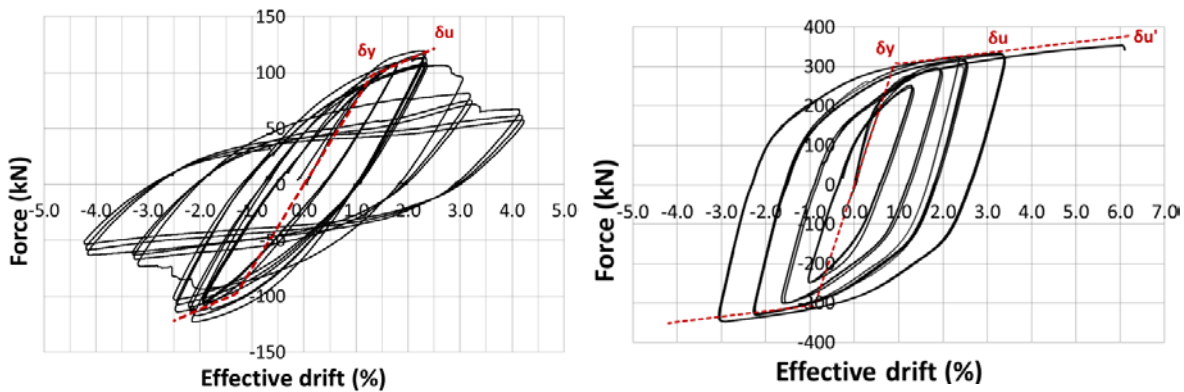


Fig. 3.33 Bilinear fit (red) of experimental curves (black) and displacements δ_y , δ_u used for ductility calculation

Table 3.14 Overstrength and ductility based on cyclic tests

FUSEIS links	Test	$\Omega = F_{\max}/F_1$	$\mu = \delta_u/\delta_y$	$q = \mu \cdot \Omega$
Hollow-section beams	T1, T2	1.50	1.92	2.9
HEA beams (S355J2)	T3 ~ T6	1.60	3.89	6.2

Despite the conservative approach for δ_u , the tested system with the hollow beam links of S700MC exhibited a behavior factor around 3. In case the 20% load degradation criterion had been used, its

ductility would increase and the behavior factor would be close to 4. For the FUSEIS with HEA beams, if the data from the monotonic test were taken into account (Fig. 3.33, δ_U), the system's ductility would significantly increase.

3.6.7 Energy dissipation

The amount of energy dissipated per cycle was calculated and is presented in the following bar charts based on the data obtained by the actuator. This is done for comparison reasons (as some tests had the same loading protocols) and has the drawback of taking into account the total absorbed energy during each test, including the amounts dissipated in the test setup.

Fig. 3.34 illustrates energy dissipation in FUSEIS with S700MC hollow beams. In test T1 the links exhibited elastic response for the first 18 loading cycles (Fig. 3.15) during which almost 6% of the total dissipated energy was absorbed by the test setup. Load degradation initiated after the 22nd cycle, while the extensive crack propagation between cycles 25-27 is demonstrated. In test T2 which had constant amplitude, energy dissipation per cycle was practically constant until the 8th loading cycle where load degradation initiated.

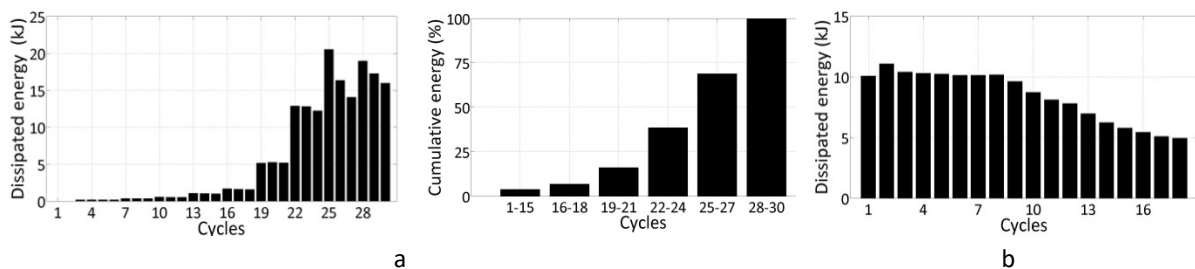


Fig. 3.34 Energy dissipation in (a) T1 (increasing amplitude) and (b) T2 (constant amplitude)

Regarding the FUSEIS with S355J2 HEA beams, in test T3 (Fig. 3.35) the loading cycles were divided in groups of three and their amplitude was increasing until the 28th cycle. Inelastic behavior of the links initiated at the 19th loading cycle (Fig. 3.21), prior to which less than 3% of the total energy was dissipated via the test setup (Fig. 3.35b). Load degradation started after the 33rd cycle and proceeded slowly.

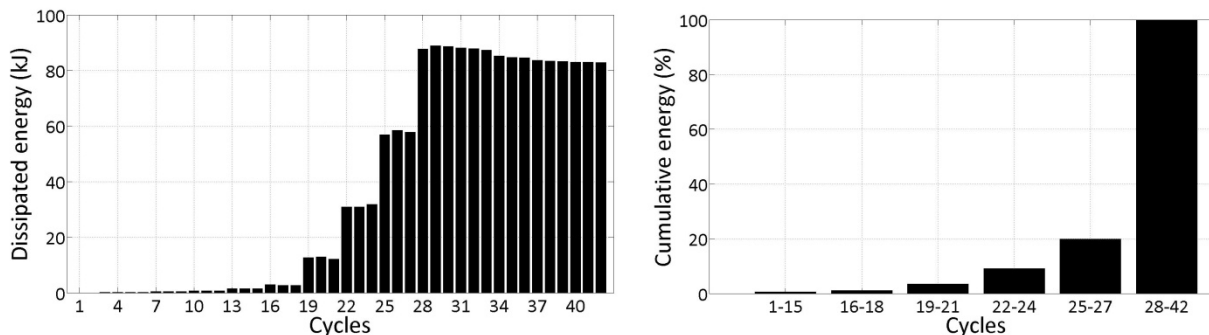


Fig. 3.35 Energy dissipation in T3 (increasing amplitude) (a) per cycle (kJ) and (b) cumulative (%)

Fig. 3.36 illustrates energy dissipation of the system with S355J2 beams during the constant amplitude tests. The graph for test T4 refers to the second part of the test involving larger loading cycles. In both tests energy dissipation per cycle was constant for many loading cycles.

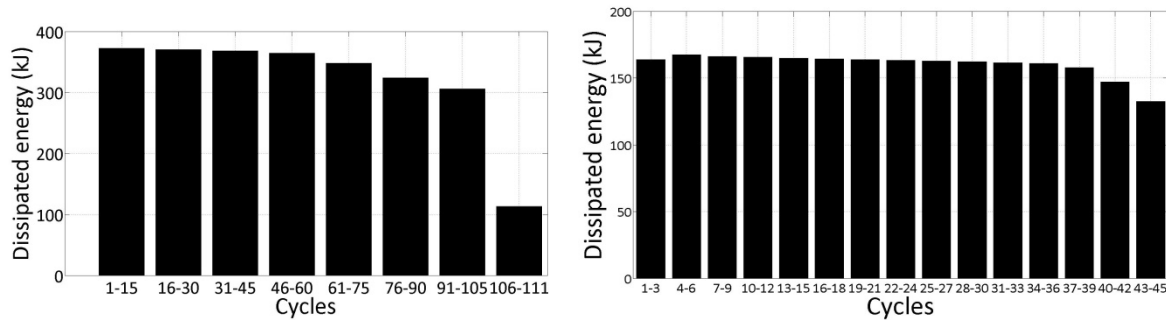


Fig. 3.36 Energy dissipation in FUSEIS with S355J2 beams, C.A. tests (a) T4 (b) T5

To explore the capacity of the systems with different beam links to absorb energy, the data obtained for tests T1 and T3 were used, as they had the same I.A. loading protocol. Considering the cycles up to crack formation (in T1), the absorbed energies are 65 kJ for T1 and 147 kJ for T3. Thus, the FUSEIS with S355J2 HEA beams dissipated 2.3 times more energy compared to the system with S700MC beams. However, the systems had significant differences in stiffness and material strength. More specifically, the average moment of inertia of the HEA links was about 6.5 times larger compared to the hollow-section links, while the respective ratio of the average plastic moduli (W_{pl}) was 4.5. On the contrary, the ratio of the materials' f_y was 0.59 while the ratio of f_u was 0.72 (Table 3.4). To conclude, despite being more ductile, the system with S355J2 HEA links did not exhibit a better capacity to dissipate energy compared to the system with S700MC hollow beams, up to the point of crack initiation in the latter.

The energy based criterion suggested by Calado and Castiglioni (1996) was examined for the I.A. tests. To do so, the absorbed energy ratios (η_i) within each group of cycles of equal displacement (i) were calculated according to the methodology described in ECCS guidelines (Fig. 3.37). For each test, a theoretical perfectly elastoplastic bilinear response was assumed and the absorbed energy ratio η_i was given by:

$$\eta_i = A_i / E_{thi} \quad \text{Eq. 3-14}$$

where A_i is the real absorbed energy and E_{thi} is theoretical one.

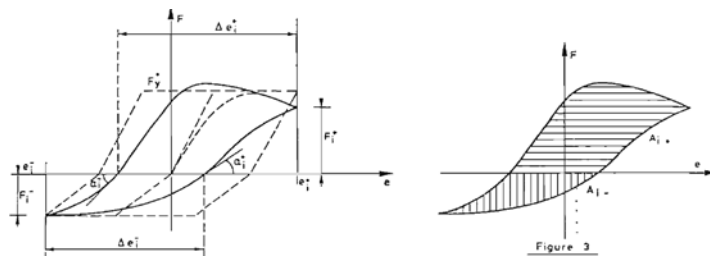


Fig. 3.37 Calculation of absorbed energy ratio according to ECCS (1986)

The energy ratios η_i were then normalized, considering as reference (η_{ref}) the first plastic loading cycle of each test. In both tests, the cycles in the plastic range had four different amplitudes and are named respectively (η_1 to η_4). According to Calado and Castiglioni (1996), failure can be assumed if $\eta_i / \eta_{ref} \leq \alpha$, where α ranges between 0.50 and 0.75. Table 3.15 gives the results of this investigation. For the FUSEIS with S700MC beams the failure criterion is met. In the cycles corresponding to η_2 the system reached its peak resistance and in the following cycles the normalized ratio η_i / η_{ref} gradually dropped. In the FUSEIS with S355J2 beams the failure criterion is not met, while the normalized ratio η_i / η_{ref} is increasing. Indeed, no cracks had occurred by the end of test T3.

Table 3.15 Energy absorbed ratios in the increasing amplitude tests (T1, T3)

FUSEIS links	η_1 (η_{ref})	η_2	η_3	η_4	η_2 / η_{ref}	η_3 / η_{ref}	η_4 / η_{ref}
Hollow profiles, S700MC (T1)	0.85	0.68	0.51	0.36	0.80	0.60	0.42
HEA, S355J2 (T3)	0.82	0.66	0.69	0.74	0.81	0.84	0.90

3.6.8 FUSEIS beams component tests

A series of tests on single FUSEIS components was conducted in the Laboratory of Aachen University (RWTH) to investigate how different (geometric and material) parameters influence damage. Fig. 3.38 shows the test setup. The specimens were mounted in a system consisting of two strong columns connected to each other via hinged members at both ends. The test frame's lower girder/column was bolted on the laboratory's strong floor while the hydraulic actuator was applying horizontal displacements via a hinged beam along the central axis of the upper column. The actuator's base was connected to a stiff retaining wall.

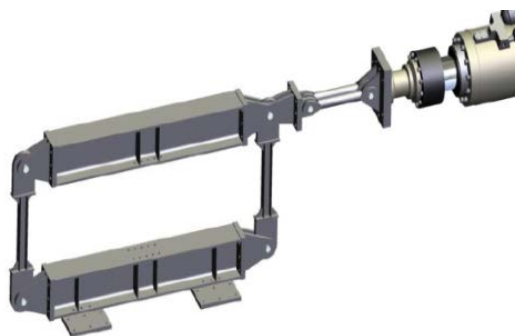


Fig. 3.38 Test setup

The various link specimens were delivered with their endplates and were bolted on to the strong columns. The clearance between the upper and the lower column of the test frame was 950mm. To

accommodate the use of links with different lengths additional built-in parts or thick plates were used as shown in Fig. 3.39.



Fig. 3.39 Mounting of FUSEIS components with different lengths

Table 3.16 gives an overview of the beam component tests performed: Six tests were performed on HEA140 beams of S355J2 and five on SHS80x4 of S700MC. The links were subjected to cyclic loading of either constant (C.A.) or increasing amplitude (I.A.) based on a modification of ECCS recommendations involving smaller steps. Estimation of the yield displacement for the loading protocols was based on numerical simulations and nominal material properties. The links were designed with RBS to shift plastic hinge formation away from the heat affected zones (HAZ). The tests were completed upon crack initiation. Fig. 3.40 and Fig. 3.41 give the results of one test on FUSEIS HEA beam link (S355J2) and one test on FUSEIS SHS beam link (S700MC).

Table 3.16 Test matrix for beam component tests

Test	Link	Steel	Length (mm)	Loading protocol	Max. amplitude (mm)	RBS dimensions
CT1	HEA140	S355J2	500	I.A.	44.8	
CT2			700	I.A.	46.7	
CT3			700	I.A.	49.0	
CT4			700	C.A.	49.0	
CT5			700	C.A.	40.1	
CT6			900	I.A.	59.1	
CT7	SHS80x4	S700MC	500	I.A.	23.4	
CT8			700	I.A.	39.1	
CT9			700	C.A.	29.3	
CT10			700	C.A.	24.4	
CT11			900	I.A.	58.8	

Note: I.A. stands for increasing amplitude and C.A. stands for constant amplitude

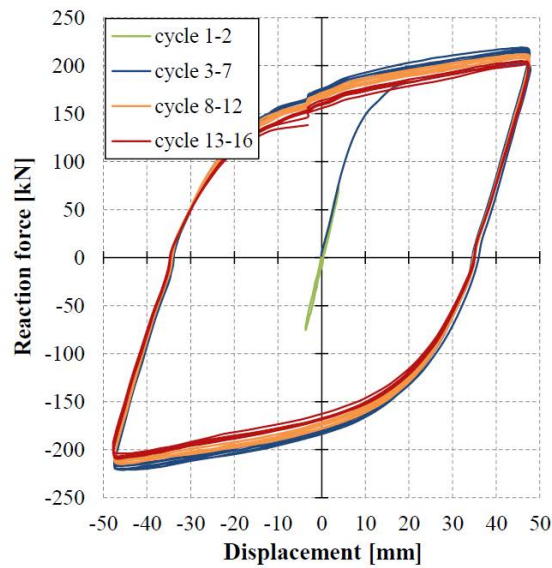


Fig. 3.40 Test CT4 (HEA fuse): response curve and crack initiation (Feldmann et al. 2017)

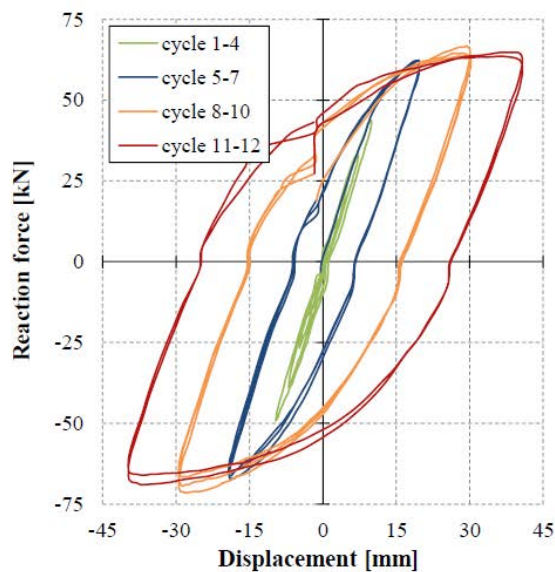


Fig. 3.41 Test CT8 (SHS fuse): response curve and crack initiation (Feldmann et al. 2017)

Table 3.17 summarizes the results of the component tests in terms of links' yield rotation (θ_y) and rotation at crack initiation (θ_{cr}). For the I.A. tests, the ratio θ_{cr}/θ_y is also given. The average ratio θ_{cr}/θ_y was 7.3 for the S355J2 HEA links while 3.7 for the S700MC SHS fuses. Furthermore, there seems to be an effect of the links' length on their critical rotation. However, no definite conclusion can be drawn as for the HEA specimens increased length caused decreased capacity, while this was not the case in the hollow-section fuses.

Table 3.17 Overview of beam component tests results

Test	Link	Length (mm)	Loading	θ_y (mrad)	θ_{cr} (mrad)	θ_{cr}/θ_y
CT1		500	I.A.	10	89.6	9.0
CT2		700	I.A.	10	66.8	6.7
CT3	HEA140	700	I.A.	10	69.9	7.0
CT4	S355J2	700	C.A.	10	69.9	-
CT5		700	C.A.	10	57.2	-
CT6		900	I.A.	10	65.7	6.6
CT7		500	I.A.	12	46.8	3.9
CT8	SHS80x4	700	I.A.	15.7	55.8	3.6
CT9	S700MC	700	C.A.	15.7	41.9	-
CT10		700	C.A.	15.7	34.9	-
CT11		900	I.A.	16.3	65.3	4.0

Note: I.A. and C.A. stand for increasing and constant amplitude respectively

3.6.9 Comparison with previous research on FUSEIS beams with S235

As mentioned, experimental investigations on FUSEIS with various types of links have been carried out in the past using S235 for the dissipative links (Vayas et al. (2013); Dougka et al. (2014)). In total six cyclic tests with increasing amplitudes were conducted on FUSEIS with either hollow or IPE beams. To achieve sequential yielding of the links, they had either different lengths (L) or profiles. Table 3.18 gives the test matrix for FUSEIS systems with S235 beams.

Table 3.18 Test matrix for FUSEIS with S235 beams (Vayas et al. 2013, Dougka et al. 2014)

TEST	Links	L (mm)	Profile
A1	IPE	600	IPE 120 to 180
A2	SHS	600	SHS 80x6 to 140x8
A3	CHS	600	CHS 88.9x6 to 168.3x6
M1	IPE	500 to 700	IPE 160
M2	SHS	500 to 700	SHS 120x8
M3	CHS	500 to 700	CHS 139.7x6

To obtain a common reference for the two experimental campaigns, the response curves in terms of effective drifts were considered (retrieved from Dougka 2016) and the simplest form of bilinear idealization was applied up to the system's peak resistance (Fig. 3.42). Ductility (μ) was given by Eq. 3-13 where δ_u , δ_y refer to the bilinear curve and overstrength (Ω) was given by Eq. 3-12, where F_{max}

is the maximum peak resistance of the system and F_1 was first significant yield. Table 3.19 summarizes the obtained factors for μ , Ω and q for each test.

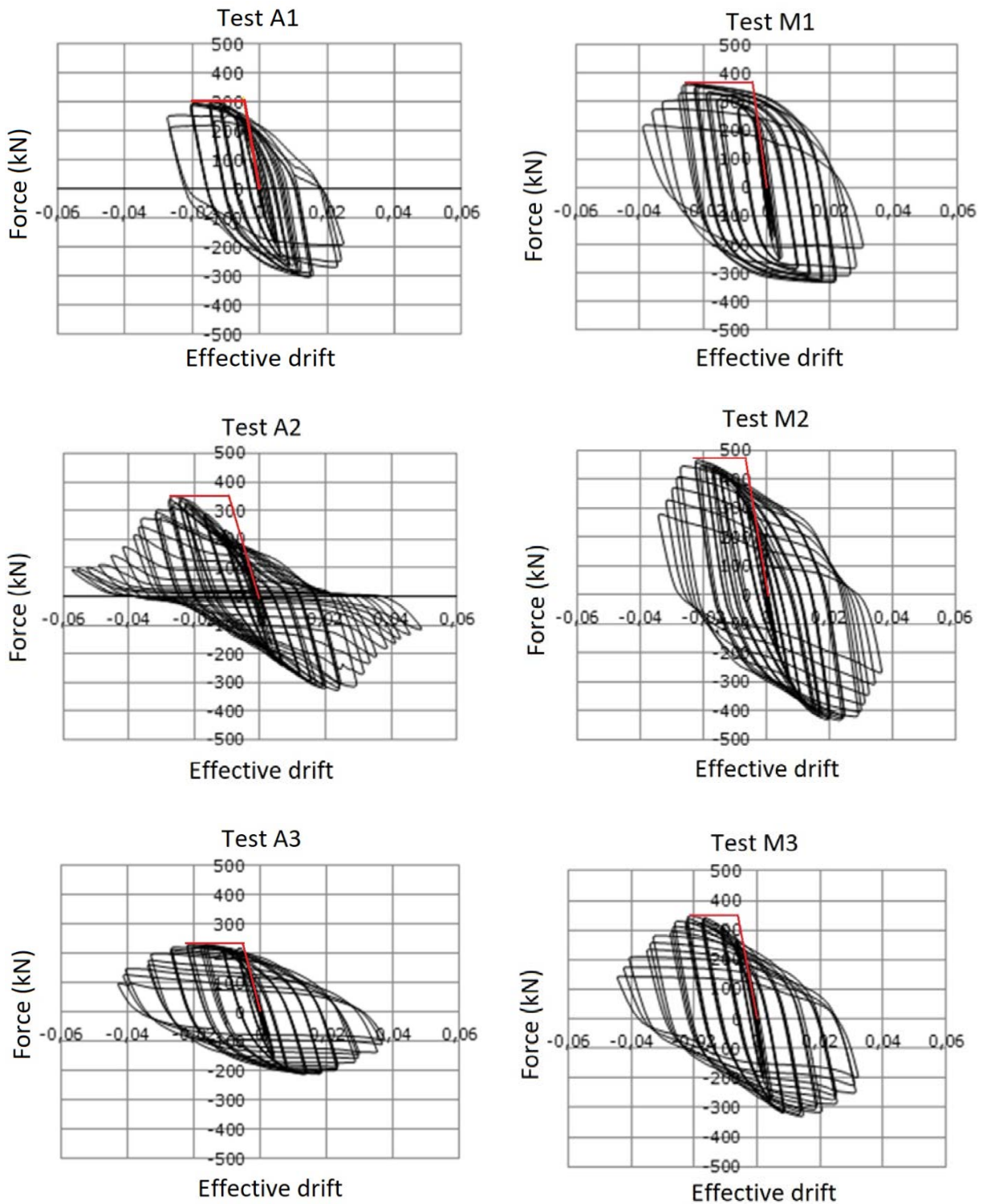


Fig. 3.42 Cyclic response of FUSEIS with S235 beams and bilinear idealization for comparison reasons

Table 3.19 Ductility, overstrength and behavior factor from tests on FUSEIS with S235 beams (bilinear approach, see Fig. 3.42)

TEST	links	Fmax (kN)	$\mu = \delta_u/\delta_y$	$\Omega = F_{max}/F_1$	$q = \mu*\Omega$
A1	IPE	303.6	4.76	1.20	5.71
A2	SHS	349.9	2.89	1.18	3.41
A3	CHS	232.4	4.40	1.72	7.57
M1	IPE	367.0	5.00	1.11	5.55
M2	SHS	466.3	3.66	1.09	3.99
M3	CHS	349.4	3.32	1.54	5.12

In Table 3.20 the average values for each type of beam profile are juxtaposed with the respective results of the tests conducted in this research (T1, T2 for S700MC hollow-section beams and T3-T6 for S355J2 HEA beams). To facilitate comparison, the ductility factors of tests T1 to T6 were recalculated based on the elastic-perfectly plastic bilinear approach and are thus somewhat smaller to their respective values in Table 3.14. Table 3.20 shows that the increase of yield strength leads to a respective reduction of ductility. More specifically, regarding hollow-sections, doubling of the actual yield strength resulted in reduction of ductility and behavior factors by approximately 50% (the ratio of the nominal f_y values is 3). In the case of open sections (IPE or HEA), comparison between S235 and S355J2 shows that for approximately 28% increase of the actual yield strength, the system's ductility decreases by almost 25%. This comparison does not account for the different system capacities.

Table 3.20 Comparison with previous cyclic tests on FUSEIS with S235 beams

Beam links	Steel	Actual yield	Ω (average)	μ (average)	$q = \mu*\Omega$
Hollow-sections	S235	352	1.38	3.57	4.93
	S700MC	740	1.50	1.72	2.58
Open sections	S235	344	1.16	4.88	5.66
	S355J2	440	1.60	3.63	5.81

3.7 Tests on FUSEIS with pin links

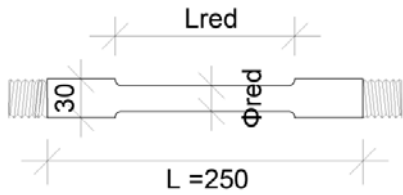
3.7.1 FUSEIS pin specimens

Two large scale cyclic tests on FUSEIS systems with pin links were conducted in the Laboratory of Steel Structures in NTUA, henceforth referred as tests T7 and T8. The tests had the same links but

different loading protocols: T7 had increasing amplitude (I.A.), while T8 had constant amplitude (C.A.), as shown in Table 3.6. The test setup included two strong columns connected via five pin links (Fig. 3.1) whose cross sections are in Table 3.21. The test frame's height was 3.4 m (distance between pin supports and actuator's axis) while the axial distance of the FUSEIS columns was 1.4 m. The material of the pins and their end plates was S500MC. The specimens consisted of cylindrical rods of 30 mm diameter and were screwed via reverse threads on plates of 25 mm thickness that were then bolted to the FUSEIS columns. Their diameter was reduced along a length (L_{red}) in their middle area, in order to shift the location of the plastic hinge away from the connections (in this case, the pins' threads). Table 3.22 gives the dimensions of the reduced sections. As mentioned before, the FUSEIS columns as well as the test rig used were available from previous investigations within another research project (Vayas et al. 2013, Dimakogianni et al. 2012, Dimakogianni 2017). In that case however the material of the pin links was S235 and larger pins were used. In the current campaign, the FUSEIS test frame is also modified. More specifically, in the previous tests the pins were screwed on the end-plates, and additionally encased in stiff receptacle hollow beams. In the current tests, the receptacle beams were omitted to allow an easy mounting of the system.

Table 3.21 Layout and dimensions of reduced parts in S500MC pin link specimens (tests T7 and T8)

Specimen	Φ_{red} (mm)	L_{red} (mm)
S1	22	150
S2	20	130
S3	20	110
S4	15	130
S5	15	110



Different combinations of Φ_{red} and L_{red} were investigated to facilitate sequential yielding of the specimens. Table 3.22 gives an overview of the links' properties. A capacity check is included, showing that the maximum bending moment developed at hinge formation ($M_c = M_{pl,Red} * L/L_{red}$) was smaller than the pin's full section moment capacity (M_{pl}) taking into account the section's reduction at the thread area.

Table 3.22 Pin links, properties of reduced sections (tests T7 and T8)

Specimen	Φ_{red}	A_{red} (m ²)	$W_{el,Red}$ (m ³)	$W_{pl,Red}$ (m ³)	M_c/M_{pl}
S1	22	3.80E-04	1.04E-06	1.77E-06	0.93
S2	20	3.14E-04	7.85E-07	1.33E-06	0.81
S3	20	3.14E-04	7.85E-07	1.33E-06	0.96
S4	15	1.77E-04	3.31E-07	5.63E-07	0.34
S5	15	1.77E-04	3.31E-07	5.63E-07	0.40

3.7.2 Cyclic response of FUSEIS with S500MC pin links

Fig. 3.43 gives the response curves of FUSEIS with pin links for tests T7 and T8 in terms of drift versus actuator force. The behavior of the system with pin links is different from that of the system with beams, as the pins develop catenary action when large displacements are applied. Initially, both types of FUSEIS links are subjected to flexure until they reach their bending capacity. Beyond this point, the beam links deform plastically up to crack initiation when the systems resistance drops. On the contrary, in FUSEIS with pins the lateral resistance of the system keeps increasing with increasing deformations well beyond the bending capacity of the pins, due to the axial forces developed in them. The transition from bending to catenary function is depicted in the tests' response curves which start forming a characteristic pointing shape after about 1.4% drift. First yield can be observed at approximately 0.8% drift.

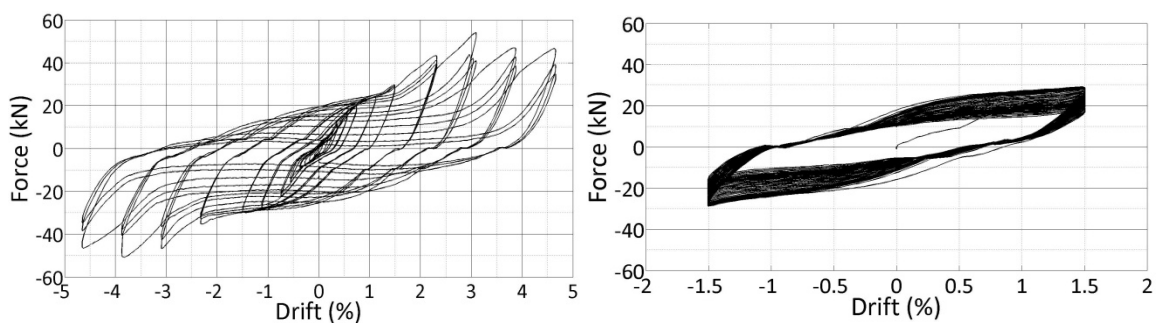


Fig. 3.43 Cyclic response of FUSEIS with pin links in tests (a) T7 and (b) T8 (36 loading cycles)

Due to the small clearance between the columns, there were no LVDTs placed to monitor the differential displacements of the links in this setup. Thus, correction of the experimental data lied on the LVDTs placed on the columns and the inclinometers. In this test frame, though, the divergences between the measurements obtained by the actuator and the columns corresponded to less than 0.1% drifts, possibly due to the fact that the developed forces were significantly smaller to those in tests T1 to T6. Bolt/end-plate slippage was also of minor importance: less than 0.4 mm in test T7 and practically zero in T8.

Fig. 3.44 shows the deformation of pin links with different extent of cross-section reduction. Fig. 3.45 provides a generic graph of a pin's deformed state in agreement with the graphs in Fig. 3.12 (the rotated system is in red and the deformed pin is added in blue). The link rotation θ used in Eq. 3-3 to Eq. 3-6 is a simplification that refers to an intermediate between the rotations of the pin's full-section and reduced-section parts (noted as θ_1 and θ_2 in Fig. 3.45)



Fig. 3.44 Pins' deformation (a) link S1 (b) link S4

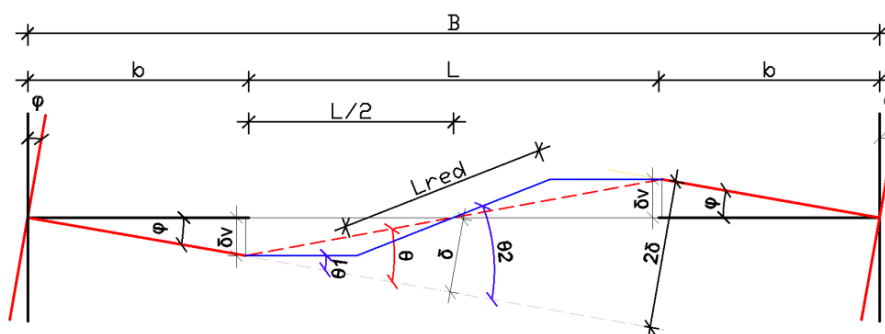


Fig. 3.45 Generic drawing of pin links' deformation (θ) for an overall system drift (ϕ)

The most common damage of the specimens was cracking towards the end of the links' reduced sections which in some cases led to complete separation (Fig. 3.46). As expected, the rods with the smallest diameters were the first to undergo fracture. In the increasing amplitude (I.A.) cyclic test (T7), first cracks were visible at 1.1% drift. However, the system's resistance kept rising with the increase of applied drifts, despite the extent of crack propagation on many specimens. Beyond 1.5% drift, the response became asymmetric due to the different rate of crack propagation for each loading direction. Consequently, the system reached its peak resistance at different drifts in the two loading directions: at overall drift 3.1% when pulled, while at 3.9% when pushed (Fig. 3.43). In few cases, cracks and deformations occurred at the rods' threads, leading to difficulties during dismounting of the specific specimens.

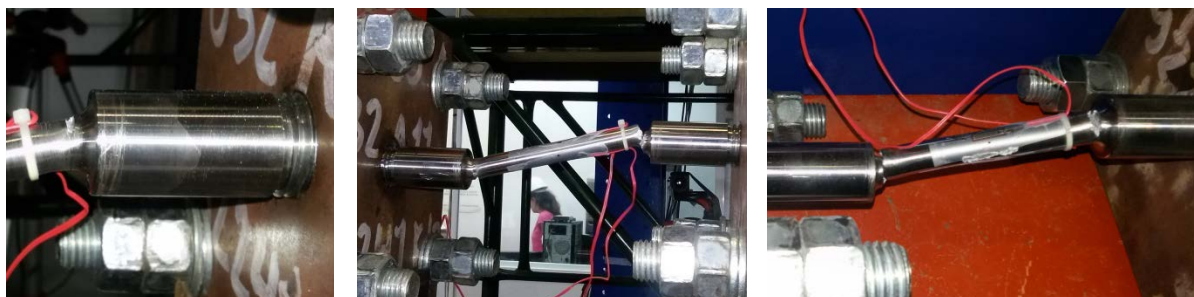


Fig. 3.46 Damage of pin links in increasing amplitude test T7: pins S2, S4 and S5

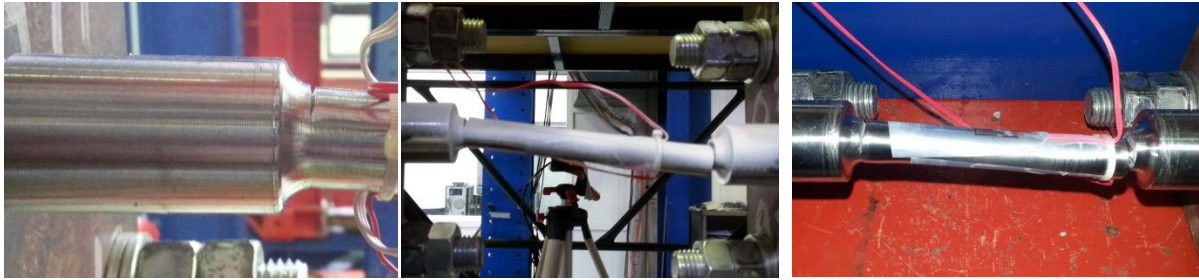


Fig. 3.47 Damage of pin links in constant amplitude test T8: pins S2, S4 and S5

3.7.3 Investigation of pins' internal forces, strain gage measurements

Strain gages were applied on some links to monitor the development of internal forces and obtain data for the verification of the numerical models. More specifically, in pins S1 and S5 two strain gages were applied in their middle sections (at the lowest (u) and highest (o) point as shown in Fig. 3.48). In addition, in S1 two extra strain gages were located towards one end of the reduced section (marked with "+"). The measured strains in both tests at are given in Fig. 3.49 and Fig. 3.50.

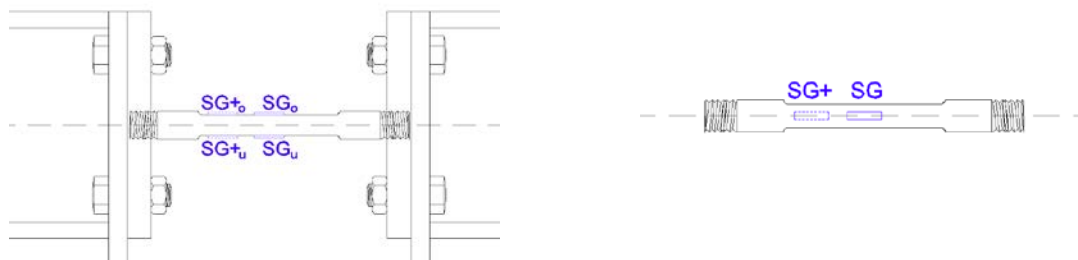


Fig. 3.48 Detail of strain gage location (front view and elevation). The dashed lines indicate additional strain gages (SG+) used only in S1

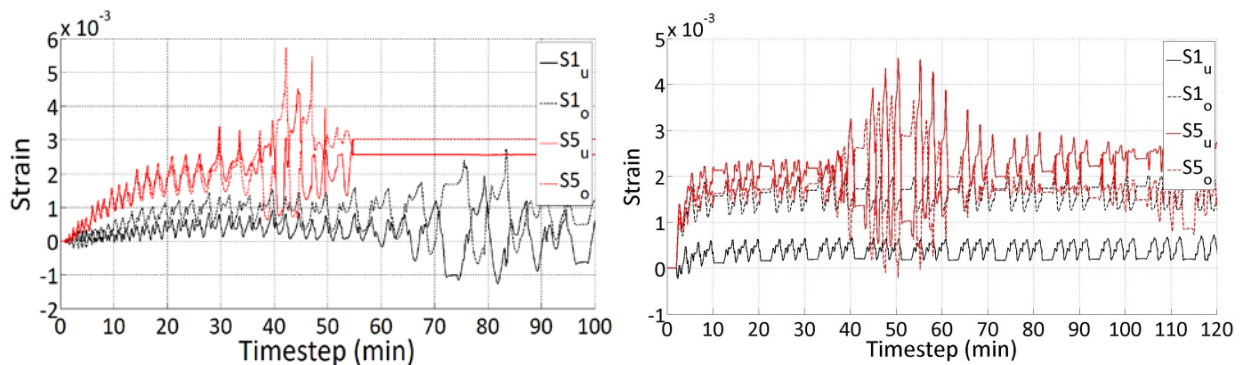


Fig. 3.49 Strain measurements at midsections of pins for tests (a) T7 (I.A.) and (b) T8 (C.A.)

In both cases, specimen S5 which had smaller dimensions (in the reduced part) developed larger strains. In test T7, the measurements for S5 (o, u) are practically the same, indicating that its mid-section was subjected to pure tension. The flatline after the 55th minute was caused by the link's

separation. On the contrary, the measurements for $S1_o$ and $S1_u$ in T7 fluctuate in a reverse way, implying combined bending and axial loading. The additional strain gages at $S1+$ (Fig. 3.50) illustrate the bending process of the link.

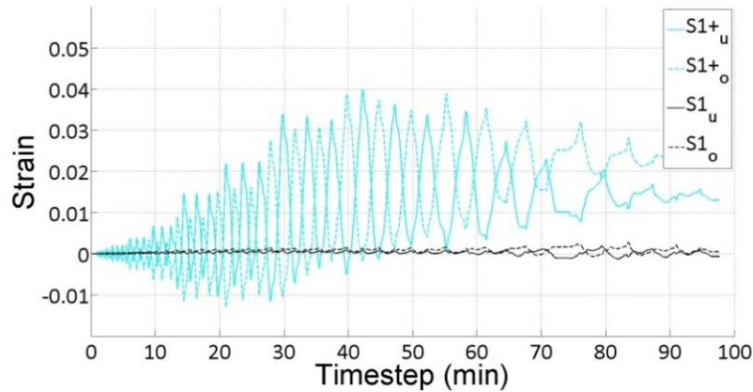


Fig. 3.50 Strain measurements at link S1 (at two locations) for I.A. test T7

Regarding T8, which had constant amplitude, the strain range developed was stabilized at approximately 10 minutes of testing (after the 3rd loading cycle) and remained such for about 30 minutes, when cracks started propagating on the specimens. The additional strain gages at $S1+$ showed that the link had yielded from the first loading cycle. Although link S5 seemed completely cut at the 21st loading cycle (at approx. 70 minutes), the strain gages kept recording strains, probably due to interlocking of the parts.

To estimate the stress levels at the monitored sections, a simplistic bilinear law for the stress-strain relationship was used, based on material tensile tests. This assumption lacks accuracy, as it does not account for the actual cyclic behavior of the material (hardening, Bauschinger effect etc). Following the simplified stress calculation, the axial forces (N) and bending moments (M) were evaluated using Eq. 3-15 and Eq. 3-16. Given that the links had different cross-sections, the internal forces N, M were normalized over each link's tensile strength $N_{pl} = A_{red} * f_y$ or maximum moment $M_{pl} = W_{pl,red} * f_u$, respectively.

$$N = 0.5 * (\sigma_u + \sigma_o) * A_{red} \quad \text{Eq. 3-15}$$

$$M = 0.5 * (\sigma_u - \sigma_o) * W_{pl,red} \quad \text{Eq. 3-16}$$

Where σ_o and σ_u are the estimated stresses in the highest (o) and lowest (u) fiber of the section.

For the first loading cycles prior to damage and/or residual deformations, the links were expected to undergo pure bending, developing opposite moments at their ends and zero moments at the middle. This was not verified by the strain gages, as the development of combined axial forces and bending moments at mid-sections was monitored from the beginning of the tests. As the strain gages were applied manually, some divergence from expectations was inevitable. Fig. 3.51 illustrates the estimated normalized axial forces in the links' mid-sections during tests T7 (I.A) and

T8 (C.A). As can be seen, the pins developed axial forces from the first minutes of the tests while in T7, link S5 reached its tensile resistance before being cut.

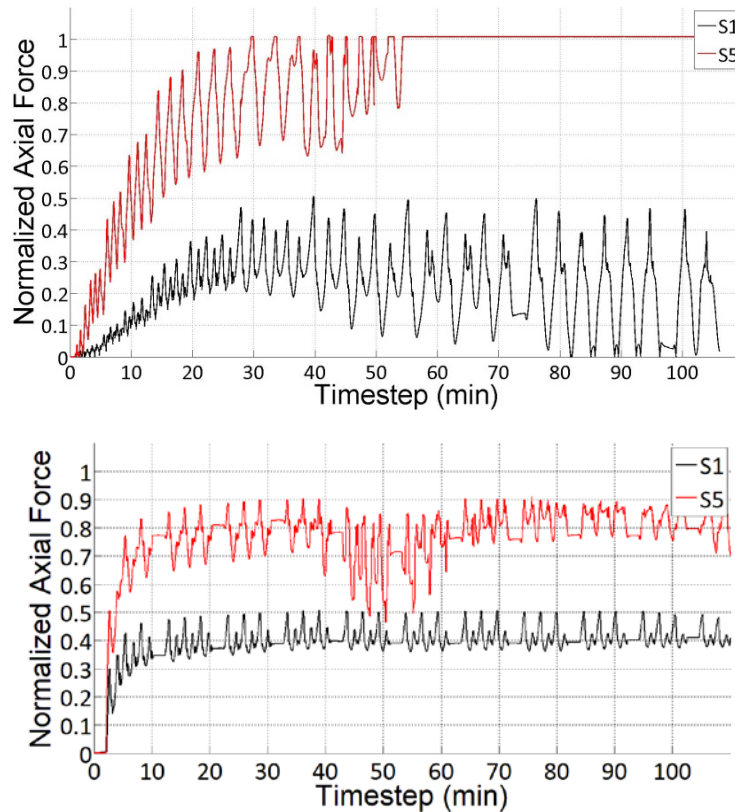


Fig. 3.51 Normalized axial forces at links' mid-sections for tests (a) T7(I.A) and (b) T8 (C.A.)

Fig. 3.52 shows the normalized bending moments in links S1 and S5 during the first 25 minutes of test T7. As can be seen in cross-section S1+, the moment reached 80% of the section's resistance. Indeed, no cracks occurred in pin S1.

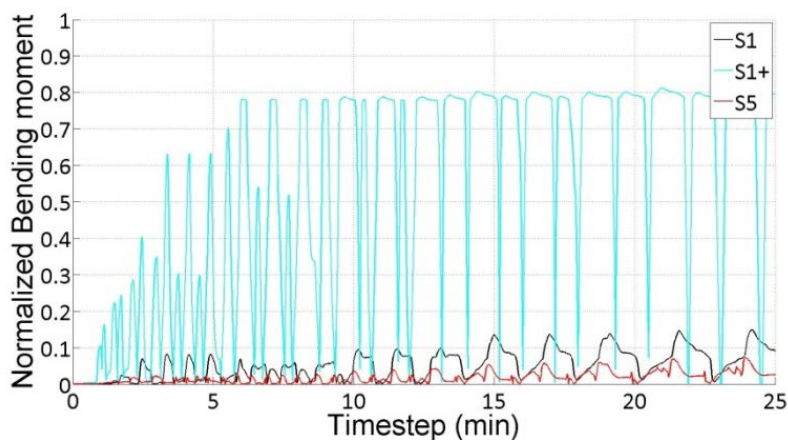


Fig. 3.52 Normalized bending moments on pins for test T7 (zoomed at first 25 minutes of tests)

3.7.4 Peak resistance and stiffness degradation

Fig. 3.53 shows the process of the system's peak-to peak stiffness (K) and lateral resistance (F) for increasing loading (T7). For the calculations of K and F the average values from the two loading directions in the first loading cycle of each triplet were considered. The first cycles prior to first yield are omitted. The system with pin links maintained its ability to withstand lateral forces at large drifts even though its stiffness had been significantly reduced. The system yielded at approximately 0.8% drift (link rotation $\theta \approx 45$ mrad, using Eq. 3-6) and at 4.7% drift ($\theta \approx 260$ mrad) it had lost almost 10% of its bearing capacity while its stiffness had decreased by 60%. The system reached its maximum resistance at approximately 3.1% drift ($\theta \approx 174$ mrad).

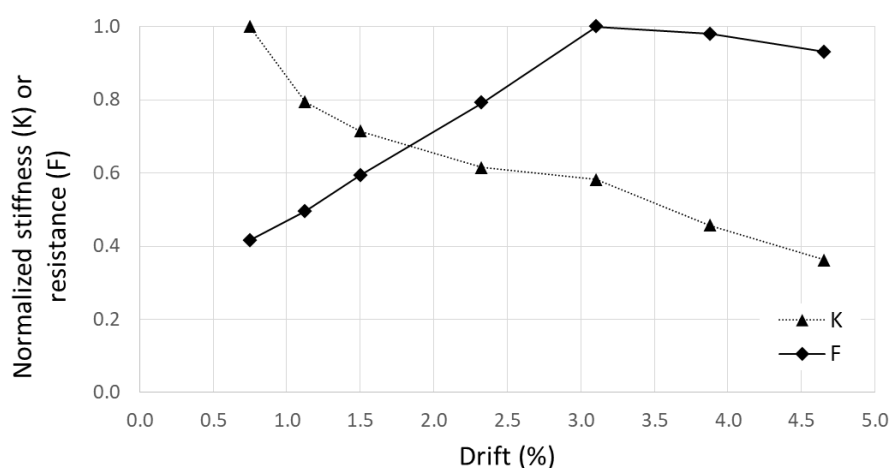


Fig. 3.53 Process of stiffness degradation and peak resistance for increasing deformations

Table 3.23 summarizes observations of crack initiation and links' separation during the tests. The applied drift is denoted as ϕ , while N refers to the number of loading cycles. The increasing amplitude test is noted as "I.A." and the constant amplitude as "C.A.".

Table 3.23 Damage observations on S500MC pin links for tests T7 and T8

Test	Max. drift ϕ_{\max}	Cycles N at ϕ_{\max}	Crack initiation (in Si link)*	Separation (of Si link)*
T7	$\pm 4.7\%$ (I.A.)	3	$\phi_{cr} = 1.1\%$, $N_{cr} = 3$ (S5) $\phi_{cr} = 1.5\%$, $N_{cr} = 1$ (S4) $\phi_{cr} = 2.3\%$, $N_{cr} = 3$ (S2)	$\phi_s = 3.1\%$, $N_s = 2$ (S5) $\phi_s = 3.9\%$, $N_s = 1$ (S4)
T8	$\pm 1.5\%$ (C.A.)	36	$N_{cr} = 6$ (S5) $N_{cr} = 9$ (S4) $N_{cr} = 14$ (S2)	$N_s = 21$ (S5), $N_s = 31$ (S4)

*For each type of damage, the critical drift ϕ and loading cycle N within the same amplitude is given

3.7.5 Energy dissipation

Fig. 3.54 shows the amount of energy dissipated during tests T7 and T8, in groups of three loading cycles. In test T7 first crack was observed at 1.1% drift corresponding to cycles 13-15. The amplitude of cycles 16-18 in test T7 corresponds to the loading cycles in test T8. Energy estimations for T8 verify crack initiation at the 6th loading cycle.

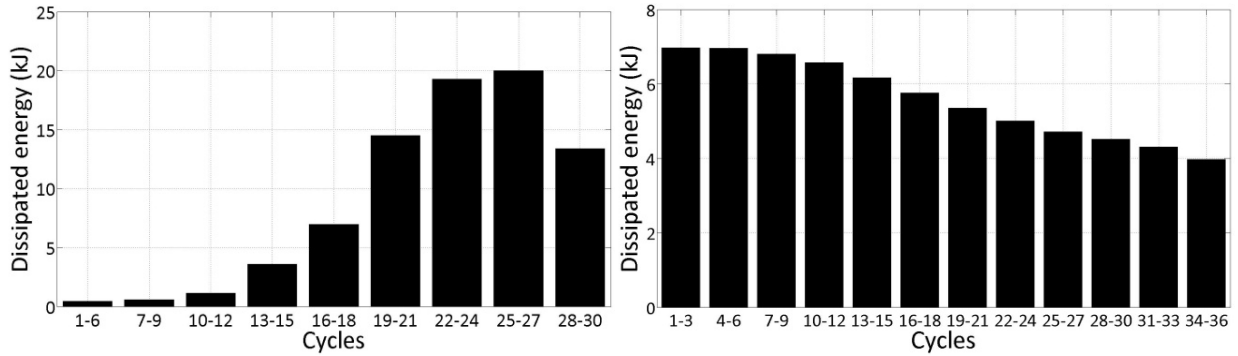


Fig. 3.54 Dissipated energy in tests (a) T7 (I.A.) and (b) T8 (C.A.)

3.7.6 Overstrength, rotation capacity and ductility of tested system

The transition of the deformed pins from bending to catenary action significantly increases the bearing capacity of the system. Its response curve is generally divided in the bending stage (elastic and plastic), the transient stage and finally the catenary stage with the characteristic “pointing” shape. The idealization of the response curve would thus require at least three lines instead of the common bilinear approach and the calculation of overstrength and ductility is based on a different methodology than in the case of FUSEIS with beam links.

Overstrength is calculated according to Eq. 3-17 and is given in Table 3.25:

$$\Omega = F_{\max, \exp} / \min (F_{Vpl}, F_{VMpl}, F_{VMplRed}) \quad \text{Eq. 3-17}$$

where $F_{\max, \exp}$ is the maximum experimental peak resistance (average of two loading directions), F_{Vpl} is system's resistance based on the plastic shear resistance of the pins (V_{pl} , Eq. 3-18) and F_{VMpl} and $F_{VMplRed}$ are the forces corresponding to the development of plastic moments on the pins' full or reduced sections (Eq. 3-19 and Eq. 3-20 respectively). Table 3.24 gives the relevant results.

$$V_{pl} = A_{red} * f_y / \sqrt{3} \quad \text{Eq. 3-18}$$

$$V_{Mpl} = 2M_{pl} / L = 2W_{pl} * f_y / L \quad \text{Eq. 3-19}$$

$$V_{MplRed} = 2M_{plRed} / L_{Red} = 2W_{plRed} * f_y / L_{Red} \quad \text{Eq. 3-20}$$

The sum of the pin links' shear forces is equal to the axial force developed in the FUSEIS columns ($\sum V = N_{col}$) and due to the moments equilibrium on the (simply supported) system, the following

equation applies between the overturning moment M_{ov} , the horizontal applied force F and the columns' axial force N_{col} :

$$M_{ov} = F \cdot H = N_{col} \cdot B \tag{Eq. 3-21}$$

where H and B are the systems height and width respectively (Fig. 3.1).

Given the systems dimensions, replacement of N_{col} with $\sum V$ in Eq. 3-21 leads to $F = \sum V \cdot B / H = \sum V \cdot 1.4 / 3.4$.

To facilitate comparison with experimental investigations on FUSEIS pins with different geometric characteristics, the normalized pin length ρ_{pin} is also included in Table 3.24, given by:

$$\rho_{pin} = L_{Red} / (M_{plRed} / V_{pl}) \tag{Eq. 3-22}$$

Table 3.24 Pins' shear forces for estimation of overstrength

Link	Full section		Reduced section		
	Φ_{red}/L_{red} (mm)	V_{Mpl} (kN)	V_{MplRed} (kN)	V_{pl} (kN)	ρ_{pin}
S1	22/150	18.36	12.07	111.87	18.54
S2	20/130	18.36	10.46	92.46	17.68
S3	20/110	18.36	12.36	92.46	14.96
S4	15/130	18.36	4.41	52.01	23.57
S5	15/110	18.36	5.22	52.01	19.94
SUM ($\sum V = N_{col}$)		91.80	44.52	388.92	-
FUSEIS resistance (F_{Vi})		37.8	18.33	160.15	-

Notes: For the full sections, diameter is 30 mm and length L is 250mm

In view of the peculiar shape of the response curves, provided ductility (μ) was calculated as the ratio of the displacement at which load degradation initiated (δ_u) over the displacement at which catenary stage began (δ_y) as shown in Fig. 3.55. Average values were used to account for the response in both loading directions and the result is in Table 3.25. This is a conservative estimation as the system yielded at smaller drifts.

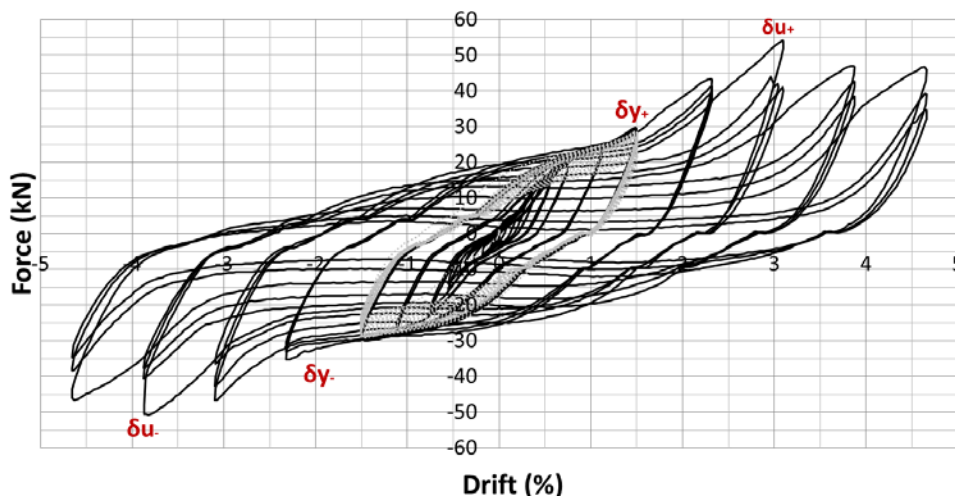


Fig. 3.55 Estimation of provided ductility $\mu = \delta_u/\delta_y$ based on T7 (data for T8 are added in grey)

Based on the results of the increasing amplitude test (T7), two limit states were assumed: crack initiation (cr) and maximum resistance (u). The corresponding overall drifts were $\phi_{cr}=1.1\%$ (Table 3.23) and $\phi_u=3.1\%$ (Fig. 3.53). According to Eq. 3-6, the respective rotations were $\theta_{cr}= 0.062= 62$ mrad and $\theta_u= 0.174= 174$ mrad. However, in test T8 where $\pm 1.5\%$ drift was applied, no cracks occurred in the first loading cycle. Thus, the aforementioned values for ϕ_{cr} , θ_{cr} are conservative since they refer to a state where the links have been subjected to ultra-low cycle fatigue (ULCF). Table 3.25 gives an overview of the evaluation of the tests' results regarding over-strength (Ω), ductility (μ) and behavior factor ($q = \mu \cdot \Omega$) as well as critical link rotations.

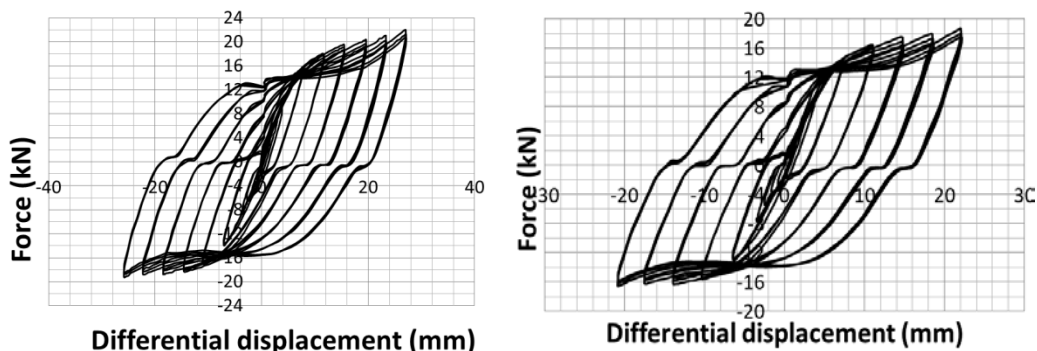
Table 3.25 Factors Ω , μ , q and critical pin rotations θ , according to I.A. test on FUSEIS with S500MC pins

FUSEIS	Test	Ω	μ	q	θ_{cr} *(mrad)	θ_u (mrad)
Pins	T7	2.7	2.3	6.2	62	174

*Crack initiation refers to the critical link S5

3.7.7 Cyclic component tests on S500MC pin links

A series of cyclic tests on single FUSEIS pin components of S500MC was conducted in the Laboratory of Aachen University (RWTH). The test setup is shown in Fig. 3.38 and Fig. 3.39. Five tests were performed using the same pin links as in the previously discussed FUSEIS system tests. The applied cyclic load had increasing amplitude, based on a modification of ECCS provisions, involving the use of smaller loading steps. Preliminary numerical models were used for the estimation of yield displacement e_y . Table 3.26 gives an overview of the tests, including the normalized pin lengths (ρ_{pin} , Eq. 3-22) based on the actual (as measured) dimensions of the links. Fig. 3.56 shows the hysteresis curves of the tests. In this experimental campaign, only the crack initiation limit state was investigated so the tests were terminated rather early compared to the system tests previously discussed. Catenary action had initiated in almost all cases, however the extent at which it could enhance the links' resistance was not explored.



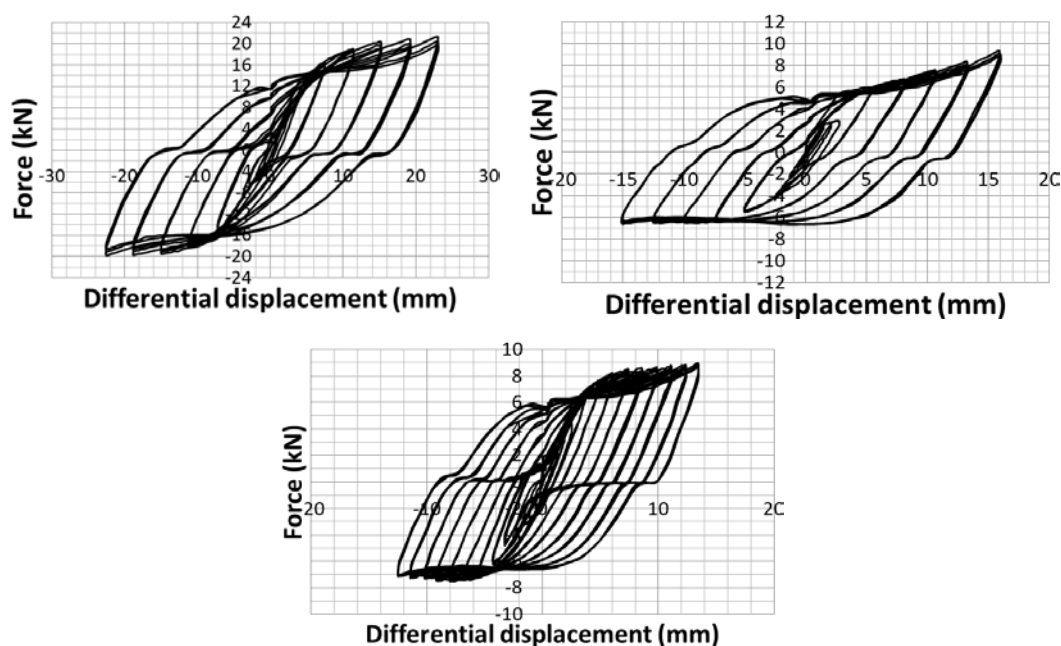


Fig. 3.56 Response curves for S500MC pin component tests (CT12 to CT16)

The overstrength factor (Ω) was calculated using Eq. 3-23 (which is a modification of Eq. 3-17), considering directly the maximum force applied by the actuator ($V_{\max, \text{exp}}$) and the theoretical shear forces of the links (Eq. 3-18 to Eq. 3-20):

$$\Omega = V_{\max, \text{exp}} / \min (V_{\text{pl}}, V_{\text{Mpl}}, V_{\text{MplRed}}) \quad \text{Eq. 3-23}$$

The Ω factors based on Eq. 3-23 are given in Table 3.26. Since the tests were terminated upon crack initiation, the obtained values are conservative, as the $V_{\max, \text{exp}}$ does not reflect the links' ultimate capacity. This is highlighted by comparison of Ω values between Table 3.25 (system tests) and Table 3.27 (component tests). Each link's rotation at crack initiation (θ_{cr}) is also given in Table 3.26. As can be seen the $\Phi 15$ pins (S4, S5 in system tests and CT15, CT16 in component tests) have significantly reduced rotation capacity compared to the rest.

Table 3.26 Test matrix for pin component tests, rotation capacity and overstrength (until crack initiation)

Test	Φ_{red} (mm)	L_{red} (mm)	ρ_{pin} (Eq. 3-22)	θ_{cr} (mrad) (Eq. 3-3)	$V_{\max, \text{exp}}$ (kN)	Ω (Eq. 3-23)
CT12	22	150	18.84	114	20.5	1.76
CT13	20	130	18.31	89	17.5	1.80
CT14	20	110	15.32	96	20.5	1.75
CT15	15	130	23.89	67	8.0	1.89
CT16	15	110	20.72	56	8.0	1.66

Notes: For the full sections, diameter is 30 mm and length L is 236mm

3.7.8 Previous research on FUSEIS with S235 pins

Experimental investigations on FUSEIS with pin links made of S235 steel had been conducted in the framework of a previous research project (Vayas et al. 2013, Dimakogianni et al. 2012, Dimakogianni 2017), as presented in Table 3.27: Eight tests (P1 to P8) on separate pin specimens (cyclic or monotonic) and two cyclic tests on FUSEIS systems (M4, M5) including five links each. Fig. 3.57 gives the response curves for a monotonic component test (P2) and a cyclic system test (M4). As can be seen, the shape of the response curve of the FUSEIS test (M4) is different from that of the current tests (Fig. 3.55), probably due to the changes in the test setup (discard of receptacle beams). The tests were carried out until fracture of the specimens (Fig. 3.58). Table 3.27 summarizes the maximum applied force (F_{max}), the normalized pin length (ρ_{pin} , Eq. 3-22), the pin's rotation capacity corresponding to the ultimate limit state (θ_u) and the overstrength (Ω , Eq. 3-17 and Eq. 3-23) for each test. The actual yield strength of the material was $f_y = 220$ MPa. As can be seen in Table 3.27 both the rotation capacity (θ_u) and the overstrength (Ω) of the pins in the monotonic tests (P1, P2) were significantly increased compared to the cyclic tests. This indicates that when the pins are subjected to cyclic loading, they fail at rather smaller deformations and develop less catenary action due to ultra-low cycle fatigue (ULCF).

Table 3.27 Test matrix of tests on S235 FUSEIS pins

Test	Pin link (Φ_{red}/L_{red})	Loading	Fmax (kN)	ρ_{pin} (Eq. 3-22)	θ_u (mrad)	Ω (Eq. 3-17, Eq. 3-23)
P1	$\Phi 45/120$	monotonic	401.9	7.3	389	10.1
P2	$\Phi 45/90$	monotonic	438.4	5.4	306	11.1
P3	$\Phi 45/150$	I.A.*	124.2	9.1	88	3.1
P4	$\Phi 45/150$	I.A.*	129.2	9.1	106	3.3
P5	$\Phi 45/120$	I.A.*	155.8	7.3	90	3.9
P6	$\Phi 45/120$	I.A.*	164.6	7.3	89	4.2
P7	$\Phi 45/90$	I.A.*	219.1	5.4	108	5.5
P8	$\Phi 45/90$	I.A.*	218.5	5.4	87	5.5
M4	$\Phi 45/150$ (1)	I.A.*	393.3**	6.89 (average)	72	3.60
	$\Phi 45/120$ (2)					
	$\Phi 45/90$ (2)					
M5	$\Phi 40/120$ (1)	I.A.*	354.1**	7.14 (average)	81	3.24
	$\Phi 45/120$ (2)					
	$\Phi 50/120$ (2)					

*I.A. stands for increasing amplitude cyclic test

** The actuator forces in the system tests are shear forces for the FUSEIS columns, while the actuator forces in the component tests are axial forces for the columns.

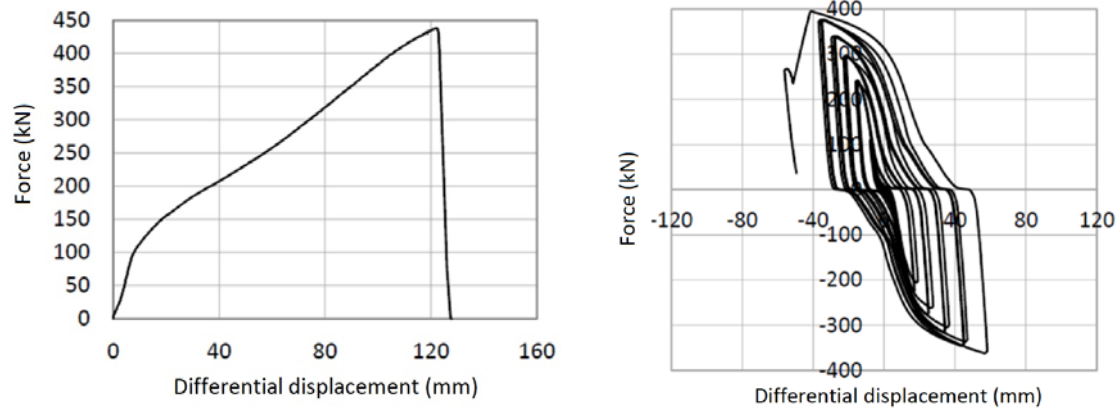


Fig. 3.57 Response curves for component test P2 and system test M4 (Dimakogianni 2017)



Fig. 3.58 Fracture of specimen in system test M4 (Dimakogianni 2017)

Fig. 3.59 and Fig. 3.60 give an overview of all tests on FUSEIS pins in terms of rotation (θ_u), overstrength (Ω) and normalized pin length (ρ_{pin}). It is reminded that the component tests on S500MC pins (AT12-AT16) were terminated at crack initiation, thus the values of θ_u and Ω are significantly smaller compared to the respective values of system test T7. Differences in the test setup and the resistances between the previous and current tests do not allow for a comprehensive comparison of the systems. Despite this, some data are summarized and juxtaposed for the two experimental campaigns. Fig. 3.59 shows that in FUSEIS system tests with S500MC pins (T7, triangle marks) the values of θ_u and ρ_{pin} are significantly increased compared to M4-M5. Fig. 3.60 shows that the provided Ω in the FUSEIS with S235 pins (M4-M5, circular marks) was larger than in T7.

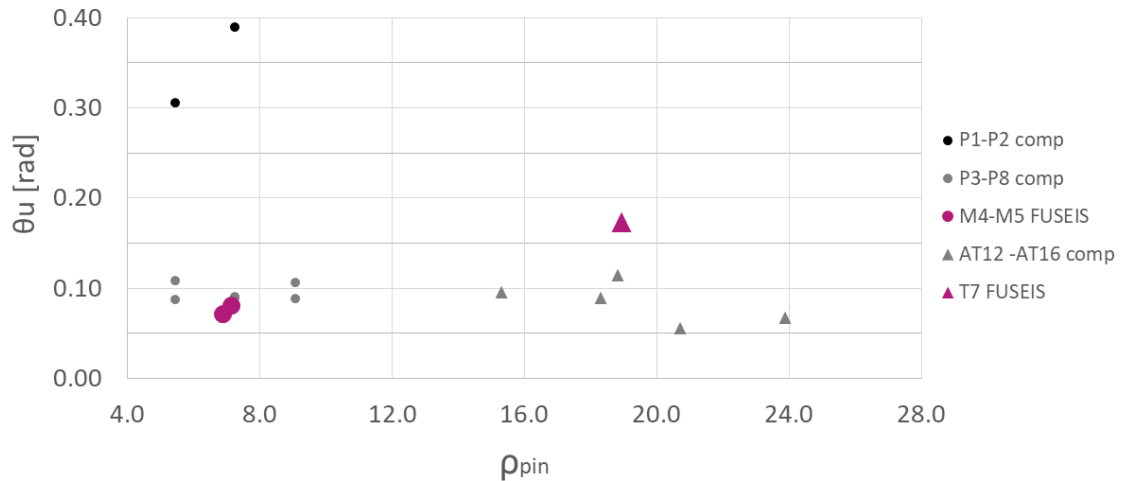


Fig. 3.59 Rotation capacity θ_u vs normalized pin length ρ_{pin} for S235 pins (circles) and S500MC pins (triangles). The tests on systems are in magenta, the component tests are in grey-scale.

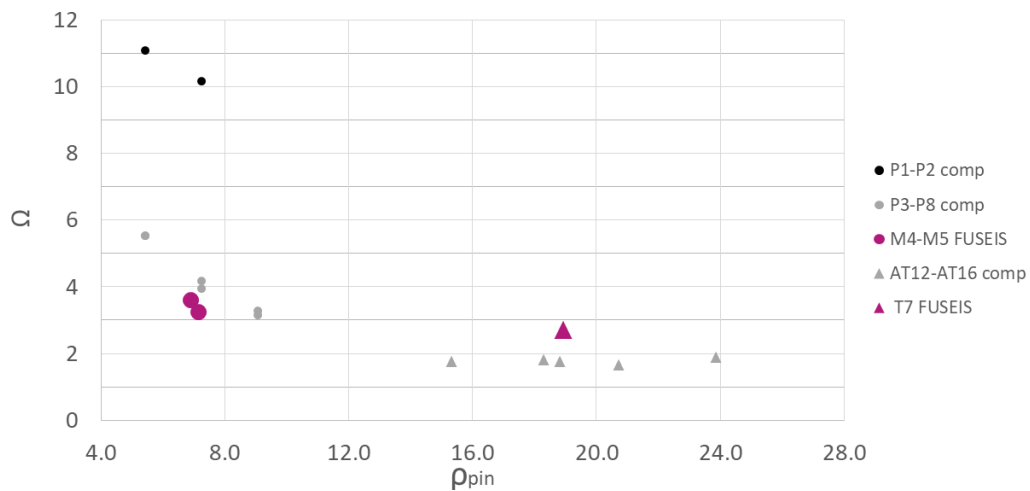


Fig. 3.60 Overstrength (Ω) vs normalized pin length (ρ_{pin}) for S235 pins (circles) and S500MC pins (triangles). The tests on systems are in magenta, the component tests are in grey-scale.

3.8 Conclusions

This chapter presents a series of large scale tests on FUSEIS systems performed in NTUA with varying types of links (hollow-section beams, HEA beams and cylindrical pins) made of three steel grades (S700MC, S355J2 and S500MC respectively). For technical reasons (capacity of Laboratories and steel producers), the systems had different capacities. Most tests involved cyclic loading with increasing or constant amplitude. FUSEIS component tests with similar specimens were conducted

in other laboratories and their results are overviewed. In addition, reference and limited comparison with previous tests involving FUSEIS with S235 links is made.

FUSEIS consist of a pair of strong columns rigidly connected by multiple links (beams or pins). They resist lateral forces via the development of axial forces in the columns and bending of the links. In addition, at large deformations the system with pin links develops catenary action. In case of a strong earthquake, damage is concentrated in the replaceable links and hence, one of the system's main advantages is reparability. In the Laboratory, replacement of each fuse specimen between the tests required approximately 45 minutes and the procedure was easy for two workers to handle. To facilitate mounting, the FUSEIS links were connected to the columns via bolted end-plates. However, this configuration highly influenced the test results, especially for the system with HEA beams in which larger forces developed. The tolerances and slippages of the numerous bolts led to "collateral" displacements and reduced the deformations sustained by the links compared to those applied on the system. In practice, the fuses could be welded to the strong columns, as suitable cutters are available in the market in case replacement is required. This solution would lead to stiffer connections and the elimination of the aforementioned "collateral" displacements.

The FUSEIS with S700MC beam links reached its peak resistance under cyclic loading at approximately 2.5% overall drift. The system with S355J2 beams did not exhibit signs of damage for cyclic loading up to 3.5% drift and monotonic loading up to 6.2%. In both systems, stiffness degradation began at approximately 1.0% drift. Overall, examination of common failure criteria such as 20% loss of resistance or stiffness under cyclic loading showed that the first criterion is not met by 3.5% drift while the latter is met at about 2.1%. The relevant link rotations are 74 mrad and 44 mrad respectively. Comparison with previous research on FUSEIS with S235 beams suggests that the increase of yield strength could lead to a respective reduction of ductility.

The system with S500MC pin links subjected to cyclic loading, yielded at approximately 0.8% overall drift and reached its peak resistance at about 3.1%. Due to the development of catenary action, it reached 4.7% drift with less than 10% strength degradation and extensive damage on the links. The links' rotation (θ) at peak resistance was approximately 174 mrad. Link rotation at crack initiation highly depended on the pin's diameters, ranging from 56 to 114 mrad. In this case, comparison with previous tests on FUSEIS with S235 pin links was not straight-forward, due to modifications of the test setup. However, there are indications that the rotation capacity of the system with S500MC is improved.

Being an innovative anti-seismic system, the FUSEIS is not included in the Codes and there are no defined limits for its deformations. With respect to the magnitude of the aforementioned drifts/rotations, the following recommendations for conventional systems such as Moment

Resistant Frames (MRF) and braced frames (BF) are given as reference. According to FEMA 356, Life Safety (LS) limit state corresponds to the displacement that is 0.75 times the deformation at peak resistance. This translates to approximately 1.9% drift for the system with S700MC beams and 2.6% for that with S355J2. For this performance level, FEMA 356 suggests that typical steel MRF may undergo drifts up to 2.5% while the respective value for BF is 1.5%. EN1998-1 states that for structures of medium ductility class the minimum rotation of a beam's plastic hinge to be ensured under cyclic loading with up to 20% strength degradation is 25 mrad. For BF with short horizontal seismic links EN1998-1 specifies the maximum link rotation at 80 mrad.

Chapter 4: Analytical and Numerical Investigations

4.1 Introduction

This chapter focuses on analytical and numerical models of the tested FUSEIS systems. The theoretical lateral resistance of the system, based on the bending capacity of the beam links and the catenary force of the pin links, is defined and compared with the experimental values.

The tested FUSEIS were simulated using three different numerical models with increasing complexity (2D or 3D finite elements), in order to serve different purposes. The first models of the systems were developed using SAP2000 commercial software. The aim was to capture the system's response via calibration of the plastic hinge properties. Based on these models, additional 2D models were created in the OpenSees framework, which is more suitable for parametric investigations and multiple dynamic analyses. Finally, the tests were simulated using 3D elements in the ABAQUS software. In this case, the main objective was the verification of the plasticity-and-damage material subroutines developed by other academic partners based on small scale material tests.

4.2 Theoretical model for lateral resistance

The FUSEIS system resists horizontal loads as a vertical Vierendeel beam combining axial force in the columns and bending of the links. When a horizontal force (F) is applied, the system deforms and the links are subjected to bending until they reach their moment capacity and plastic hinges are formed. The moment resistance of beam links designed with RBS is $M_{pl,RBS}$, while in the case of pin links with reduced middle sections it is $M_{pl,red}$. At the joints of the links' axis with the columns (Fig. 4.1) the maximum moment developed is given by:

$$\begin{aligned} M_b &= M_{pl,RBS} * B / L_{RBS} && \text{for beam links with RBS} \\ M_b &= M_{pl,red} * B / L_{red} && \text{for pin links} \end{aligned} \quad \text{Eq. 4-1}$$

The corresponding shear force is $V_b = 2M_b/B$.

Assuming that the systems' columns are pin-supported, the moment equilibrium of the system leads to the following equations:

$$F_{th} * H = N_{col} * B \rightarrow F_{th} = \sum V_b * B / H = \sum (2M_b / B) * B / H = 2 \sum M_b / H \quad \text{Eq. 4-2}$$

Where B is the system's width and H is its height (Fig. 4.1)

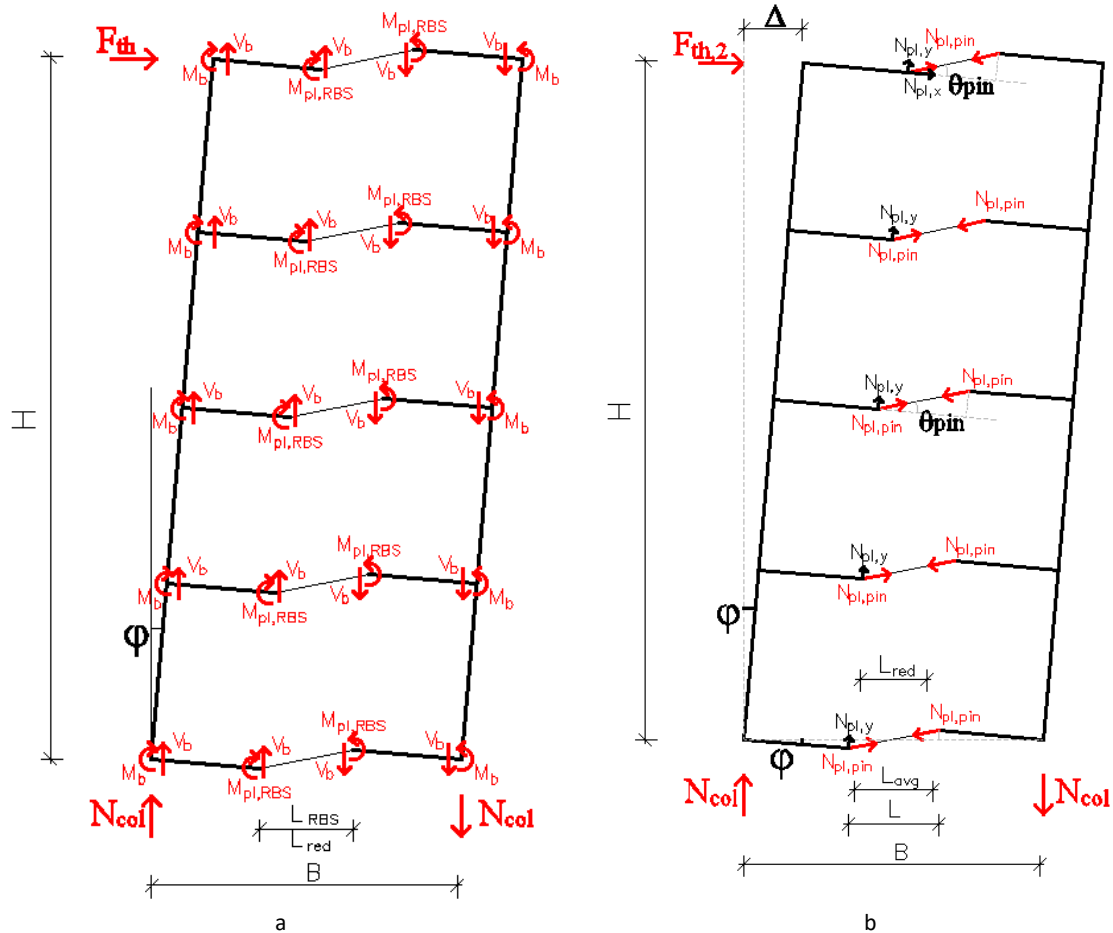


Fig. 4.1 Theoretical models for calculation of the system's strength based on (a) links' bending capacity and (b) catenary action

Eventually, the system's peak resistance F_{th} , based on the links' bending capacity, is:

$$F_{th} = 2 * \sum (M_{pl,RBS} * B) / (L_{RBS} * H) \quad (\text{beam links}) \quad \text{Eq. 4-3}$$

$$F_{th} = 2 * \sum (M_{pl,red} * B) / (L_{red} * H) \quad (\text{pin links})$$

In the FUSEIS with pin links, catenary action develops when the applied deformations increase beyond the bending capacity of the links. The system's resistance is then controlled by the links' resistance to axial forces. Due to the reduction of the pins' section, their tensile capacity is calculated as $N_{pl,pin} = A_{red} * f_y$ where A_{red} refers to the reduced diameter Φ_{red} . An additional theoretical horizontal force is introduced (F_{th2}) as a function of $N_{pl,pin}$ and rotation θ_{pin} :

$$F_{th,2} = N_{col} * B / H \approx \sum N_{pl,y} * B / H = \sum (N_{pl,pin} * \sin \theta_{pin}) * B / H \quad \text{Eq. 4-4}$$

As discussed in Chapter 3, the actual rotations developed in the pins are not the same for all specimens, as they depend on the dimensions of their reduced parts. That is why the average value θ was used (Fig. 3.45). If this assumption ($\theta_{pin} = \phi * B / L$) is applied in Eq. 4-4, the result is Eq. 4-5a. This slightly underestimates the system's capacity as the links are practically considered with a

uniform reduced section along their whole length (L). An alternative assumption would be to assume an average length L_{avg} between the full (L) and the reduced (L_{red}) lengths for the (uniform) links (Fig. 4.1). Thus Eq. 4-4 turns to Eq. 4-5b which provides increased values for $F_{th,2}$ compared to (a).

$$F_{th,2} \approx \sum N_{pl,pin} * (\phi * B / L) * (B / H) \quad (a) \quad \text{Eq. 4-5}$$

$$F_{th,2} \approx \sum N_{pl,pin} * (\phi * B / L_{avg}) * (B / H) \quad (b)$$

where ϕ is the system's drift angle

Table 4.1 gives an overview of the above. For each system, the maximum force obtained in the experiments (F_{exp}) is given along with its theoretical strength based on the links' bending capacities (F_{th} , Eq. 4-3). For F_{th} two versions are presented ($F_{th,fy}$ and $F_{th,fu}$), depending on whether the bending capacity M_{pl} is based on the material's actual yield ($W_{pl} * f_y$) or tensile strength ($W_{pl} * f_u$) respectively. The mean value between $F_{th,fy}$ and $F_{th,fu}$ gives a better approximation of the actual resistance of FUSEIS with beams, as expressed via the $F_{exp} / F_{th,m}$ ratio.

In the tests on FUSEIS with pin links, the maximum force (F_{exp}) exceeded $F_{th,fu}$ due to catenary action. Table 4.1 gives the theoretical resistance forces based on the links' tensile strength ($F_{th,2}$, Eq. 4-5) and applied deformations. As can be seen the system's strength is better approximated by $F_{th,2}$ with Eq. 4-5a underestimating and Eq. 4-5b overestimating it. In the constant amplitude test T8 ($\phi = 1.5\%$) fatigue cracks were formed and $F_{th,2}$ by Eq. 4-5b provides a rather good approach. For the increasing amplitude test T7 the reference drift is $\phi=3.1\%$, representing the system's peak resistance when pin S5 was cut and most links had already extensive cracks (Table 3.23). In this case F_{max} is better approached by Eq. 4-5a.

Table 4.1 Comparison between experimental (F_{exp}) and theoretical (F_{th}) peak resistances of FUSEIS

Test	FUSEIS links	f_y, f_u (MPa)	F_{exp} (kN)	$F_{th,fy}$ (kN)	$F_{th,fu}$ (kN)	$F_{exp} / F_{th,m}$	F_{th2} (Eq. 4-5a)	F_{th2} (Eq. 4-5b)
T1, T2	Hollow beams S700	$f_y = 740$ $f_u = 845$	117	106	121	1.02	-	-
T3,T4,T5,T6	HEA beams S355	$f_y = 440$ $f_u = 605$	340	276	380	1.04	-	-
T7	Pin links	$f_y = 510$	53			2.52	49	65
T8	S500	$f_u = 660$	30	18	24	1.43	24	32

4.3 Simulation of FUSEIS systems using beam elements

4.3.1 Basic assumptions

The FUSEIS columns were modeled as elastic beam elements and non-linear properties were assigned to the dissipative links. Additional elastic members and rigid links were used to account for the column stiffeners and the eccentricities between the members. The net length of the FUSEIS beams was subdivided to five zones representing the full sections and the reduced beam sections (Fig. 4.2). Similarly, the net length of the FUSEIS pins was separated in three zones to account for the section reduction in the middle. The supports were simulated as pins and the diaphragm action (realized in the tests by means of UPN beams) was achieved via joint constraints. The out-of-plane displacements of the frames were restricted at the top and at the bottom of the FUSEIS columns.

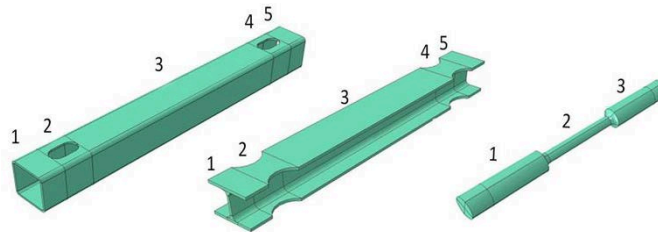


Fig. 4.2 Division of FUSEIS links in 5 or 3 zones of full and reduced section for modeling

The FUSEIS link-to-column connection was simulated as semi-rigid using rotational springs. As described in Chapter 3, the connections involved a number of bolts and tolerances which affected the stiffness and overall response of the system, especially in the case of FUSEIS beams. To achieve a more realistic simulation, their rotational stiffness (S_j) was determined by the component method (T-stubs) proposed by EN1993-1-8 according to:

$$S_j = E \cdot z^2 / (\mu \cdot \sum 1/k_i), \quad \text{Eq. 4-6}$$

where E is the modulus of elasticity, z is the lever arm, μ is a reduction factor based on the ratio M_{Ed}/M_{Rd} (Fig. 4.3) and k_i is the stiffness coefficient for each joint component.

For a single-sided beam-to-column joint with bolted end-plates and one bolt-row in tension (EN1993-1-8, Table 6.10) six stiffness coefficients (k_i) should be taken into account representing: the column web in shear (k_1), the column web in compression (k_2), the column web in tension (k_3), the column flange in bending (k_4), the end-plate in bending (k_5) and the bolts in tension (k_{10}). As the columns were stiffened, the stiffness of the column web in shear and in compression was assumed infinite ($k_1=k_2=\infty$). The rest of the parameters were calculated based on the properties of the components. In some cases the ratio M_{Ed}/M_{Rd} was larger than $2/3$ so the effective rotational stiffness was smaller than its initial value (Fig. 4.3). To account for this, multi-linear elastic springs were used.

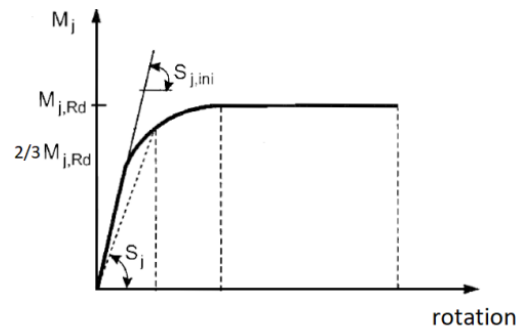


Fig. 4.3 Moment-rotation relationship of a semi-rigid joint

The nonlinearity of the dissipative members was simulated by two approaches:

- Concentrated plasticity, using SAP2000 models (moment-rotation plastic hinges)
- Distributed plasticity, using OpenSees (simulation with fiber sections)

The concentrated plasticity simulation is simpler, but requires the definition of a specific location for plastic hinge formation and a moment-rotation relationship (applicable for constant axial load). The distributed plasticity simulation is more refined. It uses a stress-strain relationship, allows yielding at any location along the element and can account for interaction between axial force and bending moments. Each member is divided longitudinally via integration points, while its sections are discretized in fibers.

The models were subjected to pushover analysis and the parameters for material non-linearity were defined by calibration with the envelope of the experimental curves for the loading cycles prior to damage. Beyond crack initiation, load degradation was partly controlled by fatigue, and thus a calibration based on the skeleton curve would be very adverse. On the contrary, the lines connecting the peak resistances of successive cycles with different amplitudes were assumed more representative of the degradation process (Fig. 4.4). An additional calibration was undertaken for the models in OpenSees with respect to cyclic loading.

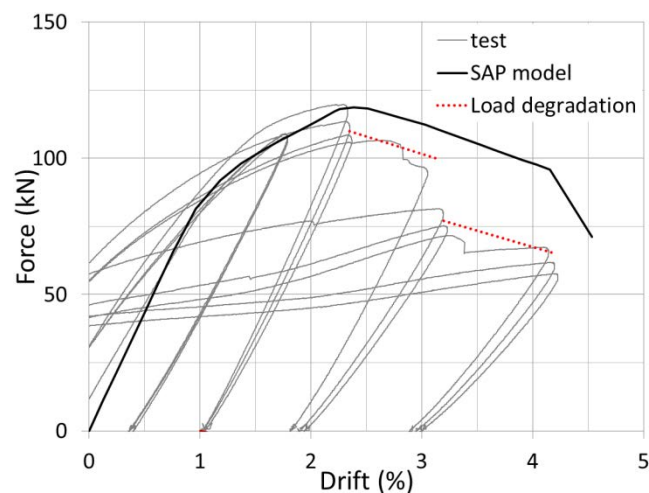


Fig. 4.4 Calibration based on envelopes of tests and load degradation indicators

4.3.2 Simulation of FUSEIS systems using SAP2000

In SAP2000 all members are initially input as elastic and can be later assigned with non-linear properties. Fig. 4.5 shows the design of the FUSEIS columns and the RBS of the hollow-sections within the application. Additional elastic members and rigid links were used for the column stiffeners and the distances between the columns' axis and the FUSEIS links (Fig. 4.6). The connections of the links to the FUSEIS columns were assumed as semi-rigid as discussed before.

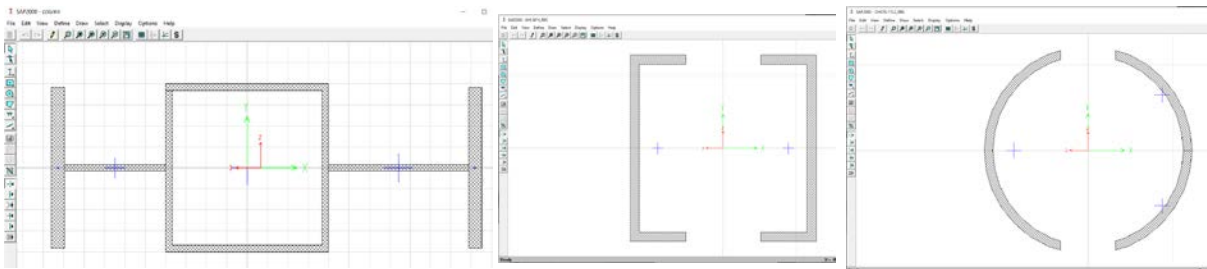


Fig. 4.5 User defined profiles (a) FUSEIS columns (b) SHS with RBS (c) CHS with RBS

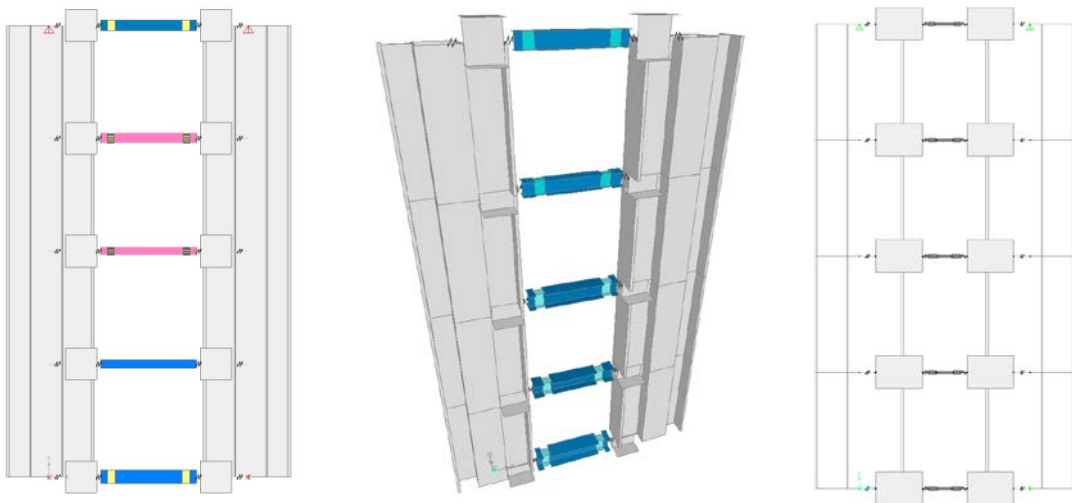


Fig. 4.6 3D extruded views of models

Potential plastic hinges were assigned in all critical locations: For the system with beams, in the middle of the RBS members and towards the end of the beams (Fig. 4.7a), for the system with pins, at the ends of the reduced parts and of the full sections (Fig. 4.7b).



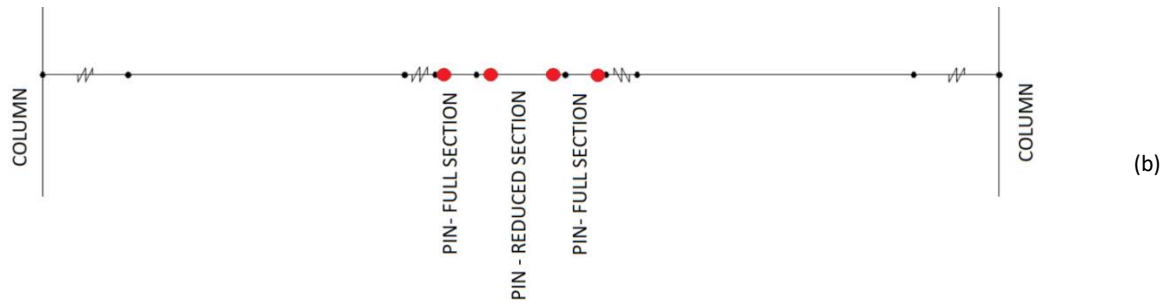


Fig. 4.7 Assignment of plastic hinges (red dots) in (a) FUSEIS with beams and (b) FUSEIS with pins

The behavior of the plastic hinges was controlled by a user-defined moment-rotation relationship as shown in Fig. 4.8. Few generic parameters were used for hinge definition, as shortly described.

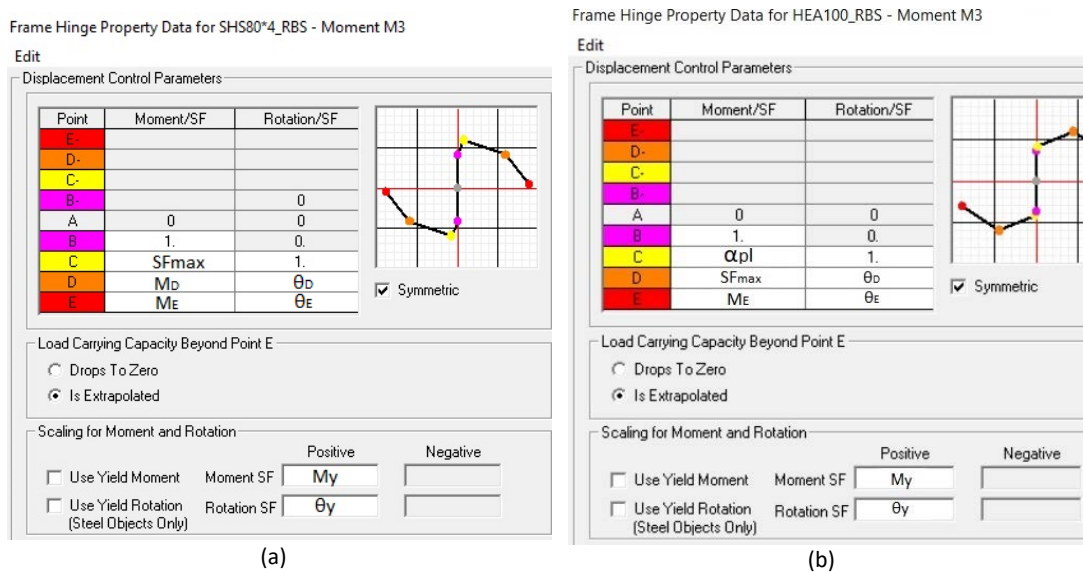


Fig. 4.8 Definition of moment-rotation relationship for plastic hinges for the FUSEIS beams (SAP2000) (a) S700 hollow-sections (b) S355 HEA profiles

For the yield rotation θ_y the relevant equation from FEMA356 was used:

$$\theta_y = W_{pl} * f_y * L_b / (6 * E * I_b) \quad \text{Eq. 4-7}$$

where W_{pl} is the plastic section modulus, f_y is the yield strength, E is the modulus of elasticity, L_b is the length of the beam and I_b is the beams moment of inertia.

For the hinges assigned in the RBS parts the above equation was modified as following:

$$\theta_{yRBS} = W_{plRBS} * f_y * L_b^2 / (6 * E * I_b * L_{RBS}) \quad \text{Eq. 4-8}$$

where W_{plRBS} is the plastic section modulus of the RBS and L_{RBS} is the reduced length (the distance between the midpoints of the RBS).

The yield moment is defined as:

$$M_y = W_{el} * f_y, \text{ for full sections} \quad \text{Eq. 4-9}$$

$$M_{yRBS} = W_{elRBS} * f_y, \text{ for RBS sections}$$

For the scale factors representing the maximum moments sustained, the following equations were used:

$$SF_{max} = M_{max}/M_y = W_{pl} * f_u / M_y, \text{ for full sections} \quad \text{Eq. 4-10}$$

$$SF_{max} = W_{plRBS} * f_u / M_{yRBS}, \text{ for RBS}$$

The shape factor (α_{pl}) of each section is given by:

$$\alpha_{pl} = W_{pl} / W_{el} \quad \text{Eq. 4-11}$$

Given the limited number of cyclic tests and the absence of monotonic tests until fracture of the links, the definition of plastic hinge rotation capacity was subjected to uncertainties. Table 4.2 gives the suggested parameters for the moment-rotation curves as determined after calibration. In the tests on FUSEIS with S700 beams, extensive cracks occurred, and thus some indicators of the process of load degradation were considered. For the system with S355 beams, no such indicators were available from the tests. In this case, however, data obtained from the monotonic test were used for the evaluation of the pushover curve. Fig. 4.9 shows the comparison between numerical (black) and experimental (gray) response curves.

Table 4.2 Overview of hinge parameters for simulation of FUSEIS beams in SAP2000 (see also Fig. 4.8)

	S700 Hollow beam links		S355 HEA beam links	
	Moment	Rotation	Moment	Rotation
C	SFmax*M _y	1*θ _y	α _{pl} *M _y	1*θ _y
D	1.0*M _y	8*θ _y	SFmax*M _y	25*θ _y
E	0.1*M _y	14*θ _y	0.8*M _y	50*θ _y

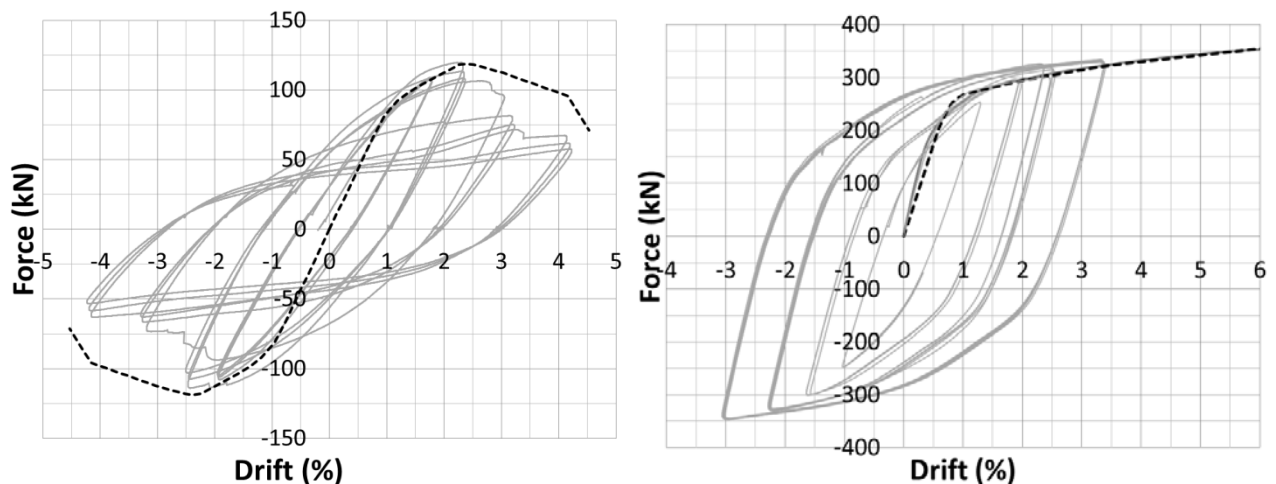


Fig. 4.9 Simulation with SAP2000, response curves for FUSEIS with (a) S700 beams (b) S355 beams (models in black, tests in gray)

The behavior of the FUSEIS with pins is different from the system with beams, as the pins develop catenary action at large deformations and therefore cannot be accurately simulated via beam

members with moment-rotation hinges. However, a simplified approach is hereby presented, using the same plastic hinge to describe the link's response at different but sequential states. According to this, the behavior of the plastic hinges is divided in the following two phases:

- a) Bending of the pins (corresponding to points A, B, C in Fig. 4.10)
- b) Catenary action (corresponding to points D, E in Fig. 4.10)

Fig. 4.10 shows the plastic hinge parameters obtained by calibration. Similar to the beam links, the yield moment M_y and SF_{max} are given by Eq. 4-9 and Eq. 4-10. The suggested value for the scale factor SF_{caten} related to peak resistance is 5.

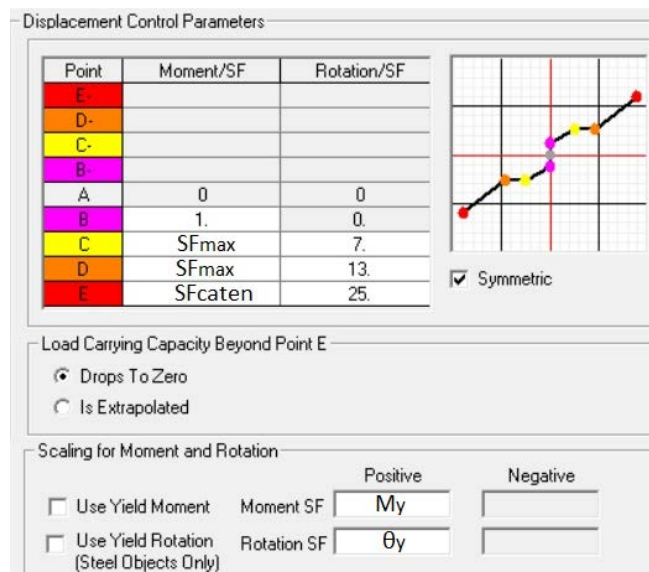


Fig. 4.10 Definition of moment-rotation relationship for plastic hinges for the FUSEIS pins (SAP2000)

In Fig. 4.11 the model's pushover curve is compared with the response curve from test T7: In Fig. 4.11a the simulated bending phase of the links is isolated while Fig. 4.11b shows the system's overall response. As can be seen, there is good agreement in terms of bending capacity, initial stiffness (as illustrated in the unloading segments) and peak resistance.

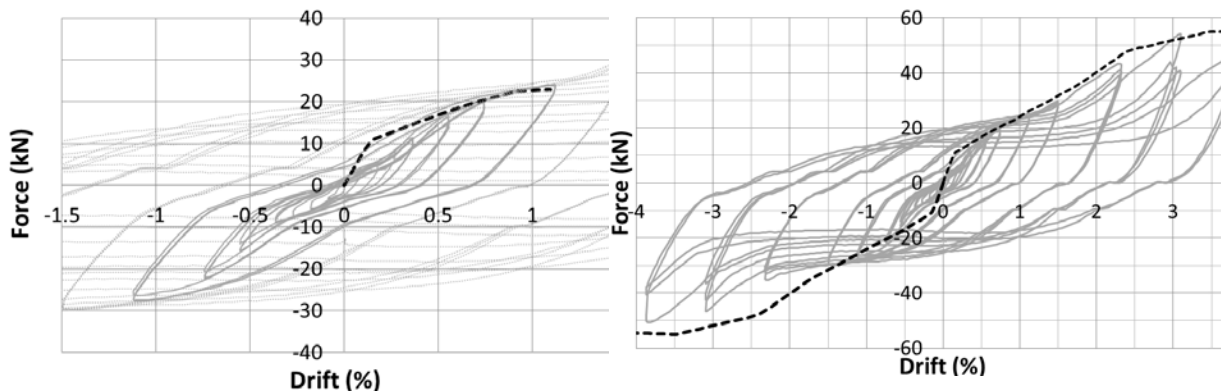


Fig. 4.11 Simulation of FUSEIS with S500 pins using SAP2000, increasing amplitude test (a) bending phase (b) bending and catenary phase

4.3.3 Simulation of FUSEIS with beams using OpenSees

Additional models of the systems with beam links were created using OpenSees as they would be more suitable for further investigations including parametric analyses that are discussed in the next chapter. This software does not have a graphic interface so no illustration of the models is available apart from a generic shape (Fig. 4.12a).

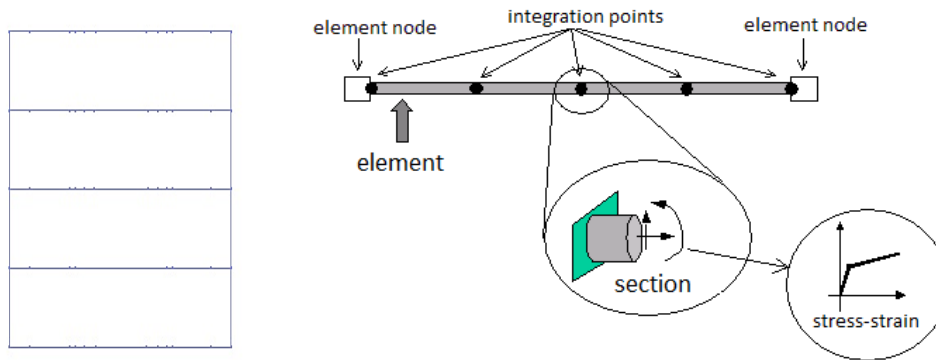


Fig. 4.12 Simulation using OpenSees (a) generic shape of FUSEIS model (b) formulation of non-linear element

Elastic members were used for the FUSEIS columns. The various eccentricities were modeled using practically rigid, elastic “dummy” elements. The semi-rigid connections of the links were modeled as multi-linear elastic springs, using “two-node links” of zero length. The nonlinear beams used for the FUSEIS links, accounted for the spread of plasticity along their length, while a grid of fibers was generated over their cross-sections. Fig. 4.12b illustrates the basic principles of the applied nonlinear elements: the members are divided via integration points, the cross-sections are discretized in fibers depending on their shape (Fig. 4.13) and each fiber is controlled by the input stress-strain curve. The material of the FUSEIS links was defined as a “uniaxial hysteretic material” whose stress-strain envelope was defined by three points in each direction. This material allows for pinching and damage considerations.

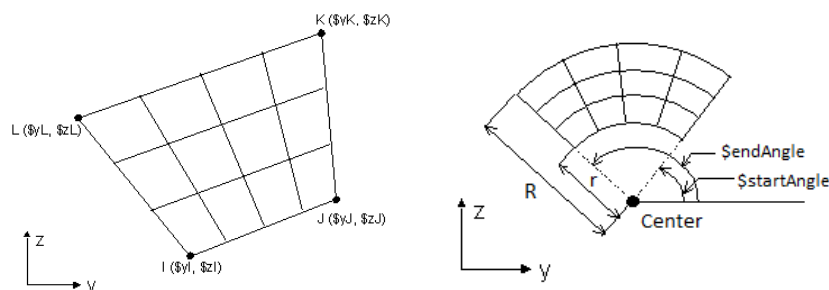


Fig. 4.13 Discretization in fibers of quadrilateral or circular shape (obtained from <https://opensees.berkeley.edu>)

Fig. 4.14 shows the comparison between numerical Pushover curves (in black) and experimental response curves (in gray).

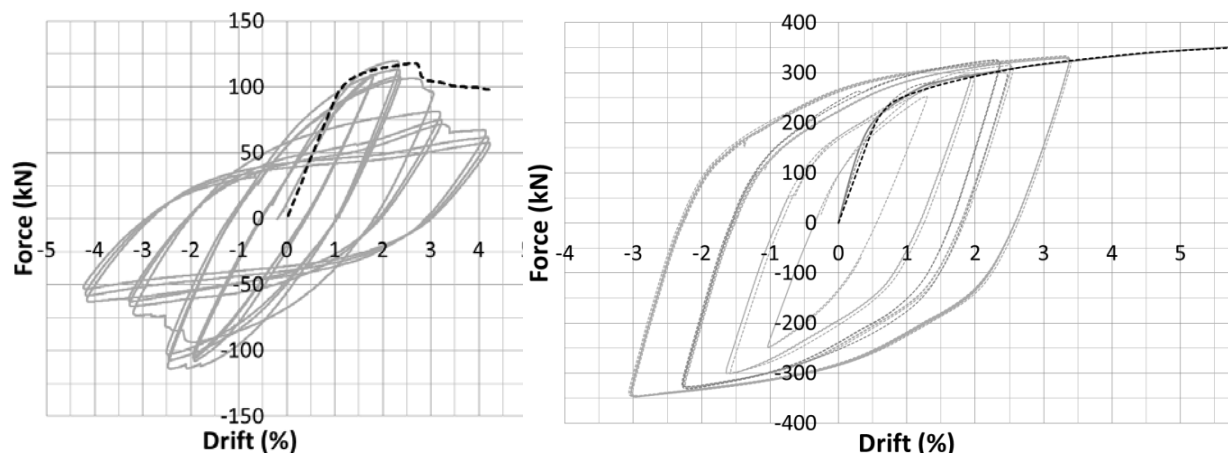


Fig. 4.14 Simulation with OpenSees, response curves for FUSEIS with (a) S700 beams (b) S355 beams (models in black, tests in gray)

The calibration of a material damage parameter was investigated based on the constant amplitude tests. Fig. 4.15 shows the results for test T2 on S700 beams and test T5 on S355 beams which are fairly satisfying in terms of force degradation.

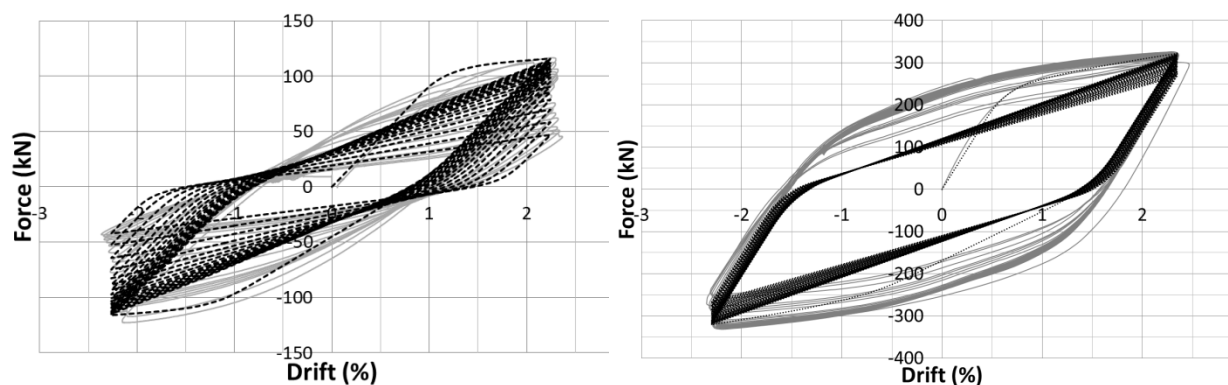


Fig. 4.15 Damage simulation in constant amplitude tests for system with (a) S700 beams (b) S355 beams (models in black, tests in gray)

4.4 Simulation using solid elements

4.4.1 Theoretical background of material simulation

The tests were simulated using solid finite elements in Abaqus FEA software. The actual material behavior was incorporated in the models via user-defined Fortran-based subroutines (UMAT) developed by RWTH-Aachen University and University of Thessaly in the framework of the "MATCH" RFCS project. Specific details on the formulation of the UMAT subroutines, the assumed material parameters and the accompanying tests for their calibration are beyond the scope of this

dissertation but can be found in the Technical Report of the research project (Feldmann et al. 2017).

In general, a hybrid experimental and numerical approach based on damage mechanics was adopted for material simulation. The material models consist of plasticity and damage parts and were calibrated with different types of material tests. The adopted methodology is based on the differentiation between damage initiation (microscopic scale, refers to microstructure developing an irreversible degradation on a given length scale) and fracture (macroscopic scale, material separation). Based on the methodology proposed by Lian et al. (2012), each material model includes three components corresponding to three phases, as follows:

- Cyclic plasticity model, characterizing material behavior until damage initiation
- Damage initiation criterion
- Damage evolution and accumulation until fracture

For the materials' cyclic inelastic behavior a combination of nonlinear kinematic and isotropic hardening rule was assumed. Isotropic hardening allows for expansion (or contraction) of the yield surface (Fig. 4.16a), while kinematic hardening accounts for the Bauschinger effect by translation of the yield surface. The degree of translation is measured by back stress parameter (α_{ij} , Fig. 4.16b). The earliest, linear forms of kinematic hardening were proposed by Prager (1949) and Ziegler (1959). Frederick and Armstrong in (1966) developed the Prager model and proposed the first non-linear kinematic hardening rule. A modification of the Armstrong-Frederick (1966) model was adopted in this research, in which the yield surface can change depending on the amount of the equivalent plastic strain. The modified model adopted was initially proposed by Ucak and Tsopelas (2011). An additional enhancement was made regarding the yield plateau region (Chatzopoulou et al. 2016).

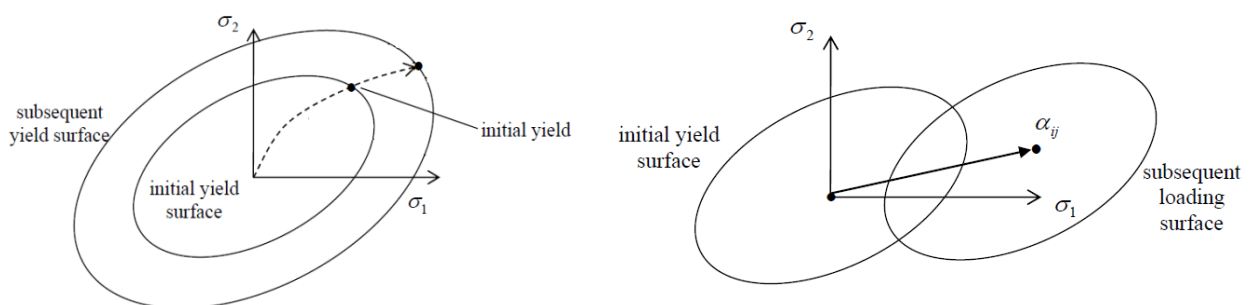


Fig. 4.16 (a) Expansion of yield surface in isotropic hardening (b) translation of yield surface in kinematic hardening

The criterion for damage initiation is based on Ohata and Toyoda “effective damage concept” (2004). They proposed a two-parameter criterion for ductile cracking of steel under large-scale

cyclic loading, the critical parameters being the effective plastic strain and stress triaxiality (Fig. 4.17a). Effective plastic strain (ϵ_{eff}) is defined as the equivalent plastic strain corresponding to back stress larger than the previously achieved maximum equivalent back stress. Stress triaxiality (η) is the ratio of hydrostatic pressure (or mean stress) to the von Mises (or equivalent) stress (σ_{vm}), as given by:

$$\eta = \frac{(\sigma_1 + \sigma_2 + \sigma_3)/3}{\sigma_{vm}} = \frac{I_1/3}{\sigma_{vm}} \quad \text{Eq. 4-12}$$

According to Ohata and Toyoda, damage initiates when the accumulated effective plastic strain ϵ_{eff} reaches a critical value (damage curve). However, in some cases (large strains and kinematic hardening saturation, loading with constant amplitude) the equivalent back stress exceeds the maximum equivalent back stress only during the first tensile loading (Fig. 4.17b), and thus effective plastic strain is not accumulated theoretically (although it accumulates in practice). To overcome this, the effective damage concept was modified and a phenomenological parameter was introduced to degenerate the maximum equivalent back stress.

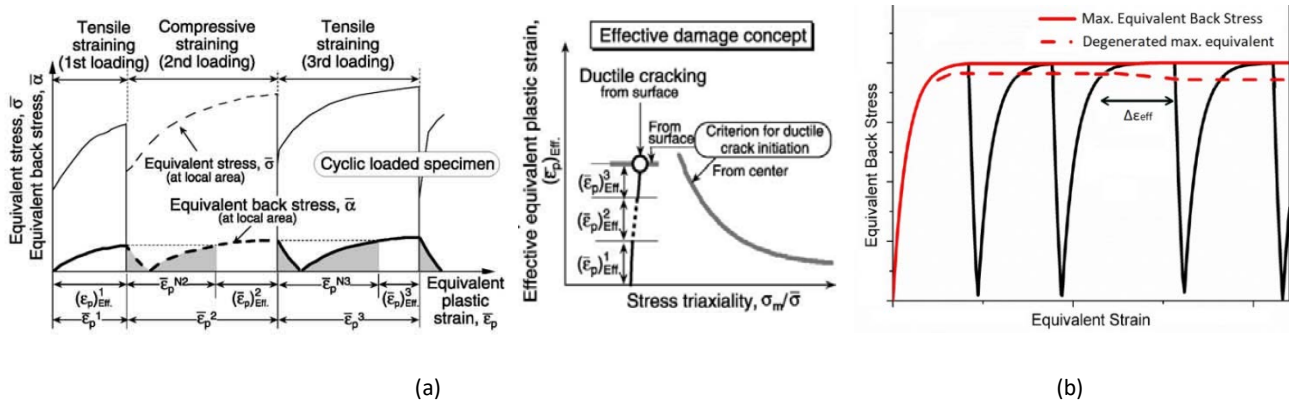


Fig. 4.17 (a) Ohata and Toyoda (2004): evolution of equivalent back stress under cyclic loading and effective damage concept (b) modification regarding maximum equivalent back stress (Feldmann et al. 2017)

To identify the point of the loading process when damage initiates, an experimentally defined criterion was used. Considering the void-controlled ductile damage mechanism (paragraph 2.2.1), damage onset corresponds to the phase of void coalescence that leads to an accelerated damage accumulation rate. The critical effective plastic strain for damage initiation (ϵ_i) belongs to a spatial Damage Initiation Locus (DIL) considering the effects of stress triaxiality (η) and Lode angle parameter (θ). Lode angle is related to the third deviatoric stress invariant. The dependency of fracture strain on triaxiality has been proved theoretically (McClintock 1968, Rice and Tracey 1969) and experimentally (Hancock and Mackenzie 1976, Mirza et al. 1996, Bao and Wierzbicki 2004). Recent studies have shown that Lode angle parameter also affects the fracture strain (Bai and Wierzbicki 2008, Barsoum and Faleskog, 2007; Gao et al. 2009) especially at lower values of stress triaxiality. For the determination of damage initiation (ϵ_i), the direct current potential drop (DCPD)

method was applied: The specimens were connected with a power source providing constant direct electric current and the electric potential changes due to discontinuities were monitored. Fig. 4.18a shows the damage initiation locus (DIL) defined in a triaxial system of strain-triaxiality-Lode angle (Feldmann et al. 2017).

Following damage onset, damage evolution is described via an internal variable D representing damage accumulation related to the plastic strain evolution, based on a modified Bai-Wierzbicki model (2008). Fracture occurs when D reaches a critical value D_{cr} which was also experimentally defined. Similarly to the damage initiation locus, the critical damage locus (D_{cr}) referring to material separation is defined in a triaxial system of D_{cr} -triaxiality (η)-Lode angle (θ) (Fig. 4.18b). As discussed, the parameters for the definition of the damage initiation and the critical damage loci were determined through tests. Specimens with varying geometries were used to achieve different stress triaxiality and Lode angle values.

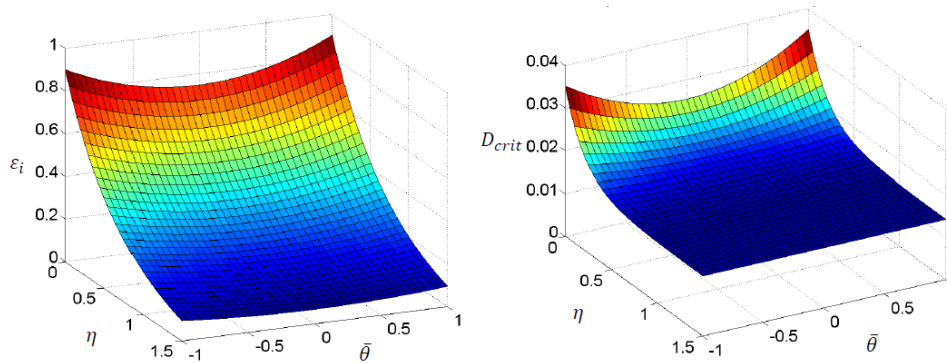


Fig. 4.18 Schematic 3D loci for (a) ductile damage initiation in the triaxial system of strain (ϵ_i)-triaxiality (η)-Lode angle (θ) and (b) critical damage (D_{cr}) in the system of D_{cr} - η - θ (Feldmann et al. 2017)

To facilitate comparison between models and tests, the material subroutines provided a number of output parameters including indicators such as “damage initiation flags” and “element deletion flags” (referring to material separation).

It is noted that in the framework of “MATCH” project, two types of material subroutines were developed and calibrated for each material depending on whether the relationship between plasticity and damage was coupled or uncoupled. The coupled models are more accurate but computationally demanding, leading to simulation of both crack initiation and propagation. In the uncoupled models there is no correlation between plasticity and damage, and thus the softening prior to failure is attributed to buckling and residual deformations, ignoring the contribution of damage. For technical reasons, the simulation of the large scale tests was carried out with the uncoupled material models, leading to less accurate approaches of stiffness degradation beyond the loading cycles where crack had occurred.

4.4.2 Description of models

The main objective of these simulations was the verification of the material subroutines in terms of plasticity and damage prediction, by applying them in more complex models compared to those used for their development. Three models were created corresponding to the three groups of tests (Fig. 4.19). In general, the computational demands for the simulations of the tests were rather large, while the application of the aforementioned material subroutines further complicated the analyses. This rendered the simulation of the tests involving many loading cycles very difficult, given the available technical equipment.

The models consisted of eight-node brick elements with enhanced hourglass control. For the dissipative members, either the general type of solid elements (C3D8) or the improved version with incompatible modes (C3D8I) was used. The FUSEIS columns were modeled with the reduced integration elements (C3D8R). Geometrical non-linearities were taken into account.

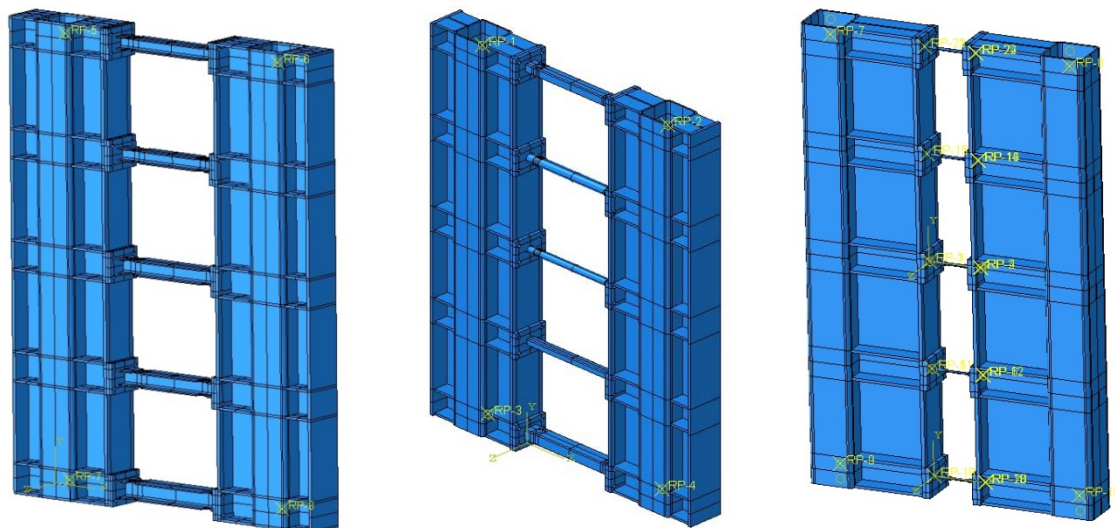


Fig. 4.19 Models of FUSEIS with (a) Hollow-section beams (b) HEA beams and (c) pin links

All parts of the models were partitioned and meshed separately and connected to each other via different constraints accounting for the systems' supports, the columns' stiffeners, the welded and bolted connections of the links. Reference points were used to control the actual boundary conditions of the systems. Equal displacements at the bottom of the columns were achieved via kinematic coupling constraint, so the relevant UPN beams (Chapter 3) were not included in the models. The mesh was finer in the critical areas of the FUSEIS links, while it was significantly coarser in the columns (Fig. 4.20). The mesh sizes in the critical areas varied, aiming to simulate damage initiation without excessively increasing the number of elements, and thus the computational time. More specifically, in the critical areas of the beam fuses, mesh size varied between 1 and 2mm, while in the pin fuses it was less than 5 mm. Given that the material subroutines were calibrated

using very finely meshed models (mesh size approximately 0.4mm) the application of finer mesh could provide more accurate results but would significantly decelerate the analyses.

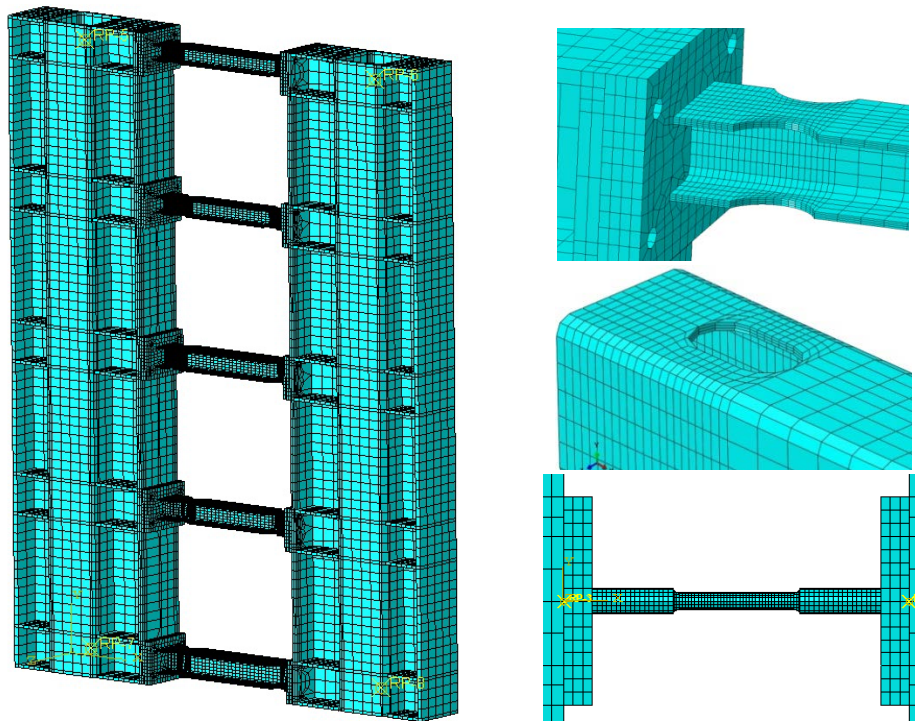


Fig. 4.20 Numerical models: mesh refinement in critical areas

4.4.3 Response of FUSEIS with beams models

Due to the required number of loading cycles up to crack initiation, only one test (T5) was simulated regarding FUSEIS with S355 HEA beams, while both tests (T1, T2) were modeled for the system with S700 hollow-section beams. In general, there was compliance of the numerical results with the experimental ones in terms of stiffness, peak resistance and hardening. As mentioned, plasticity and damage were not interdependent in the eventually applied subroutines, and thus the process of load degradation in the models was slower than in reality. Fig. 4.21 and Fig. 4.22 show a fairly good agreement between the superimposed experimental (gray) and numerical (black) response curves for the FUSEIS with beam links. The graph for test T1 (Fig. 4.21a) covers the loading cycles until crack initiation. The graphs for T2 (Fig. 4.21a) and T5 (Fig. 4.22) refer to the six first loading cycles. In most cases, crack indicators (Fig. 4.23) appeared earlier in the models than in the tests, as discussed shortly.

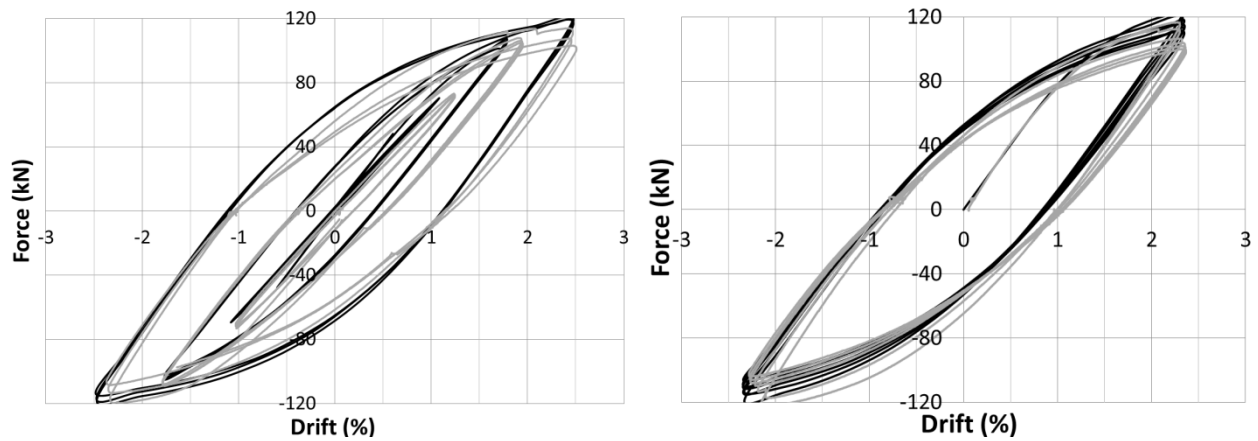


Fig. 4.21 FUSEIS with S700 beams, comparison between simulated (black) and experimental (gray) response for (a) T1 (cycles prior to cracks) (b) T2 (first 6 loading cycles)

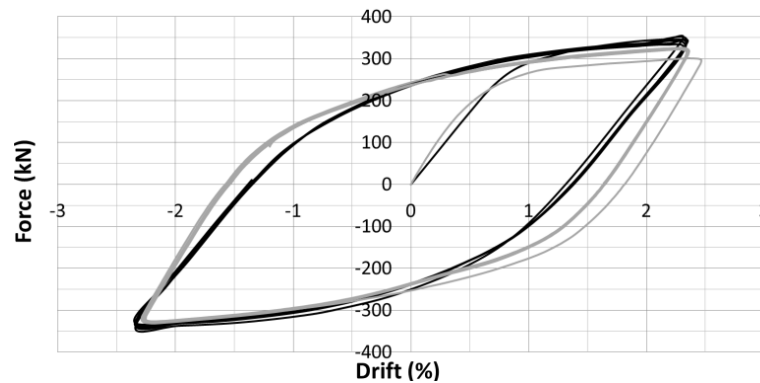


Fig. 4.22 FUSEIS with S355 beams, comparison between simulated (black) and experimental (gray) response for test T5 (first 6 loading cycles)

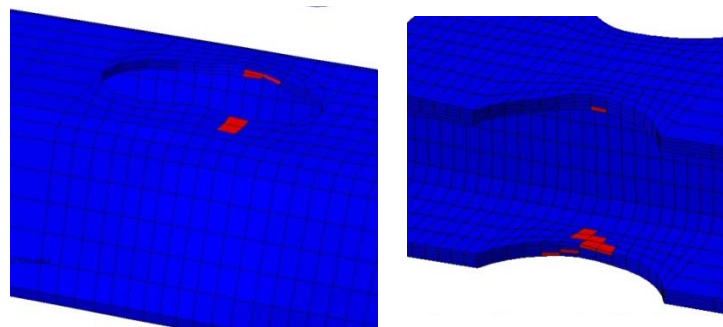


Fig. 4.23 Fracture indicators (red) in RBS regions of SHS link (S1) and HEA link (S1)

4.4.4 Response of FUSEIS with pins models

Fig. 4.24 shows the juxtaposed experimental (gray) and numerical (black) response curves for FUSEIS with S500 pin links for both increasing and constant amplitude tests (T7 and T8). In Fig. 4.24a, the simulation of T7 stops at the loading cycles prior to link separation (first cracks were

observed at 1.1% drift). In Fig. 4.24b, twelve loading cycles of T8 are simulated (the test included thirty-six cycles while cracks initiated from the sixth). Overall, the system's lateral resistance and stiffness are well approached, although the shape of the hysteresis loops is not accurately captured. The characteristic "pointing shape" of the response curves due to catenary action is more profound in the models. Fig. 4.25 shows the crack initiation indicators for test T7 in links S5 and S4. Overall, the critical locations on the pins and the damage sequence were realistically reproduced, although the numerical prediction of the critical loading cycles was conservative (Table 4.3).

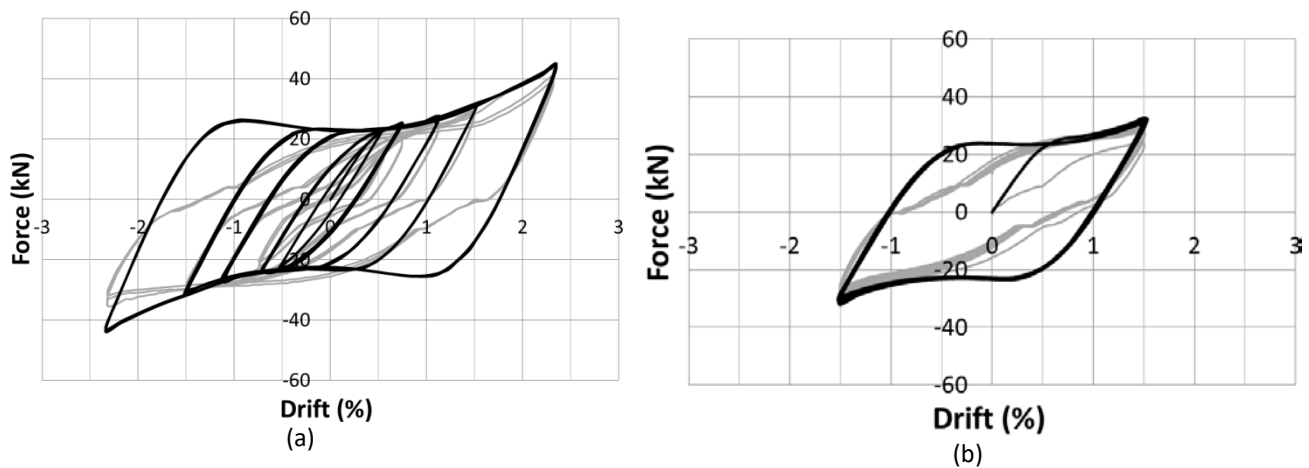


Fig. 4.24 FUSEIS with S500 pins, comparison between simulated (black) and experimental (gray) response for (a) T7 (cycles prior to link separation) (b) T8 (first 12 loading cycles)



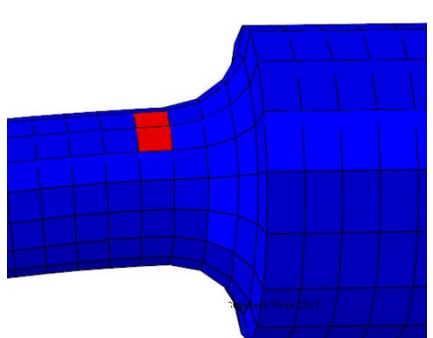
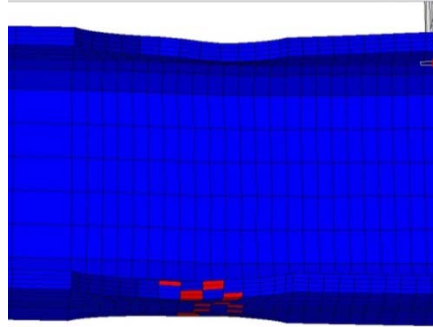
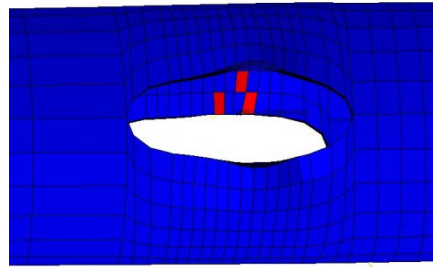
Fig. 4.25 Fracture initiation (red) in links S5 and S4

4.4.5 Evaluation of damage prediction

Table 4.3 summarizes the critical drift (ϕ) or the number of loading cycle (N) at which cracks initiated in the experiments (exp) and the simulations (sim). More details on damage of links during tests are given in Chapter 3 (Table 3.13 and Table 3.23). In general, damage simulation was more accurate for HSS and increasing amplitude tests (T1, T7), while the estimations for S355 specimens were very conservative. Damage in the heat affected zones of the links could not be simulated. To calibrate and provide an efficient numerical tool for damage prediction, improvements could be made in all levels (coupled material subroutines, mesh refinement in critical zones, more powerful computers). Fig. 4.26 gives snapshots of the actual and simulated damage in selected links.

Table 4.3 Comparison of damage in tests and simulations

FUSEIS Links	Test	Loading	Crack initiation in tests (in Si link)*	Crack initiation in models (in Si link)*
S700 Hollow beams	T1	Increasing amplitude	$\phi_{exp} = 2.5\%$ (S1,S2) $N_{exp} = 9$ (S2)	$\phi_{sim} = 2.5\%$ (S1,S2) $N_{sim} = 3$ (S1)
	T2	Constant amplitude	$N_{exp} = 10$ (S5) $N_{exp} = 15$ (S1)	$N_{sim} = 3$ (S5) $N_{sim} = 4$ (S2)
S355 HEA beams	T5	Constant amplitude	$N_{exp} \leq 34$ (S3)	$N_{sim} = 4$ (S3)
			$N_{exp} = 38$ (S4) $N_{exp} = 43$ (S1) $N_{exp} = 45$ (S2)	$N_{sim} = 4$ (S1) $N_{sim} = 5$ (S2)
S500 Pin links	T7	Increasing amplitude	$\phi_{exp} = 1.1\%$ (S5) $\phi_{exp} = 1.5\%$ (S4) $\phi_{exp} = 2.3\%$ (S2) $N_{exp} = 6$ (S5)	$\phi_{sim} = 1.1\%$ (S5) $\phi_{sim} = 1.1\%$ (S4) $\phi_{sim} = 2.3\%$ (S2) $N_{sim} = 3$ (S5)
	T8	Constant amplitude	$N_{exp} = 9$ (S4) $N_{exp} = 14$ (S2)	$N_{sim} = 3$ (S4) $N_{sim} = 7$ (S2)

* ϕ is the critical drift, N is the critical loading cycle

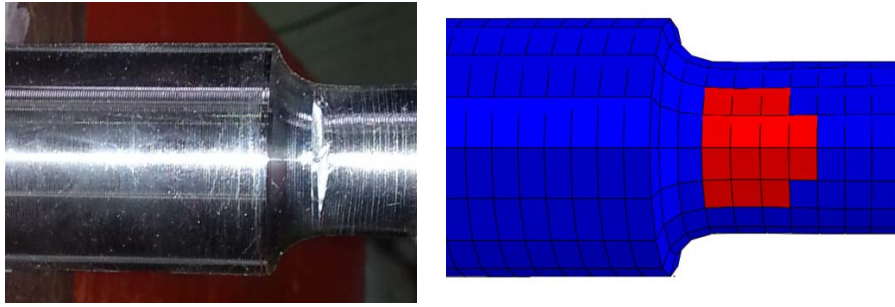


Fig. 4.26 Actual and simulated (red) damage in (a) CHS link-S2, (b) HEA-S3, (c) pin-S5 and (d) pin- S2

4.5 Conclusions

The Vierendeel theoretical model accurately describes the behavior of FUSEIS with beam links. To determine the system's lateral resistance, the mean value of the material's yield (f_y) and tensile strength (f_u) should be used. In the FUSEIS with pin links, catenary action is developed at large deformations, and thus an analytical approach accounting for the axial forces of the pins and the system's deformation is more accurate.

The systems were simulated with beam elements using two different software packages and two different approaches for material non-linearity (distributed and concentrated plasticity). Both types of models, appropriately calibrated, reproduced realistically the FUSEIS with beam links behavior. To capture the actual stiffness of these systems, the semi-rigid bolted connections of the links were considered.

Simulation using solid elements was also carried out in order to verify the material subroutines developed in the framework of this research. The subroutines were based on a hybrid numerical-experimental approach and involved the calibration of each material's plasticity and damage. The increased computational demands for these analyses limited the number of tests to be simulated. Overall, damage simulation was realistic in the increasing amplitude tests using S500 and S700 links, but conservative in the constant amplitude tests, especially for S355.

Chapter 5: Case studies and performance evaluation

5.1 Introduction

EN1993 and EN1998 provide requirements for resistance, serviceability and durability of steel structures translated to checks in the Ultimate and Serviceability Limit States. To account for the beneficial effects of ductility, EN 1998-1 has adopted the concept of behavior factor “q” which allows the reduction of the design forces, as determined by elastic analysis, by accepting a level of damage in selected members. However, EN 1998-1 suggests q-factor values for a limited number of structural systems, without considering innovative systems.

This chapter presents two case studies of low and mid-rise regular steel buildings with participation of FUSEIS beam links systems. The structures are first designed by adoption of a q-factor and later their performance is evaluated by nonlinear static and dynamic analyses. Lateral stability of the buildings is provided in the 5-story building by the combined action of FUSEIS systems and selected moment-resisting frames or solely by the FUSEIS systems in the 2-story building. The reference buildings are designed according to EN1993 and EN1998, assuming a q factor equal to 3.5 (ductility class medium- DCM), considering, in addition, the FUSEIS design guidelines provided in (Dougka 2016, Vayas (Ed) 2017, Vayas et al. 2013). High strength steel (HSS) S700 is used for the FUSEIS beams, while all other members are from S355. It is noted that such material combination does not represent the current state of practice. In addition, as will be seen later, this design approach does not fully utilize the advantages of HSS, given the relative flexibility of the FUSEIS and the fact that the seismic design of buildings is largely controlled by stiffness demands. However, this investigation’s aim is to obtain realistic cases of reference frames (archetype models) with HSS dissipative members, whose performance at defined Limit States will be evaluated.

Following the design of the case studies, representative 2D models were formulated as a basis for non-linear analyses. Material non-linearity was simulated considering both in-cycle and cyclic deterioration which is important for dynamic analyses. As a first step for performance assessment, preliminary behavior factors (q_{st}) and Limit states (in terms of inter-story deformations) were defined via pushover analysis. The response of the archetype models was then studied by means of non-linear time-history analyses, using prescribed sets of ground-motions whose amplitudes were scaled to various intensities, covering the range from elastic behavior to collapse (Incremental Dynamic Analysis - IDA). Their performance was finally evaluated with respect to the defined Limit States. To do so, two different methodologies were followed: the widely-known suggested by FEMA 695 and the recently developed by the INNOSEIS European research project.

For a system containing replaceable dissipative elements to be efficient, it should fulfill two requirements: (i) limitation of inelastic deformations to these elements only and (ii) feasibility of repair. The first can be attained via capacity design, while the latter is related with the extent of the structure's residual deformations. This issue was investigated via additional dynamic analyses using ground-motions scaled at design level.

5.2 Design of the case studies

5.2.1 Configuration, loads and selection of profiles

Two archetypes with the same plan view (Fig. 5.1) were designed and evaluated, as listed in Table 5.1: a low-rise building (2-story) and a mid-rise one (5-story). The structures are regular with three bays in each direction. Their dimensions are typical for steel structures: story height (H) is 3.4 m and the span lengths are 6.0 m and 7.0 m in the two directions. Eight FUSEIS systems were applied in each structure (four per direction), the axial distance of the FUSEIS columns being 2.0 m (magenta in Fig. 5.1). In Y direction the systems were placed only in the structure's perimeter while in X direction one system was placed in each frame's axis. In the 2-story case study, lateral stability is provided by the FUSEIS systems alone so all the beams are simply supported. In the 5-story, lateral stability is provided by the combined action of the FUSEIS systems with selected moment resisting frames (the "strong beams" are in cyan in Fig. 5.1). All columns have pinned supports.

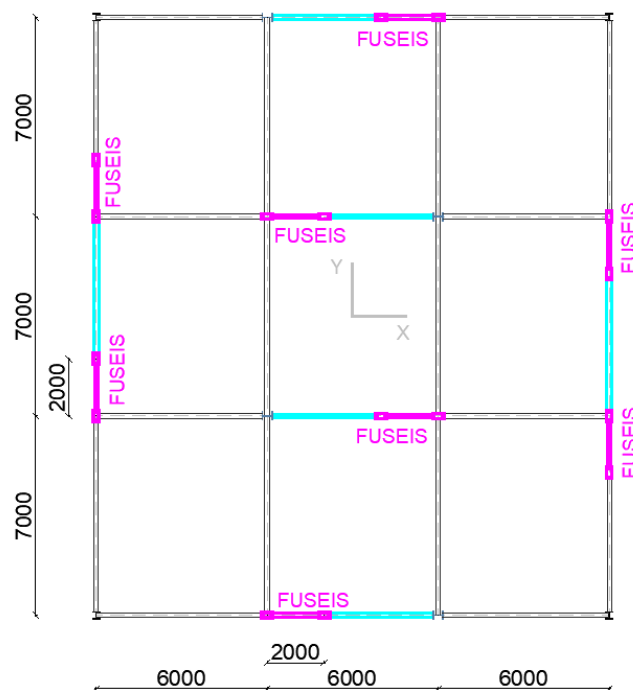


Fig. 5.1 Plan view of both case studies

Table 5.1 Case studies

Case study	CS1	CS2
Stories	5	2
Total height (H_{tot})	17.0 m	6.8 m
Lateral stability	FUSEIS + Frames	FUSEIS

The gravity loads are typical of residential and office buildings. The slabs consist of composite decks with 130 mm total depth and steel sheeting with approximately 70 mm height supported by secondary beams. Table 5.2 summarizes the load assumptions for the design. The self-weight of the steel members was automatically calculated by the software.

Table 5.2 Loads for the design of the building archetypes (EN1991-1, EN1998-1)

Gravity loads	Load (kN/m^2)
Dead (from composite slabs)	2.5
Additional dead	2.0
Imposed (category B, table 6.2 EN1991-1)	3.0
Seismic parameters	
Spectrum type	1
Peak ground acceleration	0.25g
Importance class/ factor	II/ $\gamma=1.00$
Ground type / Soil factor	B/ $S=1.2$
Period parameters T_B, T_C, T_D (sec)	0.15, 0.5, 2.0
Factor ϕ for variable actions in seismic combinations (for 5-story case study):	
- Roof	1.00
- Stories with correlated occupancies	0.80
Behavior factor q_{des}	3.50

Fig. 5.2 shows the models created for design using SAP2000 software. The loads imposed in the gravity direction were applied via surface elements with “zero properties” while the slabs’ diaphragm action was simulated via nodal constraints. To optimize utilization of the main beams in both directions the secondary beams were placed along either X or Y axis in consecutive spans (Fig. 5.3). All secondary beams were simply supported and modeled as composite members with constant effective width $b_{eff1} \approx L/4$, according to EN1994-1-1. Rigid offsets were used in all beams to account for their actual length. The FUSEIS beams were designed with reduced beams sections (RBS), in order to protect the connections areas. Therefore the fuses were divided in five zones, representing the full and the reduced sections. However, due to the relatively small dimensions of the RBS, their effect on the structure’s overall behavior during elastic analysis was of minor importance.

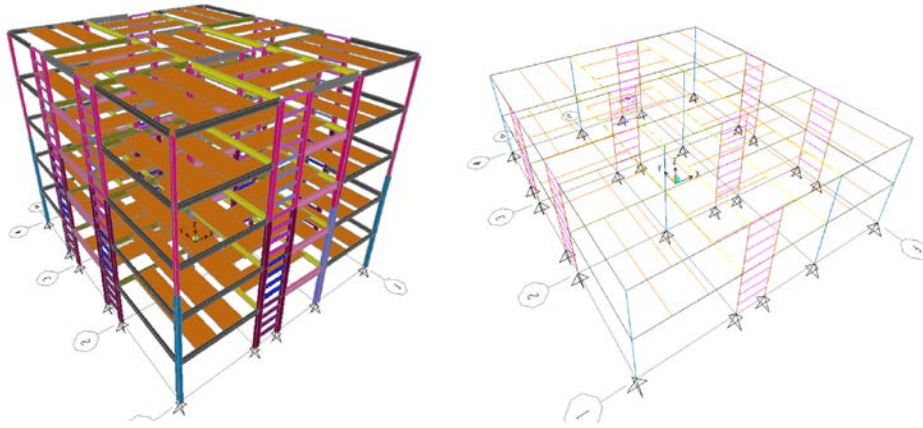


Fig. 5.2 3D view of models for (a) 5-story and (b) 2-story case study

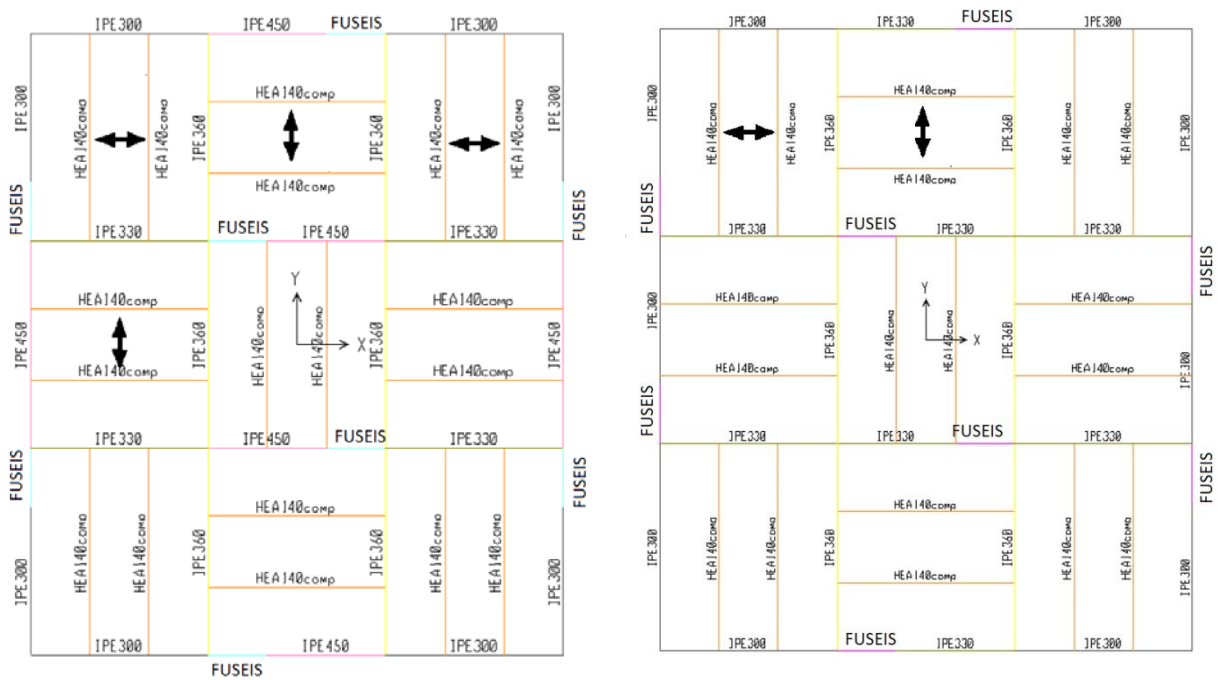


Fig. 5.3 Beam profiles and slabs' load distribution (arrows) via secondary beams (a) 5-story (b) 2-story

The following load combinations were taken into account:

-Ultimate Limit State (ULS):

$$1.35 \cdot \Sigma G + 1.50 \cdot \Sigma Q$$

-Serviceability Limit State (SLS):

$$1.00 \cdot \Sigma G + 1.00 \cdot \Sigma Q$$

-Seismic Combinations:

$$1.00 \cdot \Sigma G + 0.3 \cdot \Sigma \phi \cdot Q \pm 1.00 \cdot E_x \pm 0.30 \cdot E_y$$

$$1.00 \cdot \Sigma G + 0.3 \cdot \Sigma \phi \cdot Q \pm 1.00 \cdot E_y \pm 0.30 \cdot E_x$$

Where ΣG is the sum of the dead loads, ΣQ is the sum of the imposed loads and $E_{x,y}$ is the seismic action in direction X and Y respectively.

Table 5.3 summarizes the profiles of the members for both case studies. The FUSEIS consisted of beam links with hollow-section profiles and S700 steel, while the FUSEIS columns were hollow-sections members of S355. The rest of the frames' members were of open-section profiles and S355. In the 5-story structure, the sections of the FUSEIS beams and the columns are reduced along the height of the building, following the decrease of story shear (the profile reduction in upper stories is indicated with "/" in Table 5.3. Overall, the flexibility of the FUSEIS systems renders the limitation of inter-story drift expressed in EN1998-1, critical. In the 5-story case study, this was resolved by rigidly connecting the systems with strong beams. The above demand - combined with the material's high strength - resulted in dissipative members with rather small utilization ratios. As a consequence, the capacity design checks (which ensure the intended configuration of plastic hinges) were made using rather increased load factors. The application of HSS in this case study may seem "paradoxical" as the advantage of HSS in using significantly smaller profiles is not fully capitalized due to stiffness demands. However, the main objective is to evaluate the seismic performance of FUSEIS links made of HSS, based on case studies complying with the current codes.

Table 5.3 Profiles of members

Member	Steel	5-story (CS1)	2-story (CS2)
FUSEIS columns	S355	RHS 400x200x14.2 / RHS 300x200x10.0	RHS 400x200x12.5
FUSEIS beams (for i story)	S700	RHS250x100x8 (1) RHS220x120x7.1 (2) RHS180x120x6 (3) RHS160x80x7.1 (4) RHS140x80x5 (5)	RHS180x120x6 (1) RHS180x120x6 (2)
Columns	S355	HEB360/HEB340 (internal) HEB260/HEB180 (corners)	HEB260
Strong Beams	S355	IPE450/IPE400	-
Main Beams	S355	IPE 300 (perimeter) IPE 330, 360 (X,Y)	IPE 300 (perimeter) IPE 330, 360 (X,Y)
Secondary Beams	S355	HEA140 (composite)	HEA140 (composite)

Table 5.4 gives the properties of the reduced beam sections (RBS) of the FUSEIS beams, designed in accordance with the code provisions discussed in Chapter 3. Apart from geometric properties, the table also summarizes the most important checks regarding the RBS design, as given by the following equations:

$$M_{cf} < M_{pl,Rd,b} \quad \text{Eq. 5-1}$$

where M_{cf} is the capacity design bending moment that develops at the column face when a plastic hinge forms at the centre of the RBS and $M_{pl,Rd,b}$ is the beam's plastic moment resistance.

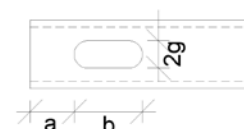
$$V_{Ed,max} / V_{pl,Rd} < 0.5 \quad \text{Eq. 5-2}$$

where $V_{Ed,max}$ is the shear force in the section of plastic hinge formation ($V_{Ed} = 2 * M_{pb,Rd,RBS} / L_{RBS}$), and $V_{pl,rd}$ is the shear resistance of the full section ($V_{pl,rd} = A_v * f_y / \sqrt{3}$).

Table 5.4 Properties of RBS in FUSEIS beams

	FUSEIS beam (story)	Full section W_{pl} (x1000 mm ³)	RBS section W_{plRBS} (x1000 mm ³)	Flange reduction 2g (mm)	Distance a (mm)	RBS length b (mm)	M_c/M_{plRdb}	$V_{Ed,max}/V_{plRd}$
CS1	RHS250x100x8 (1)	385.4	298.3	44.0	60	175.0	0.95	0.22
	RHS220x120x7.1	312.8	222.1	60.0	60	143.0	0.85	0.20
	RHS180x120x6 (3)	201.7	139.1	60.0	60	129.6	0.82	0.18
	RHS160x80x7.1 (4)	148.6	108.7	46.0	48	120.0	0.85	0.13
	RHS140x80x5 (5)	91.8	67.0	38.4	48	105.0	0.83	0.13
CS2	RHS180x120x6 (1)	201.7	151.6	48	60	129.6	0.89	0.19
	RHS180x120x6 (2)	201.7	139.1	60	60	129.6	0.82	0.18

Note: Dimensions a, b, 2g of RBS as shown below:



5.2.2 Modal analysis

Table 5.5 summarizes the modal analysis results for the first five modes of the structures in terms of periods and mass activation. In the 5-story, the first vibration mode is translational in Y direction (Fig. 5.4a) and the second is translational in X direction (Fig. 5.4b). For the 2-story the first two modes have practically the same period and activate the same mass percentage in both directions ($T_1=0.80$ sec, 92% cumulative mass participation).

Table 5.5 Modal analysis results

Mode	5-story (CS1)			2-story (CS2)		
	Period (sec)	Cumulative mass participation (X direction)	Cumulative mass participation (Y direction)	Period (sec)	Cumulative mass participation (X direction)	Cumulative mass participation (Y direction)
1	1.30	0.00	0.80	0.80	0.92	0.00
2	1.10	0.84	0.80	0.80	0.92	0.92
3	0.85	0.84	0.80	0.57	0.92	0.92
4	0.47	0.84	0.94	0.25	0.92	0.92
5	0.39	0.96	0.94	0.25	0.92	0.92

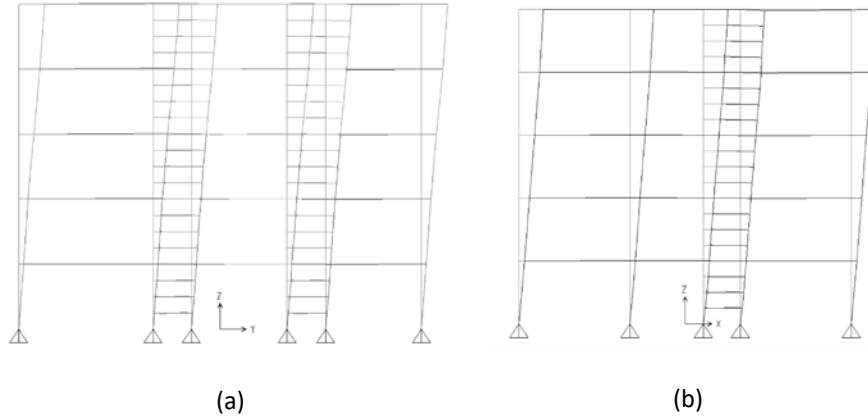


Fig. 5.4 5-story case study: (a) First mode, translational in Y direction (b) Second mode, translational in X direction

As the fundamental periods (T_i) in both directions are $T_c = 0.5 < T_i < T_D = 2.0$, equation 3.15 of EN1998-1 is checked and verified in both directions as follows:

$$S_d(T_i) \geq \beta \cdot a_g, \text{ where } \beta = 0.2 \quad \text{Eq. 5-3}$$

5-story:

$$V_{\text{tot},x}/P_{\text{tot}} = 0.087 > 0.2 \cdot 0.025 = 0.05$$

$$V_{\text{tot},y}/P_{\text{tot}} = 0.073 > 0.2 \cdot 0.025 = 0.05$$

2-story

$$V_{\text{tot},x}/P_{\text{tot}} = 0.125 > 0.2 \cdot 0.025 = 0.05$$

$$V_{\text{tot},y}/P_{\text{tot}} = 0.125 > 0.2 \cdot 0.025 = 0.05$$

where $V_{\text{tot},i}$ are the seismic forces and P_{tot} are the gravity loads in the seismic combinations.

5.2.3 Design checks

In order to perform plastic analysis, all dissipative members should have Class 1 cross-sections to ensure sufficient rotational capacity of the plastic hinges (EN1993-1, EN1998-1). This condition - primarily targeted at steels with strength up to 460 MPa - is verified using Eq. 5-4 and is rather adverse for HSS due to the reduced values of ϵ :

$$c/t \leq 72\epsilon = 41.8 \text{ (part subject to bending)} \quad \text{Eq. 5-4}$$

$$c/t \leq 33\epsilon = 19.1 \text{ (part subject to compression)}$$

where c , t length and thickness defined in Table 5.2 of EN1993-1 and $\epsilon = \sqrt{235/f_y} = 0.58$ for S700.

The most critical check was regarding the overall stiffness of the structure and the limitation of inter-story drift. According to EN1998-1, for buildings having ductile non-structural members the maximum allowed inter-story drift is 1.5%, assuming the displacements induced by the design spectrum multiplied with the behavior factor q_{des} , as follows:

$$d_r \cdot v < 0.0075 \cdot h \quad \text{Eq. 5-5}$$

where

$v=0.5$ (reduction factor, recommended value for importance classes I,II)

h is the story's height

d_r is the difference of the average lateral displacements d_s at the top and bottom of each story ($d_s = q_{\text{des}} \cdot d_e$, where d_e are displacements determined by the design response spectrum)

Table 5.6 shows the check according to Eq. 5-5 is satisfied for both case studies.

Table 5.6 Check of inter-story drifts (%)

Story	5-story case study		2-story case study	
	Inter-story drift in direction X	Inter-story drift in direction Y	Inter-story drift in direction X	Inter-story drift in direction Y
1	0.99 %	0.99 %	1.48 %	1.48 %
2	0.82 %	0.92 %	1.16 %	1.17 %
3	0.82 %	0.99 %	-	-
4	0.84 %	1.11 %	-	-
5	0.66 %	1.01 %	-	-

Regarding the influence of 2nd order effects, the following condition was checked for each story and each direction according to EN1998-1:

$$\theta = P_{tot} * d_r / (V_{tot} * h) \quad \text{Eq. 5-6}$$

where

P_{tot} refers to the gravity loads considered in the seismic design, and

V_{tot} is the total seismic story shear.

In case $0.1 < \theta < 0.2$ the 2nd order effects may be approximately taken into account by multiplying the relevant seismic action effects by a factor equal to $1/(1-\theta)$. As shown in Table 5.7 referring to the 5-story case study, the influence of 2nd order effects should be taken into account, especially in the Y direction. To do so, the internal forces caused by the seismic combinations are increased by 1.16. Regarding the 2-story, Table 5.8 shows that the 2nd order effects should also be considered, while the respective increasing factor is 1.13.

Table 5.7 Influence of 2nd order effects in 5-story case study

Story	P_{tot} (kN)	$V_{tot,x}$ (kN)	θ_x	$1/(1-\theta_x)$	$V_{tot,y}$ (kN)	θ_y	$1/(1-\theta_y)$
1	10986	951	0.114	1.13	801	0.136	1.16
2	8779	850	0.085	1.00	703	0.114	1.13
3	6576	716	0.076	1.00	590	0.110	1.12
4	4382	573	0.065	1.00	490	0.100	1.00
5	2221	359	0.041	1.00	347	0.065	1.00

Table 5.8 Influence of 2nd order effects in 2-story case study

Story	P_{tot} (kN)	$V_{tot,x}$ (kN)	θ_x	$1/(1-\theta_x)$	$V_{tot,y}$ (kN)	θ_y	$1/(1-\theta_y)$
1	4486	561	0.119	1.13	562	0.118	1.13
2	2257	361	0.073	1.00	360	0.073	1.00

According to EN1998-1, to ensure a homogenous dissipative behavior of the links, it should be checked that the maximum overstrength Ω_i , as defined in Eq. 5-7, does not differ from the minimum value by more than 25%.

Table 5.9 and Table 5.10 give the results of this check for each story and each structure. The value of $(1/\Omega_i)$ represents the utilization ratio of the links. As can be seen the fuses utilization ratios are generally small, due to their increased strength. For each case study, the $\min\Omega_i$ will be used as a reference for the capacity design checks discussed shortly.

$$\begin{aligned} \Omega_i &= M_{pl,Rd,i} / M_{Ed,i} \\ \max\Omega_i / \min\Omega_i &< 1.25 \end{aligned} \quad \text{Eq. 5-7}$$

Table 5.9 Ω factors of the FUSEIS links per story (5-story)

Story	FUSEIS beam	max (1/ Ω)	Ω_i	($\Omega_i - \Omega_{min}$) / Ω_{min} (%)
1	RHS250x100x8	0.41	2.45	0.0
2	RHS220x120x7.1	0.33	3.06	24.8
3	RHS180x120x6	0.33	3.03	23.6
4	RHS160x80x7.1	0.37	2.70	10.3
5	RHS140x80x5	0.35	2.86	16.6

Table 5.10 Ω factors of the FUSEIS links per story (2-story)

Story	FUSEIS beam	max (1/ Ω)	Ω_i	($\Omega_i - \Omega_{min}$) / Ω_{min} (%)
1	RHS180x120x6 (1)	0.49	2.06	0.0
2	RHS180x120x6 (2)	0.40	2.48	20.4

As mentioned, the design of the RBS in the FUSEIS beams was controlled by Eq. 5-1 and Eq. 5-2. In addition, the FUSEIS beams were checked against developing compression and shear that could decrease their moment resistance or rotation ability as follows (Table 5.11):

$$\begin{aligned} N_{Ed} &< 0.15 * N_{plRd} \\ V_{Ed} &< 0.50 * V_{plRd} \\ M_{Ed} &< M_{pl,Rd} \end{aligned} \quad \text{Eq. 5-8}$$

where N_{Ed} , V_{Ed} , M_{Ed} are the design forces/moments and N_{plRd} , V_{plRd} , M_{plRd} are design resistances according to EN1993.

Table 5.11 Check against compression and shear forces for the FUSEIS beams

Story	5-story (CS1)			2-story (CS2)		
	FUSEIS beam	$N_{Ed} / N_{plRd,RBS}$ (%)	V_{Ed} / V_{plRd} (%)	FUSEIS beam	$N_{Ed} / N_{plRd,RBS}$ (%)	V_{Ed} / V_{plRd} (%)
1	RHS250x100x8	1.8	8.4	RHS180x120x6	0.4	8.9
2	RHS220x120x7.1	2.3	6.1	RHS180x120x6	1.3	6.5
3	RHS180x120x6	3.9	5.4	-	-	-
4	RHS160x80x7.1	3.8	4.6	-	-	-
5	RHS140x80x5	6.0	4.0	-	-	-

As discussed in Chapter 3, the cyclic tests on FUSEIS with S700 beam links showed that the system reached its peak resistance at 2.5% drift, corresponding to approximately 54 mrad link rotation (θ). Table 5.12 summarizes the link rotations induced by the design spectrum for each FUSEIS link (corresponding to drifts from Table 5.6), which are rather smaller than 54mrad. It should be noted though, that the FUSEIS dimensions in the case studies are not the same as in the tests.

Table 5.12 Rotation of FUSEIS links (θ) induced by the design spectrum

Story	5-story (CS1)		2-story (CS2)	
	FUSEIS beam	θ (mrad)	FUSEIS beam	θ (mrad)
1	RHS250x100x8	12.4	RHS180x120x6	18.5
2	RHS220x120x7.1	11.5	RHS180x120x6	14.7
3	RHS180x120x6	12.4	-	-
4	RHS160x80x7.1	13.1	-	-
5	RHS140x80x5	11.9	-	-

To avoid brittle failures, the non-dissipative members were verified to resist the capacity design action effects as following:

$$\begin{aligned}
 N_{CD,Ed} &= N_{Ed,G} + 1.1 \cdot \gamma_{ov} \cdot \Omega \cdot N_{Ed,E} \\
 M_{CD,Ed} &= M_{Ed,G} + 1.1 \cdot \gamma_{ov} \cdot \Omega \cdot M_{Ed,E} \\
 V_{CD,Ed} &= V_{Ed,G} + 1.1 \cdot \gamma_{ov} \cdot \Omega \cdot V_{Ed,E}
 \end{aligned}
 \tag{Eq. 5-9}$$

where:

$N_{Ed,G}$, $M_{Ed,G}$, $V_{Ed,G}$ = refer to the non-seismic actions included in the seismic design combinations

$N_{Ed,E}$, $M_{Ed,E}$, $V_{Ed,E}$ = refer to the seismic design actions

$$\gamma_{ov} = 1.25$$

Ω refers to minimum overstrength or maximum ($1/\Omega$)

According to Eq. 5-9,

Table 5.9 and Table 5.10, the capacity check was performed by multiplying the seismic design actions with a factor equal to 3.37 for the 5-story (CS1) and 2.83 for the 2-story (CS2).

The columns were subjected to section and member checks according to EN1993-1, as follows:

$$N_{CD,Ed} / N_{plRd} + M_{CD,yEd} / M_{y,Rd} + M_{CD,zEd} / M_{z,Rd} \leq 1.0 \quad \text{Eq. 5-10}$$

where $N_{CD,Ed}$, $V_{CD,Ed}$, $M_{CD,Ed}$ are the capacity design forces and moments, while N_{plRd} , V_{plRd} , M_{plRd} are the design resistances.

Reduction of the moment resistances due to shear forces was not required.

The member check is dictated by the following equations (equations 6.61, 6.61 in EN1993-1):

$$N_{CD,Ed} / (\chi_y * N_{plRd}) + k_{yy} * M_{CD,yEd} / (\chi_{LT} * M_{y,Rd}) + k_{yz} * M_{CD,zEd} < M_{z,Rd} \leq 1.0$$

$$N_{CD,Ed} / (\chi_z * N_{plRd}) + k_{zy} * M_{CD,yEd} / (\chi_{LT} * M_{y,Rd}) + k_{zz} * M_{CD,zEd} < M_{z,Rd} \leq 1.0 \quad \text{Eq. 5-11}$$

where χ_y , χ_z are reduction factors due to flexural buckling, χ_{LT} is reduction factor due to lateral torsional buckling and k_{yy} , k_{yz} , k_{zy} , k_{zz} are interaction factors. The partial factor $\gamma_{M1} = 1.00$ has been omitted from the equations. The checks based on the above equations were performed by the software and the most critical members were verified additionally with hand calculations. Table 5.13 summarizes the members' utilisation ratios.

Table 5.13 Utilisation ratios for non-dissipative members

Member	5-story (CS1)		2-story (CS2)	
	Profile	Utilisation ratio	Profile	Utilisation ratio
Beams	IPE300	0.64	IPE300	0.64
	IPE330	0.68	IPE330	0.68
	IPE360	0.63	IPE360	0.63
Strong beams	IPE450	0.99	-	-
	IPE400	0.69		
Columns	HEB360	0.77		
	HEB340	0.65		
Columns (corner)	HEB260	0.20	HEB260	0.27
	HEB180	0.29		
FUSEIS columns	RHS400x200x14.2	0.90	RHS400x200x12.5	0.66
	RHS300x200x10.0	0.90		

Regarding the serviceability limit state (SLS), the deflections of the beams were checked against the following limits provided by the national annex of EN1993-1-1:

$$\delta_{\max} < L/250 \text{ and}$$

$$\delta_2 < L/300 \quad \text{Eq. 5-12}$$

where δ_2 , δ_{\max} are the beam deflections due to live loads and SLS characteristic combination respectively.

This check was critical for the design of the main beams.

The rigid connections of the structure are assumed to be designed with sufficient moment capacity to undertake the actions caused by the capacity design combinations.

5.3 Nonlinear models

2D models of the case studies were formulated, representative of an inner frame along X direction. The first models were created in SAP2000 based on the design models as shown in Fig. 5.5: the simply supported beams are depicted as interrupted, the strong beams as continuous and the FUSEIS beams are divided in five zones to account for the RBS zones. The models incorporated material and geometric nonlinearities. The loads were applied only on the beam-to-column joints. To achieve an equivalent loading state the reactions per load case were obtained from the original 3D models for each column and were used as reference.

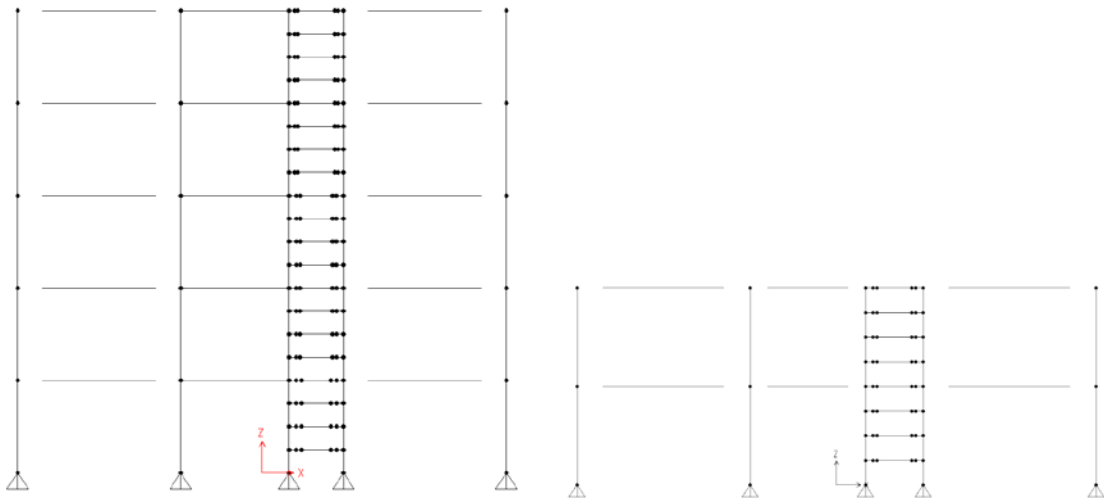


Fig. 5.5 Configuration of 2D models (in SAP2000)

Modal analysis showed very good agreement between the 3D and the 2D models (Table 5.14 and Table 5.5).

Table 5.14 Modal analysis results for simplified 2D models

Mode	5-story		2-story	
	Period (sec)	Cumulative mass participation ratio	Period (sec)	Cumulative mass participation ratio
1	1.10	83 %	0.82	92 %
2	0.39	96 %	0.19	100 %
3	0.21	99 %	-	-

The capacity curves obtained via pushover analysis are hereby presented in terms of “roof drift” (dr_{roof}) which is the ratio of roof displacement (δ_{roof}) over the structure’s total height. However this does not represent the most adverse inter-story drift throughout the pushover analysis of the 5-story model where plastic hinge formation was sequential along the structure’s height. Fig. 5.6

illustrates the evolution of inter-story drifts at three characteristic phases of the pushover analysis: first yield, maximum base shear and final step (5% roof drift). In the 2-story frame the difference between the deformation of the critical (1st) story and the average drift was rather small.

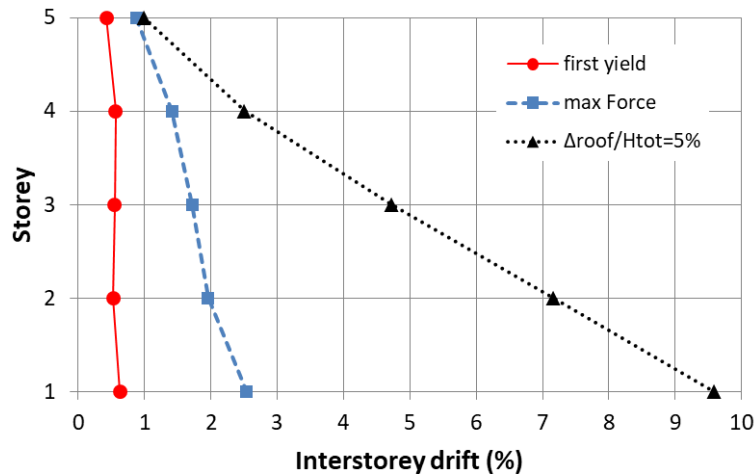


Fig. 5.6 Evolution of inter-story drifts (%) at three characteristic phases of pushover analysis for 5-story model

Material nonlinearity in the SAP2000 models was considered by assigning potential plastic hinges in all critical locations. Nominal values were assumed for the yield and tensile strengths of the materials. The plastic hinges on the beams were defined by a moment/rotation relationship while for the columns N-M interaction was considered. For the S700 fuses the suggested hinge parameters given in Chapter 4 were used. The properties of the column hinges were automatically calculated according to FEMA 356. To investigate optimization of computational time and convergence issues, two simulation approaches were compared: (a) a “lighter” version with potential hinges in the fuses’ RBS and at the ends of the strong beams and (b) a “heavier” one with additional potential hinges in the links’ full sections and the columns. The plastic mechanism in both cases was the same, while comparison of the capacity curves showed no significant effect of the additional hinges, thanks to capacity design (Fig. 5.7a). In the 5-story, first yield in a column occurred for roof displacements larger than 0.53 m. By that point, the plastic hinges in the FUSEIS links of three stories had entered their degradation phase, as indicated with yellow in Fig. 5.7b. In the 2-story no plastic hinges were activated in the columns. Hence, the approach of the “lighter” versions was preferred for the Incremental Dynamic Analyses.

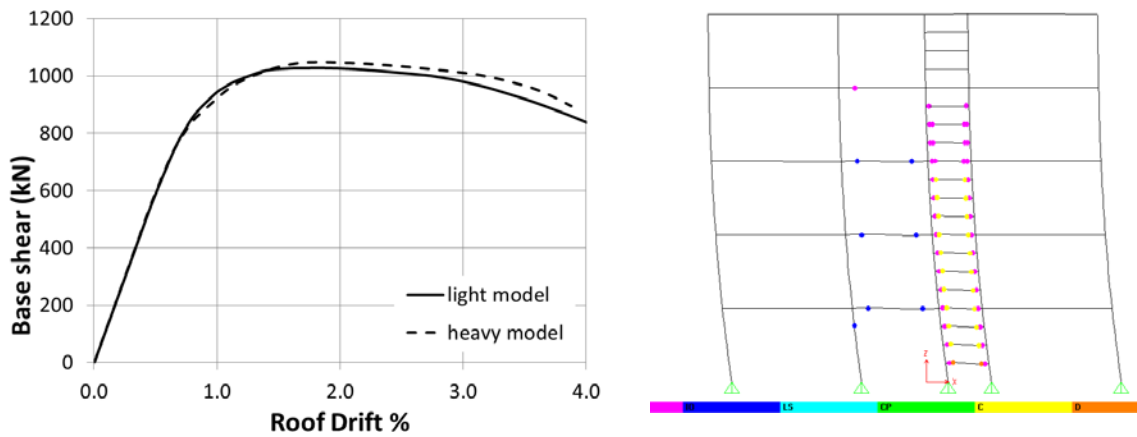


Fig. 5.7 (a) Comparison of capacity curves between “light” and “heavy” model (with additional hinges) in SAP2000 and (b) plastic hinge results at first column yield (“heavy” model)

Eventually, the case studies were modeled using OpenSees, which is a more suitable platform for the performance of Incremental Dynamic Analysis (IDA). These models incorporated the distributed plasticity concept which is regarded as more accurate and less susceptible to the effects of Rayleigh damping assumptions (Chopra and McKenna 2015). As discussed, the definition of material nonlinearity in the dissipative members is of major importance as the models should be able to reproduce both in-cycle and cyclic degradation. Nonlinear members consisting of fiber sections were used to simulate the links' RBS and the strong beams. As described in Chapter 4, uniaxial hysteretic materials were used, defined by stress-strain envelopes with three characteristic points. Nominal values were assumed for the yield and the tensile strength, while the coordinates of the third point (degradation) were obtained through calibration between the SAP2000 and the OpenSees models. The cyclic damage parameters were obtained from test calibration. To ensure that the nonlinear members would eventually reach a “fracture” state, the hysteretic materials were coupled with a “min-max” material that imposes failure of the element beyond a threshold strain value. Apart from material nonlinearity, the models were based on the same principals and produced similar results. Fig. 5.8 illustrates the consistency between the “design” (SAP2000) and “assessment” (OpenSees) models.

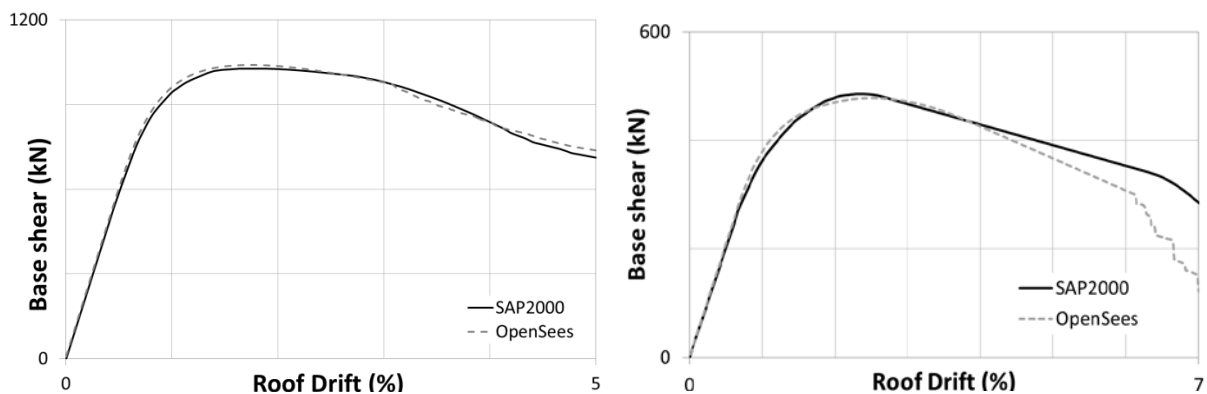


Fig. 5.8 Capacity curves of models in SAP2000 and OpenSees for (a) 5-story and (b) 2-story case study

5.4 Performance based assessment

5.4.1 Pushover analysis

Pushover analysis was performed to assess each model’s plastic mechanism and behavior factor q_{st} defined as the product of overstrength ratio (a_u/a_1) and ductility (μ) (Eq. 5-13).

$$q_{st} = \mu * a_u/a_1 \tag{Eq. 5-13}$$

$$\mu = \delta_{0.2} / \delta_y$$

As can be seen in Fig. 5.9, the overstrength ratio is the maximum base shear over the base shear at first yield, while ductility is the ratio of the roof displacement at 20% strength degradation over the “nominal” yield displacement on the bilinear fit of the capacity curve. According to EN1998-1 at least two vertical distributions of the lateral load should be applied: a uniform pattern and a “modal” pattern based on the fundamental modal shape. For the overstrength ratio, the lower factor obtained should be used. Fig. 5.10 shows the respective capacity curves for the two case studies including a linear fit on the “modal” curves and markers at (nominal) yield and at 20% load degradation. Table 5.15 gives the results obtained by Eq. 5-13. In both cases, the estimated q_{st} is larger than the assumed design factor ($q_{des} = 3.5$). However, pushover analysis does not account for either the cyclic loading demand or the seismic risk, so the behavior factors have to be reevaluated using dynamic analysis.

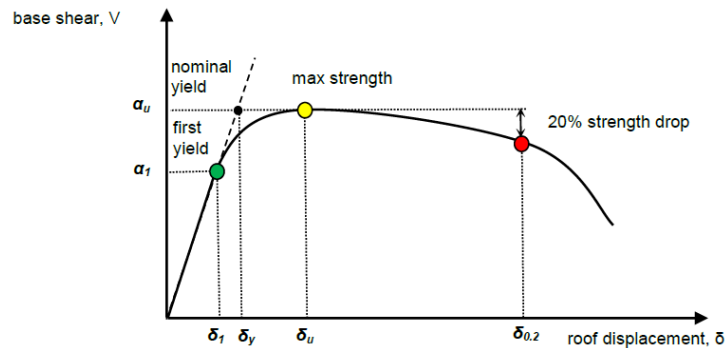


Fig. 5.9 Determination of q factor in pushover analysis (generic curve from Vamvatsikos et al. 2017)

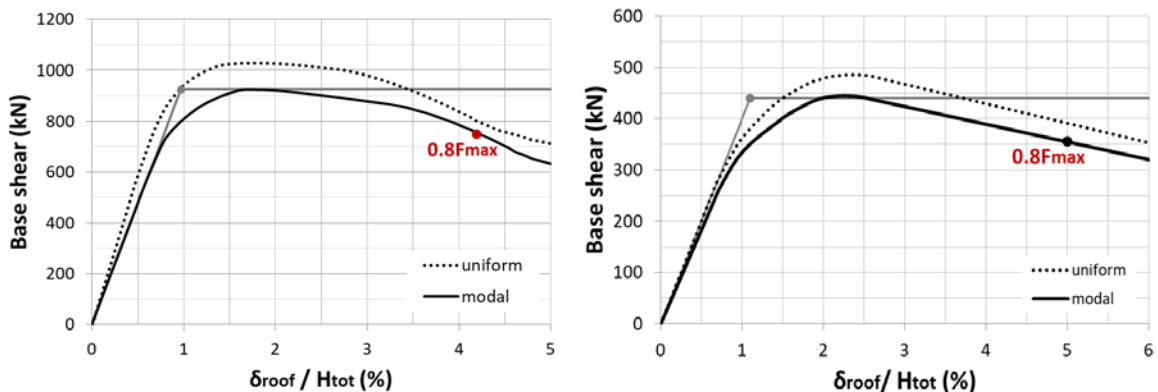


Fig. 5.10 Pushover curves using uniform and modal lateral load distribution for (a) 5-story and (b) 2-story

Table 5.15 Evaluation of behavior factor q_{st} based on pushover analysis results (Eq. 5-13)

Case study	5-story	2-story
Overstrength ratio a_u/a_1	1.7	1.7
Ductility μ	4.3	4.6
Factor q_{st}	7.4	7.7

Comparison between the responses of the two case studies showed that in the 5-story yielding of the plastic hinges was more gradual, starting from the links at the lowest stories and proceeding upwards. On the contrary in the 2-story case study all RBS members of the 1st story yielded simultaneously and were shortly followed by those of the 2nd story. This affected the definition of limit state criteria as shortly discussed.

5.4.2 Limit states for performance evaluation

The performance of the case studies was verified against two limit states, Life Safety (LS) and Collapse Prevention (CP). Regarding LS, the component-based approach described in Vamvatsikos et al. (2017) and Vulcu et al. (2017) was followed, taking into account the backbone curve of the most critical dissipative member in each model. As shown in Fig. 5.11, three characteristic points were defined in the critical component's response curve corresponding to maximum strength, 20% drop and 80% drop.

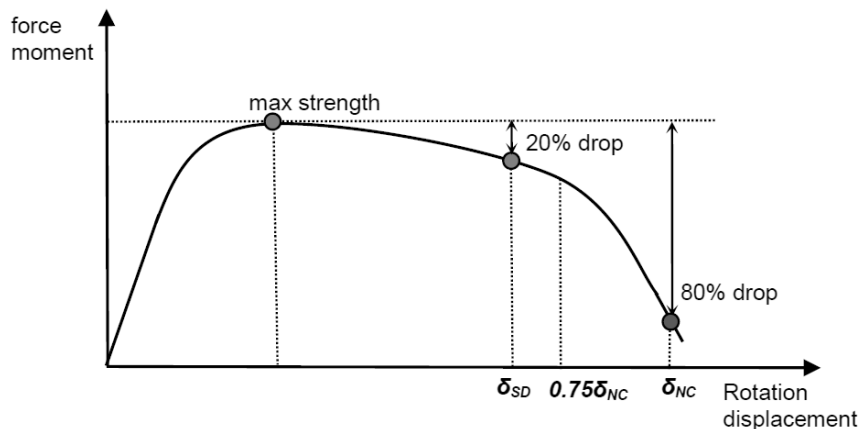


Fig. 5.11 Critical component-based performance levels (generic curve from Vamvatsikos et al. 2017)

Following the definition of these characteristic points, the following component-based performance levels were defined:

- Near Collapse (NC), which is the rotation/displacement corresponding to 80% drop (δ_{NC})
- Significant Damage (SD), corresponding to the minimum between 20% drop and $0.75\delta_{NC}$

Life Safety (LS) is assumed violated when the first link reaches Significant Damage (SD). In both models the critical fuses were in the first floor. Fig. 5.12 illustrates the SD performance levels and the points corresponding to 20% overall load degradation on the structures' capacity curves. As can be seen, in the 2-story model the yellow and red lines corresponding to SD criteria result in similar drifts, close to the point of 20% load degradation. Aiming to incorporate a more conservative criterion, the 10% moment degradation of the critical fuse was adopted (blue line in Fig. 5.12b). Given the differences between the roof drifts and the respective maximum inter-story drifts, Table 5.16 summarizes the limit states used for evaluation in both terms.

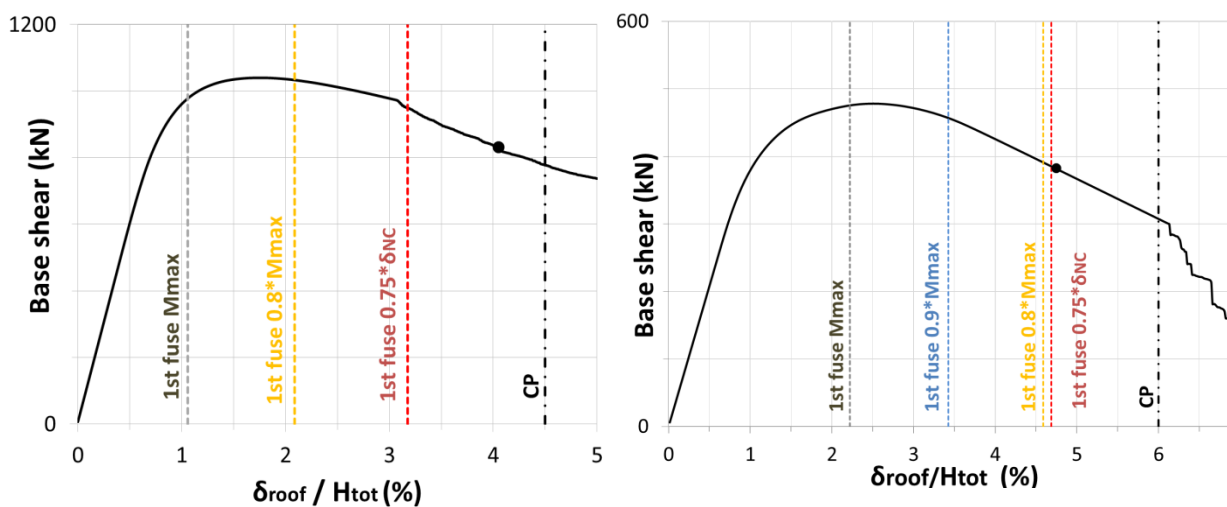


Fig. 5.12 Performance evaluation limit states on capacity curves for (a) 5-story and (b) 2-story

Regarding Collapse Prevention (CP), FEMA350 suggests a limit of 10% inter-story drift for low or mid-rise steel moment resisting frames. In this case, more conservative criteria were adopted based on the pushover results. For the 5-story, CP was correlated with the point at which the first plastic hinge in a column reached its moment bearing capacity. The 2-story model did not exhibit plastic hinge formation in the columns. However, a sudden drop of the frame's resistance can be observed for roof drift larger than 6.0%, so CP limit was defined accordingly.

Table 5.16 Limit states for performance evaluation

Limit state	5-story (CS1)		2-story (CS2)	
	LS	CP	LS	CP
Max. inter-story drift (%)	4.2	8.0	3.8	6.3
$\delta_{\text{roof}} / H_{\text{tot}}$ (%)	2.1	4.5	3.4	6.0

5.4.3 Incremental Dynamic Analysis (IDA)

5.4.3.1 Methodology and basic assumptions

Incremental dynamic analysis (IDA) is a parametric analysis method for the estimation of structural performance under seismic loads. It involves subjecting a structural model to a set of ground motions scaled to multiple levels of intensity, thus producing a set of response curves (Vamvatsikos and Cornell 2002, 2005). Some of the matlab routines developed by D. Vamvatsikos (available online in <http://users.ntua.gr/divamva/software.html>) were used for running IDA and post-processing the results. IDA results were used for performance evaluation of the two case studies according to two similar but different approaches: the widely-known FEMA 695 methodology (which is more USA-oriented) and the one recently developed within the European research project INNOSEIS. The methods are similar in the sense that they result in acceptance or rejection of the design q-factor employed in archetype buildings. However, they differ in the way they determine compliance with the requirements.

The selection of suitable measures for intensity and “damage” (referred as engineering demand parameter) as well as the post-processing of the results are of primary importance for IDA. The Intensity measure (IM) characterizes the intensity of a ground motion record. In this case, the 5%-damped first mode spectral acceleration was selected ($S_a(T_1)$), since our case studies are medium and low-height buildings, and hence first-mode dominated. As engineering demand parameter (EDP), the maximum inter-story drift ratio (dr_{max}) was selected representing the maximum recording (in absolute values) within all stories throughout each time-history analysis. According to FEMA 350 this is a primary parameter for performance evaluation as it can relate to a structure’s ability to resist p- Δ instability, to plastic rotation demands and to beam-column connection assemblies. Thus, it is a good predictor of the performance of beams, columns and connections. The assumed critical EDP values are given in Table 5.16.

The selection of ground motions creates a link between seismic hazard and structural response which is necessary for IDA. The required number of records is reduced due to the ground-motions’ scaling. According to Shome and Cornell (1999) and Vamvatsikos and Cornell (2005), scaling using a relatively efficient IM (such as $S_a(T_1)$) does not significantly bias the results, while ten to twenty records are usually enough to provide sufficient accuracy in seismic demand estimation for mid-rise buildings. In this case, two sets of ground motions were used, corresponding to each assessment methodology. For the FEMA 695 methodology the Far-Field record set was used, including twenty-two component pairs of horizontal ground motions (from sites located greater than or equal to 10 km from fault rupture) (Deierlein et al. 2008). The records correspond to fourteen seismic events around the world dating between 1971 and 1999 with magnitudes ranging from M6.5 to M7.6. The

sets include records from soft rock and stiff soil sites and from shallow crustal sources (mostly strike-slip and thrust mechanisms). According to FEMA 695, large-magnitude events dominate collapse risk and generally have longer durations of shaking, which is important for collapse evaluation. To avoid event bias, no more than two of the strongest records are taken from each earthquake. This record set is primarily intended for buildings with first-mode periods less than 4 seconds. Regarding INNOSEIS methodology, two sets of ground motions corresponding to two groups of sites across Europe are suggested, representative for medium and high-seismicity. The latter, hereby adopted, consists of sites with PGA of approximately 0.30g. The record sets are available online on <http://innoseis.ntua.gr>. Site selection was performed according to the EU-SHARE seismicity model (Giardini et al. 2013) by matching the required acceleration to the PGA with a 10% in 50 years probability of exceedance, whilst aiming at an even distribution across Europe. The resulting sites for high seismicity are: Athens (GR), Perugia (IT) and Foscani (RO). A single rock soil type was considered, with a shear wave speed in the upper 30m of 800m/s (v_{s30}), corresponding to soil type B per EN1998. Record selection was performed using the multi-site Conditional Spectrum approach (Lin et al. 2013a,b, Kohrangi et al. 2017) in order for the records to be hazard consistent with the aforementioned sites. The applied record set includes thirty ordinary recordings (not pulse-like, not long duration), derived from fifteen seismic events, appropriate for the “2% in 50 years” level of intensity.

The number of scale factors per ground-motion is arbitrary, aiming to cover the range between the structure’s elastic behavior and collapse. In this case, eight “runs” were performed for each ground-motion as an improved stepping algorithm was used that allowed increasing or decreasing of the IM steps provisionally while accounting for demand estimation by filling in the gaps created by the enlarged steps (“hunt and fill” tracing algorithm, Vamvatsikos and Cornell 2002).

IDA results in a set of points defined in (IM, EDP) coordinates for each ground-motion record, interpolation of which leads to an IDA curve. The interpolation may be linear or spline (piecewise cubic interpolation). In this case spline interpolation was adopted which provides more accurate results with fewer “runs”, as suggested by Vamvatsikos and Cornell (2005).

Incremental dynamic analysis (IDA) is accelerogram and structural model specific. Differences between the various IDA curves represent different model responses when subjected to ground-motions with different frequency characteristics, which are not predictable in advance. Therefore it is important to summarize the obtained results and quantify their randomness. The IDA curves are often summarized with the 16%, 50% and 84% fractile curves. Calculation of the median curve (50%) is a prerequisite for the estimation of the model’s median collapse intensity (S_{CT}) used in the FEMA 695 methodology and for the fragility curves as discussed shortly.

A fragility curve illustrates the estimated probability of exceeding a selected limit state at different acceleration levels. In mathematic terms, the fragility function is the probability function of seismic demand exceeding a certain limit state given the seismic intensity. The most common seismic fragility function is the lognormal cumulative distribution function (CDF). A lognormal distribution function can be defined by two parameters, the mean (μ) and the standard deviation (β) of the associated normal distribution. In this case, the mean can be obtained by the median IDA curve (e.g. for the collapse limit state $\mu = \ln(S_{CT})$), while the standard deviation represents dispersion in the results due to uncertainties. Uncertainty influences the shape of a collapse fragility curve, as additional uncertainty tends to flatten the curve. Bakalis and Vamvatsikos (2018) give an overview of methods to generate fragility curves based on IDA results.

FEMA 695 identifies the following sources of uncertainty:

- Record-to-record uncertainty (β_{RTR}), due to variability in the response of a model subjected to different ground motion records. Values ranging from 0.35 to 0.45 are consistent among various building types while $\beta_{RTR}=0.40$ is suggested for the performance evaluation of ductile systems using the Far-Field record set.
- Design requirements uncertainty (β_{DR}), related to the completeness and robustness of the design requirements
- Test data uncertainty (β_{TD}), associated with confidence in the test data used to define the system
- Modeling uncertainty (β_{MDL}), related to the model's efficiency to represent the structural response and simulate all significant deterioration modes contributing to collapse. The indirect evaluation of non-simulated collapse modes using alternative limit state checks is also taken into account.

Regarding β_{DR} , β_{TD} and β_{MDL} , the suggested values of uncertainty based on assumed information quality are: (A) Superior - 0.10 (B) Good - 0.20, (C) Fair - 0.35 and (D) Poor - 0.50. Total uncertainty (β_{TOT}) is given by:

$$\beta_{TOT} = \sqrt{\beta_{RTR}^2 + \beta_{DR}^2 + \beta_{TD}^2 + \beta_{MDL}^2} \quad \text{Eq. 5-14}$$

5.4.3.2 Performance evaluation and q factor verification, based on FEMA 695 methodology

Fig. 5.13 and Fig. 5.14 illustrate the result of the IDA analysis as a set of 44 response curves, in terms of first mode spectral acceleration ($S_a(T1)$ -g) and maximum inter-story drift. All curves exhibit a distinct linear elastic region that ends when the first nonlinearity occurs. After this, some curves

exhibit softening while others weave around the elastic slope or even exhibit hardening. As hardening at increased seismic intensity seems paradoxical, a possible explanation for multi-story buildings is that a stronger ground motion may cause earlier yielding of one floor thus turning it to a fuse that relieves the higher stories. The IDA curves “terminate” at different intensity levels. Collapse for each ground motion is presumed either directly from the analysis (dynamic instability, “flatline”) or indirectly through failure criteria (Table 5.16).

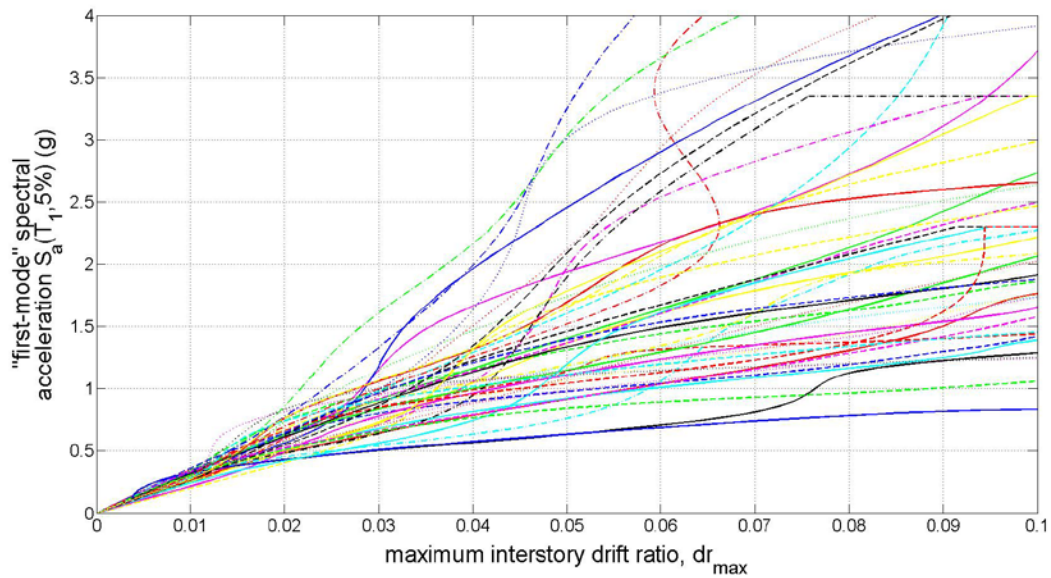


Fig. 5.13 IDA curves for 5-story case study (FEMA 695 “Far-Field” record set)

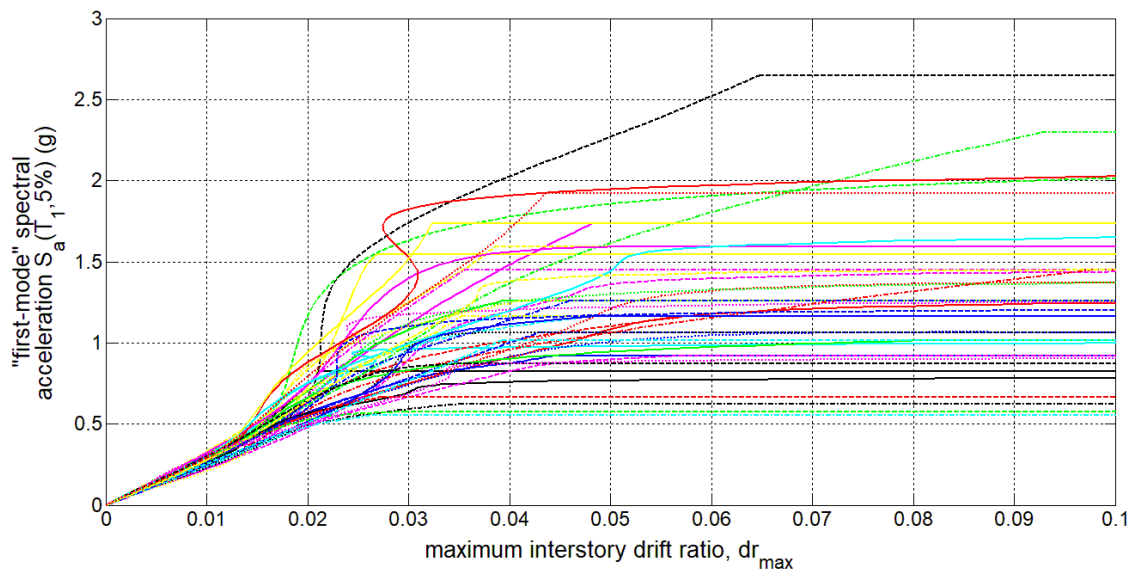


Fig. 5.14 IDA curves for 2-story case study (FEMA 695 “Far-Field” record set)

In Fig. 5.15 the IDA curves are summarized using the 16%, 50% and 84% fractiles. The intensity level at which the median curve “flatlines” or reaches the defined Collapse Prevention (CP) limit is the median collapse intensity, denoted as S_{CT} . In the 2-story model, the median curve flattens at approximately 4.5% maximum interstory drift prior to the CP limit given in Table 5.16 based on the pushover analysis.

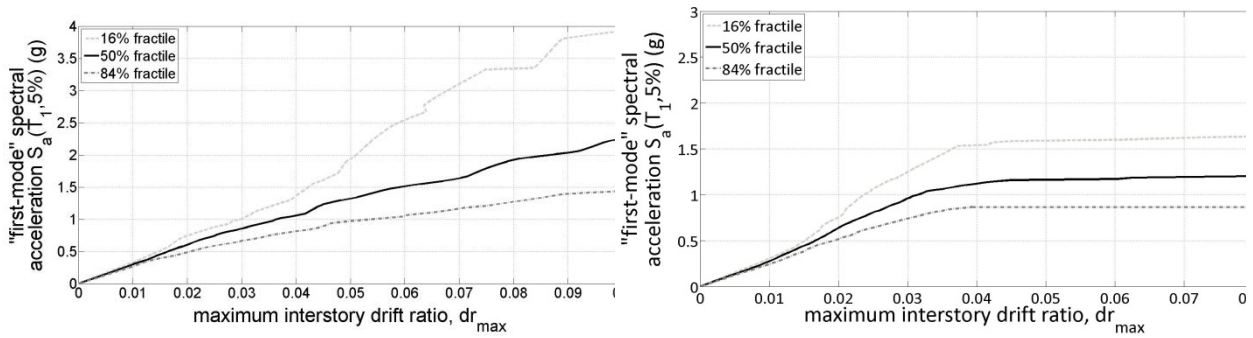


Fig. 5.15 IDA fractile curves for (a) 5-story and (b) 2-story

Acceptability is measured by comparing a “collapse margin ratio” (CMR) - after adjustments (ACMR) - to benchmark values that depend on the total system uncertainty β_{TOT} and acceptable probability of failure (10%). The collapse margin ratio (CMR), which characterizes the structure’s safety, is given by Eq. 5-15 as the ratio of the median collapse capacity S_{CT} over the intensity of the maximum considered earthquake (MCE), S_{MT} .

$$CMR = S_{CT}/S_{MT} \quad \text{Eq. 5-15}$$

The Maximum Considered Earthquake (MCE) is an earthquake with a 2% probability of exceedance in 50 years. Assuming a Poisson model for the occurrence of earthquakes, the mean return period T_R of a seismic event (which is the inverse of Mean Annual Frequency - MAF or λ) is given by:

$$T_R = 1/\lambda = -T_L / \ln(1-P) \quad \text{Eq. 5-16}$$

where T_L is the reference time period and P is the probability that at least one event will occur in T_L . Using Eq. 5-16, the return period of the MCE is $T_R = 2475$ years while its mean annual frequency (MAF) is given by Eq. 5-17a. According to American provisions (FEMA 695, ASCE 7-05) MCE is assumed to correspond to 1.5 times the design response spectrum. In this case, the 1.5 multiplication factor will be adjusted to the European standards, as described in the following paragraph.

$$\begin{aligned} \lambda(\text{MCE}) &= 1/T_R = 1/2475 = 0.000404 & \text{(a)} \\ \lambda(\text{EN1998}) &= 1/T_R = 1/475 = 0.002107 & \text{(b)} \end{aligned} \quad \text{Eq. 5-17}$$

According to EN1998-1, the reference peak ground acceleration (PGA) for each seismic zone corresponds to the return period of the seismic action for the No-collapse performance requirement. This is associated with a 10% probability of exceedance in 50 years, or else 475 years return period (Eq. 5-16) and mean annual frequency λ given by Eq. 5-17b. EN1998-1 states that the annual rate of exceedance (λ) of the reference PGA_R is given by Eq. 5-18, where the value of exponent k depends on seismicity. In general, k values are in the range of 2 to 4 while the recommended value for regions of high seismicity in Europe is $k=3$ (Acun et al. (Eds) 2012).

$$\lambda(PGA_R) = k0 * PGA_R^{-k}, \text{ suggested } k=3 \quad \text{Eq. 5-18}$$

Division of the two parts of Eq. 5-17 leads to $\lambda(\text{MCE})/\lambda(\text{EN1998}) \approx 0.192$. Application of this division in Eq. 5-18 leads to a respective ratio of accelerations ($PGA_{\text{MCE}}/PGA_{\text{EN1998}}$) equal to 1.73. This factor will be used to obtain the MCE acceleration instead of the 1.50 suggested by American provisions.

Collapse capacity can be significantly influenced by the frequency content (spectral shape) of the ground motion record set. Baker and Cornell (2006) have shown that rare ground motions, such as those corresponding to the MCE, have a distinctive spectral shape, that is peaked at the period of interest and drops off more rapidly at longer or shorter periods. Given the fact that the ground motion intensities were scaled based on the first-mode spectral acceleration ($Sa(T1)$), the effects of the spectral shape should be accounted for. FEMA 695 provides a simplified solution to this issue via tabulated spectral shape factors (SSF) based on the structure's fundamental period T and ductility (Table 7-1a in FEMA 695). The collapse margin ratio (CMR) is converted into an adjusted collapse margin ratio (ACMR) using Eq. 5-19.

$$\text{ACMR} = \text{SSF} * \text{CMR} \quad \text{Eq. 5-19}$$

Considering the previously defined fundamental periods and ductility values of the models, the spectral shape factor for the 5-story is $\text{SSF} = 1.19$ while for the 2-story $\text{SSF} = 1.16$.

Regarding uncertainties, for the 5-story case study and Life Safety (LS) performance level, the following assumptions were made: $\beta_{\text{RTR}}=0.40$, $\beta_{\text{DR}}=0.20$, $\beta_{\text{TD}}=0.20$ and $\beta_{\text{MDL}}=0.10$. Application of Eq. 5-14 led to total uncertainty $\beta_{\text{TOT,LS}} = 0.50$. For the evaluation of CP, the total uncertainty was increased by 20% to $\beta_{\text{TOT,CP}} = 0.60$, as higher uncertainties were assumed for β_{DR} and β_{MDL} . For the 2-story, the uncertainties were assumed smaller, as the model was simpler, the criterion for LS was more conservative and no plastic-hinge formation was recorded in the columns. The total uncertainties were $\beta_{\text{TOT,LS}} = 0.40$ and $\beta_{\text{TOT,CP}} = 0.45$.

Fig. 5.16 and Fig. 5.17 show the fragility curves of the two models for the two limit states examined: Life safety (LS) and Collapse Prevention (CP). For each limit state, the data points were collected from the IDA curves and translated to probabilities at different IM levels. In addition, a lognormal cumulative distribution function was drawn for each case, based on the data obtained from the median curves and the assumed uncertainties β_{TOT} . The graphs illustrate curves for two levels of uncertainties: the largest values (continuous lines) were used during evaluation process although the lowest ones provided a closer fit to the data points (dashed lines).

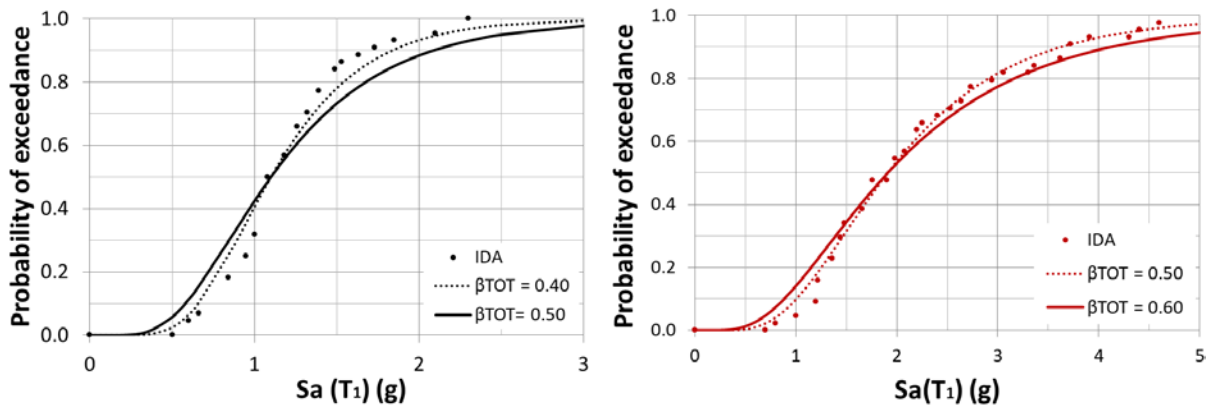


Fig. 5.16 Fragility curves for 5-story case study (a) Life Safety and (b) Collapse prevention

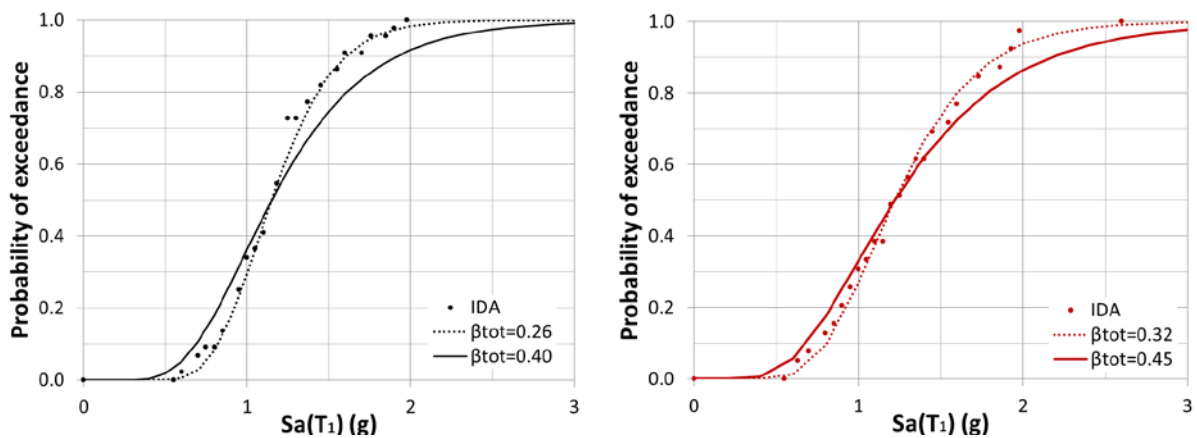


Fig. 5.17 Fragility curves for 2-story case study (a) Life Safety and (b) Collapse prevention

Acceptability is measured by comparing the ACMR to acceptable values provided in FEMA 695 for given β_{TOT} . The evaluation is based on the assumption that up to 10% probability of collapse for the maximum considered earthquake (MCE) is considered acceptable (ACMR10%). Table 5.17 gives the evaluation results for both case studies. For the 5-story, the checks are easily satisfied for both performance levels, and thus the design behavior factor is acceptable. For the 2-story the performance check is also satisfied although the ACMR values are very close to the limit of ACMR10%.

Table 5.17 Verification of q factor for both case studies (FEMA 695 methodology)

Limit State	5-story		2-story	
	LS	CP	LS	CP
Median Value (S_{CT}) – g units	1.10	1.90	1.15	1.24
Intensity of MCE (S_{MT}) – g units	0.595	0.595	0.80	0.80
Collapse margin ratio (CMR)	1.85	3.19	1.44	1.55
Spectral Shape factor (SSF)	1.19	1.19	1.16	1.16
Adjusted Collapse margin ratio (ACMR)	2.20	3.80	1.67	1.80
Total uncertainty β_{TOT}	0.50	0.60	0.40	0.45
Limit ACMR10%	1.90	2.16	1.67	1.78
Check (ACMR > ACMR10%)	ok	ok	ok	ok

5.4.3.3 Performance evaluation and q factor verification, based on INNOSEIS methodology

According to INNOSEIS methodology (Vamvatsikos et al. 2017, Tsarpalis et al. 2020, Vamvatsikos et al. 2020) the acceptance of the design q-factor lies on the comparison of the mean annual frequency (MAF) of a performance objective with an acceptable limit. The MAF of exceeding a damage state is denoted as λ_x (where x can be LS or CP, depending on the examined limit state) and is determined according to the Cornell et al. (2002) fragility-hazard convolution approach by combining the fragility curve with critical hazard curves.

The methodology consists of the following steps:

- i. Hazard estimation and selection of ground motions
- ii. Definition and design of archetype buildings using a trial q-factor
- iii. Development of accurate nonlinear models
- iv. Preliminary evaluation via pushover analysis
- v. IDA
- vi. Definition of performance criteria and estimation of respective fragility curves
- vii. Acceptance or rejection of the trial q-factor

Some of these steps have already been discussed and will not be repeated. Regarding seismic hazard and ground-motions' selection, the high-seismicity record set was used. The hazard curves (Fig. 5.18) corresponding to the high-seismicity sites were computed for each model (based on its fundamental period) and downloaded from "European Facilities for Earthquake Hazard and Risk" website (www.efehr.org).

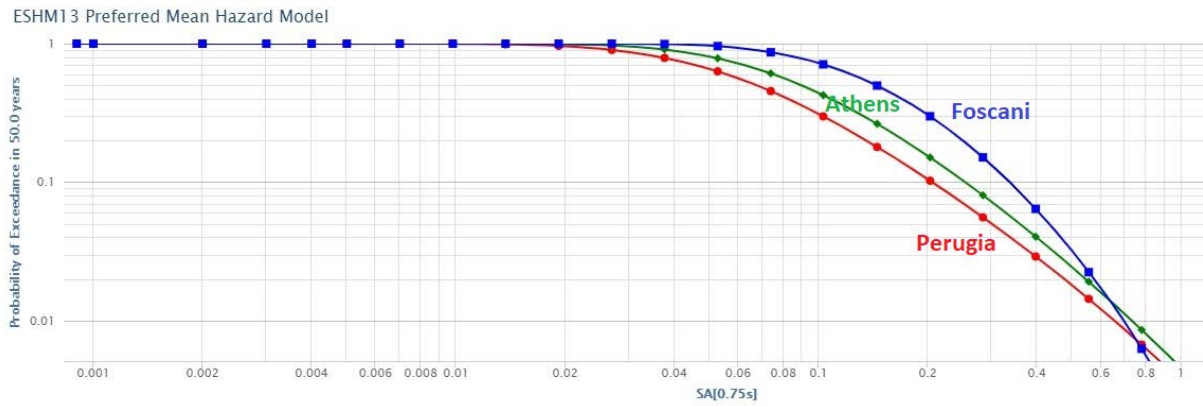


Fig. 5.18 Hazard curves for 2-story case study

Normally, the method suggests using the geometric mean of 5% damped spectral acceleration ordinates (AvgSa) as an intensity measure (IM). However, in this case, the assumed IM is the first-mode spectral acceleration ($S_a(T_1)$) in accordance with the FEMA 695 methodology previously described. Fig. 5.19 and Fig. 5.20 give the IDA results and the respective fractile curves for both case studies.

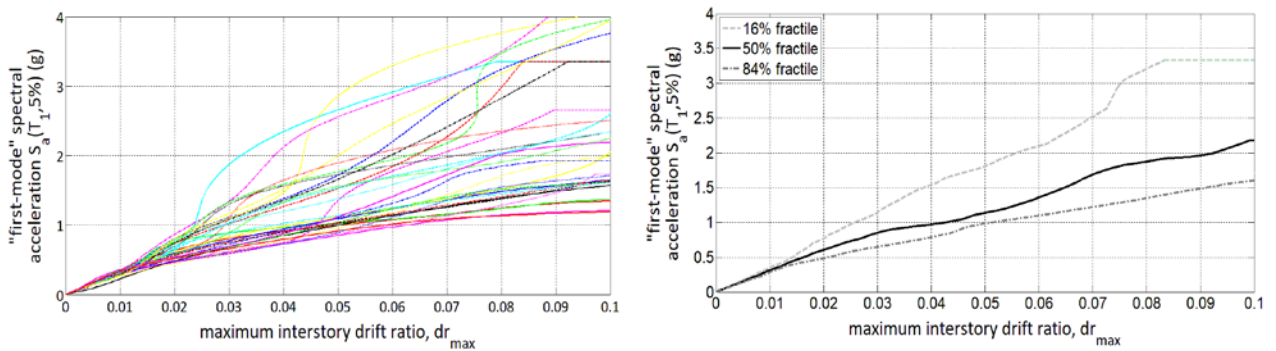


Fig. 5.19 IDA curves and fractiles for 5-story case study (INNOSEIS “high-seismicity” record set)

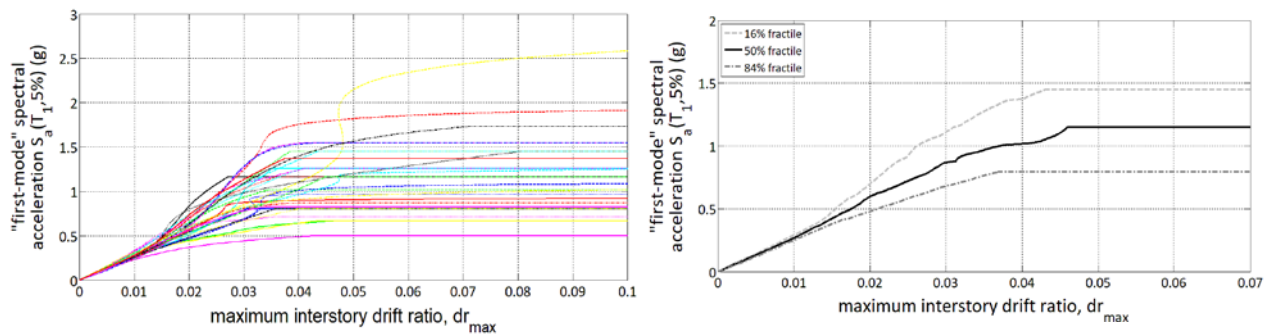


Fig. 5.20 IDA curves and fractiles for 2-story case study (INNOSEIS “high-seismicity” record set)

Regarding fragility estimation, Fig. 5.21 illustrates the fragility curves for both models for the Life Safety (LS) and Collapse Prevention (CP) limit states as given in Table 5.16. The marks represent the IDA results while the lines depict the lognormal distribution fit (LS in black, CP in red). In the 2-story

model, the median curve “flatlined” at approximately 4.5% drift which resulted in fragility curves for LS and CP rather close to each other.

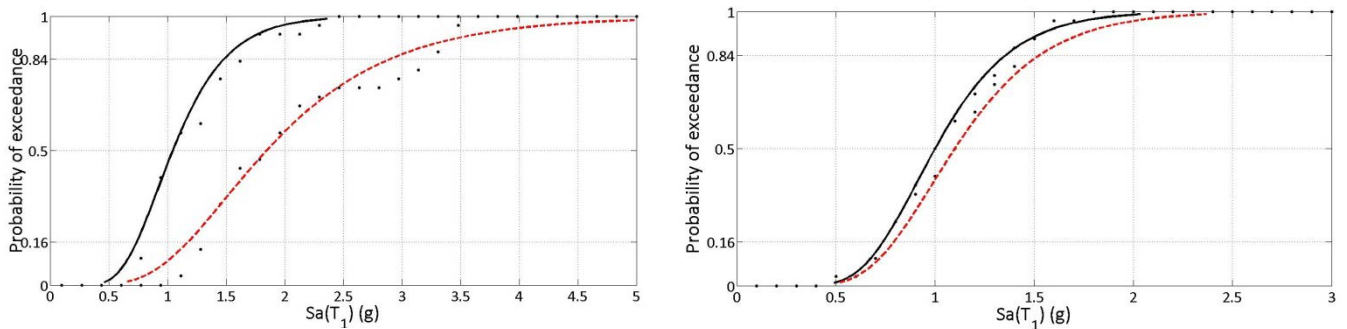


Fig. 5.21 Fragility curves for performance levels LS (black) and CP (red) for (a) 5-story and (b) 2-story model

The seismic fragility output was combined with the seismic hazard curves for Athens, Perugia and Foscani and the respective mean annual frequencies (MAF) of exceedance for each limit state were obtained (Table 5.18, λ_x). In addition, an acceptable MAF for each performance level was defined: for Life Safety (LS) a 10% probability of exceedance in 50 years and for Collapse Prevention (CP) a more conservative limit involving 2% probability of exceedance in 50 years (Table 5.18, λ_{lim}). Eventually, acceptance or rejection of the design-factor was determined by the ratio $\lambda_{lim} / \lambda_x$. As can be seen, the margin ratio was significantly larger than 1 in all cases.

Table 5.18 Verification of q factor based on INNOSEIS methodology

		5-story		2-story	
Limit State		LS	CP	LS	CP
MAF of limit state λ_{lim} (‰)		2.107	0.404	2.107	0.404
Uncertainty β (dispersion)		0.351	0.453	0.306	0.330
Athens	MAF from IDA, λ_x (‰)	0.064	0.017	0.118	0.096
	Margin Ratio ($\lambda_{lim} / \lambda_x$)	33.1	23.2	17.93	4.21
	check ($\lambda_{lim} > \lambda_x$)	ok	ok	ok	ok
Perugia	MAF from IDA, λ_x (‰)	0.044	0.012	0.092	0.076
	Margin Ratio ($\lambda_{lim} / \lambda_x$)	47.42	32.98	22.85	5.34
	check ($\lambda_{lim} > \lambda_x$)	ok	ok	ok	ok
Foscani	MAF from IDA, λ_x (‰)	0.030	0.004	0.086	0.064
	Margin Ratio ($\lambda_{lim} / \lambda_x$)	71.07	100.21	24.50	6.28
	check ($\lambda_{lim} > \lambda_x$)	ok	ok	ok	ok

Table 5.18 gives the evaluation results considering only the inherent uncertainty due to the dispersion of the IDA results. The effect of additional uncertainty on the increase of the mean annual frequencies of exceeding the limit states (λ_x) was investigated based on the assumption that it increases the dispersion of fragility without changing its median. Table 5.19 gives the results of

the additional uncertainty incorporation. As can be seen, the margin ratios are still larger than 1 despite their significant decrease.

Table 5.19 Verification of q factor based on INNOSEIS methodology (considering increased uncertainty)

Limit State	5-story		2-story		
	LS	CP	LS	CP	
MAF of limit state λ_{lim} (‰)	2.107	0.404	2.107	0.404	
Uncertainty β_{tot}	0.43	0.54	0.39	0.45	
Athens	MAF from IDA, λ_x (‰)	0.073	0.024	0.139	0.127
	Margin Ratio ($\lambda_{lim} / \lambda_x$)	28.8	16.6	15.1	3.2
	check ($\lambda_{lim} > \lambda_x$)	ok	ok	ok	ok
Perugia	MAF from IDA, λ_x (‰)	0.053	0.017	0.107	0.097
	Margin Ratio ($\lambda_{lim} / \lambda_x$)	39.7	23.9	19.7	4.2
	check ($\lambda_{lim} > \lambda_x$)	ok	ok	ok	ok
Foscani	MAF from IDA, λ_x (‰)	0.050	0.011	0.128	0.122
	Margin Ratio ($\lambda_{lim} / \lambda_x$)	42.3	36.6	16.4	3.3
	check ($\lambda_{lim} > \lambda_x$)	ok	ok	ok	ok

5.4.4 Time-history analysis for evaluation of residual deformations

To assess the feasibility of potential repairs, the models' residual deformations when subjected to ground motions causing accelerations at design level were investigated. To perform the non-linear time history analyses, the previously presented Far-Field records set was used (FEMA 695). The ground motions were scaled with respect to each model's first mode spectral acceleration ($S_a(T1)$) according to EN1998-1. For the analysis Rayleigh damping was used. The respective factors for the mass matrix and the initial stiffness matrix were calculated assuming damping ratio $\zeta=0.03$ and the first two eigen frequencies of each model. The residual deformations were estimated by calculating the mean value of the recorded drifts during the last 2 seconds of each ground motion instead of using only the last recorded output. This way, the effect of the structures oscillation, after the applied ground motions had diminished due to the relatively small damping value, was taken into account. This effect was more evident in the case of the 5-story while it was of minor importance in the 2-story. Fig. 5.22 shows the residual drifts for each case study, each story and each ground motion while the median values are marked with a "+" symbol. As can be observed, for all ground-motions the residual inter-story drift was less than 0.12% for the 5-story model and less than 0.27% for the 2-story. Residual deformations of this magnitude are not considered significant as discussed in paragraph 2.6. Fig. 5.23 illustrates the maximum interstory drifts (per story and ground motion) for the same analyses. The median values are again indicated with a "+" symbol. As can be seen,

there is large dispersion in the results while in the first story of the 2-story model, the median value slightly exceeds the EN1998-1 limit for buildings with ductile non-structural members (1.5%).

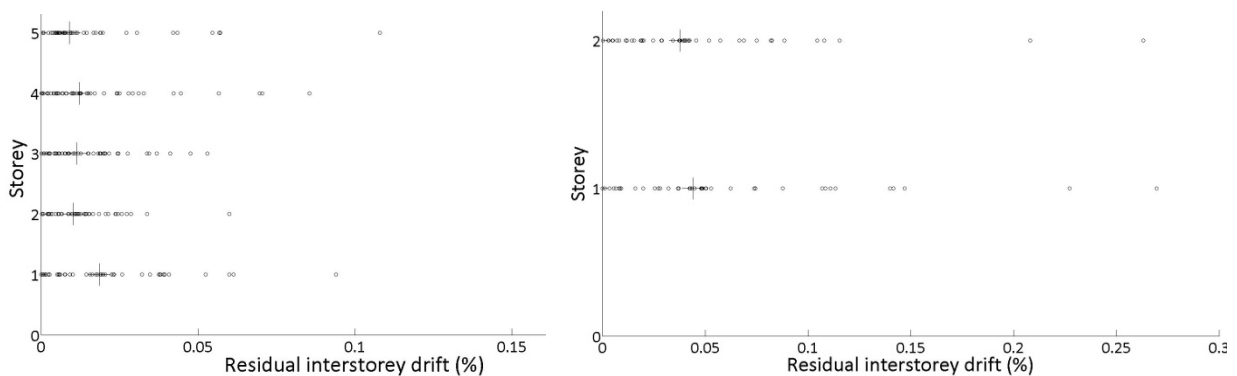


Fig. 5.22 Residual interstorey drifts per story and ground motion for (a) 5-story and (b) 2-story

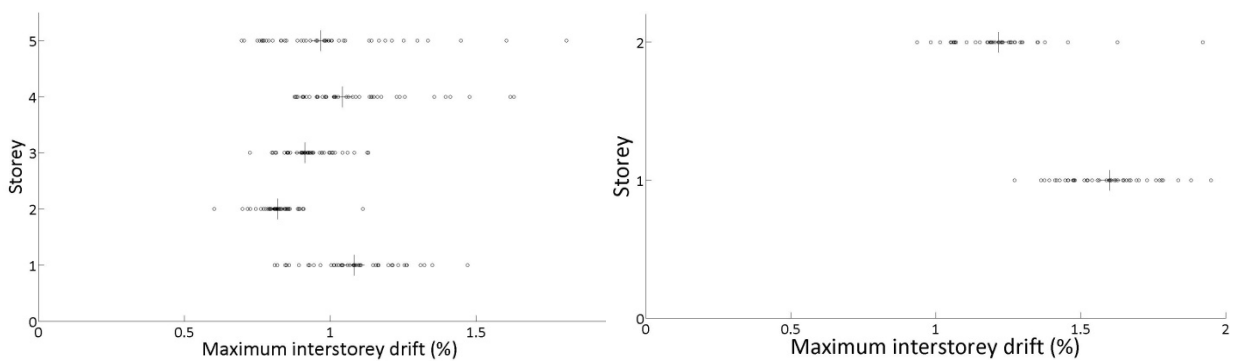


Fig. 5.23 Maximum interstorey drifts per story and ground motion for (a) 5-story and (b) 2-story

5.5 Conclusions

A 5-story and a 2-story steel building with FUSEIS with high-strength steel (HSS) links are designed in this chapter and their performance is evaluated using non-linear static (pushover) and incremental dynamic analysis (IDA). The FUSEIS consist of columns of S355 steel and hollow-section beam links of S700, similar with the test specimens described in Chapter 3. The case studies have the same plan views and applied loads and their seismic design is according to EN1998-1 (assuming q -factor 3.5). Given the flexibility of FUSEIS, the interstorey drift limitation expressed in EN1998-1 is critical for design. In the 5-story case study, this is resolved by using a combination of moment-resisting frame action and FUSEIS to provide lateral stability. Hence, strong beams are rigidly connected with the FUSEIS columns at selected locations. In the 2-story building, lateral stability is provided by the FUSEIS systems alone, and thus all beams are simply connected to the columns.

The combination of stiffness demands with the high strength of the dissipative members resulted in relatively small utilization ratios of the links and consequently increased magnification factors for the capacity checks. Overall, this application of HSS does not fully capitalize its advantage related with weight reduction. However the main scope of this research is to investigate whether dissipative elements consisting of HSS can meet the current Codes' requirements rather than suggesting a specific economic solution.

Following the design, representative 2D models are formulated for each case study, explicitly simulating material non-linearity with respect to in-cycle and cyclic degradation. To do so, the calibration results discussed in Chapter 4 are used as reference. Pushover analysis is performed resulting in similar and satisfactory behavior factors for both models. Based on the pushover results and the response of the most critical dissipative elements, limit states suitable for performance evaluation are defined in terms of inter-story drifts. More specifically, the deformation limits corresponding to Life Safety (LS) and Collapse Prevention (CP) are established for each case study.

Incremental Dynamic Analysis (IDA) is then performed following two different methodologies for performance evaluation: the widely-known FEMA 695 approach and the recently developed INNOSEIS method developed in the context of a European research project. Both methods investigate the acceptability of the q -factor applied in the design, through different processes and involve different sets of ground motions. The results of IDA are illustrated in terms of fragility graphs for each method, each model and each performance objective (LS or CP). In FEMA 695, acceptance is judged by the comparison of a calculated safety factor with acceptable values that mainly depend on the system's ductility, fundamental period and uncertainties. In INNOSEIS approach, compliance depends on the relationship between the mean annual frequency (MAF) of exceeding a limit state with an acceptable limit. An innovation of this method is that it is site specific as the MAF of each performance objective is the result of convolution between a fragility curve and a hazard curve. The above assessments resulted in the verification of the initially selected design q -factor for both case studies, although the "safety factors" of the 2-story were significantly smaller compared to the 5-story. Additional time-history analyses were performed to investigate the residual deformations of the models when subjected to ground-motions scaled at intensities corresponding to design level. The results were satisfactory as the maximum residual inter-story drift was less than 0.3% in both cases. Overall, an affirmative response is given to the question posed in this chapter's objectives. In any case, given the unconventionality of using HSS for the dissipative links, the investigation of additional archetype models would be suggested.

Chapter 6: Conclusions

6.1 Research overview

The present thesis explores experimentally and numerically the possible application of high-strength steel (HSS) in the dissipative elements of the innovative FUSEIS system. FUSEIS consists of a pair of closely-spaced strong columns rigidly connected via multiple dissipative links, which may be beams or pins. FUSEIS resists lateral loads by developing axial forces in the columns and bending in the links, while in case of pin links catenary action also develops. Part of the investigations was conducted in the framework of the European research project “MATCH”.

Recent technological advances in the steel-making process have led to the development of improved HSS that could provide substantial economic and environmental benefits. However, its structural application is still limited, while its seismic application is restricted. As discussed in Chapter 2, the main reasons for this are the different stress-strain characteristics of HSS, the lack of design rules and insufficient experimental/numerical data. The fact that current design rules practically limit the application range of HSS was highlighted.

Large-scale tests on FUSEIS involving different materials and types of links were conducted, as presented in Chapter 3. Eight tests on FUSEIS systems were performed: two on FUSEIS with S700MC hollow-section beam links, four on system with S355J2 HEA beam links and two tests on FUSEIS with S500MC cylindrical pin links. The system with S355 beams was more ductile, exhibiting no signs of damage for cyclic loading up to 3.5% drift while the system with S700 beams reached its peak resistance at approximately 2.5% drift. The system with S500 pins reached its peak resistance at about 3.1% drift under cyclic loading (corresponding to approximately 174 mrad links' rotation) and developed significant catenary action. Since there are no deformation limits applying for FUSEIS in the Codes, relevant values for Moment Resisting Frames and Braced Frames were used as reference, although direct comparison cannot be made. Without disregarding the relatively small number of tests, it could be said that the tested FUSEIS with S355 and S500 links exhibited good seismic behavior while the response of FUSEIS with S700 links was satisfactory. Comparison with previous tests involving FUSEIS with S235 beams suggested that the increase of yield strength may lead to a respective reduction of ductility. Direct comparison with previous tests on FUSEIS with S235 pins was not possible due to configuration modifications. However, there were some indications that the rotation capacity of the current system was improved.

Under Laboratory conditions, replacement of each link required approximately 45 minutes and required two workers. To facilitate mounting and dismounting, the FUSEIS links were bolted to the columns. This configuration influenced the test results, especially in the cases where larger forces developed. Therefore it was suggested to use welded connections in practice, since suitable cutters are available in case post-earthquake link replacements are required. This modification would lead to stiffer connections with no slip.

Chapter 4 focused on analytical and numerical models of the tested systems. FUSEIS resists horizontal loads as a vertical Vierendeel beam. Formulas were given for the systems' resistance considering the bending capacity of the beam links and the catenary action in the pin links. To capture the capacity of the FUSEIS with beams, the use of the mean value of the material's yield (f_y) and tensile strength (f_u) was suggested.

Simulations involved three different numerical models with increasing complexity (using 2D or 3D finite elements) in order to serve different purposes. The basic principles for each type of simulation were presented in Chapter 4. For the models consisting of beam elements, it was found that the consideration of semi-rigid connections for the links led to more accurate results. Parameters were suggested to define the properties of the fuses' potential plastic hinges (for each link type) in the template of SAP2000 commercial software. Another approach for material nonlinearity and cyclic damage in FUSEIS with beams was presented, based on the distributed plasticity concept and OpenSees platform. Finally, simulation of selected tests using solid finite elements in Abaqus was carried out. The main objective was to evaluate the innovative material subroutines developed within the MATCH project by other academic partners. The plasticity and damage parts were not coupled in the materials' constitutive equations, leading to less accurate simulation of the load degradation process. Overall, there was good agreement between experimental and numerical results. Damage simulation in terms of crack prediction was realistic in the increasing amplitude tests using S500 and S700 links but very conservative in the constant amplitude tests, especially for S355.

Chapter 5 discussed the design and performance evaluation of two case studies. They consisted of a two-story and a five-story building including FUSEIS systems with S700 hollow-section beam links. The structures were designed to comply with Eurocode's requirements, although the application of HSS in dissipative members is not currently allowed. A q -factor equal to 3.5 was considered albeit the respective suggested value by FUSEIS design guides is 5. Code's requirements for stiffness (interstory drift limitation) and class 1 cross-sections for the dissipative members did not allow for

significant size reduction of the HSS members leading to dissipative members with small utilization ratios. Despite this oxymoron aspect, the investigation's objective was to evaluate the case studies' seismic performance. To do so, non-linear analyses were performed on representative 2D models of the archetype structures. Material non-linearity was simulated according to the suggestions given in Chapter 4. Pushover analyses verified damage isolation in the dissipative links and resulted in behavior factors well above the design value. To consider cyclic loading demand on the models, Incremental Dynamic Analyses were then performed. The models were assessed at two performance levels (Life Safety and Collapse Prevention), defined on the basis of the pushover results and the response of the most critical fuses. Two methodologies were followed for performance evaluation: the widely-known FEMA 695 approach and the one recently developed during the INNOSEIS European research project. Both methods resulted in the acceptance of the case studies' design q -factor. Finally, the models' residual deformations were investigated using ground motion records scaled at design level intensities. It was shown that in both cases the residual deformations were insignificant.

6.2 Research limitations and suggestions for future investigations

The available number of HSS specimens limited the number of tests performed. Obviously the execution of more tests would have been preferable. In that case, the performance of a monotonic test prior to the cyclic tests would be useful as it would optimize the selection of suitable cyclic loading protocols while it would facilitate the simulation process. As mentioned, part of the research hereby presented was conducted in the frame of European research project "MATCH". This offered substantial benefits but also established some restrictions. One of the project's objectives was the development of material models that could be incorporated in Abaqus simulations and serve for damage prediction in various dissipative members of different steel grades. To do so, the same specimen profiles were tested in different configurations and their dimensions were determined by the capacities of all involved partners (academic and industrial). This led to FUSEIS systems with significantly different lateral resistance. In addition, the tests on FUSEIS beams involved different types of profiles: hollow-sections of S700MC steel and HEA of S355J2 steel. Considerations of the energies absorbed during the tests did not indicate a deterministic effect of the profile type. In any case, comparisons between the two systems are made with reservations regarding the size effect and the different profile type. Experimental and accompanying numerical investigations on size effect would be suggested. To focus the

investigation on the effect of stress-strain characteristics of different materials, comparative tests on links with the same cross-sections (e.g. welded I-profiles) would also be suggested.

Regarding the system with S700MC beams, five different profiles were used (square or circular) for the aforementioned reasons. This led to sequential yielding and facilitated monitoring of the damage process. However, it complicated the test's simulation using beam finite elements. Eventually similar hinge parameters were assumed for square and circular hollow-sections, which is not necessarily the case. It is thus suggested to avoid testing systems including different types of link profiles, unless relevant component tests have been conducted in advance.

Regarding the FUSEIS with S500MC pins, the specimens had very small diameters due to fabrication limitations. Test results showed that the cross-sections' size significantly affected the critical link rotation at crack initiation. Further experimental investigations involving larger pin sizes are suggested. Component tests for parametric investigations on the pins' length could produce interesting results.

As discussed, the bolted link connections facilitated mounting in the Laboratory but occasionally influenced the results. The application of welded connections was thus suggested. The efficiency of such configuration should be experimentally examined.

The suggested experimental investigations on FUSEIS with larger links would also be beneficial for further numerical investigations on building case studies. As discussed, simulation of material non-linearity in the case study models was based on the assumption that the parameters obtained from test calibration are valid for larger link lengths and sizes. To produce efficient design guidelines suitable for different link types and materials, a wider experimental and numerical database is required.

The behavior of FUSEIS with pin links is more complicated due to the catenary action developed in large deformations. As a result, their simulation using standard beam finite elements leads to oversimplifications. It would be interesting to investigate simulations with alternative approaches involving, for example, parallel materials or cable elements.

Regarding the Abaqus numerical simulations, there is some room for modeling improvements (e.g. mesh refinement in critical areas and the nonlinear properties of connectors' in the pin links). Furthermore, a coupled plasticity-and-damage model should be used for future investigations,

which was not fully functional at the time the current simulations took place. Given the significant computational demands for the simulation of the large-scale cyclic tests, solutions should be considered regarding the practicality of these numerical analyses.

Regarding the design and evaluation of building case studies, the investigation of additional structures with different numbers of stories and configurations is suggested. Furthermore, the examination of an additional limit state corresponding to damage limitation or crack initiation would be interesting. In general, when designing a building with FUSEIS, economy is related with the structure's overall stiffness. This was more evident here, as the application of HSS normally leads to reduction of member sizes which was contradicted by stiffness demands. The rigid connection of FUSEIS systems via strong beams and the combination of FUSEIS with MRF, as investigated here, gave some promising results. Parametric investigations on the same building layout involving different configurations for lateral stability could be conducted to provide optimum design solutions. Hybrid solutions could be examined in order to combine the advantages of high-strength and conventional steel.

6.3 Overall conclusion and contribution

The main objective of this research was to contribute in an ongoing international discussion on the relevance of high-strength steel (HSS) to seismic design. In this direction, large-scale cyclic tests on FUSEIS with HSS dissipative elements were conducted. Up to date, literature on cyclic tests on systems with HSS members is rather limited.

In addition, this research broadened the available database for FUSEIS innovative system which had been investigated in the past with links of S235 steel. Suggestions for design and simulation are provided, using SAP2000 and OpenSees applications. The configuration of the system with pin links was simplified in the current study.

Previous research suggested simple connections between the FUSEIS and the rest of the structure. In this case, aiming to reduce member sizes while maintaining stiffness, alternative configurations were investigated, involving rigid connections between FUSEIS systems and/or moment resisting frames.

The question posed in the introduction was not whether HSS is preferable to conventional steel but whether its hysteretic behavior can be sufficient for dissipative zones. The results were encouraging, although further investigations would be required. The tested systems exhibited satisfactory response, although their ductility decreased with yield strength. The relevant case

studies were designed with a q -factor equal to 3.5 which was later verified via different methodologies. However, it should be noted that the specific application of HSS in FUSEIS dissipative members did not seem to provide financial incentives. Viable applications of HSS in seismic resistant systems would probably have to involve a combination of conventional and high-strength steel subsystems to account for stiffness demands or be established in low-seismicity regions.

Chapter 7: References

- Abaqus 6.14 documentation, Simulia, Dassault Systèmes
- Acun B., Athanasopoulou A., Pinto A., Carvalho E., Fardis M. (2012) Eurocode 8: Seismic Design of Buildings Worked examples, European Commission, Joint Research Centre. DOI: 10.2788/91658
- Amlung L., Eichler B., Schäfer D., Vayas I., Karlos V. et al. (2009) PLASTOTOUGH: Modern Plastic Design for Steel Structures, Final Report, Research Programme of the Research Fund for Coal and Steel, European Commission
- ANSI/AISC 360–16, Specification for Structural Steel Buildings, American Institute Of Steel Construction, 2016
- ASCE 7-05, Minimum Design Loads for Buildings and Other Structures, American Society of Civil Engineers, 2006
- Avgerinou S. and Vayas I. (2020) High-strength steel on dissipative elements in seismic resistant systems: tests and simulations, *Journal of Constructional Steel Research*, 172, DOI: 10.1016/j.jcsr.2020.106173)
- Avgerinou S., Hoffmeister B., Thanopoulos P., Vayas I. (2020) Erdbebensichere Bauten mit dissipativen Elementen aus hochfestem Stahl, *Stahlbau* (submitted)
- Bai Y. and Wierzbicki T. (2008) A new model of metal plasticity and fracture with pressure and Lode dependence, *International Journal of Plasticity*, 24(6): 1071–1096. DOI: 10.1016/j.ijplas.2007.09.004
- Bakalis K and Vamvatsikos D (2018) Seismic Fragility Functions via Nonlinear Response History Analysis, *ASCE J. Struct. Eng.*, 144(10): 04018181, DOI:10.1061/(ASCE)ST.1943-541X.0002141
- Baker J.W. and Corenll A.C. (2006) Spectral shape, epsilon and record selection, *Earthquake Engng Struct. Dyn.*, 35: 1077–1095, DOI: 10.1002/eqe.571
- Ban H., Shi G., Shi Y., Wang Y. (2012) Overall buckling behavior of 460 MPa high strength steel columns: Experimental investigation and design method, *Journal of Constructional Steel Research*, 74: 140–150, DOI: 10.1016/j.jcsr.2012.02.013
- Ban H. and Shi G. (2017) A review of research on high-strength steel structures, *Proceedings of the Institution of Civil Engineers - Structures and Buildings*, ISSN 0965-0911, Volume 171 Issue 8, August, 2018, pp. 625-641, DOI: 10.1680/jstbu.16.00197
- Ban H. Y., Shi G., Shi Y. J., Wang, Y. Q. (2011) Research Progress on the Mechanical Property of High Strength Structural Steels, *Advanced Materials Research*, 250–253: 640–648. DOI: 10.4028/www.scientific.net/amr.250-253.640

- Bao Y. and Wierzbicki T. (2004) On fracture locus in the equivalent strain and stress triaxiality space, *International Journal of Mechanical Sciences* 46(1): 81–98. DOI: 10.1016/j.ijmecsci.2004.02.006
- Barsoum I. and Faleskog J. (2007) Rupture mechanisms in combined tension and shear-Experiments, *International Journal of Solids and Structures*, 44: 1768–1786, DOI: 10.1016/j.ijsolstr.2006.09.031
- Beg D. and Hlandik L. (1996) Slenderness Limit of Class 3 I Cross-sections Made of High Strength, Steel. *J. Construct. Steel Res.* Vol. 38, No. 3: 201-217
- Bjorhovde R. (2010) Performance and Design Issues for High Strength Steel in Structures, *Advances in Structural Engineering* Vol. 13 No. 3: 403-411
- Bjorhovde R. (2004) Development and use of high performance steel, *J Constr Steel Res*, 60(3): 393–400. DOI: 10.1016/S0143-974X(03)00118-4
- Bosco M., Marino E.M., Rossi P.P. (2012) Design of steel frames with buckling restrained braces, paper presented at 15th World Conference on Earthquake Engineering (15WCEE), Lisboa, September 2012
- BRI (1996) A survey report for building damages due to the 1995 Hyogo-Ken Nanbu Earthquake, Building Research Institute Ministry of Construction. Japan.
- Calado L. and Castiglioni C.A. (1996) Steel beam-to-column connections under low-cycle fatigue experimental and numerical research, paper no.1227 presented at 11th World Conference on Earthquake Engineering (11WCEE), ISBN: 0 08 042822 3
- Calado L., Proenca J.M., Espinha M., Castiglioni C.A. (2013) Hysteretic behavior of dissipative bolted fuses for earthquake resistant steel frames, *Journal of Constructional Steel Research*, 85: 151–162, DOI:10.1016/j.jcsr.2013.02.016
- Castiglioni C.A., Kanyilmaz A., Calado L. (2012) Experimental analysis of seismic resistant composite steel frames with dissipative devices, *Journal of Constructional Steel Research*, 76: 1–12, DOI:10.1016/j.jcsr.2012.03.027
- Chatzopoulou G., Karamanos S.A., Varelis G.E. (2016) Finite element analysis of UOE manufacturing process and its effect on mechanical behavior of offshore pipes, *International Journal of Solids and Structures*, 83: 13–27. DOI: 10.1016/j.ijsolstr.2015.12.020
- Chen S., Chen X., Wang Y.B., Lu Z., Li G.Q. (2016) Experimental and numerical investigations of Q690D H-section columns under lateral cyclic loading. *Journal of Constructional Steel Research*, 121: 268–281. DOI:10.1016/j.jcsr.2016.02.015
- Chen S.J., Yeh C.H., Chu J.M. (1996) Ductile Steel Beam-to-column connections for seismic resistance, *J. Struct. Eng*, 122(11): 1292-1299

- Christopoulos C. Filiatrault A., Uang C.M. (2002b) Posttensioned Energy Dissipating Connections for Moment-Resisting Steel Frames, *J. Struct. Eng.*, 128: 1111-1120, DOI: 10.1061/(ASCE)0733-9445(2002)128:9(1111)
- Choi H., Erochko J., Christopoulos C., Tremblay R. (2008) Comparison of the Seismic Response of Steel Buildings Incorporating Self-Centering Energy Dissipative Braces, Buckling Restrained Braced and Moment Resisting Frames, paper presented at 14th World Conference on Earthquake Engineering (14WCEE), October 2008, Beijing
- Chopra A.K. and McKenna F. (2015) Modeling viscous damping in nonlinear response history analysis of buildings for earthquake excitation, *Earthquake Engng Struct. Dyn.* 2016; 45:193–211, DOI: 10.1002/eqe.2622"
- Christopoulos C., Filiatrault A., Folz B. (2002a) Seismic response of self-centring hysteretic SDOF systems, *Earthquake Engng Struct. Dyn.* 2002; 31:1131–1150. DOI: 10.1002/eqe.152
- Christopoulos C., Tremblay R., Kim H.J., Lacerte M. (2008) Self-Centering Energy Dissipative Bracing System for the Seismic Resistance of Structures: Development and Validation, *J. Struct. Eng.* 2008.134:96-107. DOI: 10.1061/(ASCE)0733-9445(2008)134:1(96)
- Coburn A., Spence R. (2002) *Earthquake Protection*, 2002 John Wiley & Sons, Ltd ISBN:9780471496144
- Cornell C.A., Jalayer F., Hamburger R.O., Foutch D. (2002) Probabilistic Basis for 2000 SAC Federal Emergency Management Agency Steel Moment Frame Guidelines, *Journal of Structural Engineering* 2002; 128(4): 526–533. DOI: 10.1061/(ASCE)0733-9445(2002)128:4(526)
- Deierlein G.G., Liel A.B. , Haselton C.B., Kircher C.A. (2008) ATC 63 Methodology for Evaluating Seismic Collapse Safety of Archetype Buildings, *Structures Congress*, April 24-26, 2008, Vancouver, Canada, DOI:10.1061/41016(314)48
- Dimakogianni D. (2017) Innovative seismic resistant systems FUSEIS with ductile pins. Dissertation, National Technical University of Athens, Faculty of Civil Engineering (in greek)
- Dimakogianni D., Dougka G., Vayas I. (2015) Seismic behavior of frames with innovative energy dissipation systems (FUSEIS1-2), *Engineering Structures*, 90: 83–95. DOI: 10.1016/j.engstruct.2015.01.054
- Dimakogianni D., Dougka G., Vayas I., Karydakis P. (2012) Innovative seismic-resistant steel frames (FUSEIS 1-2) - experimental analysis, *Steel Construction* 5: 212-221. DOI: 10.1002/stco.201210026
- Dougka G. (2016) Development of seismic resistant systems for multi-story buildings. Dissertation, National Technical University of Athens, Faculty of Civil Engineering (in greek)

- Dougka G., Dimakogianni D., Vayas I. (2014a) Innovative energy dissipation systems (FUSEIS 1-1) - Experimental analysis, *Journal of Constructional Steel Research* 96: 69-80. DOI: 10.1016/j.jcsr.2014.01.003
- Dougka G., Dimakogianni D., Vayas I. (2014b) Seismic behavior of frames with innovative energy dissipation systems (FUSEIS 1-1), *Earthquakes and Structures*, Vol. 6, No. 5: 561-580. DOI: 10.12989/eas.2014.6.5.561
- Drei A., Castiglioni C.A., Calado L., Vayas I. (2006) Seismic behavior of steel braced frames with ductile INERD™ connections, presented at *Stability And Ductility Of Steel Structures (SDSS06)*, Lisbon, Portugal, September 6-8, 2006
- Dubina D., Landolfo R., Stratan A., Vulcu C. (Eds), (2013) *Application of High Strength Steel in Seismic Resistant Structures*, Proceedings of the Workshop: Naples, Italy, 2013, ISBN: 978-973-638-522-0
- Dubina D., Stratan A., Dinu F. (2008) Dual high-strength steel eccentrically braced frames with removable links, *Earthquake Engng Struct. Dyn.* 2008; 37:1703–1720, DOI: 10.1002/eqe.828
- ECCS (1986) Recommended testing procedure for assessing the behavior of structural steel elements under cyclic loads. Technical committee 1: structural safety and loadings, technical working group 1.3: seismic design. European Convention for Constructional Steelwork, Brussels
- EN10025-2, Hot rolled products of structural steels - Part 2: Technical delivery conditions for non-alloy structural steels, European Committee for Standardization, 2004
- EN10025-4, Hot rolled products of structural steels - Part 4: Technical delivery conditions for thermomechanical rolled weldable fine grain structural steels, European Committee for Standardization, 2004
- EN10025-6, Hot rolled products of structural steels - Part 6: Technical delivery conditions for flat products of high yield strength structural steels in the quenched and tempered condition, European Committee for Standardization, 2004
- EN10149-2, Hot rolled flat products made of high yield strength steels for cold forming - Part 2: Technical delivery conditions for thermomechanically rolled steels, European Committee for Standardization, 2013
- EN1991-1, Eurocode 1: Actions on structures - Part 1-1: General actions - Densities, self-weight, imposed loads for buildings, European Committee for Standardization, 2002
- EN1993-1-1, Eurocode 3: Design of steel structures - Part 1-1: General rules and rules for buildings, European Committee for Standardization, 2003
- EN1993-1-10, Eurocode 3: Design of steel structures - Part 1-10: Material toughness and through-thickness properties, European Committee for Standardization, 2003

- EN1993-1-12, Eurocode 3 - Design of steel structures - Part 1-12: Additional rules for the extension of EN 1993 up to steel grades S700, European Committee for Standardization, 2007
- EN1993-1-8, Eurocode 3: Design of steel structures - Part 1-8: Design of joints, European Committee for Standardization, 2005
- EN1994-1-1, Eurocode 4: Design of composite steel and concrete structures- Part 1.1: General rules and rules for buildings, European Committee for Standardization, 2004
- EN1998-1, Eurocode 8: Design of structures for earthquake resistance - Part 1: General rules, seismic actions and rules for buildings, European Committee for Standardization, 2003
- EN1998-3, Eurocode 8: Design of structures for earthquake resistance Part 3: Assessment and retrofitting of buildings, European Committee for Standardization, 2004
- Engelhardt M.D., Winneberger T., Zekany A.J., Potyraj T.J. (1996) The Dogbone Connection: Part II, Modern Steel Construction, August 1996
- Feldmann M. and Schaffrath S. (2017) Assessing the net section resistance and ductility requirements of EN 1993-1-1 and EN 1993-1-12, Steel Construction, 10: 354-364. DOI: 10.1002/stco.201710036
- Feldmann M. and Schaffrath S. (2018) Application of damage theory to structures made from high-strength steels, Steel Construction, 11: 257-263. DOI: 10.1002/stco.201800016
- Feldmann M., Eichler B., Schäfer D., Sedlacek G., Vayas I., Karlos V., Spiliopoulos A. (2011) Toughness requirements for plastic design with structural steel, Steel Construction Design and Research, Volume 4, Issue 2, pp. 94-113 DOI: 10.1002/stco.201110013
- Feldmann M., Hoffmeister B. et al. (2017) Material Choice for Seismic Resistant Structures (MATCH), Final Report, Research Fund for Coal and Steel, Publications of the European Union. DOI: 10.2777/482642
- Feldmann M., Schillo N., Schaffrath S. et al. (2016) Rules on high strength steel (RUOSTE), Final Report, Research Fund for Coal and Steel, European Commission 2016
- FEMA 350, Recommended Seismic Design Criteria for New Steel Moment-Frame Buildings, Federal Emergency Management Agency, 2000
- FEMA 351, Recommended Seismic Evaluation and Upgrade Criteria for Existing Welded Steel Moment-Frame Buildings, Federal Emergency Management Agency, 2000
- FEMA 355D, State of the Art Report on Connection Performance, Federal Emergency Management Agency, 2000
- FEMA 355E, State of the Art Report on Past Performance of Steel Moment-Frame Buildings in Earthquakes, Federal Emergency Management Agency, 2000

- FEMA 356, PRESTANDARD AND COMMENTARY FOR THE SEISMIC REHABILITATION OF BUILDINGS, Federal Emergency Management Agency, 2000
- FEMA 695, Quantification of Building Seismic Performance Factors, Federal Emergency Management Agency, 2000
- Frederick C.O. and Armstrong P.J. (1966, 2007) A mathematical representation of the multiaxial Bauschinger effect. *Materials at High Temperatures* 24(1): 1–26. DOI: 10.3184/096034007X207589
- Fukumoto Y. (1996) New constructional steels and structural stability, *Engineering Structures*, Vol. 18, No. 10, pp. 786-791, 1996
- Galambos T. V., Hajjar J. F., Earls, C. J., Gross J.L. (1997). Required properties of high-performance steels. Rep. No. NISTIR 6004, National Institute of Standard and Technology (NIST).
- Gao X., Zhang G., Roe C.(2009) A study on the effect of the stress state on ductile fracture, *International Journal of Damage Mechanics* 19(1): 75–94. DOI:10.1177/1056789509101917 "
- GB 50017-2017, Standard for design of steel structures, National Standard of the People's Republic of China, Beijing 2017
- GB50011-2010, Code for seismic design of buildings, National Standard of the People's Republic of China, Beijing 2010
- Geradin M., Pinto A., Dimova S. (Eds, 2008) Commentary And Worked Examples to EN1993-1-10 "Material toughness and through thickness properties" and Other Toughness Oriented Rules in EN 1993, JRC Scientific and Technical Reports, JRC 47278, EUR 23510 EN, European Communities, 2008
- Giardini D., Woessner J., Danciu L., Crowley H., Cotton F., Grünthal G. et al. (2013) Seismic Hazard Harmonization in Europe (SHARE): Online Data Resource, DOI: 10.12686/SED-00000001-SHARE
- Green P.S., Sauce R., Ricles J.M. (2002) Strength and ductility of HPS flexural members, *Journal of Constructional Steel Research* 58 (2002):907–941
- Günther H.P., Raoul J., Kuhlmann U. (2005) Use and application of high-performance steels for steel structures. International Association for Bridge and Structural Engineering (IABSE-AIPC-IVBH), Zürich, Switzerland
- Haijjer G. (1961) Economy of High Strength Steel Structural Members, *Journal of the Structural Division*, 1961, Vol. 87, Issue 8, p. 1-24
- Hai L.T., Li G.Q., Wang Y.B., Sun F.F., Jin H.J. (2019) Experimental investigation on cyclic behavior of Q690D high strength steel H-section beam-columns about strong axis, *Engineering Structures* 189, p. 157–173, DOI: 10.1016/j.engstruct.2019.03.060

- Hancock J. W. and Mackenzie A. C. (1976) On the mechanisms of ductile failure in high-strength steels subjected to multi-axial stress-states, *Journal of the Mechanics and Physics of Solids*, 24(2-3), 147–160. DOI:10.1016/0022-5096(76)90024-7
- Hjelmstad K.D. and Popov E.P. (1984) Characteristics of eccentrically braced frames, *J. Struct. Eng.* 1984.110:340-353
- Hu F., Shi G., Shi Y. (2017) Experimental study on seismic behavior of high strength steel frames: Global response, *Engineering Structures* 331: 163-179. DOI: 10.1016/j.engstruct.2016.11.013
- Kanyilmaz A., Muhaxheri M., Castiglioni C.A. (2019) Influence of repairable bolted dissipative beam spllices (structural fuses) on reducing the seismic vulnerability of steel-concrete composite frames, *Soil Dynamics and Earthquake Engineering* 119: 281-298. DOI: 10.1016/j.soildyn.2019.01.007
- Karidakis Ph., 2011, Innovative systems for stiffness and energy dissipation (INSTED). Dissertation, National Technical University of Athens, Faculty of Civil Engineering (in greek)
- Kato B. (1990a) Role of Strain-hardening of Steel in Structural Performance, *ISIJ International*, Vol. 30 (1990), No. 11, pp. 1003-1009
- Kato B. (1990b) Deformation Capacity of Steel Structures, *J. Construct. Steel Research* 17 (1990) 33-94
- Khatib I.F., Mahin S.A., Pister K.S. (1988), *Seismic Behavior of Concentrically Braced Steel Frames*. Report No. UCB/EERC-88/01, Earthquake Engineering Research Center, University of California, Berkeley
- Kohrangi M, Vamvatsikos D, Bazzurro P. (2017) Site dependence and record selection schemes for building fragility and regional loss assessment, *Earthquake Engng Struct. Dyn.*, vol. 46 (10): 1625-1643. DOI: 10.1002/eqe.2873
- Kuwamura H. (1998) Fracture of steel during an earthquake state-of-the-art in Japan, *Engineering Structures*, Volume 20, Issues 4–6: 310-322, DOI:10.1016/S0141-0296(97)00030-8
- Lee C.H, Han K.H., Uang C.M., Kim D.K., Park C.H., Kim J.H. (2013) Flexural Strength and Rotation Capacity of I-Shaped Beams Fabricated from 800-MPa Steel, *J. Struct. Eng.*, 139(6): 1043-1058, DOI: 10.1061/(ASCE)ST.1943-541X.0000727
- Leon T. R. and Yang C.S. (2003) Special Inverted-V-Braced Frames with Suspended Zipper Struts, *International Workshop on Steel and Concrete Composite Construction, IWSCCC*, National Center for Research on Earthquake Engineering, Taipei, Taiwan
- Li T.J, Li G.Q., Chan S.L., Wang Y.B. (2016a) Behavior of Q690 high-strength steel columns: Part 1: Experimental investigation, *Journal of Constructional Steel Research* 123 (2016) 18–30, DOI: 10.1016/j.jcsr.2016.03.026

- Li T.J., Liu S.W., Li G.Q., Chan S.L., Wang Y.B. (2016b) Behavior of Q690 high-strength steel columns: Part 2: Parametric study and design recommendations, *Journal of Constructional Steel Research* 122 (2016) 379–394, DOI:10.1016/j.jcsr.2016.03.027
- Lian J., Sharaf M., Archie F., Münstermann S.(2012) A hybrid approach for modelling of plasticity and failure behavior of advanced high-strength steel sheets, *International Journal of Damage Mechanics* 22(2): 188-218. DOI: 10.1177/1056789512439319
- Lin T., Haselton C.B., Baker J.W. (2013a) Conditional spectrum-based ground motion selection. Part I: Hazard consistency for risk-based assessments, *Earthquake Engng Struct. Dyn.*, 42: 1847-1865. DOI: 10.1002/eqe.2301
- Lin T., Haselton C.B., Baker J.W. (2013b) Conditional spectrum-based ground motion selection. Part II: Intensity-based assessments and evaluation of alternative target spectra, *Earthquake Engng Struct. Dyn.*, vol 42: 1867–1884. DOI: 10.1002/eqe.2303
- Mazzolani F.(Ed.) (2000) *Moment Resistant Connections of Steel Frames in Seismic Areas: Design and Reliability*, E & FN Spon ed., 2000.
- McClintock FA (1968) A criterion for ductile fracture by growth of holes. *Journal of Applied Mechanics* 35(2):363–371
- McDermott J.F. (1969a) Plastic Bending of A514 Steel Beams, *Journal of the Structural Division*, 1969, Vol. 95, Issue 9, Pg. 1851-1871
- McDermott J.F. (1969b) Local Plastic Buckling of A514 Steel Members, *Journal of the Structural Division*, 1969, Vol. 95, Issue 9, Pg. 1837-1850
- Mirza M.S., Barton D.C., Church P. (1996) The effect of stress triaxiality and strain-rate on the fracture characteristics of ductile metals. *J Mater Sci* 31, 453–461, DOI:10.1007/BF0113916
- Moore K., Malley O.J., Engelhardt M. (1999) Design of reduced beam section moment frame connection, *Structural Steel Educational Council: Technical Information and Product Service*. California, 1999
- Ohata M. and Toyoda M. (2004) Damage concept for evaluating ductile cracking of steel structure subjected to large-scale cyclic straining, *Science and Technology of Advanced Materials*, 5:1-2, 241-249, DOI: 10.1016/j.stam.2003.10.007
- Open System for Earthquake Engineering Simulation (OpenSees), <https://opensees.berkeley.edu/>
- Plumier A., Doneux C., Castiglioni C.A., Brescianini J., Crespi A. et al. (2004) Two INnovations for Earthquake Resistant Design - The INERD Project, Final Report. Research Fund for Coal and Steel, Publications of the European Union. <http://hdl.handle.net/2268/20815>
- Plumier A. (1990) New idea for safe structure in seismic zone. *Proceedings of IABSE symposium, mixed structures including new materials*. 1990. p. 431_36, Brussels.

- Popov E.P. and Engelhardt M.D. (1988) Seismic Eccentrically Braced Frames, *J. Construct. Steel Research* 10: 321-354
- Popov E.P., Blondet M., Stepanov L. (1996) Application of dog bones for improvement of seismic behavior of steel connections, Report no UCB/EERC 96/05. USA, 1996.
- Prager W. (1949) Recent Developments in the Mathematical Theory of Plasticity, *Journal of Applied Physics* 20, 235 (1949); DOI: 10.1063/1.1698348
- Rasmussen K.J.R and Hancock G.J. (1992) Plate Slenderness Limits for High Strength Steel Sections, *J. Construct. Steel Research* 23: 73-96
- Rice JR and Tracey DM (1969) On ductile enlargement of voids in triaxial stress fields. *Journal of the Mechanics and Physics of Solids* 17(3): 201–217
- Ricles J.M., Sause R., Green P.S. (1998) High-strength steel: implications of material and geometric characteristics on inelastic flexural behavior, *Engineering Structures*, Vol. 20, pp. 323-335
- SAP2000, Structural and Earthquake Engineering Software, Computers and Structures Inc
- Sause R. and Fahnestock L.A. (2001) STRENGTH AND DUCTILITY OF HPS-100W I-GIRDERS IN NEGATIVE FLEXURE, *J. Bridge Eng.* 2001.6: 316-323
- Schillo N. and Feldmann M. (2018) Experiments on the rotational capacity of beams made of high-strength steel, *Steel Construction*, 11: 42-48. DOI: 10.1002/stco.201810009
- Shi G. and Chen X. (2018), Research advances in HSS structures at Tsinghua University and codification of the design specification, *Steel Construction*, 11: 286-293. DOI: 10.1002/stco.201800023
- Shi G., Ban H., Bijlaard F.S.K, (2012) Tests and numerical study of ultra-high strength steel columns with end restraints, *Journal of Constructional Steel Research*, 70: 236–247, DOI: 10.1016/j.jcsr.2011.10.027
- Shi G., Hu F.X., Shi Y.J. (2014) Recent research advances of high strength steel structures and codification of design specification in China, *Int J Steel Struct*, 14(4): 873–87. DOI: 10.1007/s13296-014-1218-7
- Shi G., Wang M., Wang Y., Wang, F. (2013) Cyclic Behavior of 460 MPa High Strength Structural Steel and Welded Connection under Earthquake Loading, *Advances in Structural Engineering*, 16(3), 451–466. DOI: 10.1260/1369-4332.16.3.451
- Shome N. and Cornell C. A. (1999) Probabilistic Seismic Demand Analysis of Nonlinear Structures, RMS Report-35, Reliability of Marine Structures Group, Stanford University, Stanford.
- Spangemacher R. (1992) Zum Rotationsnachweis von Stahlkonstruktionen, die nach dem Traglastverfahren berechnet werden. PhD thesis, RWTH Aachen, 1992.

- Steenbergen H.M.G.M., Bijlaard F.S.K., Daniels B.J. (1996) The influence of material properties on plastic hinge rotational capacity and strength. TNO Report 96-CON-R1224
- Takeuchi T. (2018) Buckling-Restrained Brace: History, design and applications, 9th International Conference on Behavior of Steel Structures in Seismic Areas (STESSA 2018) Christchurch, Newzealand, February 14-16, 2018 , <https://www.researchgate.net/publication/323522666>
- Tenchini A., Rebelo C., Da Silva L. et al. (2011) Seismic performance of high strength steel building, paper presented at EUROSTEEL 2011, Budapest
- Thanopoulos P., 2006, Behavior of seismic resistant steel frames with energy absorbing devices. Dissertation, National Technical University of Athens (in greek) <https://www.didaktorika.gr/eadd/handle/10442/16259>
- Tremblay R. and Christopoulos C. (2005) Self-centering energy dissipative brace apparatus with tensioning elements. Int. Publication No. WO05085543, World Intellectual Property Organization
- Tremblay R., Lacerre M., Christopoulos C. (2008) Seismic Response of Multistory Buildings with Self-Centering Energy Dissipative Steel Braces, *J. Struct. Eng.* 2008.134:108-120, DOI: 10.1061/ASCE 0733-9445 2008 134:1 108
- Tsarpalis P, Bakalis K, Thanopoulos P, Vayas I, Vamvatsikps D (2020) Pre-normative assessment of behavior factor for lateral load resisting system FUSEIS pin-link, *Bull Earthquake Eng*, 18: 2681–2698, DOI: 10.1007/s10518-020-00799-y
- Ucak A. and Tsopeles P. (2011) Constitutive Model for Cyclic Response of Structural Steels with Yield Plateau, *Journal of Structural Engineering*, 137(2): 195–206. DOI: 10.1061/(ASCE)ST.1943-541X.0000287
- Uriz P. and Mahin S.A (2008) Toward Earthquake-Resistant Design of Concentrically Braced Steel-Frame Structures, PEER Report 2008/08, Pacific Earthquake Engineering Research Center, University of California, Berkeley
- Valente M., Castiglioni C.A., Kanyilmaz A. (2016) Dissipative devices for earthquake resistant composite steel structures: bolted versus welded solution, *Bull Earthquake Eng*, 14: 3613, DOI: 10.1007/s10518-016-0002-9
- Vamvatsikos D. and Cornell C.A. (2002) Incremental Dynamic Analysis, *Earthquake Engng Struct Dyn*, vol 31(3), Special Issue: Special Topics Issue on Performance-based Earthquake Engineering, p. 491-514, DOI: 10.1002/eqe.141
- Vamvatsikos D. and Cornell C.A. (2005) Seismic performance, Capacity and Reliability of Structures as seen through Incremental Dynamic Analysis, Report no. 151, The John A. Blume Earthquake Engineering Center, Department of civil and Environmental Engineering , Stanford University

- Vamvatsikos D., Bakalis K., Kohrangi M., Thanopoulos P., Vayas I., Castiglioni C.A., Kanyilmaz A. et al. (2017) Innovative anti-seismic devices and systems - The INNOSEIS Project, D2.1 Recommended procedure for EN1998-compatible behavior factor evaluation of new structural systems. Research Programme of the Research Fund for Coal and Steel. http://innoseis.ntua.gr/deliverables/INNOSEIS_D2.1_QFactorMethodologyReport_revFinal.pdf
- Vamvatsikos D., Bakalis K., Kohrangi M., Pyrza S. (2020) A risk-consistent approach to determine EN1998 behavior factors for lateral load resisting systems, *Soil Dynamics and Earthquake Engineering*, Volume 131, DOI: 10.1016/j.soildyn.2019.106008
- Van Es S., Slot H., Steenbergen H., Maljaars J., Pijpers R. (2018) Use of HSS and VHSS in steel structures in civil and offshore engineering, *Steel Construction*, 11: 249-256. DOI: 10.1002/stco.201800018
- Vayas I. (2003) ΣΙΔΗΡΕΣ ΚΑΤΑΣΚΕΥΕΣ- ΑΝΑΛΥΣΗ ΚΑΙ ΔΙΑΣΤΑΣΙΟΛΟΓΗΣΗ, ΕΚΔ. ΚΛΕΙΔΑΡΙΘΜΟΣ, ISBN:960-209-668-3 (in greek)
- Vayas I. (Ed.), (2017) Innovative anti-seismic devices and systems, INNOSEIS Project RFCS-02-2015. ECCS- European Convention for Constructional Steel. ISBN: 978-92-9147-136-2 (<http://innoseis.ntua.gr/>)
- Vayas I. and Thanopoulos P. (2005) Innovative dissipative (INERD) pin connections for seismic resistant braced frames. *International Journal of steel structures* 5(5): 453-464
- Vayas I., Karydakis Ph., Dimakogianni D., Dougka G., Castiglioni C.A., Kanyilmaz A. et al. (2013) Dissipative devices for seismic-resistant steel frames (FUSEIS), Final Report. Research Fund for Coal and Steel, Publications of the European Union. DOI: 10.2777/88177
- Vayas I., Dougka G., Dimakogianni D. (2014) Umbau und Erweiterung des Kindergartens der Deutschen Schule Athen, *Bauingenieur* 8, H. 6, 212-221
- Vayas I., Ermopoulos J., Ioannidis G. (2019) Design of steel structures to Eurocodes, Springer, ISBN 978-3-319-95473-8
- Verswijver K., De Meyer R., Denys R., De Kooning E. (2009) The Writings of Belgian Engineer Arthur Vierendeel (1852-1940): Homo Universalis or Contemporary Propagandist?, Proceedings of the Third International Congress on Construction History, Cottbus, 2009, ISBN
- Vulcu C., Stratan A., Ciutina A., Dubina D. (2017) Beam-to-CFT High-Strength Joints with External Diaphragm. I: Design and Experimental Validation, *J. Struct. Eng.*, 2017, 143(5): 04017001
- Wallin K. (2011) Fracture Toughness of Engineering Materials: Estimation and Application, EMAS Publications

- Wang Y.B., Li G.Q., Cui W., Chen S.W. (2014) Seismic behavior of high strength steel welded beam-column members, *Journal of Constructional Steel Research*, 102: 245–255, DOI: 10.1016/j.jcsr.2014.07.015
- Wang Y.B., Li G.Q., Cui W., Chen S.W., Sun F.F. (2015) Experimental investigation and modeling of cyclic behavior of high strength steel, *Journal of Constructional Steel Research*, 104: 37–48, DOI: 10.1016/j.jcsr.2014.09.009
- Wickersheimer D.J. (1976) The Vierendeel, *Journal of the Society of Architectural Historians*, Vol. 35, No. 1, pp. 54-60, URL: <http://www.jstor.org/stable/988971>
- Xie Q. (2004) State of the art of buckling-restrained braces in Asia, *Journal of Constructional Steel Research* 61 (2005) 727–748, DOI: 10.1016/j.jcsr.2004.11.005
- Xie Q. (2005) State of the art of buckling-restrained braces in Asia, *Journal of Constructional Steel Research* 61 (2005) 727–748, DOI: 10.1016/j.jcsr.2004.11.005
- Yang C.S., Leon R.T., Des Roches R. (2008a) Design and behavior of zipper-braced frames, *Engineering Structures* 30 (2008): 1092–1100
- Yang C.S., Leon R.T., DesRoches R. (2008b) Pushover Response of a Braced Frame with Suspended Zipper Struts, *Journal of Structural Engineering*, ASCE, October 2008: 1619-1626, DOI: 10.1061/(ASCE)0733-9445(2008)134:10(1619)
- Yang T.Y, Moehle J.P, Stojadinovic B. (2009) Performance Evaluation of Innovative Steel Braced Frames, PEER Report 2009/103, Pacific Earthquake Engineering Research Center, University of California, Berkeley
- Ziegler (1959) Ziegler H. (1959) A modification of Prager’s hardening rule, *Quart. Appl. Math.* 17 (1959), 55-65, DOI: 10.1090/qam/104405

Curriculum vitae in brief

Stella Avgerinou was born in Athens in 1987. She holds a Diploma in Civil Engineering from the National Technical University of Athens - NTUA (2010) and a MSc in Analysis and Design of Earthquake Resistant Structures from NTUA (2012). In June 2013, she joined the Institute of Steel Structures of the School of Civil Engineering (NTUA) as a PhD student, under the supervision of prof. I. Vayas. She completed her doctoral studies in June 2020. As a researcher in NTUA, she has participated in several experimental campaigns and course lectures and she has supervised students' diploma theses. In addition, she has participated in various European Research Projects for which she has also handled administrative issues. Since 2010, she has been working as a free-lancer civil engineer, mostly in collaboration with civil engineers N. Avgerinos and prof. I. Vayas. Her main subjects are: structural analysis and design of buildings and bridges and seismic design of steel pallet racks.

Publications in peer-reviewed journals

1. Avgerinou S., Vayas I., Adamakos K., "Stahl in der Bildhauerei – Tragwerksentwurf der Skulptur "le chemin de l'eau" in Paris", *Stahlbau*, Vol. 85 (Januar 2016), pp.52-58, Ernst & Sohn, DOI: 10.1002/stab.201610350
2. Avgerinou S., Lignos X., Thanopoulos P., Spiliopoulos A., Vayas I., "Moment-resisting-frames under cyclic loading: Large scale tests and validation of plasticity and damage numerical models", *Soil Dynamics and Earthquake Engineering* 115 (2018), <https://doi.org/10.1016/j.soildyn.2018.08.036>
3. Vayas I., Avgerinou S., Thanopoulos P., "Versagen eines Regallagers in Athen", Ernst & Sohn Verlag für Architektur und technische Wissenschaften GmbH & Co. KG, Berlin · *Stahlbau* 87 (2018), Heft 1, DOI: 10.1002/stab.201810553
4. Avgerinou S., Lignos X., Tsarpalis D., Vayas I., "Full-scale tests on used steel storage racks", Ernst & Sohn Verlag für Architektur und technische Wissenschaften GmbH & Co. KG, Berlin. *Steel Construction* 12 (2019), No. 3, DOI: 10.1002/stco.201900009
5. Avgerinou S., Vayas I., "High-strength steel on dissipative elements in seismic resistant systems: tests and simulations", *Journal of Constructional Steel Research*, 172 (2020), <https://doi.org/10.1016/j.jcsr.2020.106173>
6. Avgerinou S., Hoffmeister B., Thanopoulos P., Vayas I., "Erdbebensichere Bauten mit dissipativen Elementen aus hochfestem Stahl", *Stahlbau* (2020) (submitted)

Publications in special issues

1. Vayas I., Avgerinou S., "Full scale tests on moment-resisting-frames under cyclic loading", Ernst & Sohn Verlag für Architektur und technische Wissenschaften GmbH & Co. KG, Berlin · ce/papers 1 (2017), No. 5 & 6, <https://doi.org/10.1002/cepa.570>

Papers presented in conferences

1. Adamakos K., Avgerinou S., Vayas I., "Estimation of the behavior factor of steel storage pallet racks", COMPDYN2013 (4th International Conference on Computational Methods in Structural Dynamics and Earthquake Engineering), Kos 2013
2. Avgerinou S., Adamakos K., Vayas I., "Structural design of sculpture formed with thin plate hollow sections and stainless steel", 8th Hellenic National Conference of Steel Structures, Tripoli 2014
3. Avgerinou S., Vayas I., "Behaviour of high strength steel FUSEIS seismic resistant systems", COMPDYN2015 (5th International Conference on Computational Methods in Structural Dynamics and Earthquake Engineering), Crete 2015
4. Vougioukas E., Avgerinou S., Theocharis K., "Response of repaired fuse beams to dynamic testing", COMPDYN2017 (6th International Conference on Computational Methods in Structural Dynamics and Earthquake Engineering), Rhodes 2017
5. Avgerinou S., Lignos X., Thanopoulos P., Vayas I., "Full scale tests on moment-resistant-frames under cyclic loading", EUROSTEEL 2017, Copenhagen 2017
6. Avgerinou S., Lignos X., Spiliopoulos A., Thanopoulos P., Vayas I., "Full scale tests on steel moment-resistant-frames under cyclic loading", 9th Hellenic National Conference of Steel Structures, Larisa, 2017

Publications in the framework of RFCS European Research Project MATCH (RFSR-CT-2013-00024)

1. "Material Choice for Seismic Resistant Structures (MATCH project), Final Report" , Feldmann M., Hoffmeister B., Schaffrath S., Bartsch H., Munstermann S., Vayas I., Avgerinou S., Salvatore W., Karamanos S. et al., RFSR-CT-2013-00024, Research Fund for Coal and Steel, Publications of the European Union, 2017